A sub-millimetre study of massive star formation within the W51 complex and Infrared Dark Clouds

A thesis submitted to the University of Hertfordshire
in partial fulfilment for the degree of Doctor of Philosophy

H A L Parsons

2011

Abstract

Despite its importance the fundamental question of how massive stars form remains unanswered, with improvements to both models and observations having crucial roles to play. To quote Bate *et al.* (2003) computational models of star formation are limited because "conditions in molecular clouds are not sufficiently well understood to be able to select a representative sample of cloud cores for the initial conditions". It is this notion that motivates the study of the environments within Giant Molecular Clouds (GMCs) and Infrared Dark Clouds (IRDCs), known sites of massive star formation, at the clump and core level.

By studying large populations of these objects, it is possible to make conclusions based on global properties. With this in mind I study the dense molecular clumps within one of the most massive GMCs in the Galaxy: the W51 GMC. New observations of the W51 GMC in the ^{12}CO, ^{13}CO and C^{18}O (3 – 2) transitions using the HARP instrument on the JCMT are presented. With the help of the clump finding algorithm CLUMPFIND a total of 1575 dense clumps are identified of which 1130 are associated with the W51 GMC, yielding a dense mass reservoir of $1.5 \times 10^5\,\mathrm{M}_\odot$ contained within these clumps. Of these clumps only 1% by number are found to be super-critical, yielding a super-critical clump formation efficiency of 0.5%, below current SFE estimates of the region. This indicates star formation within the W51 GMC will diminish over time although evidence from the first search for molecular outflows presents the W51 GMC in an active light with a lower limit of 14 outflows. The distribution of the outflows within the region searched found them concentrated towards the W51A region.

Having much smaller sizes and masses, obtaining global properties of clumps and cores within IRDCs required studying a large sample of these objects. To do this pre-existing data from the SCUBA Legacy Catalogue was utilised to study IRDCs within a catalogues based on 8 μm data. This data identifies 154 IRDC cores that are detected at 850 μm and 51 cores that were not. This work suggests that cores not detected at 850 μm are low mass, low column density and low temperature cores that are below the sensitivity limit of SCUBA at 850 μm. Utilising observations at 24 μm from the Spitzer space telescope, allows for an investigation of current star formation by looking for warm embedded objects within the cores. This work reveals 69% of the IRDC cores have 24 μm embedded objects. IRDC cores without associated 24 μm emission ("starless" IRDC cores) may have yet to form stars, or may contain low mass YSOs below the detection limit. If it is assumed that cores without 24 μm embedded sources are at an earlier evolutionary stage to cores with embedded objects a statistical lifetime for the quiescent phase of a few $10^3 - 10^4$ years is derived.

Acknowledgements

'The miracle isn't that I finished...The miracle is that I had the courage to start.'
John Bingham

Thompson I can barely believe we made it! Thank you for all you did: from the basics of physics (never do maths at high altitude) to your Jedi mind tricks ("it will all be OK") and the emotional support: it's been a heavy few years. The same thank you goes to Antonio, whom I must thank for banning the 's' word so I had to push myself, allowing me to fulfil my ultimate dream of observing in Hawaii and soon to work with the big blue box, SCUBA-2. Thank you to Mila and Mira who treated me like one of the *ohana*, and Jane who enjoyed stealth supervision.

Jim Collett, thank you for dealing with the multitude of embarrassing 'problems' I had, always making me leave your office with not only a greater understanding of all manner of things but also with food in hand. John the computer expert for keeping me out of trouble (and for rm -i) and the secretaries Avis, Kathy and Lorraine.

I would like to thank all those who work for the JAC including TOs: Jim Hoge who taught me amongst many thing that man can survive on three hours of sleep. The other TOs at the JCMT for keeping me in check up at the summit and who enjoyed being part of the 'shout out' from Radio 1 whilst observing in Hawaii, and the support astronomers for keeping me in check from sea-level. Thank you to David Berry and the JAC staff for all their help with my various starlink problems (and GAIA-3D: I love it!). 'Dank je wel' also goes to those at the University of Groningen for sparking my interest in this subject.

To all the astronomy postgrads, especially my room mates who enjoyed sharing all my weather updates (yes I really do love windows that much) its been fun! Same goes for the brain trust and my closest friends- I don't know where I'd be without all your support. Not forgetting Robert who is sadly missed.

Andrew who has supported me throughout, from the highs of Mauna Kea to the lows of paper writing (I think we can by pass Aunt Helen's advice about wall papering) thank you so much from the bottom of my heart. Same goes to my brother Robin (my new grammar guru along with my sister-in-law Anneke) and sister Sara (hope you enjoyed our "applied mathematics"). Dad who did not make it to see me graduate the first time round I know he would be proud for pursuing my dream, persevering when times were tough and smiling all the way. Finally I wish to thank and dedicate this Thesis to my mother who passed away in September 2010. The biggest source of inspiration, support and encouragement.

Mum I did it.

Contents

List of Figures

List of Tables

Chapter 1

Introduction

'An original idea. That can't be too hard. The library must be full of them.'
Stephen Fry

In the Southern Hemisphere, towards the constellations of Scorpius, Sagittarius and Ophiuchus the rich band of starlight known as the Milky Way reaches its maximum in intensity towards the centre of our Galaxy. Spanning away from these constellations in an anticlockwise direction this band of light stretches through Aquila, Cygnus, Cepheus, and Perseus until we reach Auriga, in the Northern hemisphere, the location of the Galactic anti-centre. Beyond this point we can circle back around to the Galactic centre passing through Orion, Canis Major, Vela and Crux, the southern cross. As we pan across this band of starlight, that is the plane of the Galaxy, dark dust lanes become evident to the observer. These dark dust lanes, opaque at visible wavelengths, reveal their secrets when observed at infrared, sub-millimetre, and radio wavelengths, as sites of star formation. Understanding how these sites produce stars has far-reaching consequences for modern astrophysics.

1.1 Star Formation

All stars are formed from the material within interstellar medium in what are known as molecular clouds: the dark dust lanes seen in Fig. 1.1. For a star to form a sufficient amount of material must collapse, becoming increasingly compact. Gravity must overcome counter compressive forces such as gas and magnetic pressure, turbulence and rotation. Molecular clouds make ideal environments for material to collapse and for stars to form, due their ability to radiate away excess energy. A star is born once the core of this collapsed material becomes hot enough (1.5×10^7 K) and the pressure high enough to enable nuclear fusion within and further collapse is halted as the star comes into hydrostatic equilibrium and becomes a Zero Age Main Sequence star. With the night sky brightly lit by stars one may assume that this process of star formation is abundant within our own Galaxy, however with a mass of $10^{11}\,\mathrm{M}_\odot$ (Fich and Tremaine, 1991), and with a star formation rate of $\sim 4\,\mathrm{M}_\odot\,/\,\mathrm{yr}$ (Smith *et al.*, 1978; Diehl *et al.*, 2006) we see that star formation on galactic scales is an inefficient process, approximated to 2% (Myers *et al.*, 1986), where the star forming efficiency, SFE, can be defined by the following (where M_* is stellar mass and M_{cloud} is cloud mass):

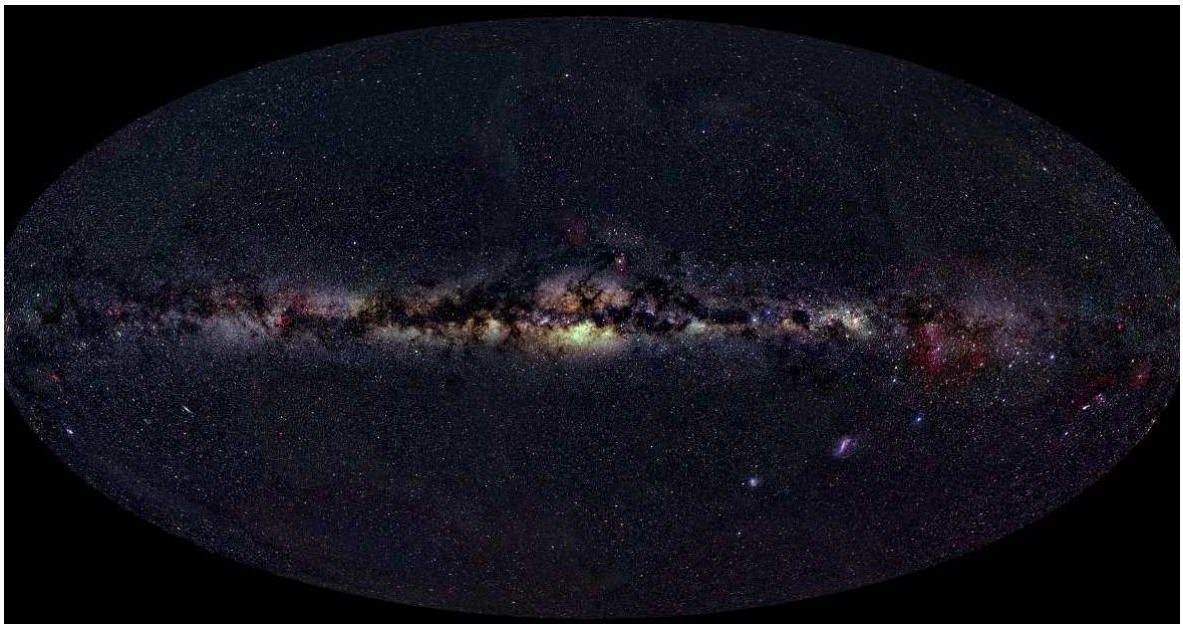

Figure 1.1: Dark dust lanes evident against the bright background starlight of the Milky Way (reproduced from Mellinger 2008).

$$\mathrm{SFE} = \frac{M_*}{M_* + M_{\mathrm{cloud}}} \tag{1.1}$$

Despite this apparent inefficiency in the star formation process on galactic scales the fact remains that stars do form, and they form over a wide mass range from $0.075\,\mathrm{M}_\odot$ (Burrows *et al.*, 2001) up to $150\,\mathrm{M}_\odot$ and beyond (see Crowther *et al.* 2010). These mass limits are set by the physics involved in producing energy via nuclear fusion within a star. At the lower mass end stars lack sufficient mass to produce the core temperatures needed to sustain nuclear fusion via the proton-proton chain. The upper mass limit is determined by the amount of mass that can be supported against a strong radiation pressure preventing a star from gaining more mass, known as the Eddington limit[1]. The relative proportion of zero age main sequence stars (stars that are newly born) with differing masses is what is known as the Initial Mass Function (IMF, see Fig. 1.2). The main reason the IMF is of such importance to astronomers is that it appears to be uniform throughout the Galaxy with a larger number of solar mass stars than high mass stars ($> 8\,\mathrm{M}_\odot$) observed within the Galaxy. It is also important to theoretical astronomers as learning to reproduce this IMF can help to constrain various models of star formation. This IMF is usually described by one or several power laws:

$$\frac{dN}{dM} \propto M^{-\alpha} \tag{1.2}$$

where α typically equals 2.35 (Salpeter, 1955). A refined IMF by Kroupa 2001 uses multiple

[1]Eddington limit $L_{\mathrm{edd}} = \frac{4\pi G m_p c M}{\sigma_T}$ is derived from a balance of the gravitational force and the force exerted by the radiation

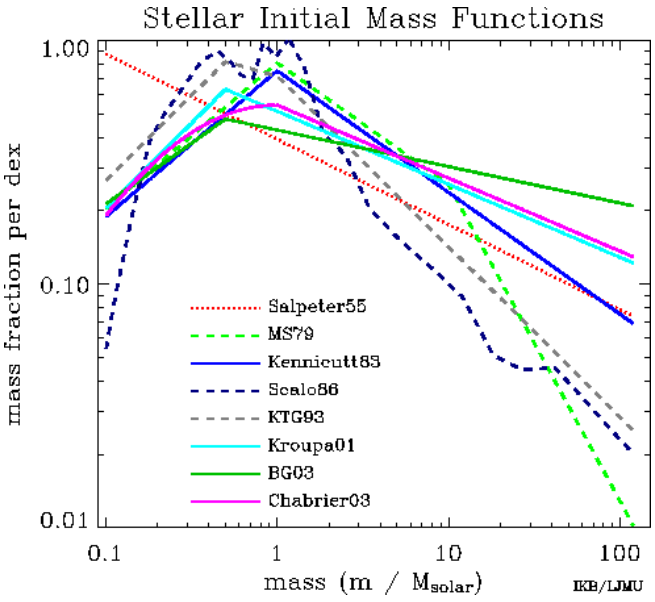

Figure 1.2: The initial mass function from a range of sources for comparison. IMFs taken from: Salpeter (1955), Miller and Scalo (1979), Kennicutt (1983), Scalo (1986), Kroupa *et al.* (1993), Kroupa (2001), Baldry and Glazebrook (2003), and Chabrier (2003). Image courtesy of Ivan K. Baldry.

power laws with $\alpha = 0.3 \pm 0.7$ between $0.01-0.08\,\mathrm{M}_\odot$, $\alpha = 1.3 \pm 0.5$ between $0.08-0.5\,\mathrm{M}_\odot$ and $\alpha = 2.3 \pm 0.3$ for masses greater than $0.5\,\mathrm{M}_\odot$.

This observed distribution has been found to be constant over a range of environments (Kroupa 2001; McKee and Ostriker 2007). To investigate the origins of the IMF astronomers look to the environments and processes from which stars are formed. As seen by the form of the IMF the majority of stars have masses $< 8\,\mathrm{M}_\odot$ and unsurprisingly the formation of these stars are better understood than their rarer high mass counterparts.

The star formation process for these stars, with masses $<8\,\mathrm{M}_\odot$, can be broken into four stages. These stages are observationally defined by increasing black-body temperatures from the infrared-visible SED (spectral energy distribution)[2] of young stellar objects (YSOs, Lada 1987; Andre *et al.* 1993, 2000). The term YSO is used to describe any star whose luminosity is produced by accretion as opposed to nuclear reactions (which will occur when it evolves onto the main sequence as a zero age main sequence star). Classically YSOs are categorised into four classes that are believed to follow an evolutionary sequence from Class 0 and Class I (also known as proto-stars) to Class II (known as classical T Tauri stars) and Class III (known as weak T Tauri stars). These classes and their corresponding SEDs are shown in Figure 1.3. Below is an outline of each of the four classes of YSO (Andre *et al.* 2000 and Purcell 2006):

Class 0 objects are accreting proto-stars in which a hydrostatic core has formed but is yet to accumulate the majority of its final mass from its large surrounding spheroidal envelope. The SED for a Class 0 object resembles a single blackbody with a temperature between 20

[2]based on the gradient of the SED between $1-20\,\mu$m (Lada, 1987)

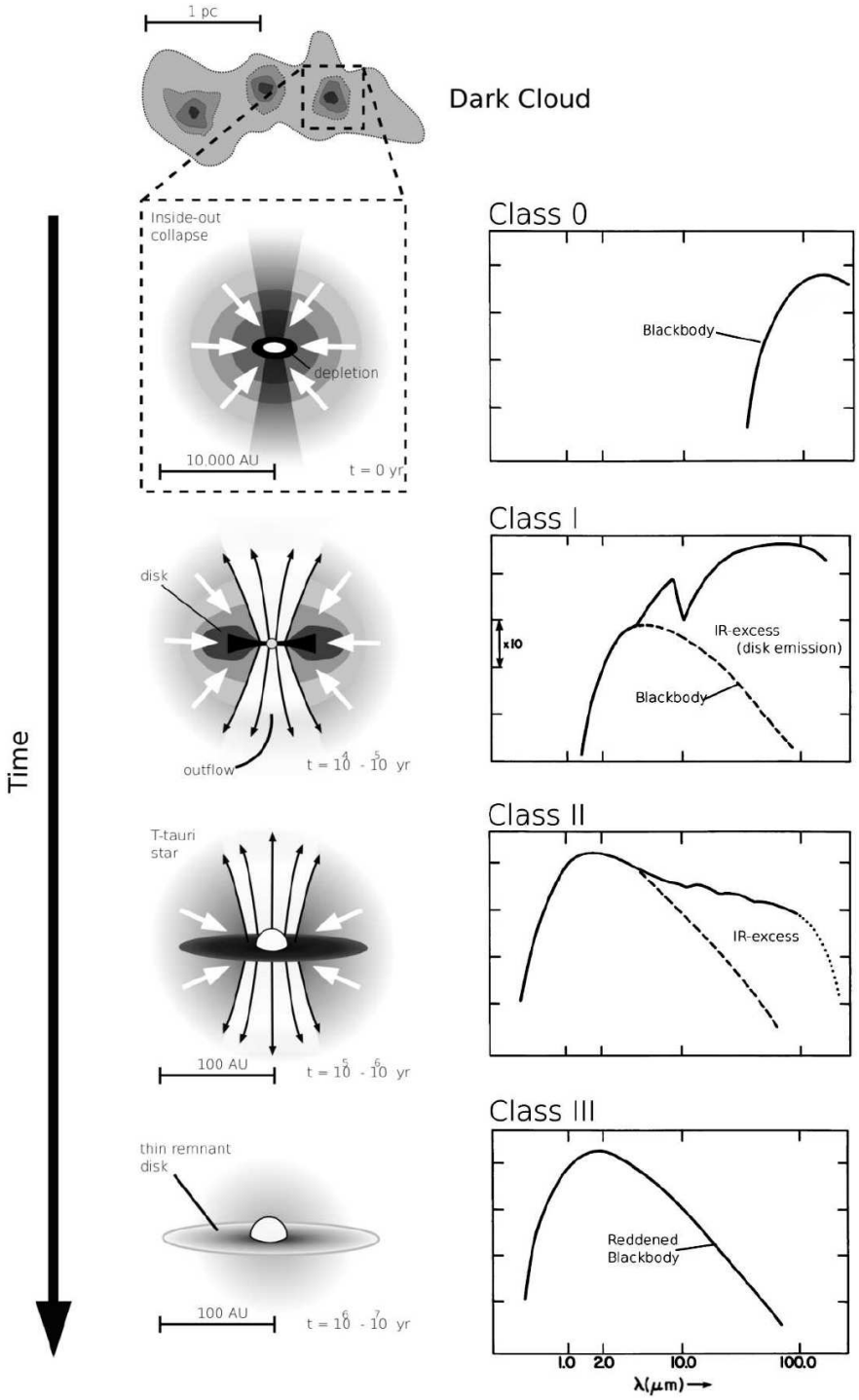

Figure 1.3: Image of the classification scheme for YSOs based on observed SEDs. This image was taken from Purcell (2006) which was originally adapted from Lada and Wilking (1984) and van Dishoeck and Blake (1998)

and 30 K. At this stage outflows are observed indicating the formation of a disk-like structure within.

Class I objects are associated with higher temperatures. They have SEDs that are distinct by their two components: first, a profile that corresponds to a $50-100$ K blackbody that originates from the accreting envelope, and second, a component that originates from the disk. At this stage in the evolution, an accretion disk has formed and bipolar outflows and jets are observed. At this stage the YSO has accreted more than half the total mass of the original envelope onto the core.

Class II objects are surrounded by a large circumstellar disk (also known as a proto-planetary disk from which planets may eventually form) which continues to accrete matter. This disk is exposed as the outflows, stellar winds and strong surface activity have swept away much of the envelope of accreting material. Class II objects are also know as Classical T-Tauri stars.

Class III objects (weak T-Tauri stars) have a depleted circumstellar disk and are now well described by a single blackbody SED that peaks in the near-infrared and optical wavelengths. Finally, the cores of the young stellar objects heat up sufficiently for thermonuclear reactions to begin.

This description of star formation is applicable for stars $< 8\,M_{\odot}$. Determining the nature of massive star formation is more difficult in comparison due to theoretical and observational complexities.

1.2 Massive Star Formation

Massive stars ($> 8\,M_{\odot}$) may be defined as a separate class of star compared to low mass stars based on two distinct phases: firstly when they produce ionising photons with energies ($>$ 13.6 eV) sufficient to create an HII region, and secondly when they undergo violent supernovae explosions at the end of their lives. These two distinct phases underpin the importance of massive stars on both local and galactic scales, enriching the Universe with heavier elements produced as they undergo nuclear fusion and during their subsequent violent deaths via neculeosynthesis. These stars sculpt the surrounding material with the production of HII regions, stellar outflows, winds and supernovae explosions, with each process helping in either the inducement or suppression of the formation of future generations of stars. It is emission from massive stars that dominates in external Galaxies, tracing the structure of the different galaxies, as well as driving the chemical evolution.

Despite the pivotal role of massive stars for Galaxy evolution there is a fundamental lack of understanding as to how these stars form. From an observational perspective, understanding massive star formation is hampered for four main reasons:

i) The IMF dictates that massive stars are fewer in number and therefore statistically found at larger distances from the Sun.

ii) Massive stars by their nature require vast amounts of material to form, resulting in a protostar cocooned within a large reservoir of material that hampers observations of the protostars within.

iii) Massive stars evolve onto the main sequence quickly whilst still accreting/embedded within their prenatal material. A typical O or B star is found to spend $\sim 10-20\%$ of its main sequence lifetime in the embedded phase (Wood and Churchwell, 1989a).

iv) They are predominantly found within clustered environments, with $> 70\%$ of O stars, and many B stars found to form in binaries or multiple systems (Mason *et al.*, 2009). In the Trapezium cluster in Orion the OB stars are found to have an average of 1.5 companion stars, compared to 0.5 companion stars in low-mass stellar clusters (Zinnecker and Yorke 2007, and references therein).

Theoretically the problem for massive stars is that the two important time-scales in star formation conflict with each other above a certain limit. First the time scale over which a cloud can collapse under its own gravity is determined by the free fall time scale, $t_{\rm ff}$, as given by:

$$t_{\rm ff} = \left(\frac{3\pi}{32G\rho}\right)^{1/2} \tag{1.3}$$

where G is the gravitational constant and ρ is the density of the gas. This equation is derived by considering the conversion of gravitational potential energy into kinetic energy for a cloud of gas collapsing under the influence of gravity alone. As the cloud collapses the thermal energy produced can provide pressure, which, unless dissipated, would halt the further collapse of the cloud. The time it takes for a cloud to radiate away this thermal energy is determined by the Kelvin Helmholtz time scale, $t_{\rm KH}$, and is given by:

$$t_{\rm KH} = \frac{GM_\star^2}{R_\star L_\star} \tag{1.4}$$

where $M_\star$ is the stellar mass, $R_\star$ is the stellar radius and $L_\star$ is the stellar luminosity. This equation simply originates from the luminosity being the amount of gravitational potential energy emitted per unit time. For the majority of stars it is seen that $t_{\rm KH} > t_{\rm ff}$, with stars evolving onto the main sequence once they have accreted all of their material. A problem occurs when $t_{\rm KH} < t_{\rm ff}$, in this case the cloud will not have had time to radiate away its energy before the star becomes opaque with thermal pressure building up to the point that thermonuclear reactions may proceed. The problem is then how do massive stars accrete more mass whilst undergoing nuclear fusion that produces radiation pressure to further prevent collapse[3]? What we do know is that stars that satisfy the inequality $t_{\rm KH} < t_{\rm ff}$ do exist and are observed (with masses up to $\sim 300\,{\rm M}_\odot$ i.e. Crowther *et al.* 2010), the question is *how*.

1.2.1 Theoretical models: nature or nurture?

There are two main theoretical models of massive star formation that overcome this problem of massive star formation proceeding despite this radiation pressure. The models can be nicely summed up using the phrase by Bonnell *et al.* (2004): nurture versus nature. The

[3]Consider the Sun ($\rm M/M_\odot = 1$, $\rm R/R_\odot = 1$ and $\rm L/L_\odot = 1$) and Rigel ($\rm M/M_\odot = 17$, $\rm R/R_\odot = 70$ and $\rm L/L_\odot = 66,000$, Guinan *et al.* 2010). The Sun is found to have $t_{\rm KH} \sim 10^7$ years with Rigel found to have $t_{\rm KH} \sim 10^3$ years, four orders of magnitude faster. We see that the free fall time-scale for a molecular clump/core (with densities on the order of $10^6\,{\rm cm}^{-3}$) are on the order of 10^7 years.

nurture argument considers the influence of the environment on the final mass of the star, with particular emphasis on location and size (known as the competitive accretion model). At the heart of the nature argument is that massive stars form via monolithic collapse of a gravitationally bound core, essentially a scaled up version of low mass star formation where the final mass of the star is dictated by the mass of the clump from which it was formed.

Competitive accretion and stellar mergers

The competitive accretion model, first proposed by Bonnell *et al.* (1997), argues that massive stars form from the same material with a common gas reservoir and are affected by two factors within this environment: location and size. In this model the most massive stars form in the centre of the region as they dominate the potential well. These more massive protostars, close to the centre of the potential well, have a greater influence in accreting further material (in both terms of volume and rates) particularly in comparison to those protostars forming on the edge of a region (Bonnell *et al.* 1997; Bonnell *et al.* 2001a; Bonnell *et al.* 2001b).

This model of massive star formation would indicate that if all massive stars formed in this way then there would be a lot of structure seen within clusters, a term known as mass segregation). Observational evidence of young clusters suggest that mass segregation does exist with massive stars forming preferentially in the centre (i.e. Preibisch *et al.* 2000 Stanke *et al.* 2006; Hasan and Hasan 2011). However this evidence has been criticised by Ascenso *et al.* (2009a, 2009b) for being unable to disentangle true mass segregation from incompleteness.

Another theory for the formation of massive mass stars is the Stellar Mergers model (Bonnell *et al.*, 1998). This model requires high stellar densities $\sim 10^8\,\mathrm{stars/pc^3}$ to allow grazing collisions to form the massive stars. With such high densities (in comparison the Orion Nebula Cluster has a density of $10^4\,\mathrm{stars/pc^3}$ (Muench *et al.*, 2008)) this theory is unlikely to account for the formation of the majority of massive stars, however it may be important in forming the most massive stars. Observationally this theory also proves to be problematic as very high angular resolution is required to test it.

Monolithic collapse

As stated the monolithic collapse model is essentially a scaled up version of low mass star formation where protostars form from a reservoir of material that is initially gravitationally bound via disk accretion with molecular outflows removing excess angular momentum (McKee and Tan, 2003). This model has two main limitations: the requirement of high accretion rates to overcome the fast evolution of massive protostars compared to low mass protostars, and the prevention of further fragmentation of the core into lower mass protostars during formation.

Observational support for this model has been an observed distribution of clump masses (known as the clump mass distribution, CMF) seen to closely resemble the distribution in stellar masses (Reid and Wilson, 2006a), as described by the IMF, observed disks and outflows around massive protostars similar to that seen in low mass star formation (Sandell *et al.*, 2003), and gravitationally collapsing massive cores (Birkmann *et al.*, 2007).

Two-dimensional simulations of this monolithic collapse model, including rotation and an accretion disk, found an upper limit was reached for massive stars at $40\,\mathrm{M_\odot}$ for sperically symet-

ric accretion flows. This work has been built on by Krumholz *et al.* (2009) who have utilised the ever increasing capabilities of computers and were able to perform three-dimensional simulations. Krumholz *et al.* (2009) and Kuiper *et al.* (2010) found that 'gravitational and Rayleigh-Taylor instabilities channel gas onto the star system through nonaxisymmetric disks and filaments that self-shield against radiation while allowing radiation to escape through optically thin bubbles[4].' With non axisymentric accretion resulting from instabilities caused by companion stars formed from gravitational instabilities in the disk (Krumholz *et al.*, 2009).

It is only recently, through this three-dimensional computational modelling discussed above, that radiation pressure has been found not to present a barrier for massive star formation (Krumholz *et al.*, 2005, 2009; Kuiper *et al.*, 2010). This diminishes the need for alternative modes of star formation leading to a more elegant view[5] of stars forming via a single mechanism at all mass scales, whilst other methods of massive star formation may play a role, it may be to a much lesser extent than first thought. In reality however observations are yet to be at a stage to enable an evidence based claim of one model over another.

Improvements to the modelling of massive stars will undoubtedly come from advances in the observed characteristics of massive star forming regions. Bate *et al.* (2003) states that computational models of star formation are limited as *"conditions in molecular clouds are not sufficiently well understood to be able to select a representative sample of cloud cores for the initial conditions"*. It is this notion that motivates the study of the most massive molecular clouds and the dense clumps/cores within which massive stars are known to form.

1.3 Molecular Clouds

What we know for certain is that *all* stars form from the material contained within the Interstellar Medium (ISM), in what are known as molecular clouds. There are several types of molecular clouds within the Galaxy, all are composed of 99% gas and 1% dust and all are dominated by molecular Hydrogen (∼99% by number). Molecular clouds, located throughout the Galaxy, form by a process known as self shielding. In this process Far-UV photons may destroy/prevent molecules forming at the periphery of clouds by photodissociation, creating what is known as a photodissociation region (PDR). As a result these photons do not penetrate the material present behind this PDR layer (with column densities on the order of $10^{21}\,\mathrm{cm}^{-2}$), and molecules that subsequently form are protected by this layer and by the extinction properties of the dust grains.

Molecular clouds have a broad mix of physical characteristics in terms of size ($0.1-100\,\mathrm{pc}$) mass ($10-10^6\,\mathrm{M}_\odot$), density ($10^2-10^4\,\mathrm{cm}^{-3}$), and temperature ($5-300\,\mathrm{K}$). As a result the classification of molecular clouds is non trivial, reflected in the observed power law distribution of molecular cloud masses, empirically described by $\mathrm{dN(M)/dM}\propto\mathrm{M}^{-1.5}$ (Solomon *et al.*, 1987) for masses over $10^5\,\mathrm{M}_\odot$. Another major characteristic of these clouds is the velocity dispersion relation, described by: $\sigma \propto r^{0.5}$ (Dame *et al.* 1986, Solomon *et al.* 1987) prompting the view of molecular clouds as turbulent (Larson, 1981). Turbulence is believed to play an important

[4]also known as the "flashlight effect", whereby radiation (beyond the dust sublimation front) within a disk is preferentially directed in the polar axis (Yorke and Sonnhalter, 2002)

[5]consider Occam's razor and the principle of parsimony, where the most likely hypothesis is the one that needs the least number of new assumptions

role in regulating star formation within molecular clouds both creating over densities, from which stars may form, and providing support against collapse, a process known as gravo-turbulent fragmentation (Mac Low and Klessen, 2004). This velocity dispersion relation is one of three relations that are referred to as the Larson relations.

1.3.1 The Larson relations

The Larson relations are a set of empirically derived expressions first described by Larson in 1981. From observations of ~ 50 molecular clouds and condensations over scales $0.1 < r < 100\,\mathrm{pc}$, Larson (1981) found the following:

$$\sigma\,(\mathrm{km/s}) \propto r^{p}\,(\mathrm{pc}) \tag{1.5}$$

$$\sigma\,(\mathrm{km/s}) \propto M^{q}\,(\mathrm{M}_{\odot}) \tag{1.6}$$

$$< n(H_2) > (\mathrm{cm}^{-3}) \propto r^{z}\,(\mathrm{pc}) \tag{1.7}$$

where σ is the line-width, r is the size and n is the number density. Larson (1981) obtained values based on observations for the first two relations of $p = 0.38$, $q = 0.2$ and derived the third relation, $z = -1.1$, from equations 1.5 and 1.6. These laws, we see, are not independent[6]. This work was built on by Solomon *et al.* (1987) who used data from ~ 270 clouds within the Galaxy and found $p = 0.5$, $q = 0.25$, and $z' = 0.0$ (for column density, cm^{-2}).

Further observations of molecular clouds have indicated a scatter in Larson's third relation (i.e. Heyer *et al.* 2009; Lombardi *et al.* 2010). These findings are consistent with the view that this third Larson relation is an artefact of the limitation of observational tracers as opposed to a physical property, i.e. observations based on molecular line emission requires regions to be dense enough to have molecules but not too dense so the lines remain optically thin (Mac Low and Klessen, 2004).

What can be taken from these Larson relations is that molecular clouds are gravitationally bound entities[7], and from observations of line widths they are supersonic in nature, i.e. velocities greater than the local sound speed (Mac Low and Klessen, 2004; McKee and Ostriker, 2007). Finally these relations imply a transient nature to molecular clouds. Based on Larson's first law it is possible to obtain a dissipation timescale ($t_{\mathrm{d}} \approx L/\sigma$):

$$t_{\mathrm{d}} \approx (9.8\,\mathrm{Myr}) \left(\frac{L}{100\mathrm{pc}}\right) \left(\frac{\sigma}{10\mathrm{km\,s}^{-1}}\right)^{-1} \tag{1.8}$$

which, for a cloud with $\sigma = 10\,\mathrm{km/s}$, L =0.1 – 100 pc, we find yields a dissipation timescale of order of $10^5 - 10^7$ years (Williams *et al.*, 2000; Mac Low and Klessen, 2004), consistent with observational finding from star clusters (Bash *et al.*, 1977; Leisawitz *et al.*, 1989).

[6] $N\,(\mathrm{cm}^{-2}) \propto M(\mathrm{M}_{\odot})/R(\mathrm{pc})^2 \propto n(\mathrm{cm}^{-3})R(\mathrm{pc})$

[7] from equation 1.11 (see Section 1.6.1), we see: $v \propto {M_{virial}}^{0.5}$, so for a cloud of line width v or σ we see $M_{Larson} > M_{virial}$

Cloud Type bubbly	A_V (mag)	n_{tot} (cm^{-3})	L (pc)	T (K)	M ($M_\odot$)
Dense Cores/Bok Globules	10	10^4	0.1	10	10
Dark Cloud Complexes	5	500	10	10	10^4
Giant Molecular Clouds	2	100	50	15	10^5
IRDCs	100	10^4	5	15	10^4

Table 1.1: Physical properties of typical Molecular Clouds, adapted from (Stahler and Palla, 2005) with additional information from Rathborne *et al.* (2007).

1.3.2 Molecular cloud types

The classification of molecular cloud types is determined by their broad mix of physical characteristics as shown in Table 1.1. Nearby and at the low mass end of the scale are Dark Globules also known as Bok Globules. These clouds are 'observed' in extinction against background starlight (Bok and Reilly, 1947), and contain masses on the order of $1 - 100\,M_\odot$. They are found in isolation and as such are believed to have been removed from parental clouds by external events. Bok Globules have similar properties to the dense cores located within large complexes, and with such low masses they are believed to host only low mass star formation.

A well studied Bok Globule is Barnard 68 (known as B68) in the constellation of Ophiuchus at a distance of ~ 125 pc (Barnard, 1919). With an average size of 12500 AU and a central density of $2.5 \times 10^5\,cm^{-3}$, B68 has total cloud mass of $2M_\odot$ (Redman *et al.*, 2006). Observations have shown B68 to be a starless core with a centrally peaking density profile. Temperatures are cooler towards the core than the envelope ($\sim$10 K) consistent with observations indicating freeze out of molecules in the core.

Moving up the scale in mass are Dark Cloud Complexes with masses $10^3 - 10^4\,M_\odot$ (Mundy, 1994). Like Bok Globules they host low mass stars and are 'observed' in extinction against background starlight. The dark cloud complex Taurus at a distance of 140 pc is one of a collection of molecular clouds that make up what is referred to as the Gould belt. At a mass of $10^4\,M_\odot$ Taurus is quite a massive cloud and yet only low mass star formation has been observed within (Kenyon *et al.* 2008; Davis *et al.* 2010; Elias 1978; Onishi *et al.* 2002)

At the high mass end of the spectrum are the recently discovered class of molecular clouds known as Infrared Dark Clouds: IRDCs (Perault *et al.* 1996; Egan *et al.* 1998). These clouds have been suggested to be the high mass counterpart to Bok Globules, with much higher masses ($100 - 10^4\,M_\odot$) and densities. I leave further details and discussion of IRDCs to Section 1.5. Finally at the very high mass end we reach Giant Molecular Clouds/Complexes GMCs, with masses on the order of $10^4 - 10^6\,M_\odot$. It is within these last two classes of clouds (IRDCs and GMCs) that massive stars are found to form, consistent with the idea that the final mass of a star increases with the mass of the cloud (Larson, 1982).

1.4 Giant Molecular Clouds

In the constellation of Orion lies our closest and most well known example of a massive star forming region: the Orion GMC. This massive molecular cloud at a distance of 450 pc and containing a mass of $10^5\,M_\odot$, is well known to be forming massive stars. One particular cluster in Orion A is found to have over 56 members, with spectral types O6 – B2. Star formation is still ongoing in Orion with many of the stages of massive star formation (see Section 1.6) observed (see reviews by Genzel and Stutzki 1989 and O'Dell (2001)) and is just one of many thousands of GMCs found throughout the Galaxy. These structures are substantial in Galactic terms containing ∼80% of the molecular hydrogen in the Milky Way (Stahler and Palla, 2005). GMCs typically have sizes ~ 100 pc and masses $\sim 10^5 - 10^6\,M\odot$, and are strongly clumped with typically $\sim 5-10\%$ of GMCs by volume filled by Clumps (e.g. Stutzki and Guesten (1990)).

1.4.1 Formation of GMCs

The theory of how GMCs were formed can be split into two concepts: "bottom-up" where smaller clouds combine by agglomeration to form larger entities, and "top-down" from large scale instabilities in the ISM (McKee and Ostriker, 2007). In the "bottom-up" scenario smaller clouds combine by inelastic collisions, a slow process which would mean destructive forces resulting from star formation would hamper GMCs obtaining higher masses once star formation began. A lack of evidence of GMCs existing without indicators of massive star formation implies that the onset of star formation within GMCs is rapid. This scenario, whilst possible for the formation of some molecular clouds and perhaps some lower mass clouds, is unlikely to be the only mechanism responsible for GMC formation. The second, and more likely scenario is the "top-down" scenario in which clouds form either via large scale gravitational instabilities in the ISM or by forced compression by supernovae, turbulence or spiral wave shocks (Dobbs 2007; McKee and Ostriker 2007). However recent simulations by Dobbs (2009) with both warm and cold ISM components show that a combination of the formation mechanisms proposed is expected to play a role in the formation of GMCs.

1.4.2 Evolution

It has been estimated that less than 10% of GMCs within the Galaxy show no sign of star formation (Blitz, 1993). Statistically these clouds are likely to be young (< 3M yr) GMCs, the Maddalena-Thaddeus cloud is the closest example, with a mass of $10^6\,M_\odot$ (Maddalena and Thaddeus, 1985) and only low mass star formation observed within (Megeath *et al.*, 2009). At the other end of the age spectrum, based on observations of clouds associated with open and young clusters, it is believed that GMCs are destroyed or dissipated on timescales ∼10 Myr (Leisawitz, 1990). In this context we see Orion, and other well studied GMCs such as G305 (Clark and Porter, 2004), slot into this evolutionary picture as a middle aged GMC still actively producing massive stars.

Despite having this global evolutionary picture of GMCs it remains unclear how star formation propagates through the natal GMC on local scales. In particular, the role the first generation of massive stars plays in triggering, regulating and terminating subsequent star formation

activity is uncertain (Blitz, 1993). The need to understand and parameterise the dense clumpy nature of GMCs is evident, particularly with regard to variations on a cloud to cloud basis. Blitz (1993) posed four questions: (i) Is the clumpy nature of GMCs primordial or a result of star formation? (ii) how do clumps eventually form stars? (iii) If O and B stars form from the most massive clumps can we identify these clumps? (iv) if collisions between clumps are inelastic can we use the clump ensemble to tell us about the history of the GMC?

It is clear from observational evidence that massive stars form almost exclusively within GMCs, however observations within the past decade have revealed massive stars forming within another class of molecular clouds: IRDCs (i.e. Rathborne *et al.* 2005; Ormel *et al.* 2005).

1.5 Infrared Dark Clouds

Until the late 1990s it was believed that all massive stars formed within GMCs, however with the advent of infrared space telescopes such as the Midcourse Space eXperiment (MSX) and the Infrared Space Observatory (ISO) a new class of molecular clouds known as Infrared Dark Clouds, IRDCs, were discovered (see Fig. 1.4). These newly discovered clouds were later found to harbour signposts of massive star formation. IRDCs were first discovered by Perault *et al.* (1996) and Egan *et al.* (1998). Perault *et al.* (1996) reported numerous dark features observed by ISO at 15 μm that the authors suggested corresponded to dense regions: candidates for the precursors of star formation sites. Egan *et al.* (1998) reported ∼2,000 dark objects seen in extinction from 7 to 100 μm by MSX (see Fig. 5.2). Lis and Carlstrom (1994) and Lis and Menten (1998) also reported a dark core (M0.25-0.01) at wavelengths $< 70\,\mu$m during studies of GMCs in the galactic centre using ISO and CSO (Caltech Submillimeter Observatory). Although their exact origins remain unclear, Egan *et al.* (1998) suggests that IRDCs were formed from "naked cores left behind after the envelopes of giant molecular clouds have been dispersed", in a similar fashion to the way Bok Globules are believed to form. Observations of IRDCs have found the majority to be filamentary in structure with typical aspect ratios around ∼2 (Peretto and Fuller, 2009). The "Nessie" IRDC complex is likely to be one of the most extreme cases with a length of ∼80 pc and width of ∼0.5 pc (see Fig. 1.4) giving it an aspect ratio of ∼160 (Jackson *et al.*, 2010).

In the decade since their discovery, our understanding of the physical properties of IRDCs has increased and it is now known that these objects are cold (< 25 K) dense (10^5 cm^{-3}) regions, on scales of $1-10$ pc, with masses ranging between 10^2-10^5 M$_\odot$ (Rathborne *et al.*, 2006). Currently observations suggest that cold dense starless cores found within IRDCs are the precursors to hot molecular cores (Jackson *et al.* 2008a and references therein), indeed Rathborne *et al.* (2007) report on a hot molecular core found within an IRDC. Other tracers of massive star formation such as HII regions and Class II methanol masers (Carey *et al.* 1998; Pillai *et al.* 2006b; Chambers *et al.* (2009); Battersby *et al.* 2010) have been found in association with a number of IRDCs (these different tracers are examined in more detail in the next section). An evolutionary sequence for IRDCs has been proposed by Jackson *et al.* (2010), where initially an IRDC will be observed to contain several dark cores (see Fig. 5.1 in Chapter 5), then observed to appear more segmented and disrupted due to the effects of expanding HII regions (see Fig. 1.4), with the final stage similar to Orion and other massive star forming regions. The association of IRDCs with massive star formation is not exclusive

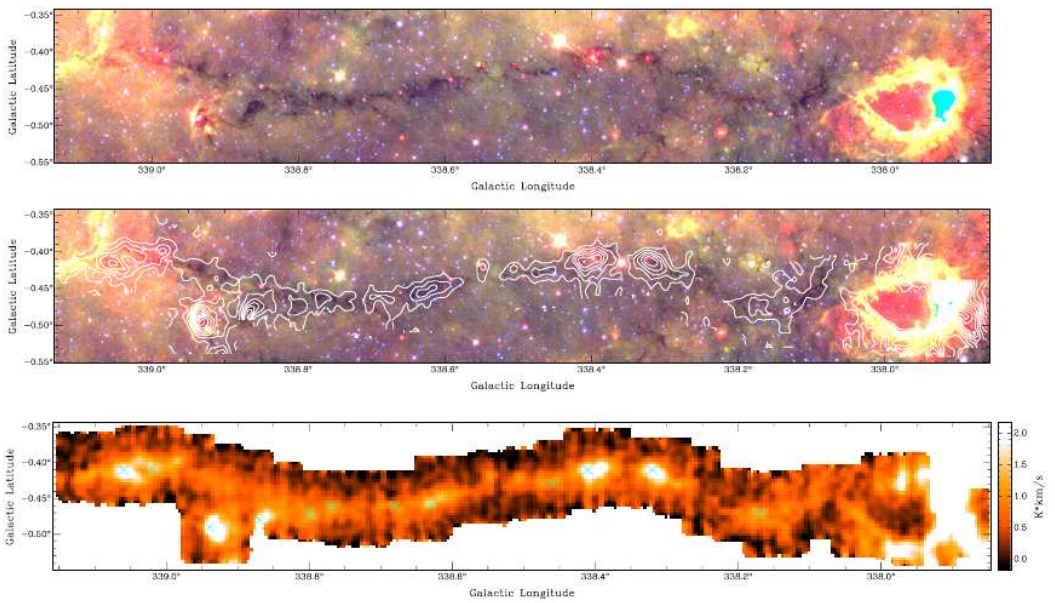

Figure 1.4: The "Nessie" IRDC complex (Jackson *et al.*, 2010). Top panel: a false three-color image of the Nessie Nebula. The 3.6 μm (blue) and 8.0 μm (green) emission is from GLIMPSE, and the 24 μm (red) emission is from MIPSGAL. Middle panel: the false three-colour mid-IR image of the Nessie Nebula from the top panel overlaid with integrated HNC (1-0) contours from the Mopra telescope. Note the excellent correspondence between the HNC emission and the 8 μm extinction. Bottom panel: an HNC (1-0) integrated intensity map from the Mopra telescope with core positions marked with cyan crosses. Both image and caption are taken from Jackson *et al.* (2010).

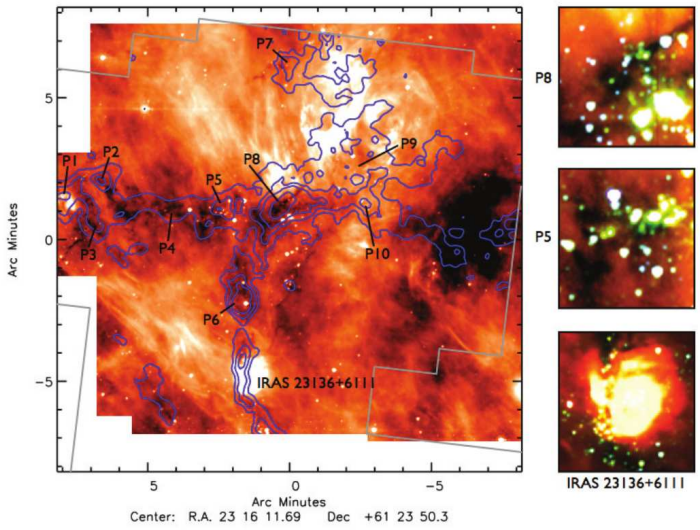

Figure 1.5: An IRDC in the outer galaxy at a distance of ∼3 kpc: G111.80+0.58, taken from Frieswijk *et al.* (2008). This images has $C^{18}O$ (2–1) contours (2, 3, 4 and 6 K kms^1) overlaid on IRAC 8 μm emission The right images show a false-color close-up of positions P8, P5 and IRAS23136+6111. The displayed emission is from the four IRAC channels, i.e., 3.6 μm (blue), 4.5 μm (green), 5.8 μm (yellow) and 8 μm (red).

and a number of individual studies find only low to intermediate mass young stellar objects embedded within IRDCs (van der Wiel and Shipman, 2008), with Kauffmann and Pillai (2010) estimating that only a small fraction of these clouds, $\sim 1\%$ by number, are forming massive stars, although these will be the most massive and dense of the IRDC population.

An unsurprising consequence of the detection method for identifying IRDCs is the fact that their Galactic distribution follows the mid-infrared background of the Galaxy. IRDCs are predominantly found in the first and fourth Galactic quadrants and near to the Galactic mid-plane (Jackson *et al.*, 2008b), precisely where the mid-infrared background is greatest. IRDCs however are not limited to the inner Galaxy (within 90° of the Galactic Centre) with Frieswijk *et al.* (2007) and Frieswijk and Shipman (2010) demonstrating how to identify potential IRDCs by searching for statistically redder colour distributions compared to local surroundings in the Two Micron All Sky Survey (2MASS) Point Source Catalogue. This process identified over a thousand IRDC candidates e.g. G111.80+0.58 seen in Fig. 1.5. It is clear from these studies that the outer galactic distribution of IRDCs is not well known.

It is seen that even with the increasing studies of IRDCs in the inner Galaxy (Simon *et al.* 2006a; Peretto and Fuller 2009; Ragan *et al.* 2009) many questions still remain. These include: what is the proportion of IRDCs associated with indicators of star formation? What are typical ages of IRDCs?

1.6 Observed stages of massive star formation

As was discussed in Section 1.2.1 it is believed that massive stars were formed either via monolithic collapse of a single gravitationally bound core or via the process of competitive accretion. It was seen that the monolithic model is likely to be the primary mechanism with competitive accretion undoubtedly playing a role in this formation process. Aiding this discussion are the numerous observations of massive star forming regions, leading to a tentative evolutionary picture of massive star formation as shown in Fig. 1.6. I outline each of these stages below.

1.6.1 Clumps and cores

Molecular clouds of all types are observed to have hierarchical internal structures comprised of clumps and cores. It is the process of fragmentation and collapse of the material within a molecular cloud to form a clump that is the starting point for the star formation process (image (i) in Fig. 1.6). Clumps are defined as over densities in a molecular cloud that may or may not contain cores from which single or multiple stars are born (known as star forming and "starless" clumps respectively, Williams *et al.* 2000). The next stage in this process is the fragmentation and collapse of material within the clumps to form cold cores ($\mathrm{T} \sim 10$–$20\,\mathrm{K}$) that will continue to collapse.

It is possible to investigate if a clump or cores is likely to collapse by considering the equation for Hydrostatic Equilibrium (equation 1.9) which describes the balance of gravity by a pressure Gradient (assuming magnetic pressure and turbulence are negligible):

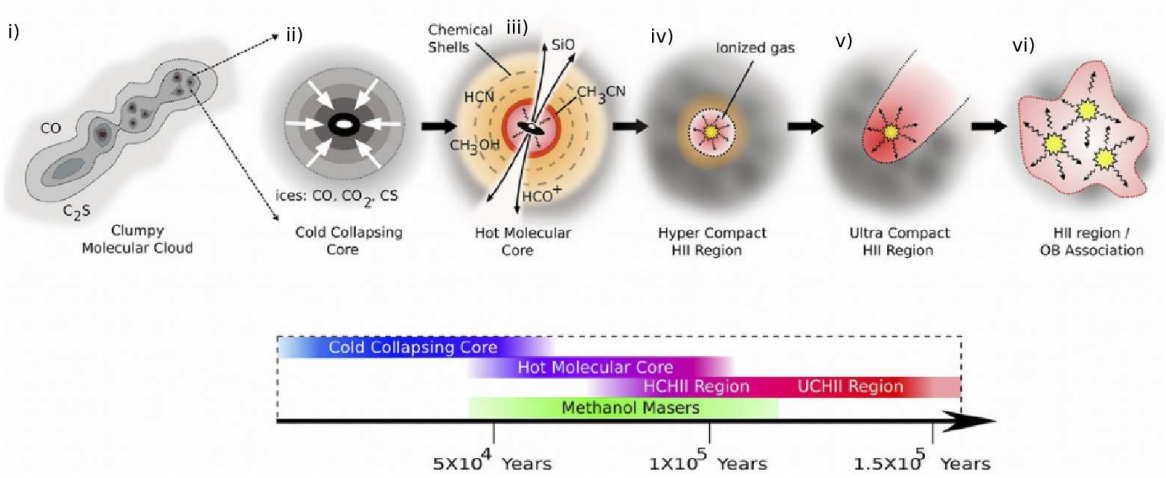

Figure 1.6: Illustration of the proposed evolutionary scenario of a cluster of massive stars, presented with permission from Cormac Purcell (see Purcell (2006) for an earlier version of this figure).

$$\frac{dP}{dr} = \frac{-G\rho M_{\rm clump}}{R^2} \tag{1.9}$$

where $M_{\rm clump}$ is the mass of the clump/core and R is the radius of the clump/core from which a star may form. This equation, in equilibrium leads to the Virial Theorem

$$2{\rm KE} = -{\rm GPE} \tag{1.10}$$

where KE is the kinetic energy of the cloud and GPE is the gravitational potential energy of the cloud. This equation may rearranged to express the mass which satisfies these conditions ($M_{\rm virial}$):

$$M_{\rm virial} = \frac{5}{3}\frac{v^2 R}{G} \tag{1.11}$$

This equation implies that a clump/core is likely to collapse if it is super–critical, with a virial parameter ($M_{\rm clump}/M_{\rm virial}$) greater than one. Studies of molecular clouds show that in general the majority of clumps are found to be sub-critical (e.g. Carr 1987) and therefore do not follow the Larson (Larson, 1981) relations (Kramer *et al.* 1996; Onishi *et al.* 2002; Buckle *et al.* 2010).

1.6.2 Hot Molecular Cores

When this cold collapsing core (image (ii) in Fig. 1.6) begins to form a massive protostar within the energy produced heats up the surrounding molecular gas to temperatures in excess of 100 K. At these temperatures molecules that have formed on the surface of dust grains will

sublimate producing high abundances of complex saturated molecules (image (iii) in Fig. 1.6) forming what is known as a Hot Molecular Core (HMC). HMCs are physically defined as small ($< 0.1\,\mathrm{pc}$) dense ($> 10^7\,\mathrm{cm}^{-3}$) regions with rich molecular lines (Olmi *et al.*, 1993; Charnley, 1997; Hatchell *et al.*, 1998; Kurtz *et al.*, 2000; Fontani *et al.*, 2007). Their low mass counterpart is known as a Hot Corino and is found in the innermost regions of Class 0 objects. To date the number of HMCs observed only reach into the tens of objects, which limits age estimates of these objects, although it is clear they are less than 10^5 years based on chemical models (Hatchell *et al.*, 1998; Kurtz *et al.*, 2000; Fontani *et al.*, 2007).

1.6.3 HII regions

A fundamental property of massive stars is that they have high surface temperatures ($\sim 3 \times 10^4\,\mathrm{K}$) and hence large luminosities, as seen in the empirically derived Mass-Luminosity relation for stars on the main sequence ($\mathrm{L} \propto \mathrm{M}^3$; Prialnik 2000). A consequence of these large luminosities (stars of spectral type O or early B-type) is the production of ionising UV photons and the inevitable production of an HII region (Krishna Swamy, 2005) (less than this and a reflection nebula will form instead). To form an HII region within a molecular cloud requires photodissociation of H_2 molecules by UV photons with energies $> 11.2\,\mathrm{eV}$ ($\lambda \sim 110.8\,\mathrm{nm}$; Whittet 1992) and then successive photoionisation of the resulting HI (energies $> 13.6\,\mathrm{eV}$, $\lambda \sim 91.2\,\mathrm{nm}$). This process also destroys dust grains that can only survive up to $\sim 2,300\,\mathrm{K}$ (Tan, 2003). The formation of the HII region to the point where the rate of ionisation equals the rate of recombination occurs nearly instantaneously, and the point at which these two process equal is known as the Stromgren radius (R_s) and is given by:

$$R_\mathrm{s} = \left(\frac{3}{4\pi} \frac{S_\star}{n_0^2 \beta_2} \right)^{1/3} \tag{1.12}$$

where $S_\star$ is the Lyman continuum photon rate, n_0 is the number density of neutral Hydrogen atoms, and β_2 is the recombination coefficient (see Dyson and Williams 1997). Photons that do escape will have energies $<13.6\,\mathrm{eV}$ but a fraction will still be energetic enough to dissociate the molecular hydrogen creating what is known as a PDR. As with the HII region this layer/PDR region is limited by the number of photons with energies $> 11.2\,\mathrm{eV}$ (Whittet 1992; Stahler and Palla 2005).

The ionising UV photons within the HII region create a factor of four increase in the number density within the HII region (as each H_2 molecule produces two protons and two electrons). If we consider the equation of pressure of an ideal gas: $p = nkT$, we see that it is an increase in number density combined with a temperature difference ($\sim 10^4\,\mathrm{K}$ inside the HII region compared to $\sim 10 - 100\,\mathrm{K}$ outside) that drives the pressure expansion of the HII region into the natal molecular cloud.

This expansion of the HII region is dependent on several factors including spectral class of star, whether multiple ionising stars, age, density of material and size of natal molecular cloud (for density bound HII regions). As the HII region expands its classification changes from a Hypercompact (HC) HII region, $< 0.01\,\mathrm{pc}$ in size (Sewiło *et al.* 2008), to an UCHII $< 0.1\,\mathrm{pc}$ in size (Churchwell 2002; Thompson *et al.* 2006), compact (C) and then a full HII regions. Although it has been suggested that the HCs may only form around single stars with multiple

stars forming UCHII regions (Kurtz, 2005). These stages are shown in Fig. 1.6. The final extent of an HII region may be classically described as one of the following:

i) density bounded HII regions: boundary determined by the limit of the cloud (it essentially runs out of material to be ionised).

ii) ionising bounded HII regions: determined by the balance between ionisation and recombination.

Typically this process is described as a uniform expansion but as we have discussed the material within molecular clouds typically has density gradients and inhomogeneities leading to the majority of HII regions being non-spherical, i.e. Blister or Champagne flows. A study of Ultracompact (UC) HII regions found only 5% to be spherical, 30% cometary and the remainder irregular (Stahler and Palla, 2005).

Age estimates for UCHII regions was originally calculated from the sound speed of the ionised material within an UCHII region. At a size of 0.1 pc and a sound speed of 10 km/s in an ionised medium an age estimate of 10^4 years is obtained. However this estimate was found to conflict with observations of the number of UCHII regions observed. From a statistical approach we see that if the number of O stars in the Galaxy was taken to equal 17,000 (as reported by Wood and Churchwell 1989a) and UCHII regions had an age on the order of 10^4 years ($< 2\%$ of the lifetime of a O star) it would be logical to assume that there were ~ 300 UCHII region in the Galaxy. However number estimates for these objects are much higher and bring the age estimate up to the order of 10^5 years (Testi *et al.*, 1999; Wood and Churchwell, 1989b; Kurtz *et al.*, 2000).

The detection of HII regions occurs at varying wavelengths from optical emission as a result of recombination, via Hα emission with a wavelength of 6563 Å, thermal infrared emission from the dust, or radio emission from bremsstrahlung (also known as free-free emission) from the ionised gas.

1.6.4 Masers

Masers, compact sites of intense and narrow molecular line emission, have been known to be associated with star formation for quite some time (Townes, 1993). Masers are good signposts for star formation, requiring high densities ($10^6 - 10^{11}$ cm^{-3}), and a pumping mechanism to form and sustain an inverted population of the masing species. This pumping mechanism may be either collisional, produced by shocks, or thermal (radiative), with the latter often present in regions of massive star forming such as UCHII regions (Walsh *et al.* 1997; Kurtz and Hofner 2005). Stimulated emission may then occur either spontaneously which may then stimulate further emission, or may be stimulated by seed photons from a background source, leading to further stimulated emission as before. This emission may be from regions as small as a few AU with brightness temperatures up to 10^{12} K (Cesaroni 2005, see Section 2.2 for further details on brightness temperatures). It is the variation in the pumping mechanism for masers which results in masers tracing a range of environments (Phillips, 1998).

To date OH masers, H_2O masers, and Class I methanol (CH_3OH) masers (identified by their narrow emission), have been found to trace regions of both low and high mass star formation

(Weaver *et al.* 1965; Cheung *et al.* 1969; Menten 1991; Ellingsen *et al.* 2007). These masers are collisionally pumped by outflows as they interact with the ambient high density material. In contrast to these are Class II methanol masers. Class II methanol masers (believed to be radiatively pumped: Sobolev *et al.* 2007), are identified by their complex spectrum and have been found to be exclusively associated with massive star formation. As such Class II methanol masers are a unique tool for identifying the early signs of massive star formation (Cyganowski *et al.* 2008; Menten 1991).

Although work on age estimates and an evolutionary scenarios for Class II methanol masers is still ongoing ages estimates are typically on the order of 10^4 years (van der Walt, 2005; Ellingsen *et al.*, 2007; Breen *et al.*, 2010).

1.7 Thesis motivation

The overarching aim of this thesis is to understand massive star formation from a dense clump/core perspective. We know massive stars are important in astronomy, both in the local environment and on galactic and extragalactic scales, however the nature of the dense molecular environment in which they form is only just becoming constrained on global scales. We know all massive stars form within either GMCs or IRDCs but what we want to understand is what makes these locations particularly suitable for massive star formation? To do this we must look at the dense molecular clumps and cores within GMCs and IRDCs.

The approach I use in this thesis is to study large populations of these objects to enable conclusions based on global properties. I begin by considering the dense molecular clumps within one of the most massive GMCs in the Galaxy: the W51 GMC. On a more specific level the aim is to investigate:

- the physical properties of the clumps within the W51 GMC
- the proportion that are likely to go on to form massive stars
- the efficiency of the GMC at this level
- relation between the clumps more likely to form stars and the global distribution of dense molecular material
- evidence of outflow activity within the W51 GMC

I then consider the dense molecular clumps within the recently discovered IRDCs. The approach used here is different. Having much smaller sizes and masses, to obtain a large sample of molecular clumps we utilise pre-existing data from the SCUBA Legacy Catalogue to study the IRDCs in our Galaxy. Again on a specific level I aim to investigate:

- the physical properties within IRDCs
- the proportion that are associated with star forming indicators
- differences in those clumps associated/not associated with star formation

- ages of these objects

As the age of survey astronomy is upon us this research unveils the potential of studies of dense molecular material to contribute to a unified theory of massive star formation.

1.8 Thesis structure

In Chapter 2 I discuss the physics at sub-millimetre wavelengths that is to be used within this thesis. In particular I underline three important equations: the Brightness Temperature, the equation of radiative transfer and the detection equation. I then detail the physics behind the techniques that will be used in this thesis to obtain the physical properties of the clumps and cores detected within this work.

Chapter 3 presents what is currently known about the W51 GMC. I then present the new observations taken of the W51 GMC region region with HARP and ACSIS on the JCMT. I give a brief description of instrumentation and observation methods used. I then detail the data reduction process used from the raw data files to the final image of the W51 GMC. Finally I detail the process of decomposing the W51 GMC into individual molecular clumps using CLUMPFIND.

Chapter 4 presents the physical properties of the dense clumps within the W51 GMC, and looks at the global properties such as the Clump Mass Function (CMF) and Star Formation Efficiency (SFE) of the GMC. I also take a qualitative look for signs of outflow activity within the W51 GMC.

In Chapter 5 I present my research into galactic IRDCs utilising data from the SCUBA Legacy Catalogue. I outline how the original catalogue of IRDC cores produced by Simon *et al.* (2006a) was obtained and how I identified those IRDCs with emission features within the SCUBA Legacy Catalogue (Di Francesco *et al.*, 2008). I then look at the global properties of the IRDC cores identified in particular I investigate the proportion of cores associated with MIPSGAL sources. This work was published in MNRAS in November 2009 (Parsons *et al.*, 2009).

Finally in Chapter 6 I summarise and conclude the work done in this thesis, bring together the ideas and results within Chapters 3, 4 and 5. I finish by outlining future work arising from this Thesis.

Chapter 2

Astrophysics at sub-millimetre wavelengths

'quicquid nitet notandum' - Whatever shines should be observed
Sir William Herschel

Information in astronomy is typically reliant on radiation falling on detectors. Understanding the process of the emission of this radiation *and* its detection is key to obtaining physical information about the source observed. This thesis predominantly uses information from radiation emitted in the sub-millimetre region of the spectrum, the region of the electromagnetic spectrum with wavelengths between $0.35-1\,\mathrm{mm}$. To this end this chapter aims to describe the techniques used to analyse radiation at these wavelengths (see Rohlfs and Wilson 2004).

2.1 Observing molecular clouds

So why observe in the sub-millimetre at all? As we saw in Chapter 1, molecular clouds are opaque at optical wavelengths due to their high densities and cold ($\sim 15\,\mathrm{K}$) temperatures. They make ideal environments for material to collapse and for stars to form, due their ability to radiate away excess energy. Radiation observed at these wavelengths originates from thermal emission produced by the cold dust as continuum emission, or via collisionally induced rotational/vibrational line emission of molecules. Considering first the emission from the cold dust and using Wien's displacement law:

$$\lambda_{\mathrm{peak}}\, T = 0.002898\,\mathrm{K\,m} \tag{2.1}$$

where λ_{peak} is the wavelength at the peak intensity for a black body that has a temperature T, we see that the emission from these regions originates from the tail of a black body distribution from cold dust[1]. Continuum observations, the basis of the work I present in Chapter 5, at these wavelengths originates from the cold dust emitting as a grey body[2]. Examples include

[1] at a temperature of $15\,\mathrm{K}$ we see λ_{peak} is $\sim 200\,\mu\mathrm{m}$

[2] a black body modified for the effects of emissivity ε. A true black body would have $\varepsilon = 1$ however most dust in molecular clouds follows $\varepsilon < 1$.

emission from small dust grains such as PAH (Polycyclic Aromatic Hydrocarbons). Dust particles play an important role in the chemistry of molecular clouds acting as catalysts for the formation of many complex molecules. By the nature of their low abundance (recall $< 1\%$ by mass), continuum observations of the dust are ideal tracers of molecular cloud structure, having low optical depths.

Molecular clouds are composed of 99% gas with ∼99% of this gas composed of molecular Hydrogen, H_2. Despite the prevalence of H_2, the cool temperatures at which these clouds exist prevent this molecule from being observed directly. At these cool temperatures emission typically originates from molecular rotational/vibrational transitions. Due to the lack of permanent dipole moment (H_2 has a symmetric distribution of charge), radiation from H_2 cannot be emitted via spontaneous rotational/vibrational transitions (although H_2 may be observed if shocked or heated by UV radiation fields; Krishna Swamy 2005). As an inert element, Helium, the second most abundant atom in the universe, does not exist in molecular form.

It is Carbon Monoxide (CO), the most abundant molecule in the ISM after H_2, that is used as a tracer of molecular clouds (i.e. Rathborne *et al.* 2009; Buckle *et al.* 2010; Davis *et al.* 2010; Graves *et al.* 2010). When CO becomes optically thick less common CO isotopologues, such as ^{13}CO or C^{18}O are needed to trace a cloud's structure. It is observations using these isotopologues that will form the basis of the work in Chapters 3 and 4. In denser and colder environments CO and other molecules undergo "freeze-out" and so other molecules are required for observations (Bergin and Langer, 1997). Less abundant tracers such as NH_3 or CS that have high dipole moments are ideal as they require high densities to become excited and allow detection..

2.2 Intensity and the brightness temperature

When making molecular line or continuum observations the aim is to recover how much energy was originally emitted and/or absorbed from the source being observed. What we observe is the intensity of the radiation. The intensity is how much of the original energy is detected as it passes through a unit area into unit solid angle, per second, per unit frequency.

Assuming the object observed is a black body then the intensity of the radiation emitted, B_ν at a particular wavelength or frequency may be described by Planck's law:

$$B_\nu(T) = \frac{2h\nu^3}{c^2}\frac{1}{e^{\frac{h\nu}{kT}} - 1} \tag{2.2}$$

where h is Planck's constant, ν is the frequency of radiation, k is Boltzmann's constant, and T is the brightness temperature. What we see here is that the intensity of radiation from a black body is both wavelength and temperature dependent.

Planck's law as described in equation 2.2 may be simplified at lower frequencies and longer wavelengths, i.e. in the sub-millimetre regime. This is known as the Rayleigh Jeans approximation. At lower frequencies when $h\nu << kT$ the exponential term in equation 2.2 may be expanded to $\frac{h\nu}{kT} + 1$. Substituting this approximation into the Planck equation obtains the Rayleigh-Jeans approximation:

$$B_\nu(T) = \frac{2k\nu^2}{c^2}T \tag{2.3}$$

This result, $B_\nu(T) \propto T$, is important for sub-millimetre and radio astronomers who typically report source strengths in terms of T, also known as the brightness temperature or receiver temperature ($T_{\rm R}$, as used in section 2.5). We see that the brightness temperature may be defined as the temperature of a black body (of a particular flux) provided it fills the telescope beam.

2.3 Rotation lines from linear molecules

With regard to spectral line emission from molecular ro-vibrational transitions this thesis deals solely with emission from CO and so we limit our discussion here to linear molecules only (recommending further reading from Townes and Schawlow 1975 and Rohlfs and Wilson 2004 for non-linear molecules).

Emission of a photon from a rotational transition of a molecule will occur provided there is a permanent electric dipole moment[3] and the molecule changes angular momentum. Rotational transitions are characterised by the rotational quantum number J (where $J = 0,\ 1,\ 2,\ 3...$), where molecules are governed by the selection rule that $\triangle J = \pm 1$. Within a particular rotational energy level, the number of ways an electron can fill an energy level with differing quantum numbers, is known as the statistical weight (also known as degeneracies, g_J) and is given by $g_J = (2J + 1)$. Energies relating to a particular rotation level are given by:

$$E_J = B\,J(J + 1) \tag{2.4}$$

where B is the rotation constant[4]. From the previous equation we see that differences between energy levels is given by:

$$E_{J+1} - E_J = 2B(J + 1) \tag{2.5}$$

From these values it is possible to calculate the wavelength at which a particular transition occurs for ^{12}CO (3-2) equates to 345.8 GHz (867 μm). Using $h\nu = kT$ we see this transition corresponds to a characteristic temperature of 16.6 K for ^{12}CO (3-2) and 5.5 K for ^{12}CO (1-0). From equation 2.5 it is easily seen that more massive molecules have rotational transitions closer together due to their smaller rotational constants.

The way in which linear molecules are distributed into these rotational levels is governed by *i)* density *ii)* temperature of the gas *iii)* emission or *iv)* absorption of background photons. Collisional excitation is predominantly via collisions with the abundant molecule H_2. When collisions dominate the distribution of molecules in rotation levels, as opposed to radiation, we can assume that the region observed is in thermal equilibrium (TE). In TE the relative population of each excitation level (n_l/n_u) is given by a combination of both the single

[3] a molecule with an even distribution of charge will not experience a change in electric field as it undergoes a change in its rotational state

[4] $B = \hbar^2/2I$ where I is the moment of inertia and is therefore isotopologue dependant. For ^{13}CO B = 55101.011 MHz, for ^{12}CO B = 57635.968 MHz, and for C^{18}O B = 54891.420 MHz. These values have been taken from http://spec.jpl.nasa.gov/

excitation temperature (given by Boltzmann distribution, $T_{\rm ex}$) and the statistical weights for different energy levels. Thus we see the population of the energy levels are given by the following equation:

$$\frac{n_u}{n_l} = \frac{g_u}{g_l} e^{-h\nu/kT_{\rm ex}} \tag{2.6}$$

The motivation for examining rotational transitions of linear molecules within this section is due to the use of CO as a tracer for the dense molecular content within the W51 GMC (see Chapters 3 and 4). Although TE is unlikely to apply to the entire content of most molecular clouds, whose temperatures may vary widely, it is possible to use the assumption that on local volume scales TE may hold (known as LTE, local thermal equilibrium). **In the cases, where TE holds, the excitation temperature of the gas can be taken to equal the kinetic temperature of the gas.**

2.4 Radiative transfer

The previous sections detailed how, in the Rayleigh-Jeans limit, the intensity of radiation is proportional to brightness temperature, and how spectral line emission from rotational transitions arise. What was not examined was *how* the intensity of emission travelling through a medium will change depending on the absorption, emission or scattering processes occurring within the medium. This gain or loss in intensity at a particular frequency over a length, s, is described by the absorption and emission coefficients, κ and ε respectively, and is known as the *equation of radiative transfer*:

$$\frac{dI_\nu}{ds} = -\kappa_\nu I_\nu + \varepsilon_\nu \tag{2.7}$$

Radiative transfer in terms of Einstein coefficients

For observations of spectral lines (particularly when calculating column densities, as we will see in section 2.6.2), it is useful to express the equation of radiative transfer in terms of the Einstein coefficients (A_{ul}, B_{ul}, B_{lu}, see Fig. 2.1) that describe the process of absorption and emission, to detail how the levels in a particular transition are populated. The probability of spontaneous emission is given by $P_e = A_{ul}$ and the probability of stimulated emission and absorption is given by $P_s = B_{ul}U$ and $P_a = B_{lu}U$ respectively. U is the energy density of the radiation field and is given by:

$$U = \frac{4\pi \bar{I}_\nu}{c} \tag{2.8}$$

where $\bar{I}$ is the mean intensity over all solid angles. If there is no net change of intensity within a medium (i.e. total emission equals total absorption) then the following must hold:

$$n_u A_{ul} + n_u B_{ul} U = n_l B_{lu} U \tag{2.9}$$

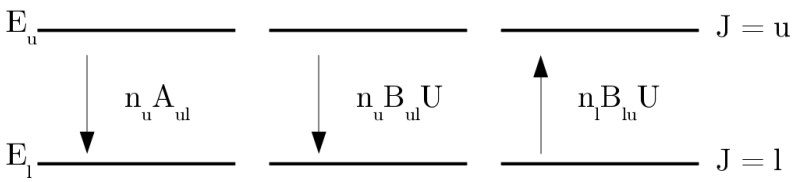

Figure 2.1: Illustration of the process of emission and absorption in term of the Einstein coefficients between upper and lower transition levels.

where n_l and n_u is the number densities of atoms in the lower and upper levels respectively. Rearranging we find that:

$$U = \frac{A_{ul}/B_{ul}}{(n_l/n_u)(B_{lu}/B_{ul}) - 1} \tag{2.10}$$

When a gas is in TE its kinetic temperature may be obtained from its excitation temperature. Substituting 2.6 into 2.10 we find:

$$U = \frac{A_{ul}/B_{ul}}{(g_l/g_u)(B_{lu}/B_{ul})(e^{h\nu/kT}) - 1} \tag{2.11}$$

U, the energy density, is related to the Planck function (see equation 2.2) via equation 2.8. Under TE the two equations will equal provided:

$$g_l B_{lu} = g_u B_{ul} \tag{2.12}$$

$$A_{ul} = \frac{8\pi h\nu^3}{c^3} B_{ul} \tag{2.13}$$

It should be noted that this Einstein coefficient A_{ul} has a specific form when considering an electric dipole (i.e. a molecule such as CO) which may be expressed as:

$$A_{ul} = \frac{64\pi^4\nu^3}{3hc^3}\mu^2\frac{(J+1)}{g_u} \tag{2.14}$$

where μ is the permanent dipole moment of the molecule. The radiative transfer equation (see equation 2.7) can also be written in term of Einstein coefficients. Following the derivation in Rohlfs and Wilson 2004 (where we consider the total energy over a range of frequencies, considering all the atoms present and considering, where necessary, the energy density of the stimulating source) we obtain:

$$\frac{dI}{ds} = -\frac{h\nu}{c}[n_l B_{lu} - n_u B_{ul}] I_\nu \phi_\nu + \frac{h\nu}{4\pi} n_u A_{ul} \phi_\nu \tag{2.15}$$

where ϕ_ν is the normalised line profile described by $\phi_\nu = d\nu^{-1}$. From comparing equation 2.15 with the original radiative transfer equation we see it is possible to express the absorption and emission coefficients (κ_ν and ε_ν relating to the physics within the medium) in terms of Einstein coefficients (the small scale physics):

$$\kappa_\nu = \frac{h\nu}{c} n_l B_{lu} \left[1 - \frac{n_u}{n_l}\frac{B_{ul}}{B_{lu}}\right] \phi_\nu \tag{2.16}$$

$$\varepsilon_\nu = \frac{h\nu}{4\pi} n_u A_{ul} \phi_\nu \tag{2.17}$$

Equation 2.16 may also be expressed in the following way by using the Boltzmann equation (see equation 2.6), to yield:

$$\kappa_\nu = \frac{c^2}{8\pi}\frac{1}{\nu^2}\frac{g_u}{g_l} n_l A_{ul} \left[1 - e^{-h\nu/kT}\right] \phi_\nu \tag{2.18}$$

This result will be used later in this Chapter when we use the absorption coefficient to derive column densities.

2.5 The detection equation

The equation of radiative transfer as given by equation 2.7 expressed how the intensity of radiation may increase or, as is more likely, diminish as it travels through a medium. If we recall at sub-millimetre wavelengths it is useful to express flux in terms of temperature. It is therefore important for astronomy at sub-millimetre wavelengths to be able to express how the received temperature in terms of the background temperature, the brightness temperature and the opacity of the medium (known as the detection equation).

To derive the detection equation we begin by considering the equation of radiative transfer (equation 2.7) in the limits of local thermodynamic equilibrium (no change over ds) and so the intensity of the radiation depends only on T. In this limit $dI_\nu/ds = 0$ and so:

$$I_\nu = S_\nu = B_\nu(T) = \frac{\varepsilon_\nu}{\kappa_\nu} \tag{2.19}$$

This ratio of emission to absorption is known as Kirchhoff's Law where S_ν is the source function. The absorption coefficient κ_ν is described as the number of collisions per unit length. Optical depth, $d\tau_\nu$ (also known as dust opacity), describes how well radiation can pass through a medium and is dependent on κ_ν. The change in optical depth is described by:

$$d\tau_\nu = -\kappa_\nu ds \tag{2.20}$$

Optical depth is equal to the cross sectional area of a dust grain, σ_λ, multiplied by the column density, $N(H_2)$, i.e. $\tau_\lambda = \sigma_\lambda . N(H_2)$. To look at how intensity varies with optical depth it is possible to substitute equation 2.20 into 2.7 and use equation 2.19 to yield:

$$-\frac{1}{\kappa_\nu}\frac{dI_\nu}{ds} = \frac{dI_\nu}{d\tau_\nu} = I_\nu - S_\nu \tag{2.21}$$

the above differential equation can be solved by multiplying through by the integrating factor $e^{\tau'_\nu}$ and integrating by parts over the range from $\tau'_\nu = 0$ to $\tau'_\nu = \tau_\nu$.

$$\int_0^{\tau_\nu} e^{\tau'_\nu} \frac{dI_\nu}{d\tau_\nu} d\tau'_\nu = \int_0^{\tau_\nu} (S_\nu - I_\nu) e^{\tau'_\nu} d\tau'_\nu \tag{2.22}$$

using the method of integration by parts this becomes:

$$[I_\nu e^{\tau'_\nu}]_0^{\tau_\nu} - \int_0^{\tau_\nu} I_\nu e^{\tau'_\nu} d\tau'_\nu = \int_0^{\tau_\nu} (S_\nu - I_\nu) e^{\tau'_\nu} d\tau'_\nu \tag{2.23}$$

$$[I_\nu e^{\tau_\nu}]_0^{\tau_\nu} = \int_0^{\tau_\nu} S_\nu e^{\tau'_\nu} d\tau'_\nu \tag{2.24}$$

putting in the limits this becomes:

$$I_\nu e^{\tau_\nu} - I_\nu(0) = \int_0^{\tau_\nu} S_\nu e^{\tau'_\nu} d\tau'_\nu \tag{2.25}$$

rearranging and dividing though by e^{τ_ν} we see:

$$I_\nu = I_\nu(0) e^{-\tau_\nu} + \int_0^{\tau_\nu} S_\nu e^{\tau'_\nu} e^{-\tau_\nu} d\tau'_\nu \tag{2.26}$$

This equation may be resolved further if the source function is constant and does not vary with optical depth, such that $S_\nu = S_\nu(0) = S_\nu(\tau_\nu)$, in this case:

$$I_\nu = I_\nu(0) e^{-\tau_\nu} + [S_\nu - S_\nu e^{-\tau_\nu}] \tag{2.27}$$

$$I_\nu = S_\nu + e^{-\tau_\nu}(I_\nu(0) - S_\nu) \tag{2.28}$$

For large optical depths $\tau_\nu(0) \to \infty$ then $e^{-\tau_\nu} \to 0$. In this case $I_\nu = S_\nu$ which in the case of TE $I_\nu = S_\nu = B_\nu(T)$ which is described by the Planck Function. To obtain the observed brightness we need to subtract the background intensity from the intensity emitted from the source (as given by equation 2.28):

$$I_\nu(obs) = I_\nu - I_\nu(0) = (S_\nu - I_\nu(0))(1 - e^{-\tau_\nu}) \tag{2.29}$$

The observed brightness equation 2.29 can be expressed in terms of received temperature T_R recall equation 2.3. It is also possible to express S_ν in terms of an excitation temperature (T_ex) and $I_\nu(0)$ in terms of a background temperature (T_{bg}) typically taken as the Cosmic Microwave Background radiation that has a temperature of 2.7 K. We can express both S_ν and $I_\nu(0)$ in terms of T_R by combining equations 2.2 and 2.3 to obtain:

$$T_\mathrm{R} = \frac{h\nu}{k} \frac{1}{e^{h\nu/kT} - 1} \tag{2.30}$$

Substituting equation 2.30 into the observed brightness equation (equation 2.29) results in:

$$T_{\rm R} = \frac{h\nu}{k}\left[\frac{1}{e^{h\nu/kT_{\rm ex}}-1} - \frac{1}{e^{h\nu/kT_{bg}}-1}\right](1-e^{-\tau_\nu}) \tag{2.31}$$

which may be simplified using ($T_o = h\nu/k$):

$$T_{\rm R} = T_o\left[\frac{1}{e^{T_o/T_{\rm ex}}-1} - \frac{1}{e^{T_o/T_{bg}}-1}\right](1-e^{-\tau_\nu}) \tag{2.32}$$

this is known as the *detection equation*. This detection equation is important as it links the observable quantity $T_{\rm R}$ to the physical properties of the source $T_{\rm ex}$ and τ_ν. **During observations where an 'off source' region of sky is subtracted from 'on source' emission it is seen that the CMB in the above equation becomes automatically subtracted.**

2.6 Deriving physical properties

To relate the intensity of the radiation emitted from a source to the physical properties of the emitting region is vital for astronomers. Below I discuss the methods to obtain these properties used within this thesis.

2.6.1 Optical depth

Equation 2.32 showed that the observed temperature of radiation is related to the source temperature, background temperature and opacity. If we make the assumption that the background temperature, excitation temperature, the beam filling factor and the telescope beam efficiency[5] remain constant we may derive a formula that relates the ratio of two transitions, i.e. ^{13}CO and C^{18}O to the optical depth:

$$R_{1318} = \frac{T_{\rm R}(^{13}CO)}{T_{\rm R}(C^{18}O)} \approx \frac{1-e^{-\tau_{13}}}{1-e^{-\tau_{18}}} \tag{2.33}$$

if the lines are optically thin then it is possible to obtain opacities for either ^{13}CO or C^{18}O if we assume an abundance ratio X of ^{13}CO with respect to C^{18}O:

$$R_{1318} \approx \frac{1-e^{-\tau_{13}}}{1-e^{-\tau_{13}/X}} \tag{2.34}$$

the abundance ratio for ^{13}CO to C^{18}O is generally found to be $\sim 10^{-2}$ (Wilson *et al.* 1981; Frerking *et al.* 1982; Wilson 1999). The abundance ratio for ^{12}CO to ^{13}CO is found to be $\sim$60 (Langer and Penzias, 1990).

[5]The ratio of the solid angle of the main beam to the solid angle of the antenna.

2.6.2 Column density

To obtain the column density we use the equation for optical depth (see equation 2.20), the equation for the absorption coefficient, κ_{nu}, as described by 2.16, and the integral of the number density along the line of sight ($N_l = \int_0^s n_l ds$), to yield:

$$\tau_\nu = \frac{c^2}{8\pi}\frac{g_u}{g_l}\frac{A_{ul}N_l}{\nu^2 d\nu}\left[1 - e^{h\nu/kT}\right] \tag{2.35}$$

see Lang (1980) and Garden *et al.* (1991). Now we have an expression in terms of column density in the lower level, N_l, rather than number density. Using $dv/v = d\nu/\nu$ and integrating over the the velocity range we can now rearrange equation 2.35 to obtain the total column density for the lower level:

$$N_l = \frac{8\pi\nu^3}{c^3 A_{ul}}\frac{g_l}{g_u}\left[1 - e^{h\nu/kT}\right]^{-1}\int \tau_\nu dv \tag{2.36}$$

We relate the total column density for the lower level to the total column density over all levels via the Boltzmann equation (equation 2.6) and the partition function ($Z(t)$):

$$N_l = \frac{g_l}{Z(T)}\, N_{tot}\, e^{-hBJ(J+1)/kT} \tag{2.37}$$

where $Z(T)$ can be expressed as:

$$Z(T) = \sum_{J=0}^{\infty} g_J\, e^{-hBJ(J+1)/kT} \approx \frac{k}{hB}\left(\frac{T + hB}{3k}\right) \tag{2.38}$$

Finally by substituting equation 2.14 into equation 2.36 and using equations 2.37 and 2.38 we obtain an expression for the total column density, as given below (see Garden *et al.* 1991):

$$N_{tot} = \frac{3k}{8\pi^3 B\mu^2}\frac{e^{hBJ(J+1)/kT}}{(J+1)}\frac{(T + hB/3k)}{1 - e^{-h\nu/kT}}\int \tau_\nu dv \tag{2.39}$$

where μ is the permanent electric dipole moment[6] and $\int \tau_\nu d\nu$ may be obtained using equation 14.55 in Rohlfs and Wilson (2004):

$$T\int \tau_\nu d\nu = \frac{\tau_0}{1 - e^{-\tau_0}}\int T_{MB_\nu} d_\nu \tag{2.40}$$

where $\int T_{MB_\nu} d_\nu$ is essentially the integrated intensity ($\mathrm{K\,km\,s^{-1}}$).

[6] See http://spec.jpl.nasa.gov/

2.6.3 Temperature

To obtain the excitation temperature of a source it is possible to use the detection equation (see equation 2.32) under the assumption of LTE. If the line is optically thick (which is the case we use in Chapter 4)[7] then as $\tau_\nu(0)$ increases $e^{-\tau_\nu} \rightarrow 0$ and equation 2.32 simplifies to:

$$T_{\rm R} = T_o \left[\frac{1}{e^{T_o/T_{\rm ex}} - 1} - \frac{1}{e^{T_o/T_{bg}} - 1} \right] \tag{2.41}$$

recall $T_o = h\nu/k$. The above equation may be rearranged to give:

$$T_{\rm ex} = \frac{T_o}{ln\left[1 + \frac{T_o}{T_{\rm R} + T_o/(e^{T_o/T_{bg}} - 1)}\right]} \tag{2.42}$$

This excitation temperature $T_{\rm ex}$ relates to relative abundances of molecules in different energy levels and under LTE gives an indication of the temperature of the region being observed.

2.6.4 Masses

We obtain the mass of an object within this thesis by two methods i) based on column density estimates of the object ii) based on the luminosity of the object. The former method can be used for emission lines (as used in Chapter 4), and the latter method for continuum emission (as used in Chapter 5). The first method considers a column of mass M such that:

$$M \; = \; N A \, \mu \, {\rm m}_H \tag{2.43}$$

where N is the column density of H_2 (obtained using the method in section 2.6.2), which is multiplied by the projected area on the sky (A), the mean molecular weight of the gass (μ) and the mass of hydrogen (${\rm m}_H$).

To obtain masses in terms of the luminosity of an object we use the equation presented by Hildebrand (1983). To obtain this equation we first consider the equation of radiative transfer, equation 2.7. If there is no net loss or gain in intensity within a cloud, and provided I_ν has no spatial variations it is possible to write equation 2.7 as:

$$\varepsilon_\nu = \kappa_\nu B_\nu(T) \tag{2.44}$$

We can express κ_ν in terms of the mean free path (more specifically the inverse of the mean free path) to build an equation:

$$\varepsilon_\nu = n'_d \sigma_d Q_\nu(a) B_\nu(T) \tag{2.45}$$

where n'_d is the number density of the dust, σ_d is the cross sectional area, and $Q_\nu(a)$ is the extinction efficiency[8] and a is the grain radius (typically $\sim 1\,\mu$m or smaller). This equation

[7] See Shinnaga *et al.* (2008) as an example of obtaining $T_{\rm ex}$ in the optically thin regime.

[8] dependent on absorption and scattering

may be multiplied by the volume of the dust and by 4π to convert from ε_ν, the energy per unit volume per solid angle per unit time, into luminosity L:

$$L = 4\pi n_d \sigma_d Q_\nu(a) B_\nu(T) \tag{2.46}$$

where the n_d is the volume number density of the dust. We can then express the above in terms of the observable flux F

$$F = \frac{n_d \sigma_d Q_\nu(a) B_\nu(T)}{d^2}. \tag{2.47}$$

Rearranging the above in terms of volume number density we may obtain an equation in terms of dust mass (M_d) by using $M_d = n_d\, v\, \rho_d$ where n_d is the number of dust particles, v is the volume of a dust grain (hence the total volume of dust is given by: $N_d\, v$) and ρ_d is the density of the dust. This yields:

$$M_d = \frac{F d^2 V \rho_d}{\sigma_d Q_\nu(a) B_\nu(T)} \tag{2.48}$$

which may be expressed as:

$$M_d = \frac{F d^2 \rho_d}{Q_\nu(a) B_\nu(T)} \frac{4}{3} a. \tag{2.49}$$

The above is the dust mass, if we want to obtain the clump or core mass we must take into account the fact that typically the ISM is composed of 99% gas and 1% dust. To account for this we express the above using the dust mass coefficient C_ν to obtain a cloud clump or core mass M:

$$M = \frac{d^2 F_\nu C_\nu}{B_\nu(T)} \tag{2.50}$$

where:

$$C_\nu = \frac{4}{3} \frac{a}{Q_\nu(a)} \rho_d \left(\frac{M_g}{M_d} \right) \tag{2.51}$$

where M_g/M_d is the gas to dust ratio. C_ν is typically taken to be a power law in frequency and it is therefore possible to convert between values quoted at differing frequencies using:

$$C_\nu = C_{\nu_0} (\nu_0/\nu)^\beta \tag{2.52}$$

where β is the emissivity index ($\beta \approx 1.85$, Ossenkopf and Henning 1994), also known as the optical gradient, which may change across a cloud, depend on grain size, shape, coating (no mantles, thin ice mantle, thick ice mantle), mixtures and coagulation (Hildebrand 1983), although this will change C_ν by no more than a factor of two (Ossenkopf and Henning 1994). In this work we use the value of $\mathrm{C}_\nu = 50\,\mathrm{g\,cm^{-2}}$ at $850\,\mu$m which is taken from Kerton *et al.* (2001).

Chapter 3

The W51 GMC Catalogue

'Houston, Tranquillity Base here. The Eagle has landed'
Neil Armstrong

The motivation of this Thesis is to look for and study the natal sites of massive star formation. We begin by studying the W51 GMC, located in the constellation of Aquila. We chose to study the W51 GMC in particular due to its extreme characteristics in terms of mass, luminosity, complex morphology and distance. Our aim will be to build up a picture of the future for star formation within this particular GMC, looking at the places where stars are likely to form: dense molecular clumps.

3.1 The W51 GMC

In this section I give a brief literature review of the W51 GMC before going on to Section 3.2, where I detail the motivation behind obtaining molecular observations of this particular GMC.

3.1.1 Morphology

The W51 GMC, located in the Sagittarius arm of the Galaxy, was originally identified by Westerhout (1958) from 21 cm continuum emission, produced by thermal emission from the HII regions. Historically the W51 GMC complex has been discussed in terms of two main regions: W51A and W51B, identified by their thermal radio emission (Bieging 1975; Kundu and Velusamy 1967; Mufson and Liszt 1979). A third component, W51C, a supernova remnant distinguished by its non-thermal emission was also identified (Koo and Moon, 1997b).

Further studies revealed W51A to consist of two major HII complexes know as G49.5–0.4 and G49.4–0.3 (see Fig 3.1) each containing several compact HII regions (Mufson and Liszt 1979; Mehringer 1994). Similarly W51B is composed of numerous smaller HII components including G49.2–0.3, G49.17–0.21, G49.10–0.27, G49.1–0.4, G49.0–0.3 and G48.9–0.3 (Fig 3.1), again each with compact HII regions within (Martin, 1972).

More recently, with the advance of astronomical techniques such as integral field spectroscopy, the W51 complex has been decomposed based on radial velocity data. This is particularly useful as W51, at a galactic longitude of 49°, intersects the Sagittarius arm tangentially and extends several kpc along this arm, resulting in multiple clouds lying along the same line of sight (Mufson and Liszt, 1979). What was found is that the W51 GMC can be decomposed into two distinct regions: the W51 complex and the High Velocity Stream (HVS, Carpenter and Sanders 1998; Koo 1999; Okumura *et al.* 2000; and Okumura *et al.* 2001).

The HVS is so called as it exceeds the maximum velocity expected based on its kinematic distance and galactic rotation curve (Brand and Blitz, 1993)[1] at the Sagittarius tangential point (at l=49°). If we take $l = 49°$, and a distance to W51 between 6 – 8 kpc (see discussion in the following section) then we see this position corresponds to radial velocities ($v_{\rm R}$) around $55\,{\rm km\,s^{-1}}$. The HVS, with velocities on the order of $> 65\,{\rm km\,s^{-1}}$ is well above velocities explained by Galactic rotation alone and so are believed to be streaming motions caused by a spiral density wave (Burton and Shane 1970; Koo 1999).

3.1.2 Distance

The position of the W51 GMC at the tangent point of the Sagittarius arm leads not only to complications in understanding its morphology but also makes distance determinations non-trivial. From the literature we find a range of heliocentric distance estimates to the W51 GMC, which we summarise in Table 3.1 and discuss in detail below.

Based on 21 cm absorption features Sato (1973) determined the distance to two HII regions in W51A to be ∼8 kpc. Carpenter and Sanders (1998) used a proper motion study of masers within G49.5-0.4 to derive a similar distance estimate of 7.0±1.5 kpc. Imai *et al.* (2003) also use this method and determine a distance to W51 North of 6.1 ± 1.3 kpc. Some parts of W51A have been found to lie at a different distance possibly as result of projection effects from clouds at differing distances. Sato *et al.* (2010) using 22 GHz H_2O masers obtained a parallax distance of $5.41\,{\rm kpc}^{+0.31}_{-0.28}$ to W51. Russeil (2003) reports a distance to W51A of 5.5 kpc. W51 IRS 2 has been found to lie at a distance of $5.1\,{\rm kpc}^{+2.9}_{-1.4}$ (Xu *et al.*, 2009). Sato (1973) also determined distances to HII regions in W51B based on 21 cm absorption and found them located at a distance ∼6.5 kpc. Koo (1999) also report a distance between 6.4 and 6.9 kpc based on kinematic CO observations.

A significantly smaller distance, of 2.0±0.3 kpc, has also been determined using spectroscopic parallaxes to newly formed OB stars associated with W51A by Figuerêdo *et al.* (2008). However, as discussed by Clark *et al.* (2009), the reason for an underestimation in this distance estimate is likely to be a result of the adoption of an incorrect reddening law, multiplicity or incorrect spectral classification.

[1] which is an empirical expression: $V_s = V_0 \left[a_1 \left(\frac{\rm R}{R_0} \right)^{a_2} + a_3 \right]$ where $a_1 = 1.00767\,{\rm km\,s^{-1}}$, $a_2 = 0.0394$, $a_3 = 0.00712\,{\rm km\,s^{-1}}$, V_0 is the radial velocity of the Sun ($220\,{\rm km\,s^{-1}}$) and R_0 is the distance from the Sun to the Galactic centre (8.5 kpc). For a full derivation of kinematic distance determinations see Purcell (2006).

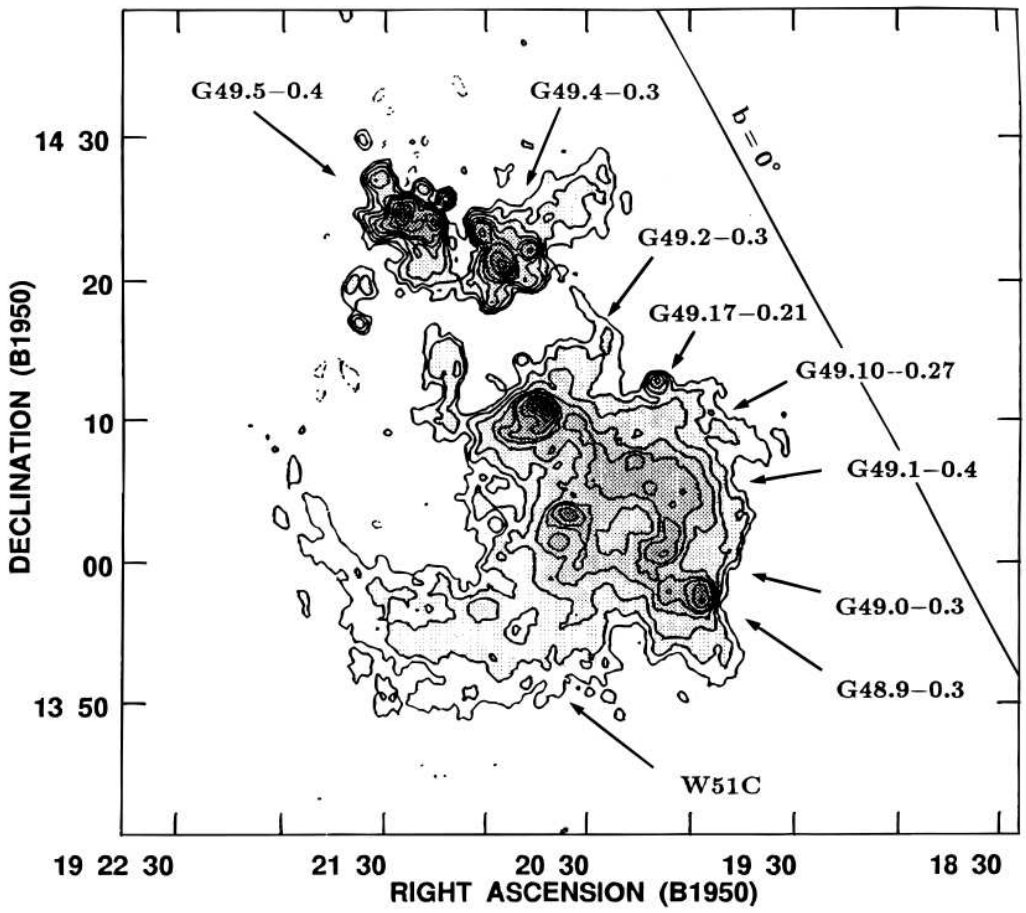

Figure 3.1: A 21 cm radio continuum map of the W51 complex. The map was made by combining VLA data and 21 cm Bonn survey data. The contour levels are 0.015, 0.03, 0.06, 0.12, 0.2, 0.3, 0.6, 1.0, 1.5, and 2.4 Jy beam^{-1}. The arrows point at the labelled radio continuum sources, including the large shell-type source W51C SNR. G49.5-0.4 and G49.4-0.3 both contain several discrete components, whereas the other "G" sources appear as single discrete components. G49.10-0.27 is a relatively weak source at (19h20m15s.2, 14°7'10"). Image reproduced from Koo and Moon (1997a).

Distance (kpc)	Region	Reference
8.0	W51A	Sato (1973)
7.0±1.5	W51A	Carpenter and Sanders (1998)
6.1 ± 1.3	W51A	Imai *et al.* (2003)
5.5	W51A	Russeil (2003)
2.0±0.3	W51A	Figuerêdo *et al.* (2008)*
$5.1^{+2.9}_{-1.4}$	W51A	(Xu *et al.*, 2009)
$5.41^{+0.31}_{-0.28}$	W51A	Sato *et al.* (2010)
6.5	W51B	Sato (1973)
6.4 – 6.9	W51B	Koo (1999)

Table 3.1: Summary table of distance estimates to the the two main regions (W51A and B) in the W51 GMC. Distances are listed in chronological order. *See end of Section 3.1.2 for discussion of this particular distance estimate.

3.1.3 Size and mass

Size and mass estimates for regions within the W51 GMC are numerous, and are hampered by the distance problem, as discussed in the previous section. Considering the large scale structure, size estimates typically place W51A as having a diameter of 30 pc (Scoville and Solomon 1973; Mufson and Liszt 1979) with the HVS stretching up to 100 pc in length with a large aspect ratio (Carpenter and Sanders 1998; Kang *et al.* 2010).

Stellar mass estimates from near infrared studies of the complex, show the W51A complex to contain a stellar mass of $1.76 \times 10^4\,\mathrm{M}_\odot$ Okumura *et al.* (2000). Three of the compact HII regions within the W51B region contain a stellar mass of $\sim 1.4 \times 10^4\,\mathrm{M}_\odot$ Kim *et al.* (2007). Kumar *et al.* (2004) reported a total sum of stellar mass in clusters to be on the order of $3 \times 10^4\,\mathrm{M}_\odot$.

Separate mass estimates for the molecular content based on sub millimetre observations reveal W51B to be on the order of $1.21 \times 10^5\,\mathrm{M}_\odot$ (adopting a distance of 8.5 kpc), from ^{12}CO (1–0) and (2–1) observations (Koo, 1999). Carpenter and Sanders (1998) mapped the entire region in ^{12}CO and ^{13}CO (1–0) and found mass estimates of $1.19 \times 10^6\,\mathrm{M}_\odot$ for the W51 GMC and $1.9 \times 10^5\,\mathrm{M}_\odot$ for the HVS, based on a distance estimate of 7 kpc. Based on the literature Carpenter and Sanders (1998) place the W51 GMC complex in the upper 1 % by size and upper 5–10 % by mass of GMCs.

3.1.4 Star forming indicators

The W51 GMC was originally identified by the detection of thermal emission from HII regions within the complex (Westerhout 1958; Bieging 1975; Kundu and Velusamy 1967). Since then numerous studies have provided further evidence for current and ongoing massive star formation in the W51 GMC.

Observations of the current stellar content of W51 have revealed several embedded star clusters associated with the HII complexes identified in Fig. 3.1. The brightest of all, G49.5-0.4

(Mehringer, 1994) in W51A, contains eight compact HII regions within (W51a–h; Koo and Moon 1997b) with two major components: W51d and W51e, associated with two embedded clusters IRS1 and IRS2 (Goldader and Wynn-Williams 1994; Kumar *et al.* 2004). These clusters clearly show the W51 GMC as a particularly active massive star forming region. With the W51d IRS1 cluster found to be larger and more luminous than the Orion-Trapezium cluster (Genzel *et al.*, 1982), and the IRS2 cluster containing 12OB stars (Goldader and Wynn-Williams, 1994).

Evidence for the ongoing formation of massive stars is provided by observations of YSOs, (Kang *et al.* 2010 estimate that 1% of the mass of the W51 GMC is currently in the the form of YSOs), MYSOs (Barbosa *et al.*, 2008), UCHII regions (Kumar *et al.* 2004; Sollins *et al.* 2004; Barbosa *et al.* 2008), H_2O, ammonia and methanol masers (Schneps *et al.* 1981; Zhang and Ho 1995; Phillips and van Langevelde 2005), and hot molecular cores (Barbosa *et al.*, 2008). High angular resolution (∼0.4") observations have also provided evidence for a massive protostar forming within W51 that has a circumstellar disk/molecular ring with an outflow (Zapata *et al.*, 2009).

3.1.5 Lifetime estimates

Age estimates have been made for the lifetime of star formation within the W51 GMC. These age estimates are primarily based on expansions of HII regions, with observations indicating age estimates ranging between 0.7 – 3 Myrs (Okumura *et al.* 2000; Kumar *et al.* 2004; Kim *et al.* 2007). The G49.03–0.3 HII region probably contains the youngest cluster (Kumar *et al.*, 2004). An upper limit to age estimates equal to 9 Myr is based on the lack of evidence of Red Giant Branch stars (RGBs, Clark *et al.* 2009).

3.1.6 Star formation efficiencies

We have seen from the literature that massive star formation within the W51 GMC is ongoing. The question that might leap out is whether the current star formation within the W51 GMC is particularly vigorous or not. An indication of how 'well' the W51 GMC is producing stars may be gleaned by its SFE (see equation 1.1). Variations in SFE estimates arise from the different regions being observed, and the different methods used to obtain the total stellar mass and cloud mass.

SFE vary between 2 – 17% within the literature (Williams and McKee 1997; Koo 1999; Okumura *et al.* 2000; Kumar *et al.* 2004; Kim *et al.* 2007). These variations arise from observations of specific regions, as an example Koo (1999) found a SFE of ∼7% and ∼15% for two regions within W51B, in comparison to Okumura *et al.* (2000) who determined a SFE for G49.5-0.4 (within W51A) between ∼2-8%. Kim *et al.* (2007) reports a SFE for the W51 cloud of 7 % for cloud (including the G48.9-0.3 and G49.0-0.3 regions) but a much higher 17% for G49.2-0.3 region. These variations in SFEs appear to be a result of the star forming history of the W51 GMC being more vigorous in particular locations. An external, cloud-cloud collision event, has been cited as the most likely cause and will be discussed further in the following section.

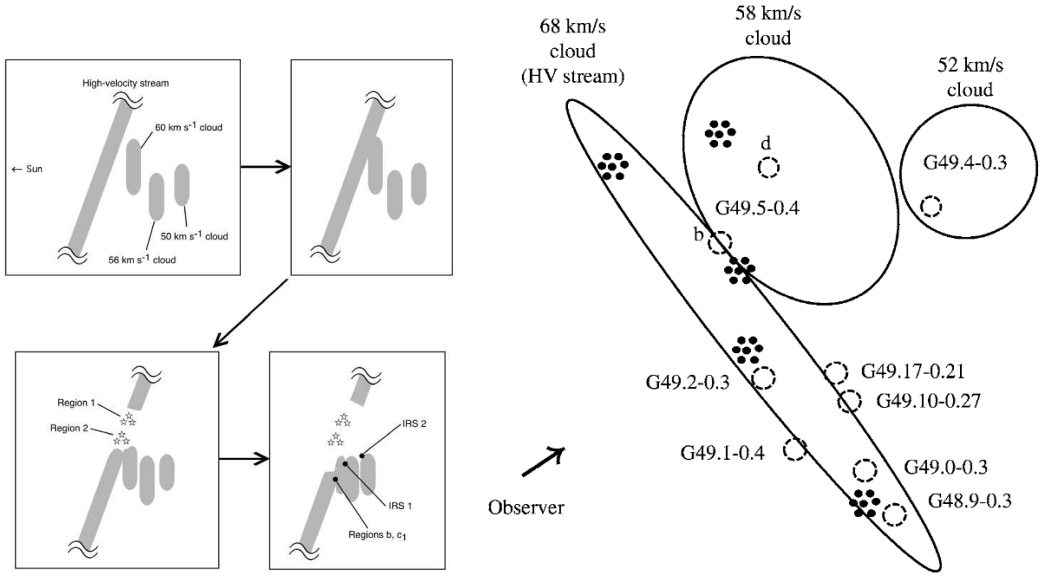

Figure 3.2: Left: Schematic representation of the kinematics and evolution of the molecular clouds towards G49.5–0.4 (Okumura *et al.*, 2001). Right: Schematic diagram of the W51 HII regions, YSO clusters, and molecular clouds in W51. Dashed circles and filled dots represent the HII regions and YSO clusters, respectively (reproduced from Kang *et al.* 2010).

3.1.7 Star formation in W51: colliding clouds

What we have seen from the previous sections is that the W51 GMC is a very active region of star formation. Embedded clusters are found to have ages (0.5-3 Myr) and locations (stretching across a length of ~ 100 pc) that indicate a star formation scenario consistent with an external triggering event or multiple sites (Clark *et al.* 2009; Kumar *et al.* 2004; Carpenter and Sanders (1998))[2]. This places W51 in contrast to other GMCs, i.e. the G305 GMC, which appears to be a wind blown cavity (Hindson *et al.*, 2010).

What has been proposed is that star formation within the W51 GMC has been primarily triggered from a cloud-cloud collision (Scoville *et al.*, 1986) between the W51 complex and the HVS (Arnal and Goss (1985); Pankonin *et al.* (1979); Kumar *et al.* 2004; Carpenter and Sanders 1998; Kang *et al.* 2010) as is schematically shown in both images in Fig. 3.2. The evidence for cloud-cloud collisions is based upon the morphology of the region (Anathpindika, 2009) and the coincidence of HII regions (G49.5-0.4 and G49.17-0.21) located at the point where there is an apparent pile up of clouds (Arnal and Goss 1985; Okumura *et al.* 2001; Kang *et al.* 2010). It is believed that this collision of clouds has been caused by the passage of a spiral density wave (Carpenter and Sanders 1998; Kang *et al.* 2009). This triggering of star formation via cloud-cloud collision is by no means unique to W51, with Duarte-Cabral *et al.* (2011) concluding that star formation within the Serpens molecular cloud could have

[2]This can be seen by examining the sound speed ($c_s = (kT/\mu\, m_{\rm H})^{1/2}$) within W51. For a typical speed of $10\,{\rm km\,s^{-1}}$, we see it would take 10 Myr to travel the 100 pc length of the GMC, in contrast to ages observed which are typically < 3 Myr.

Figure 3.3: Left: The approach to the JCMT (far left), SMA, CSO, Subaru and Keck Telescopes also visible. Right: The dish.

resulted from cloud collisions, based on models of the region. Active star formation within the W51 GMC has also been suggested to be a result of the interaction of a nearby supernova remnant with the W51B cloud (Koo and Moon 1997b; Koo *et al.* 2005). On local scales (i.e. G49.0-0.3 and G48.9-0.3) there are also examples of star formation resulting from expanding HII shells (Kang *et al.*, 2010).

3.2 Motivation

W51 is observed to be going through a particularly strong episode of star formation. This is determined by the following: the life of a MYSO is of the order of 10^4 years which is 1% the life of a GMC (of the order of 10^6 years) and the total mass fraction of MYSOs is observed to be 1% of the W51 GMC mass. The current SFE is observed to be of the order of $\sim 10\%$ (Koo, 1999), which if taken to be the final SFE of the GMC would mean an average SFE for the W51 complex of 0.1%. With star formation rates within W51 observed to be higher than this (typically by an order of magnitude) it indicates that the W51 GMC is currently at a particularly active point in its life (Kang *et al.*, 2010). Is this vigorous star formation reflected in the properties of the natal material from which stars form? Does the natal material indicate how star formation is likely to proceed within W51?

Answering these questions requires observations of the dense molecular clumps from which stars are formed. To date molecular observations of the W51 GMC, (needed to investigate the earliest stages of star formation), are predominantly for the ground states of ^{12}CO and ^{13}CO, tracing the extended emission within the complex at low angular resolution (Koo 1999: ^{12}CO (J = 2–1) and (J = 1–0), Carpenter and Sanders 1998: ^{12}CO (J = 1–0) and ^{13}CO (J = 1–0), and Kang *et al.* (2010): ^{12}CO (J = 2–1) and ^{13}CO (J = 2–1)). Although some higher angular resolution observations (again of the ground state of ^{13}CO) have been made, these have been over smaller regions, typically surrounding one of the known HII regions within the W51 GMC (Koo 1999; Okumura *et al.* 2001; and Sollins *et al.* 2004).

The importance of observing higher rotational energy states of CO is seen when considering

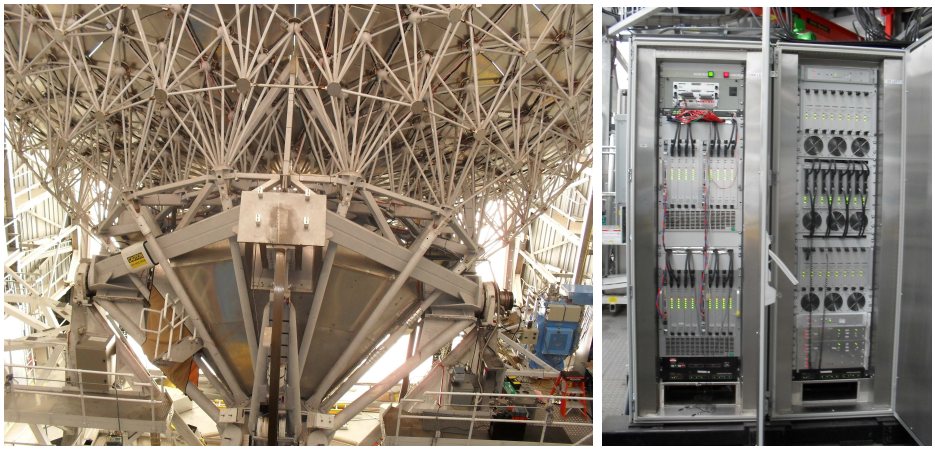

Figure 3.4: Left: The back of the JCMT dish with HARP (instrument in blue) seen on the right. Right: Part of the hardware that makes up ACSIS.

the critical densities of the molecules: the density at which the probability of spontaneous emission is the same as the probability of stimulated absorption. For the (1–0) transition of ^{12}CO this critical density[3] is found to be $7{\times}10^2\,\mathrm{cm}^{-3}$ and $5 \times 10^4\,\mathrm{cm}^{-3}$ for the (3–2) transition. These critical densities translate into Jeans masses on the order of $1\,\mathrm{M}_\odot$ for the ground state and $0.1\,\mathrm{M}_\odot$ for the ^{12}CO (3–2) transitions (taking a temperature of $\sim$12 K), thus the higher transitions traces material that has lower jeans masses thresholds and so we see further into the beginning of the star formation process. It is the high critical densities *combined* with the high abundance of these molecules which makes observations of ^{12}CO (J = 3–2) and its isotopologues ideal for tracing the bulk of the dense material within star forming regions. Observations of this type are crucial to trace the molecular content of the complex before any massive young stellar objects have had enough time and energy to ionise their surrounding material, making them visible in the infrared. This is the material responsible for star formation in W51 GMC and so a detailed analysis of where and what state this reservoir is in, is needed for an understanding of this giant complex. In this chapter, we present new high resolution and high S/N molecular observations of the entire complex.

3.3 Observations and data reduction

3.3.1 Instrumentation

The W51 GMC was mapped using the HARP (Heterodyne Array Receiver Program) receiver with the back-end spectrometer ACSIS (Auto-Correlation Spectral Imaging System) on the 15 m James Clerk Maxwell Telescope, JCMT[4], located on Mauna Kea, Hawaii, at 4092 m (see

[3]critical density (n*): $\mathrm{n}^*\sigma\nu = \mathrm{A}_{ul}$ where A_{ul} is the probability of spontaneous emission (recall Equation 2.14), ν is the velocity (typically $1\,\mathrm{km\,s}^{-1}$) and σ is the cross sectional area, approximately $10^{-16}\,\mathrm{cm}^{-2}$ (see Rohlfs and Wilson 2004 Section 16.2.1).

[4]The James Clerk Maxwell Telescope is operated by the Joint Astronomy Centre on behalf of the Scientific and Technology Facilities Council of the UK, the Netherlands Association for Scientific Research, and the

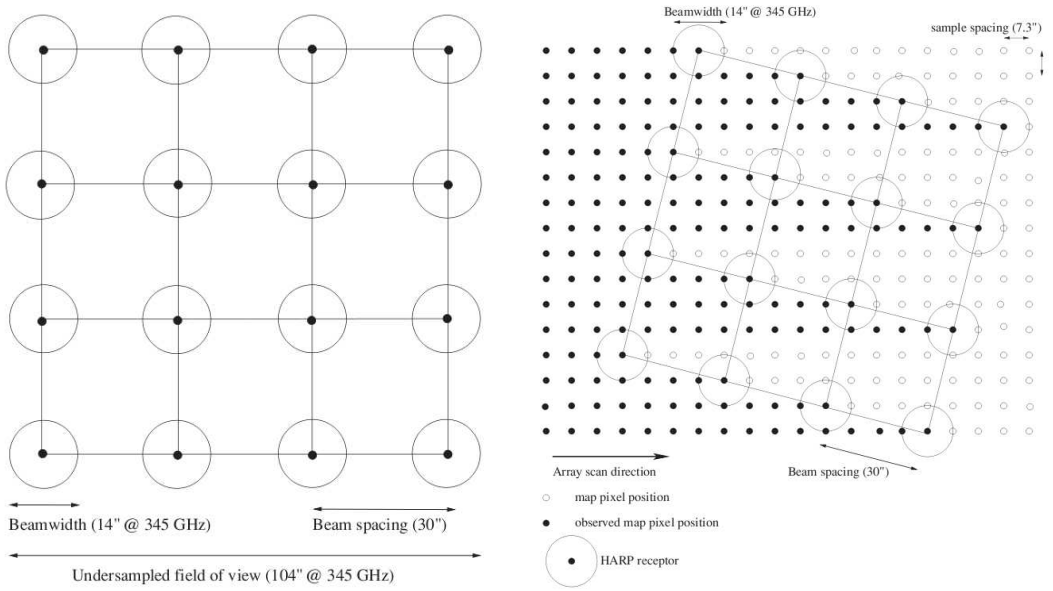

Figure 3.5: Left: HARP footprint. Right: HARP scan (reproduced from Buckle *et al.* 2009).

Fig. 3.3 and Fig. 3.4).

ACSIS is a digital auto-correlator spectrometer. ACSIS as a back end to each of the 16 HARP receptors is analogous to an integral field spectroscopy unit taking multiple spectra at the same time allowing an image to build up. ACSIS allows a choice of either wide band (1 GHz in bandwidth, using both sub-bands, with 1024 channels) or high resolution (250 MHz bandwidth, single sub-band mode, with 8192 channels yielding 31 kHz channel spacing: Buckle *et al.* 2009).

HARP is a heterodyne instrument which means it "mixes" the high frequency (astronomical) signal with a lower frequency (the Local Oscillator), producing a beat frequency. This mixing is done via a SIS (Superconductor-Insulator-Superconductor) junction. The beat frequency, for technological reasons, needs to be at lower frequencies than the original signal so it may be transmitted, amplified and passed onto a spectrometer (further information see Smith *et al.* 2008a).

HARP has 16 SIS receptors that operate between 325 and 375 GHz. The receptors are arranged in a 4×4 array separated by 30" (see left image in Fig. 3.5), which with a beam size of 14" means the sky is under-sampled (Buckle *et al.*, 2009). HARP has several observing modes to account for this with rastering as the most efficient technique to cover a large region such as the W51 GMC. This involves rotating the k-mirror so that the array is at an angle of 14.04° with respect to the scan direction[5], allowing for a fully sampled image (see right image in Fig. 3.5).

National Research Council of Canada.

[5]http://www.jach.hawaii.edu/software/jcmtot/het_example.html

3.3.2 Observations

The area mapped by HARP was covered by a minimum of two repeats, with perpendicular scan directions, in order to build up signal and minimise sky and system uncertainties: a technique known as "basket weaving" (see Fig. 3.7). The large extent of the W51 GMC, required the region to be split into 13 sub-maps typically $1020'' \times 1020''$ in size (see Fig. 3.7, 900" coverage with 30" run in and 30" overlap), observed with a scan spacing of 1/2 an array (58.2"). The choice in size was made as long rasters are more efficient to map large regions. However size is limited by time as calibration/pointing checks are performed hourly.

The data, taken in May 2008, comprises of ∼36 hours observing time taken in Grade 2/3 weather ($0.05-0.12\ \tau_{225\,\mathrm{GHz}}$, where $\tau_{225\,\mathrm{GHz}}$ is the sky opacity at 225 GHz, as measured by the CSO radiometer). Weather (more importantly the amount of water in the atmosphere during an observation) is important as the number of photons reaching detectors in the sub-millimetre regime is affected by the amount of water in the atmosphere. This is known as the PWV (Precipitable Water Vapour), essentially the height, in mm, a column of water would measure if the water in the atmosphere above that specific location was condensed. Figure 3.8 illustrates how the atmospheric transmission is wavelength and PWV dependent, where a PWV less than 1.00 mm ($\tau_{225\,\mathrm{GHz}} < 0.05$) is deemed a really good observing band and greater than 2.75 mm ($\tau_{225\,\mathrm{GHz}} > 0.12$) is poor. Other molecules present in the atmosphere, such as O_2, also absorb radiation at specific wavelengths compounding the problem of observing at these wavelengths.

Observations of ^{13}CO and C^{18}O in the J = 3–2 transition were obtained simultaneously using the multi-subsystem mode of ACSIS, as was ^{12}CO (J = 3–2) and H^{13}CN^{+} (J = 4–3). A band width of 250 MHz was chosen for the observations, with a spectral resolution of 61 kHz, providing a velocity resolution of $0.08\,\mathrm{km\,s^{-1}}$.

3.3.3 Calibration and atmospheric corrections

The aim of the calibration process is to place the signal observed onto a standard temperature scale, account for atmospheric effects and correct for any inefficiencies of the telescope. There are several steps to this process as outlined below (Thompson 1999; Smith *et al.* 2008a):

i) To calibrate a source signal to a temperature scale the receiver observes the response of the system to two or more sources with known temperatures (typically known as the "hot" and "cold" loads, Kutner and Ulich 1981). For HARP the cold load is the ambient temperature at ground level and the hot load is at about 40 K above ambient temperature[6].

ii) Removal of atmospheric variations by subtracting the sky signal (which at 850 μm is $\sim$2,000 $\mathrm{Jy\,beam^{-1}}$) at a particular reference position or frequency is required. This is done by switching the telescope so it receives a signal from a "blank" patch of sky. This is either done by a position switch, beam switch or frequency switch. In our observations we use a position switch, with a technique known as "shared-offs", which is the only position switch method available for this mode of observations. Shared-offs have the disadvantage that the sky noise becomes correlated across the image however shared-offs are hugely advantageous in comparison to "separate-offs" (every position within the image there is a separate reference

[6] www.mrao.cam.ac.uk/projects/harp/public/Project_Overview.pdf

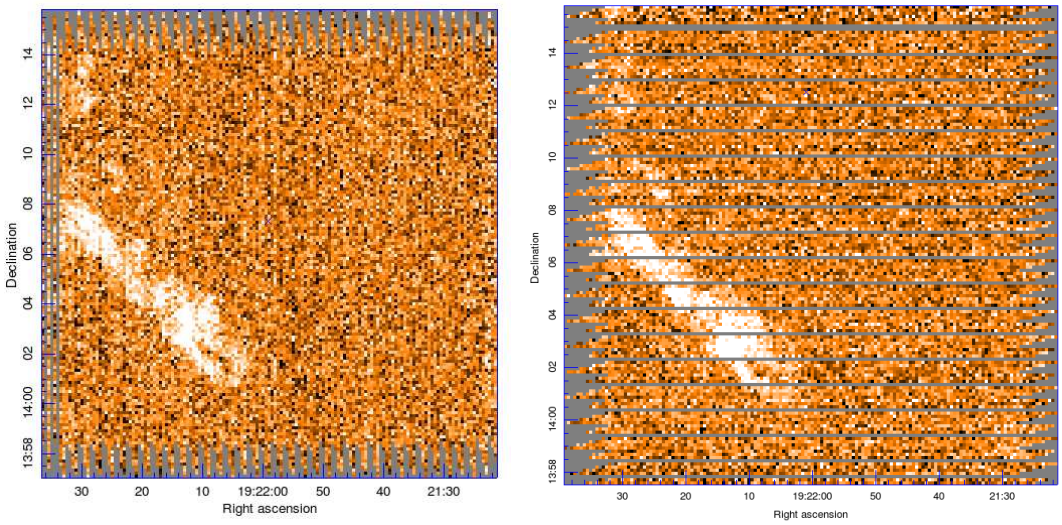

Figure 3.6: Raw data cubes from map 5 (see Fig. 3.7 for the position of map 5) ^{13}CO in position-position-velocity space. The scans are at an angle of 90° with respect to each other to allow a basket weaving technique to be used during the data reduction process.

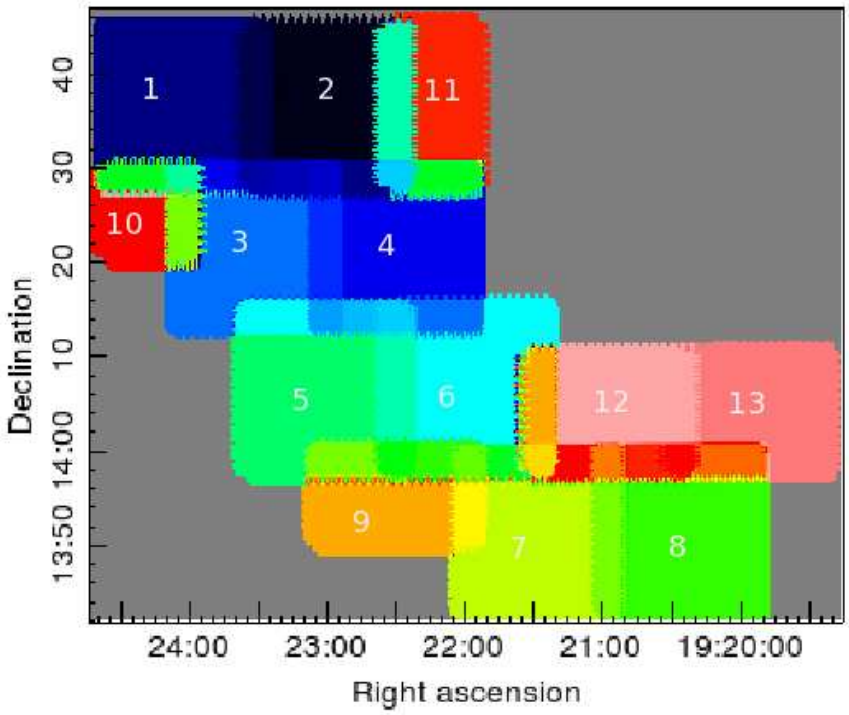

Figure 3.7: Image of the area observed by HARP depicting the individual coverage areas for the 13 individual maps.

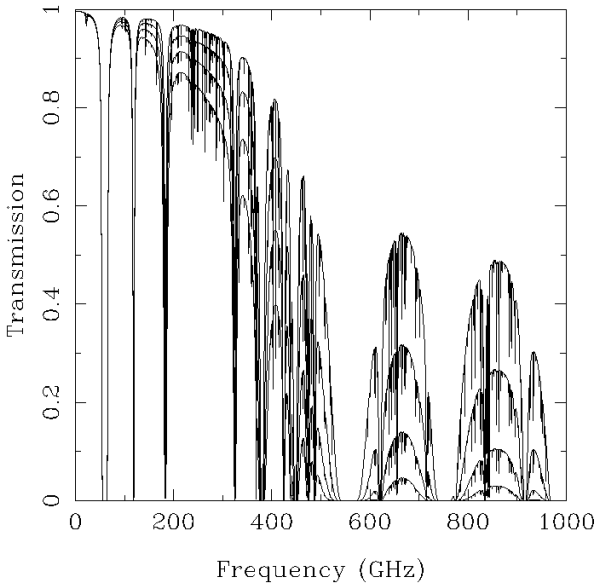

Figure 3.8: Atmospheric transmission for the summit of Mauna Kea (at an altitude of 4,200 m), over a range of frequencies and varying PWV/opacities. Lines from top to bottom: 'exceptional' weather $\tau_{225\,\mathrm{GHz}} = 0.03$; boundary between Grade 1/2 $\tau_{225\,\mathrm{GHz}} = 0.05$; boundary between Grade 2/3 $\tau_{225\,\mathrm{GHz}} = 0.08$; boundary between Grade 3/4 $\tau_{225\,\mathrm{GHz}} = 0.12$ (www.submm.caltech.edu/cso/weather/).

position observation) as the separate-offs require the *same* amount of observing time off source as is spent on source. After an initial check of three potential sites, the reference position was chosen for all observations as: $19^h18^m03.8^s$, $+14°01'53''$.

iii) The extinction correction for elevation dependence of atmospheric opacity. This is required as the intensity of radiation is reduced by $e^{-\tau A}$ where A is the air mass and τ is the atmospheric opacity at zenith.

iv) Correction for telescope efficiency. Planetary data may also be taken during observing and this data is used to calculate the telescope's main beam efficiency, η_{mb}. If planetary data is not available then it is possible to use values provided by the JCMT from other observations[7]. Main beam efficiencies are required to obtain the main beam brightness temperature T^*_{mb} from the antenna temperature T^*_A as shown in equation 3.1. The radiation temperature T^*_{R} is the antenna temperature corrected for forward scattering and spillover[7] (η_{fss}), where $\eta_{fss} = 0.88$ see equation 3.2.

$$T_{mb} = \frac{T^*_A}{\eta_{mb}} \tag{3.1}$$

$$T^*_{\mathrm{R}} = \frac{T^*_A}{\eta_{fss}} \tag{3.2}$$

[7] www.jach.hawaii.edu/JCMT/spectral_line/General/status.html

During data reduction we used the main beam brightness temperature with a main beam efficiency of $\eta_{mb} = 0.63$ for all the isotopologues[7].

In addition to the above the pointing accuracy of the telescope is checked hourly and is done on a known point source close to the location of the observations. These standard spectra are also taken at the start and end of each new observation taken with a different instrument and/or frequency to check that the through put of the signal is correct, that the telescope is focused and is correctly tuned. An estimate can be made based on a comparison to representative spectra published on the JCMT web pages.

3.3.4 Data reduction

The raw data that HARP generates is a series of spectra ordered by receptor and time (see Fig. 3.9). It is the data reduction process that produces a cube containing calibrated spectra ordered in Right Ascension, Declination with Velocity in the third axis. The data were reduced using the automated astronomical data reduction pipeline: ORAC-DR (Cavanagh *et al.*, 2008). ORAC-DR was used with the recipe, REDUCE_SCIENCE_NARROWLINE, that has been developed specifically for Galactic sources. ORAC-DR takes each raw time series in a set of observations and creates a cube. ORAC-DR then checks the quality of the data against specific requirements that may be user defined, known as the Quality Assurance (QA[8]). The first QA check that data goes through is the check on the system temperatures for each receptor compared to the mean of all receptors.

ORAC-DR then fits a rough baseline to the data and then does a QA check on the mean rms values for each receptor compared to the mean of all the receptors. It then checks for variations in rms values as calculated by the system temperatures to those within the spectra on a spectrum by spectrum basis. If necessary those receptors or spectra that violate the QA are set to 'bad'. ORAC-DR then removes gross features and any time variations and repeats the whole process for all observations within a group of observations, in the case of W51, those observations that make up one of the 13 mapped areas. The next step in the pipeline is to produce a group file from the raw input time series, a baseline is created using this group file by smoothing in spatial and frequency coordinates to create a baseline region mask. A baseline is then applied and the spatial uniformity is checked over the central 50% of the map. The uniformity of rms with respect to frequency is also checked. This baseline is then applied to the raw input time series files and the process of producing a group file (all observations for an individual map for a particular isotopologue) and the method is repeated.

The data are then re-gridded into RA, Dec and velocity cubes, and are re-binned to a velocity of 0.5 km/s to improve signal to noise with a noise improvement of $\sqrt{n}$ where n is the number of bins[9]. Finally the individual cubes were combined and the maps co-added using a nearest-neighbour algorithm chosen to prevent smoothing of the data (nearest-neighbour is defined as assigning the input pixel value completely to the single nearest output pixel[10]). Blank pixels present after this combining and co-adding are a result of sky rotation during the observing run.

[8] www.jach.hawaii.edu/JCMT/surveys/docs/QA_v1.0.pdf

[9] To convert between velocity and frequency resolution it is possible to use: $dv/c = d\nu/\nu$

[10] http://starlink.jach.hawaii.edu/starlink

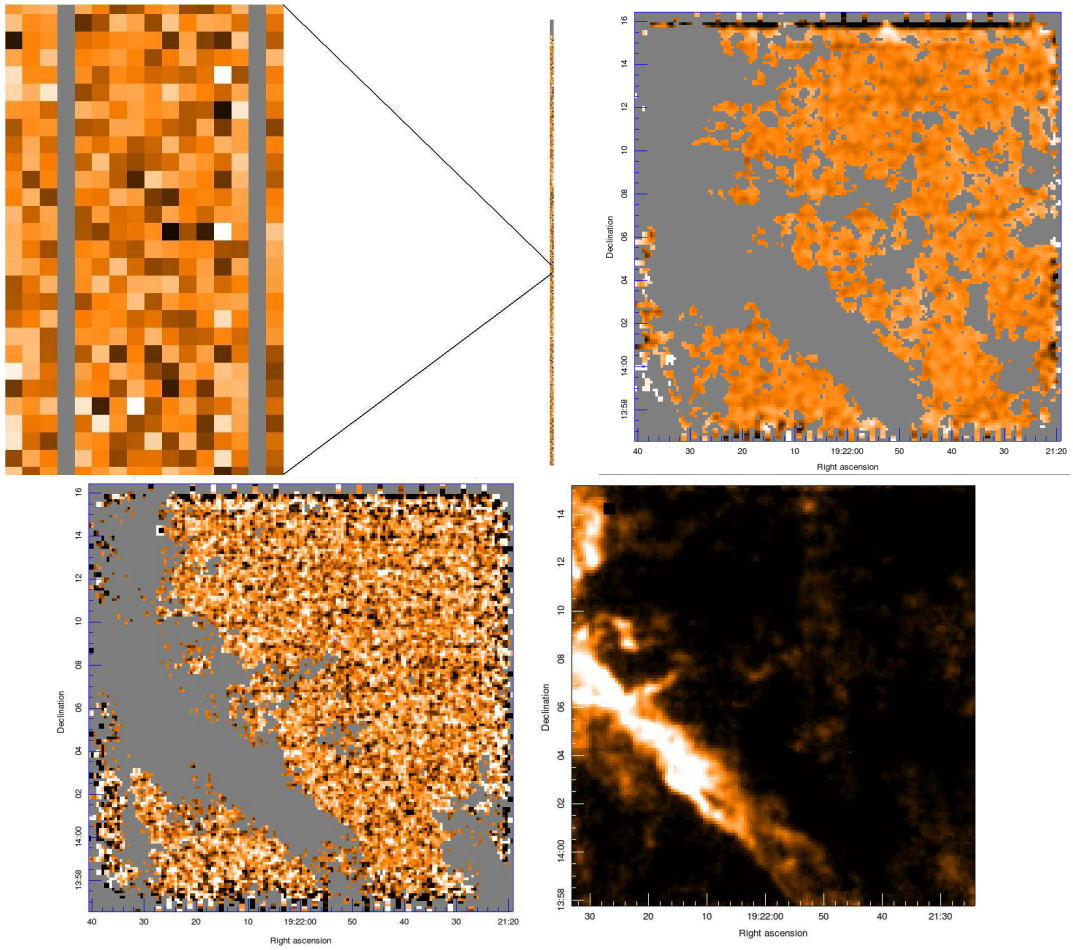

Figure 3.9: Top left: The raw data as it is output from ACSIS. The data are ordered by receptor-time-velocity. On the left is a zoom in of the data on the right. The 16 pixels in the x-axis are the data from the 16 HARP receptors. Note receptors R04 (also known as H03) and R15 (H14) do not contain data. Top right: baseline created for map 5 ^{13}CO (for a single plane within the cube). Bottom left: baseline applied to the map 5 cube. Note regions of emission are excluded from this baseline mask. Bottom right: the final map 5 ^{13}CO integrated intensity image.

QA parameter	Value
BADPIX_MAP	0.1
GOODRECEP	13
TSYSBAD	1500
FLAGTSYSBAD	0.5
TSYSMAX	600
TSYSVAR	0.5
RMSVAR_RCP	1.0
RMSVAR_SPEC	0.2
RMSVAR_MAP	0.6
RMSTSYSTOL	0.30
RMSTSYSTOL_QUEST	0.025
RMSTSYSTOL_FAIL	0.05
RMSMEANTSYSTOL	1.0
CALPEAKTOL	0.2
CALINTTOL	0.2
RESTOL	1
RESTOL_SM	1

Table 3.2: Table of QA parameters and the values as used

3.3.5 Clump identification

The aim of this Chapter is to produce a catalogue of the dense clumps located within the W51 GMC, the reservoir available to form stars. To decompose the W51 GMC into clumps we look to automated clump detection programs to deal with the large volume of data involved. Automated clump detection programs are beneficial as they are objective, repeatable, and remove problems arising from classification by eye in complex areas and in particular where there is position-velocity data available. In this paper we use the CUPID (part of the STARLINK project software[10]) clump finding algorithm CLUMPFIND (Williams *et al.*, 1994). This algorithm was chosen in preference to other algorithms as no prior clump profile is assumed for each clump and it is a widely used algorithm (Moore *et al.* 2007; Buckle *et al.* 2010) which makes for better comparison between regions. CLUMPFIND works in a 'top-down' method by contouring the data and finding peaks within the data and then contouring down to a defined base level (see Fig **??**), detecting new peaks along the way and assigning pixels associated with more than one peak to a specific clump using the 'friends-of-friends' algorithm (Williams *et al.*, 1994).

Variations in rms estimates between maps as a result of changing τ, elevations levels and receiver performances required that the CLUMPFIND algorithm was used on signal to noise maps. The output of this CLUMPFIND process was then used to produce a mask to extract the true values (as opposed to the signal to noise values) from the original maps. The output parameters from the CLUMPFIND process are given in Table 3.3[11]

The peak and centroid positions, were reported in both the spatial and velocity axes. The size

[11] www.starlink.rl.ac.uk/star/docs/sun255.htx/sun255.html

Peak1-3	The position of the clump peak value on axis 1-3.
Cen1-3	The position of the clump centroid on axis 1-3.
Size1-3	The size of the clump along pixel axis 1-3.
Sum	The total data sum in the clump.
Peak	The peak value in the clump.
Volume	The total number of pixels falling within the clump.

Table 3.3: Table of output parameters and their definitions from the CLUMPFIND process as described in the STARLINK software.

of the clump is defined as the "RMS deviation of each pixel centre from the clump centroid, where each pixel is weighted by the corresponding pixel data value[11]", and as such we see that CLUMPFIND makes no assumption on the shape of a clump.

Although the algorithms vary in parameters, a minimum requirement of a $10\,\sigma$ detection was chosen to recover dense clumps but avoid regions of low surface brightness emission within the data. A minimum clump size of 16 pixels was also chosen. We also set the criterion that a clump must be detected in *both* ^{13}CO J = 3–2 *and* C^{18}O J = 3–2. To ensure all clumps in the C^{18}O data had detections the CLUMPFIND mask produced from the ^{13}CO data was used to extract clumps within the C^{18}O data. The parameters chosen for the CLUMPFIND algorithm were: DeltaT ($5\,\sigma$), which sets the contour level spacing and Naxis=3, which considers pixels that at the corners of a cube (of dimensions 3×3 surrounding a central pixel) to be adjacent to the central pixel during the CLUMPFIND process[11]).

Without knowing the true underlying clump population or a greater understanding of the various clump finding algorithms, which is beyond the scope of this thesis, it is difficult to choose one algorithm over another. The large body of existing work based upon clumps identified by CLUMPFIND, i.e. Rathborne *et al.* (2009), leads us to choose the CLUMPFIND algorithm over other algorithms for ease of comparison and familiarity.

By choosing CLUMPFIND, we follow Schneider and Brooks (2004) and Curtis and Richer (2009) in advising caution to the comparison of catalogue results and trends based on physical properties where the data has been analysed with different techniques, when the original data format is position-position data as opposed to position-position-velocity (Smith *et al.*, 2008b), or when the comparison is between molecular line and continuum data (Pineda *et al.*, 2009).

3.4 Results

3.4.1 Morphology

The complex clumpy nature of the W51 GMC is clearly seen in Fig. 3.11. Part of this complex nature is a result of projection effects from its situation at the tangential point of the Sagittarius arm where multiple clouds lie along the line of sight (Mufson and Liszt, 1979). Classically the W51 GMC has been discussed in terms of two main regions W51A and W51B, identified by their radio emission (Kundu and Velusamy 1967; Mufson and Liszt 1979; Kumar *et al.* 2004). More recently, this decomposition has been based on radial velocity data

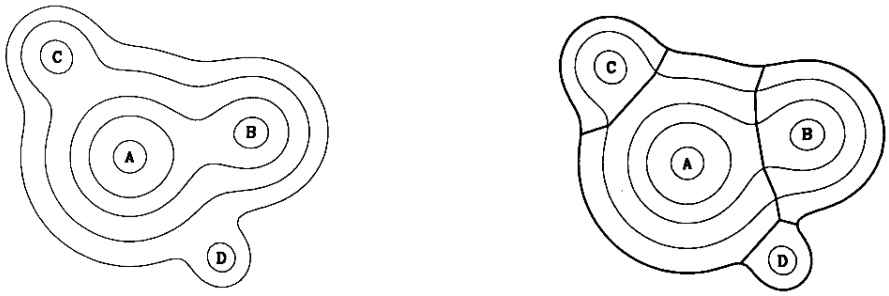

Figure 3.10: A graphical representation of how the CLUMPFIND algorithm works (reproduced from (Williams *et al.*, 1994)).

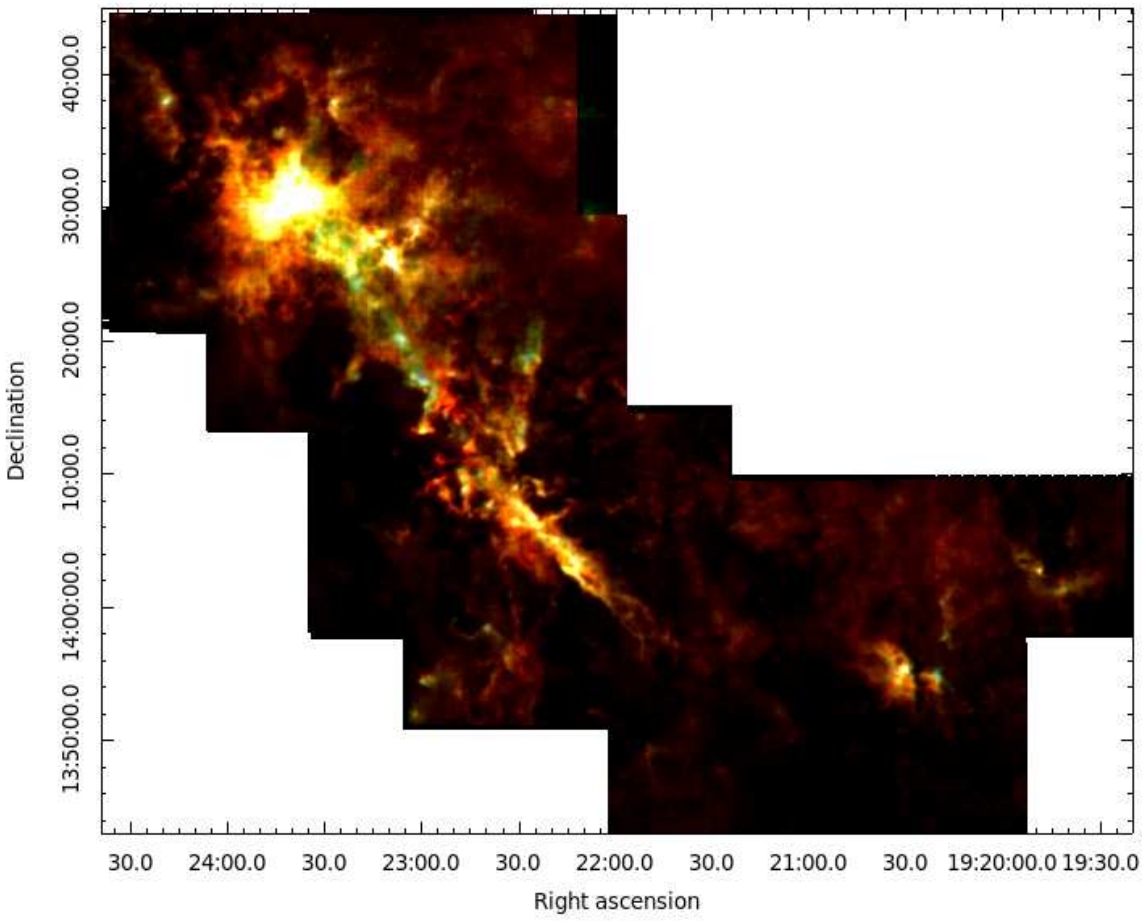

Figure 3.11: Three colour integrated intensity image of the W51 GMC: ^{12}CO (red: scaled between $5-200\,\mathrm{K\,km^{-1}}$) ^{13}CO (green: scaled between $5-75\,\mathrm{K\,km^{-1}}$) and C^{18}O (blue: scaled between $5-25\,\mathrm{K\,km^{-1}}$).

of the W51 GMC into the W51 complex and the High Velocity Stream (HVS) (Carpenter and Sanders 1998; Koo 1999; Okumura *et al.* 2000; and Okumura *et al.* 2001).

The position-velocity structure of the W51 GMC is shown in Fig. 3.12 and a histogram of clump velocities identified within this region, as discussed in Section 3.4.2 is given in Fig. 3.13. These figures show the complex nature of the W51 GMC with many components overlapping in radial velocity although the overall structure of the W51 complex, designated by Carpenter and Sanders (1998) as emission between 56–65 $\mathrm{km\,s^{-1}}$, and the HVS as emission greater than 65 $\mathrm{km\,s^{-1}}$ is visible. It should be noted that the small peak around 20 $\mathrm{km\,s^{-1}}$ is due to emission located at 19:20:31 +13:55:23 in RA and Dec (seen in Fig. 3.11), which was not in the coverage area of the study by Carpenter and Sanders (1998), and hence not present within their data.

In the top image of Fig. 3.12 we see the emission contributing to the W51A region originates from fragmented emission between 49–53 $\mathrm{km\,s^{-1}}$. Carpenter and Sanders (1998) suggest that this emission is either a complex of individual clouds or remnants from larger clouds associated with HII region G49.4-0.3.

The middle image of Fig. 3.12 clearly shows W51A, roughly circular in shape with a size of approximately 30±10 pc (at a distance of 6.5±1.5 kpc). Emission originating from the elongated structure that is the High Velocity Stream (HVS) is also detected in the bottom image of Fig. 3.12.

The HVS is delineated in velocity with a peak at $\sim 68\,\mathrm{km\,s^{-1}}$ (Carpenter and Sanders, 1998). Our data clearly shows the HVS to be an elongated structure stretching roughly 1° in length and 5' in width running approximately parallel to the Galactic plane at b$\sim$ 3.5°. At a distance of 6.5 kpc the HVS is estimated to extend approximately $100\,\mathrm{pc}^{+40}_{-10}$ in length and approximately 10 pc in width, giving rise to an aspect ratio >10. Fig. 3.12 also shows pockets of higher integrated intensity visible throughout the entire length of the HVS at fairly regular intervals. Also visible are two noticeable breaks in the otherwise continuous structure of the HVS,: one around RA: 19:22:47 Dec: 14:12:47 and the other around RA: 19:24:10 Dec: 14:36:10. From the images included in Fig. 3.12 we see that making clear distinctions between structures in velocity space is difficult as there is much overlap and complexity.

Emission offset in position and velocity (between 5–35 $\mathrm{km\,s^{-1}}$) from the W51 GMC was also detected by HARP within the mapped area.Carpenter and Sanders (1998) and Koo (1999) determined this emission to be nearby molecular clouds (<2 kpc), which in Fig. 3.11 is the majority of the emission seen up to a RA of 19:21:00.0.

3.4.2 Clump catalogue

A total of 1575 clumps are identified within the region mapped by HARP. The output of the clump finding algorithms are the position of the clump peak and clump centroid position in each of the three axes, the size of the clump in each axis, total sum in the clump, peak value of the clump and the total number of pixels within the clump. The clump catalogue is given in Tables A.2 and **??**.

To distinguish between those clumps associated with the W51 GMC and the foreground emission, we search for clumps with velocities $> 56\,\mathrm{km\,s^{-1}}$. We designate those 445/1575 clumps with velocities less than 56 $\mathrm{km\,s^{-1}}$ as not associated with the W51 GMC (recall Section

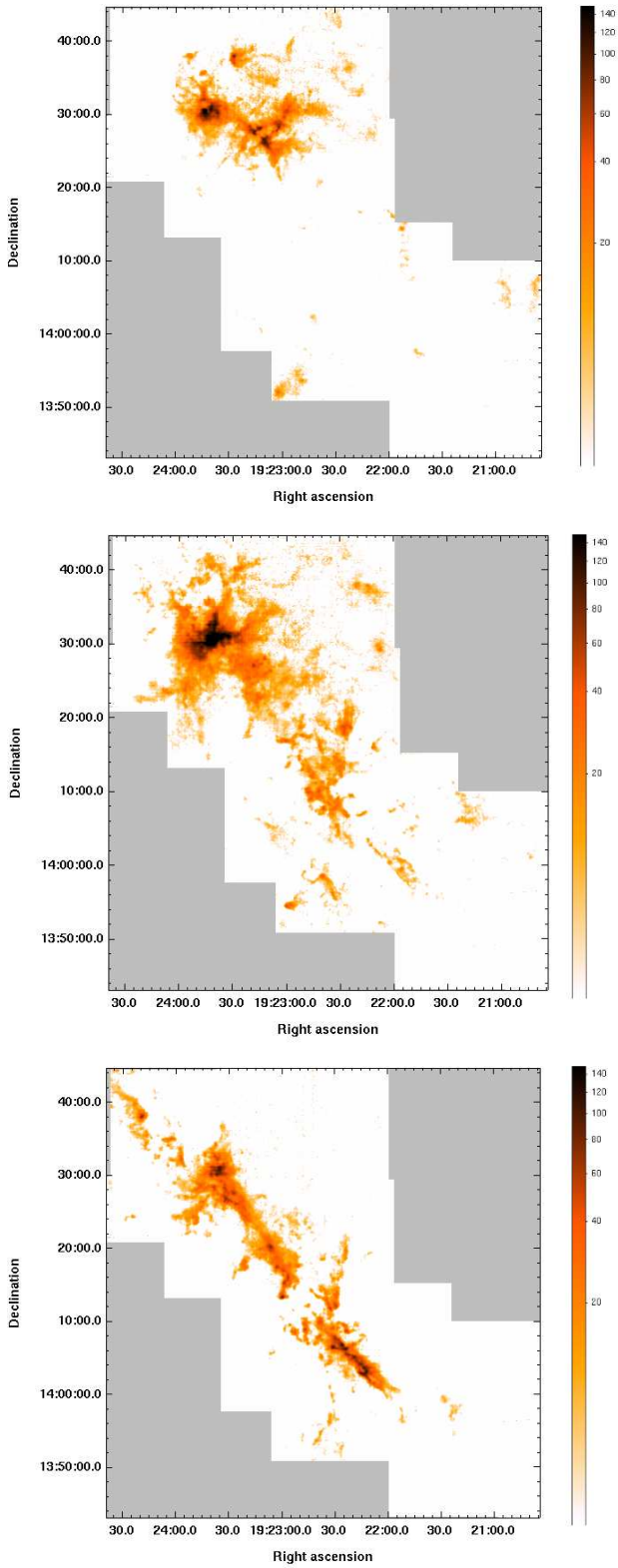

Figure 3.12: ^{13}CO (3-2) integrated intensity images of the W51 GMC. Top: integrated between 45-55 km s^{-1}. Middle: integrated between 55-65 km s^{-1}, essentially the W51 complex. Bottom: integrated between 65-75 km s^{-1}, the HVS. Images exclude coverage on far right where emission is below 40 km s^{-1}.

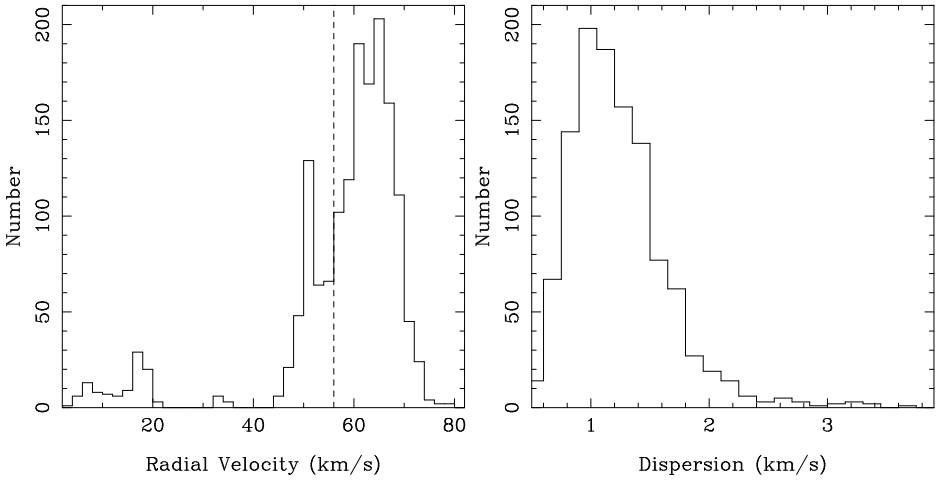

Figure 3.13: Left: Histogram of clump radial velocities for the 1575 clumps identified by CLUMPFIND, the 56 km s^{-1} cut-off for the W51 GMC, as used by Carpenter and Sanders 1998, is marked by the dashed line. Right: Histogram of ^{13}CO clump dispersion line widths for the 1130 clumps identified by CLUMPFIND that are associated with the W51 complex.

3.4.1). These clumps are given in Table A.2 for completeness only but we do not examine them in further detail as they do not form part of this investigation. We decided to follow the convention of Carpenter and Sanders (1998) for the choice of velocity cut for ease of comparison i.e. to the peak position of the ^{13}CO clumps. It is noted that this method of categorising those clumps associated/not associated with the W51 GMC based on a simple velocity cut is an oversimplification (as seen in Fig. 3.12 and Fig. 3.13), however, without a better understanding of the overlapping distributions of clump populations (in both position and velocity) there will undoubtedly be clumps incorrectly included or excluded from the sample. This same problem also occurs when assigning clumps identified to be associated with either the W51 complex or the HVS. Using central positions of the clumps or using positions as determined by the C^{18}O data as an alternative basis for clump classification does not affect the number of clumps by more than 2%, it also does little to change the physical properties derived later in this paper.

Integrated intensity values were determined for the 1130 clumps with velocities greater than 56 km s^{-1}. We find average integrated intensity values for the 1130 clumps associated with the W51 GMC range between 1–103 K km s^{-1} with a median of 4 K km s^{-1}.

One-dimensional ^{13}CO velocity dispersions ($\sigma_{^{13}\mathrm{CO}}$) were estimated by taking the size along axis 3 as determined by CLUMPFIND (e.g. Buckle *et al.* 2010). These values range between 0.5–3.7 km s^{-1} with a median of 1.2 km s^{-1} and are shown in Fig. 3.13. The lower value to this range is set at the binned resolution of the data 0.5 km s^{-1} which will be an upper estimate of the lower one-dimensional velocity dispersion. It is possible to get a feeling for these values by looking at the integrated-velocity-dispersion for the 0.1 km s^{-1} velocity resolution data (see left image in Fig. 3.14). We estimate that errors on the velocity dispersion are on the order of a half binned spatial resolution, 0.25 km s^{-1}.

Diameters of clumps used within this paper are the geometric averages of the values reported

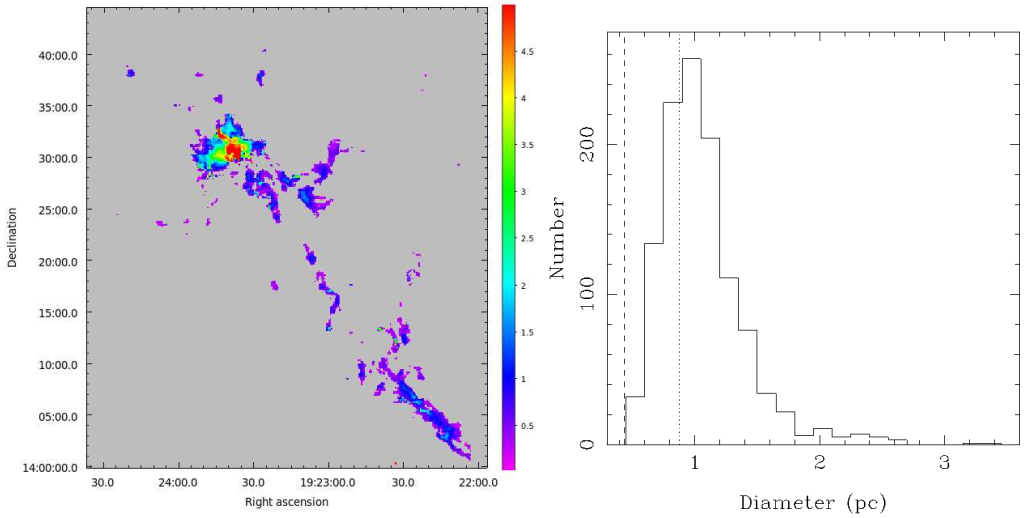

Figure 3.14: Left: Integrated-weighted-velocity-dispersion, from $0-5\,\mathrm{km\,s^{-1}}$, for ^{13}CO emission taken from data with resolution of $0.1\,\mathrm{km\,s^{-1}}$. Pixels are displayed if they have emission $> 10\,\sigma$. Right: Histogram of clump diameters (pc) for the 1130 clumps identified by CLUMPFIND that are associated with the W51 complex. The beam FWHM of the JCMT is indicated by the dashed line, dotted line indicates complettion limit.

by CLUMPFIND (see Section 3.3.5). We adopt a single distance of 6.5 kpc (see Section 3.1.2) and obtain diameters ranging between 0.5–3.4 pc with a median of 1.0 pc with errors dominated by the distance uncertainty (6.5 ± 1.5 kpc). With a 16 pixel detection criterion and limits on the size in the spatial and velocity axis as described in Section 3.3.5, it is noted that the clumps we detect are likely to be incomplete below diameters of $\sim$1 pc, i.e the maximum size the smallest clump can have whilst remaining within the 16 pixel detection limit. This incompleteness is seen in the histogram of clump diameters as given in Fig. 3.14. The histogram shows a turn over around 1 pc, above the FWHM of the beam of the JCMT. A turnover at the FWHM would have indicate a complete sample down to the resolution limit. Systematic errors originating from the CLUMPFIND algorithm are non-trivial to quantify and so throughout the following Chapter we report a representative error analysis which is likely to be a lower limit to the true uncertainty.

3.5 Summary

In this Chapter I presented a literature review of the W51 GMC and outlined the motivation for a wide area, high resolution, molecular line map of the W51 GMC. I present a new catalogue of dense clumps within the W51 GMC that have been detected by HARP in ^{13}CO (3–2) and identified using the CLUMPFIND algorithm. To identify dense clumps required detections to have a peak signal of $10\,\sigma$ in the ^{13}CO and a $3\,\sigma$ detection in C^{18}O. The clumps also have to contain a minimum of 16 pixels and have sizes greater than the telescope resolution in RA, Dec and velocity ($\triangle$RA ≥ 14" or $\triangle$Dec ≥ 14" or $\triangle \mathrm{v} \geq 0.5\,\mathrm{km\,s^{-1}}$). Clump emission was integrated down to a minimum contour level of $2\,\sigma$ to ensure the maximum

amount of clump emission was traced with a contour increment of $5\,\sigma$ used to distinguish between neighbouring clumps.

Obtaining the physical properties of these dense molecular clumps, examining their global properties and searching for signs of current star formation is the focus for our next Chapter.

Chapter 4

Physical properties of dense clumps in the W51 GMC

'All clouds are clocks, even the cloudiest of clouds.'
Karl Popper

In the previous Chapter it was shown that the W51 GMC is one of the most massive GMCs within the Galaxy, with a high star forming efficiency and a starburst-like history. Despite being such an active GMC previous studies, that have tried to understand the early stages of massive star formation, have been hampered by its structural complexity, lying at the tangential point of the Sagittarius arm combined with its distance. I described the method by which I have obtained a catalogue of dense molecular clumps in the W51 GMC. This Chapter focuses on the physical properties of these clumps: temperatures, densities and masses. I then look at the global properties of these clumps, their formation efficiency, their mass distribution and their locations within the W51 GMC. Finally I examine locations of outflow activity within the W51 GMC: signposts of current active star formation.

4.1 Physical properties

In this section I present the physical properties of the clumps identified by CLUMPFIND (see Section 3.3.5 Chapter 3). These clumps are presented in Tables A.2 and **??**.

4.1.1 Opacities

We obtain opacities based on ratios of the receiver temperatures for ^{13}CO ($T_{\rm R}^{*}(^{13}{\rm CO})$) and C^{18}O ($T_{\rm R}^{*}(C^{18}O)$) at the peak of the clump emission, assuming that the excitation temperature, T_{ex}, beam filling factor and telescope beam efficiency remain constant for a particular observed source (i.e. Myers *et al.* 1983, Ladd *et al.* 1998, Buckle *et al.* 2010 and Curtis *et al.* 2010a). These two lines are observed simultaneously which makes the assumptions (the beam filling factor and efficiency) good. The ratio R_{1318} is given by (same as equation 2.34):

$$R_{1318} \approx \frac{1 - e^{-\tau_{13}}}{1 - e^{-\tau_{13}/X}} \tag{4.1}$$

where τ_{13} is the optical depths of ^{13}CO and X is the abundance ratio of ^{13}CO relative to C^{18}O molecules. If the lines are optically thin then this ratio tends to the abundance ratio. Estimating abundance ratios is non trivial and can vary across a range of environments across the Galaxy (Wilson and Rood, 1994) and within regions e.g. within photon dominated regions (Störzer *et al.*, 2000).

To estimate X we inspected the variation of R_{1318} across the region observed by HARP (shown in Fig. 4.1). Obtaining a good estimate of R_{1318} across the region requires the extent of the emission along the radial velocity axis to be the same for both isotopologues thus tracing the same gas. In order to ensure this we applied a $5\,\sigma$ cut to the C^{18}O data and used this as a mask to extract the ^{13}CO data. From Fig. 4.1 we find $R_{1318} \sim 6 - 8$, but decreasing to 2 towards the more dense regions. This decrease to lower values is likely due to the ^{13}CO being optically thick at the filament cores rather than due to changes in abundance (e.g. freeze out). As we can only make the assumption that R_{1318} tends to X in optically thin regions we use the values obtained in the less dense regions, resulting in a value of $X[^{13}\mathrm{CO}/\mathrm{C}^{18}\mathrm{O}] = 7 \pm 1$.

The decrease in R_{1318} we see is consistent with observations by Curtis *et al.* (2010a) who report $R_{1318} \sim 7$ at edges of the emission regions and 2 – 4 towards the centre of the densest regions. Buckle *et al.* (2010), investigating Orion B, find the ratio tending to 10 ± 2 at the edge of the C^{18}O emission in NGC 2024 and 7.5 ± 1.5 in NGC 2071. Both regions have ratios tending to ~ 2 in the denser parts. Our estimate of $X[^{13}\mathrm{CO}/\mathrm{C}^{18}\mathrm{O}] = 7 \pm 1$ is consistent with these observations. By assuming this abundance holds for the whole of the W51 GMC, and that any variations in R_{1318} are due to optical depth effects only, τ_{13} may be calculated for all clumps.

In Fig. 4.1 we present a histogram of the ^{13}CO opacities obtained using equation 4.1 for the 1130 clumps. We see that the clumps are found to be predominantly optically thick, with values of τ_{13} up to 11.9 with a median of 2.6 and with 94% of the clumps having $\tau_{13} \geq 1$. The main source of error in determining optical depths lies in the determination of $X[^{13}\mathrm{CO}/\mathrm{C}^{18}\mathrm{O}]$. By decreasing $X[^{13}\mathrm{CO}/\mathrm{C}^{18}\mathrm{O}]$ to 6 we find the number of clumps that are optically thick decreases to 85% with a median $\tau_{13} = 2.0$ whilst increasing $X[^{13}\mathrm{CO}/\mathrm{C}^{18}\mathrm{O}]$ to 8 takes the number of optically thick clumps up to 98% with a median $\tau_{13} = 3.0$. A further source of uncertainty originates from the fact that as the observed R_{1318} tends to X in equation 4.1, τ_{13} tends to zero, so smaller values of τ_{13} have greater associated uncertainties.

4.1.2 Temperature

To obtain the excitation temperatures of the clumps we make three assumptions; first that the clumps are in local thermodynamic equilibrium, second that the emission line used in this determination is optically thick (as shown in Fig. 4.1) and third that the emission fills the beam (see Fig. 3.14). We calculate excitation temperatures using ^{13}CO in preference to ^{12}CO because ^{12}CO is likely to be self absorbed within such a dense and complex environment. With these assumptions we use the equation and method outlined in Section 2.6.3 and using equation 2.42 we find that for ^{13}CO J = 3–2 :

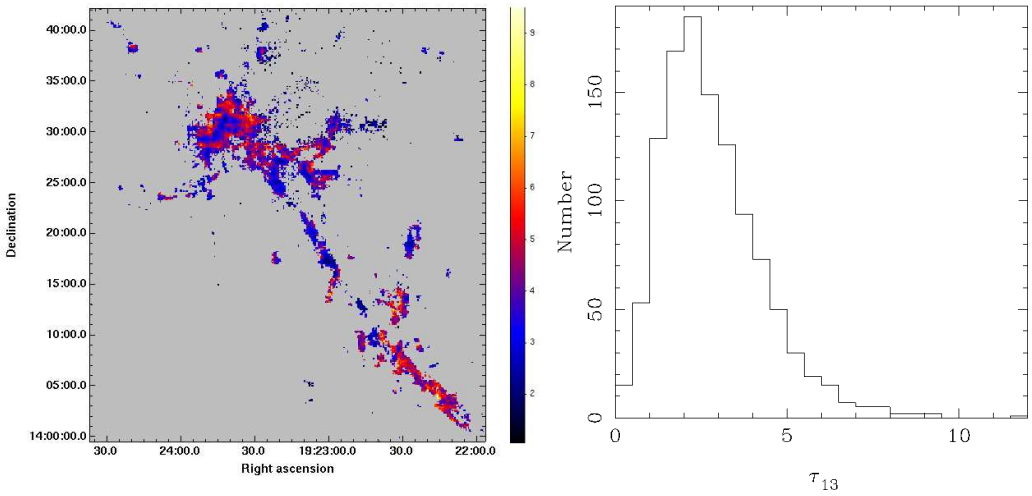

Figure 4.1: Left: Ratio of ^{13}CO to C^{18}O for the W51 GMC, this image does not cover the entire region observed but shows the main regions of interest. Pixels are displayed if peak intensities $>5\,\sigma$. Right: Histogram of clump ^{13}CO opacities for the 1130 clumps identified by CLUMPFIND.

$$T_{\rm ex} = \frac{15.9{\rm K}}{ln\left[1 + 15.9{\rm K}/(T_{\rm R} + 0.045{\rm K})\right]} \tag{4.2}$$

Excitation temperatures were derived for the 1130 clumps in our catalogue and range between 7-56 K with a median temperature of 12 K. A histogram of clump excitation temperatures is given in Fig. 4.2. Temperatures derived here are lower estimates for $T_{\rm ex}$ as they may be affected by any line asymmetries present and beam dilution.

4.1.3 Column densities

Once temperatures have been determined it is possible to calculate values for column densities for ^{13}CO, correcting for optical depth effects by using the opacities calculated in Section 4.1.1, and using the equations 2.39 and 2.40. For ^{13}CO (3-2), with $\nu = 330.588$ GHz $B = 55101.011$ MHz and $Z = 0.11 \times 10^{-18}$ esu cm, we see:

$$N_{^{13}{\rm CO}} = \frac{(2.26 \times 10^{13})(e^{31.72/T_{\rm ex}})(T_{\rm ex} + 0.88)}{1 - e^{-15.87/T_{\rm ex}}} \frac{1}{T_{\rm ex}} \left(\frac{\tau_0}{1 - e^{-\tau_0}}\right) \int T_{mb} dv \ {\rm cm}^{-2} \tag{4.3}$$

Column densities in terms of H_2 as opposed to ^{13}CO are determined using the abundance ratio $[^{13}{\rm CO}]/[{\rm H_2}] \sim 10^{-6}$ which is based on $[^{12}{\rm CO}]/[{\rm H_2}] \sim 10^{-4}$ and $[^{13}{\rm CO}]/[^{12}{\rm CO}] \sim 10^{-2}$ (Wilson *et al.* 1981; Frerking *et al.* 1982; Wilson 1999).

The $N_{\rm H_2}$ values determined range between $7.4 \pm 1.2 \times 10^{20}$ and $5.6 \pm 0.9 \times 10^{22}$ cm^{-2}, with a median $5.6 \pm 0.8 \times 10^{21}$ cm^{-2} with errors originating from uncertainties in opacities and so the abundance ratio. A histogram of H_2 column densities is given in Fig. 4.2.

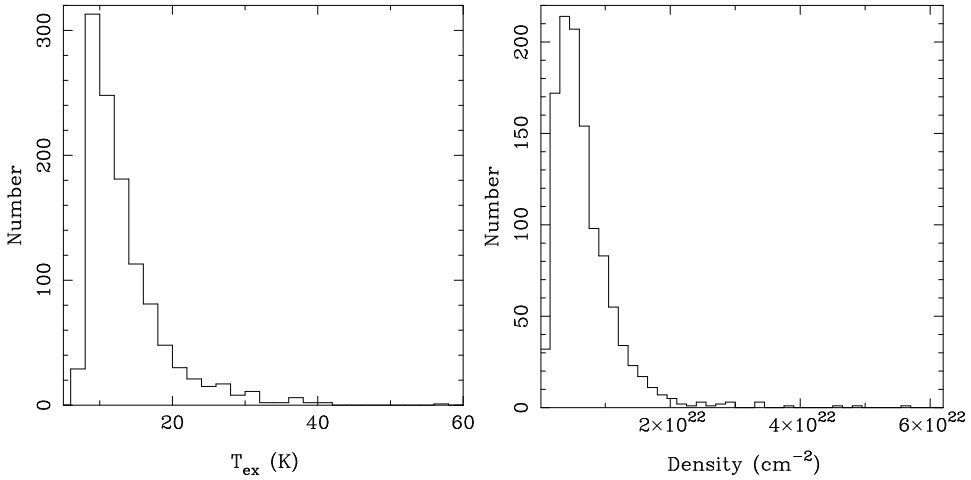

Figure 4.2: Left: Histogram of clump excitation temperatures for the 1130 clumps identified by CLUMPFIND. Right: Histogram of H_2 column densities for the 1130 clumps identified by CLUMPFIND.

Volume densities, calculated by assuming an extent in the radial direction which is equal to the diameters of clump (calculated in Section 3.4.2), are of the range $0.1 \pm 0.01 \times 10^3$ to $2.9^{+0.3}_{-0.2} \times 10^4$ with a median of $1.8^{+0.2}_{-0.1} \times 10^4\,\mathrm{cm}^{-3}$. With some volume densities lower than the critical density for ^{13}CO (3–2)[1] we see that there may be some degree of sub-thermal excitation and our initial assumption of LTE does not hold for all clumps.

Surface densities are calculated by multiplying the column density by the mass of molecular hydrogen. Within the W51 GMC we find surface densities ranging between $0.002 - 0.19\,\mathrm{g\,cm}^{-2}$ with a median of $0.02\,\mathrm{g\,cm}^{-2}$ (with errors pushing these surface density values down to $0.002 - 0.16\,\mathrm{g\,cm}^{-2}$ or up to $0.003 - 0.21\,\mathrm{g\,cm}^{-2}$ both with median values on the order of $0.02\,\mathrm{g\,cm}^{-2}$).

4.1.4 Mass

Once the column density and size of a clump has been determined it is possible to calculate the mass of the clump via equation 2.43, which may be expressed as:

$$M_{\mathrm{LTE}} = A N_{^{13}\mathrm{CO}} \frac{[\mathrm{H_2}]}{[^{13}\mathrm{CO}]} \mu_{\mathrm{H_2}} m_{\mathrm{H}} \tag{4.4}$$

where A is the area of the clump $N_{^{13}\mathrm{CO}}$ is the source averaged column density, the abundance ratio is again assumed to be $[\mathrm{H_2}]/[^{13}\mathrm{CO}] \sim 10^6$, $\mu_{\mathrm{H_2}}$ is the mean molecular weight of the gas per H_2 molecule ($\mu_{\mathrm{H_2}} = 2.72$ to include hydrogen, helium, and the isotopologues of carbon monoxide, i.e. Buckle *et al.* 2010) and m_{H} is the mass of hydrogen.

Our clump mass estimates, based on the assumption of LTE, range between $10 - 1{,}700\,\mathrm{M}_\odot$ with a median of $90\,\mathrm{M}_\odot$. Sources of error in mass come from distance estimates and also the abundance ratio. This means that the masses of the clumps may lie anywhere within the range

[1] $2 \times 10^4\,\mathrm{cm}^{-3}$

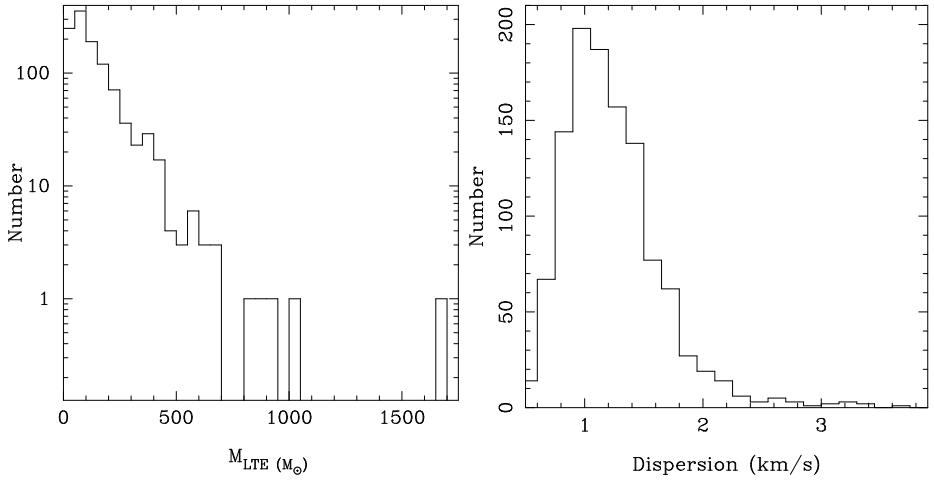

Figure 4.3: Left: Logarithmic histogram of clumps masses ($M_\odot$) for the 1130 clumps identified by CLUMPFIND. Right: Histogram of clump dispersion line widths for the 1130 clumps identified by CLUMPFIND.

10 – 860 $M_\odot$ with a median of 50 $M_\odot$ (taking a distance of 5 kpc and an $X[^{13}CO/C^{18}O]$ of 6) or 10 – 2,950 $M_\odot$ with a median of 160 $M_\odot$ (taking a distance of 8 kpc and an $X[^{13}CO/C^{18}O]$ of 8). These estimates may also be lower limits due to the depletion of CO onto the dust at low temperatures and high densities with dust mass estimates needed to investigate how much this will affect these values for the complex.

Summing the masses determined for individual clumps from equation 4.4, we find a total mass for dense material of 1.5×10^5 $M_\odot$ for the entire W51 GMC (including W51 complex and the HVS). Again, variations in distance estimates and abundance ratios means this value may vary between 17.7×10^4 $M_\odot$ and 2.7×10^5 $M_\odot$.

4.1.5 Clump criticality

To investigate whether the clumps are sub or super-critical, and so likely to collapse, we first determined if they are supported thermally or via turbulence. To do this we compare line widths observed to those predicted to be produced from thermal processes alone using:

$$\triangle v_{\rm FWHM} = \left(\frac{8ln(2)kT_{\rm ex}}{m_{^{13}\rm CO}}\right)^{1/2} \tag{4.5}$$

where $\triangle v_{\rm FWHM}$ is the expected line width produced by thermal processes, and $m_{^{13}\rm CO}$ is the molecular mass of ^{13}CO. These expected values range between 0.1 and 0.3 km s^{-1} but in reality we observe dispersion line widths that span a range between 0.5 and 3.66 km s^{-1} with a median of 1.2 km s^{-1}. From these values we see all the clumps have lines that are super-thermal indicating that turbulence dominates within these clumps. To determine if the clumps are sub or super-critical we determine the virial mass, $M_{\rm v}$, of each clump:

$$M_{\rm v} = R\sigma^2_{v,3D}/G \tag{4.6}$$

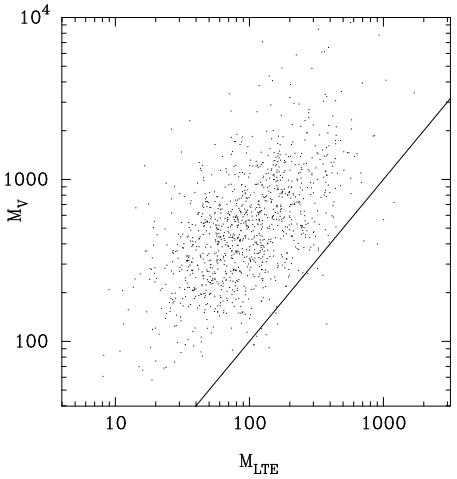

Figure 4.4: Plot of virial mass (M_v) to clump mass (M_{LTE}) for the 1130 clumps identified by CLUMPFIND. Clumps with a ratio $M_{LTE}/M_v \geq 1$ are super-critical and likely to collapse. The line of equality is plotted so we see clumps that lie above and to the left of this line, the majority of the clumps in our sample, are sub-critical, with 1 % of the clumps by number being super critical.

which assumes a clump density profile of $\rho \propto r^{-2}$ (MacLaren *et al.* 1988; Williams *et al.* 1994). In the equation R is the clump radius, G is the gravitational constant and $\sigma^2_{v,3D}$ is the three-dimensional velocity dispersion as given by:

$$\triangle v^2 = \sigma^2_{v,3D} = 3\left[\sigma^2_{\rm CO} + \frac{kT}{m_H}\left(\frac{1}{\mu} - \frac{1}{m_{^{13}\rm CO}}\right)\right] \tag{4.7}$$

where $\sigma^2_{\rm CO}$ is the one-dimensional velocity dispersion of CO (see Section 3.4.2), k is the Boltzmann's constant, T is the kinetic temperature of the gas which we assume to equal the excitation temperature (i.e. Buckle *et al.* (2010)).

Errors in M_v originate from errors in both size (originating in distance) and line widths, both of which are obtained using CLUMPFIND and as stated in Section 3.4.2 are not easily quantified. To get a handle on the errors we estimate these to be as stated in Section 3.4.2 for R and on the order of 0.25 km/s in velocity dispersion (σ^2_{CO}), half the binned spectral resolution. A clump is likely to collapse if it is super-critical with a virial parameter, $M_{LTE}/M_v > 1$. Of the 1130 clumps associated with the W51 GMC we find they span a range of virial parameters 0.01 – 2.8 with a median of 0.2 with 1 % of the clumps by number (14/1130) and 4 % by mass, found to be super-critical. A plot of the distribution of virial mass vs clump mass is given in Fig. 4.4.

Errors associated with determining the virial parameter (FWHM, distance and abundance ratio) result in a range of 0.1 – 22 % of clumps, by number, being super-critical. Errors also arise from the assumption of a spherical geometry.

Kolmogorov Smirnov (KS) tests (see Section 5.3.2, Chapter 5) were applied to the sub and super-critical clump populations; comparing diameters, opacities, temperatures, column densities and masses.The KS tests revealed that the super-critical clumps have physical properties

that indicate that they are not from the same population as the sub-critical clumps to a significance of $>99\%$. This difference in the populations is evident when considering the skewness of the super-critical clumps compared to the sub-critical clumps. Skewness, an indication of the symmetry of a population, where the mode and mean of a population are approximately equal Wall and Jenkins (2003). A value of zero indicates symmetry, a positive skew indicates a population where the mean in significantly higher than the mode. We find the super-critical clumps consistently having higher positive skew values (a greater proportion of outliers at higher values) than the sub-critical clumps.

4.2 Global properties

In our study we have located 1130 clumps associated with the W51 GMC using the CLUMPFIND algorithm. We find these clumps have characteristic diameters of 1.0 pc (0.5 – 3.4 pc), excitation temperatures of 12 K (7 – 56 K), densities of 5.6×10^{21} cm^{-2} (7.4×10^{20} – 5.6×10^{22} cm^{-2}) and masses of 90 M$_\odot$ (10 – 1,700 M$_\odot$) with 1 % of clumps by number found to be super-critical. With a total mass (including all clumps with radial velocities >56 km s^{-1}) of 1.5×10^5 M$_\odot$ this places the W51 GMC in the top end (5–10 %) of GMCs in terms of mass (i.e. Solomon *et al.* 1987; Carpenter and Sanders 1998; Hindson *et al.* 2010).

In this section we focus first on the global properties of the W51 GMC, such as the amount of dense material contained within the W51 complex and HVS, the clump forming efficiency of the region and the distribution of clump masses. Finally we combine what we know about the properties of the complex and of the individual clumps to yield an insight into the incipient star formation potential of the W51 GMC.

4.2.1 Clump forming efficiencies

Star formation has been found to be an inefficient process. On the Galactic level the star forming efficiency (SFE) is observed to be $\sim$2% (Myers *et al.*, 1986). This inefficiency is due to either of two reasons: it is an inherently inefficient process or it is a slow process and so appears to be inefficient (Bonnell *et al.*, 2011). From the observations presented in this thesis (see Section 4.1.4) we find that the entire W51 GMC has a total dense molecular reservoir for star formation on the order of 3.1×10^5 M$_\odot$ (a higher value than reported in Table 4.1 as this covers clumps up to 79 km s^{-1}, the top of our velocity range). These dense clumps formed from the molecular material traced by Carpenter and Sanders (1998), in ^{12}CO (1–0).

It is possible to make the distinction between dense and diffuse clumps if we consider the critical densities (n*, recall Section 3.2) of the two transitions: ^{12}CO (1–0) and ^{13}CO (3–2). The critical density of ^{12}CO (1–0) is a factor of 30 times lower than the critical density of ^{13}CO (3–2); 7×10^2 cm^{-3} compared to 2×10^4 cm^{-3}. ^{12}CO (1–0) and therefore traces both high and low density material, with ^{13}CO (3–2) tracing only the denser regions. As a result we may obtain a dense clump forming efficiency (CFE) for the complex by comparing our mass estimates ($M_{\rm dense}$) with the mass estimate from all the maerial ($M_{\rm dense} + M_{\rm diffuse}$) as determined by Carpenter and Sanders (1998). We obtain the CFE using:

Region	M_{LTE} ($\times 10^5\,M_\odot$)	M_{XCO} ($\times 10^5\,M_\odot$)	CFE (%)	SCFE (%)
W51 GMC	1.5	11	14	0.5
W51 complex	1.0	9.5	11	0.6
HVS	0.4	1.5	29	0.1

Table 4.1: Table of physical properties for clumps within the velocity range ($56-71\,km\,s^{-1}$) as used by Carpenter and Sanders (1998). M_{LTE} estimates are from this paper and diffuse mass estimates M_{XCO} come from Carpenter and Sanders (1998) re-calculated to a distance of 6.5 kpc. Other properties reported are the: CFE (clump forming efficiency) and the SCFE (super-critical clump forming efficiency).

$$\mathrm{CFE} = \left(\frac{M_{\mathrm{dense}}}{M_{\mathrm{dense}} + M_{\mathrm{diffuse}}} \right) \tag{4.8}$$

For a direct comparison we only include clumps with velocities between $56-71\,km\,s^{-1}$ ($56-65\,km\,s^{-1}$ for the W51 complex and $65-71\,km\,s^{-1}$ for the HVS as defined by Carpenter and Sanders 1998) see Table 4.1. We find for the complex as a whole a CFE of $14 \pm 1\%$ with a lower ($11 \pm 1\%$) and a higher ($29 \pm 2\%$) value for the W51 complex and HVS respectively (see Table 4.1). Errors on this CFE originate from the M_{LTE} estimates derived within this thesis, as outlined in Section 4.1.4, and from the masses reported by Carpenter and Sanders (1998). The authors do not indicate the reliability of these values and so are not included in these representative errors. An additional source of error originates in the assumption that the ^{12}CO (1–0) traces both the diffuse material and the *same* dense material as traced by the ^{13}CO (3-2) emission.

From the CFE values derived we find the following results. First we established that the CFE within the entire complex is much higher than the Galactic SFE and is higher than SFEs previously reported for the W51 GMC (2-8%, Okumura *et al.* 2000). This seems to be well established with similar CFE values for other GMCs, i.e. the CFEs of NGC2024 and NGC2071, two regions within the Orion B complex, have a reported CFE of of 33% and 24% respectively based on the mass ratio of ^{12}CO to ^{13}CO (Buckle *et al.*, 2010).

The second result we find is a tentative increase in efficiency between the HVS ($29 \pm 2\%$) compared to the W51 complex ($11 \pm 1\%$). Differences in CFEs have been observed across other complexes, i.e. W3 has a CFE for dense clumps of 26% in the High Density Layer and only 5% in the diffuse cloud (Moore *et al.*, 2007). Moore *et al.* (2007) conclude that the formation of dense clumps is more efficient when it has been shocked by external interactions. This enhancement in efficiency within the HVS may reflect the proposed cloud cloud collision that is believed to have triggered past star formation within the GMC complex.

These CFE values only go so far in unlocking the picture of star formation as not all clumps necessarily go on to form stars. We saw in Section 4.1.4 that 4% of the clumps by mass within the complex are super-critical ($M_{LTE}/M_v > 1$) and have the potential to form stars. It is therefore more informative to report the formation efficiency of super-critical clumps (SCFE), as this is more likely to reflect a truer picture of how the star formation efficiency

will evolve over future generations. We estimate the SCFE using:

$$\mathrm{SCFE} = \left(\frac{\mathrm{M_{sup}}}{M_{\mathrm{dense}} + M_{\mathrm{diffuse}}} \right) \tag{4.9}$$

where M_{sup} is the mass of super-critical clumps. We find a SCFE for the W51 GMC, of $0.5^{+2.3}_{-0.5}$%, W51 complex of $0.6^{+2.6}_{-0.5}$% and $0.1^{+3.5}_{-0.1}$% for the HVS (as given in Table 4.1). Errors here are similar to before but are also affected by errors in distance, abundance ratio and the FWHM of the clumps.

This leads us to our third result that the SCFEs obtained are lower than SFE reported for the W51 GMC (2-8%, Okumura *et al.* 2000). This result is dependant several factors: *i)* the fractional mass within the super-critical clumps that will go on to the final star (which would decrease this estimate), *ii)* the number of sub-critical clumps containing super-critical cores within them (which would increase this estimate), *iii)* the formation of future cores from the diffuse gas. Placing a quantitative value on these other factors is non trivial as it must account for possible fragmentation, resolution limitations with the current data and other factors such as the a hotly debated mode of massive star formation (see McKee and Ostriker (2007)). If we consider this SCFE for the whole complex of $0.5^{+2.3}_{-0.5}$% independently, it would indicate that star formation will likely diminish over time unless some future triggering event occurs. Considering the SCFE may not tell the entire story of the future of star formation within W51. Buckle *et al.* (2010) studying condensations within the Orion B, complex also find the majority of clumps to contain $\mathrm{M_v} > \mathrm{M_{LTE}}$. Buckle *et al.* (2010) cite large uncertainties in distance estimates, fractional abundances, excitation temperatures and assumed density profile, result in the inability to make definitive conclusions about any particular condensation. Additionally evidence based on molecular outflows indicates that star formation within this region *is* ongoing as discussed further in Section 4.3.

Another way we can consider the future of star formation within the W51 complex is by comparing the surface densities observed within the GMC to those observed within massive star forming regions. Observational studies such as Plume *et al.* (1997) and those outlined in McKee and Tan (2003) and McKee and Ostriker (2007), find that massive stars have only been observed in regions with surface densities greater than $\sim 1.0\,\mathrm{g\,cm^{-2}}$ and only low mass stars form when surface densities are around $\sim 0.03\,\mathrm{g\,cm^{-2}}$ or lower, with theoretical justification provided by Krumholz and McKee (2008). Surface densities, derived within Section 4.1.3, range between $0.002 - 0.19\,\mathrm{g\,cm^{-2}}$ (median of $0.02\,\mathrm{g\,cm^{-2}}$). These surface densities are lower than expected for sites of massive star formation but are consistent with observations by Elia *et al.* (2010) and Roy *et al.* (2011) who find values down to $0.001\,\mathrm{g\,cm^{-2}}$. Elia *et al.* (2010) derived values $< 1\,\mathrm{g\,cm^{-2}}$ from two regions within the Herschel Infrared GALactic plane survey (Hi-GAL) key-project data (Molinari *et al.*, 2010a). Roy *et al.* (2011) found a similar result based on BLAST (Balloon-borne Large Aperture Submillimeter Telescope, Pascale *et al.* 2008) observations of the Cygnus-X star forming region. A likely explanation for these low surface density values was proposed by Roy *et al.* (2011) who suggested that these values may evolve to higher surface densities over time, with the cold precursors of dense clusters having massive reservoirs yet to be channelled by gravity into a higher surface density state and so being more extended objects than clumps.

4.2.2 Clump Mass Distribution

The Clump Mass Distribution (CMD) describes the relative frequency of clumps with differing masses, and is commonly fitted by a power law:

$$\frac{dN}{dM} \propto M^{-\alpha} \tag{4.10}$$

The shape of the CMD has been seen to resemble the stellar Initial Mass Function (IMF) that describes the relative frequency of stars with differing masses (e.g. Salpeter 1955; Kroupa 2001) over a range of environments (Kramer *et al.* 1998; Motte *et al.* 1998; Nutter and Ward-Thompson (2007); Simpson *et al.* 2008). For example, observations of Orion find single power law fits to a CMD of $\alpha = 1.3$ and $\alpha = 1.7$ for NGC 2024 and NGC 2071 respectively, and 2.3 and 2.6 for the upper slope of a double power law characterising the CMD (Buckle *et al.*, 2010). Observations of dense clumps within W3 by Moore *et al.* (2007) also find α values between $1.5-1.66$ for CMDs obtained using a single power law and $1.8-1.85$ for the higher mass end (above what they call the $\log 1.8$ mass structure, see Moore *et al.* 2007 for further details).

Understanding the relationship between the CMD and the IMF can help constrain star formation models (Bate and Bonnell 2005 and Reid and Wilson 2006a) although the full physical meaning remains unclear due to a number of complications: (i) differing forms of the distribution (ii) completeness limitations (iii) nature of the objects (iv) multiplicity (v) efficiency (vi) time-scales (vii) physical size-scales (viii) telescope resolution (ix) distance, as discussed by Curtis and Richer (2009) and Reid *et al.* (2010). Nevertheless it is instructive to compare the CMD of the W51 GMC with other nearby regions in order to investigate differences caused by distance.

We used a differential form of the CMD as it allows for a more straightforward accounting of uncertainties (see Fig. 4.5). To minimise Poisson uncertainties caused by fixed bin widths we follow the method of Maíz Apellániz and Úbeda (2005) using a variable bin width with a fixed number of clumps per bin (e.g. Reid and Wilson 2006a and Reid and Wilson 2006b). Maíz Apellániz and Úbeda (2005) states that the ideal number of bins used should equal $2N^{0.4}$ where N is the number of data points. When fitting to our data we do not want to include points below the completeness level of our data. We follow Curtis *et al.* (2010a) and calculate the 'sample average completeness limit', $\mathrm{M_{limit}}$, which is the mass of an average sized clump at the $10\,\sigma$ detection threshold. We take the median clump size, velocity dispersion and opacity from clumps with higher σ limits to ensure the median values we do use are unaffected by incompleteness. From this we calculate $\mathrm{M_{limit}} = 200\mathrm{M}_{\odot}$. We use χ^2 fitting technique to fit a single power law to our CMD for clumps with masses $\mathrm{M_{LTE}} > \mathrm{M_{limit}}$.

Chi-square fitting

Chi-square fitting is a useful tool to obtain a best fit model for data where errors are known i.e the CMD which has two free parameters: a slope α, and a y-axis intercept C. In our specific case the data is the number of clumps within a mass bin with errors originating primarily from Poisson statistics. Below is the expression for Chi-square:

p	v					
	1	2	3	4	5	6
68.3%	1.00	2.30	3.53	4.72	5.89	7.04
90%	2.71	4.61	6.25	7.78	9.24	10.6
95.4%	4.00	6.17	8.02	9.70	11.3	12.8
99%	6.63	9.12	11.3	13.3	15.1	16.8
99.73%	9.00	11.8	14.2	16.3	18.2	20.1
99.99%	15.1	18.4	21.1	23.5	25.7	27.8

Table 4.2: $\triangle\chi^2$ as a function of Confidence Level (p) and Degrees of Freedom (Press *et al.*, 1986).

$$\chi^2 = \sum_{i=1}^{k} \left(\frac{O_i - E_i}{\sigma_i} \right)^2 \tag{4.11}$$

where O_i is the data as it is observed, E_i is the expected value based on a specific model and σ_i is the error (in this case $\sqrt{n}$, where n is the number of clumps in a particular bin). To obtain the best fit of the data to the model χ^2 is calculated for each variation of the model as it changes with the varying free parameters. The model with the most appropriate free parameters is one with the smallest χ^2 value.

To get a feeling of confidence of the χ^2 fit it is possible to calculate the reduced Chi-square, χ^2_{red}. This statistic gives us a feeling of the goodness of fit.

$$\chi^2_{red} = \chi^2/v \tag{4.12}$$

where v is the degrees of freedom associated with χ^2 which for k bins and N parameters is given by:

$$v = k - N \tag{4.13}$$

Fitting to α and C gives N = 2. A $\chi^2_{red} < 1$ indicates that the errors on the fit have been overestimated, and a $\chi^2_{red} >> 1$ indicates a poor fit. Ideally a χ^2_{red} value between 1-2 indicates a good fit. To obtain error estimates on the parameters α and C we look at what maximum and minimum parameters values would be given for $\chi^2 + \triangle\chi^2$, where $\triangle\chi^2$ depends on the level of confidence and number of parameters, as shown in Table 4.2.

Chi-square fitting to the CMD

We find that the W51 GMC is best described by $\alpha = 2.4^{+0.2}_{-0.1}$, with $\chi^2_{red} = 4.0$. We also find that both the W51 complex and the HVS are best described by this same single power law ($\alpha = 2.4$) within the errors.

Our value of $\alpha = 2.4^{+0.2}_{-0.1}$ is higher than other single power law fits to other regions, but it is in agreement to the upper mass end of two-component power law fits reported in the literature (i.e. Moore *et al.* 2007; Buckle *et al.* 2010). This is unsurprising as due to completeness we

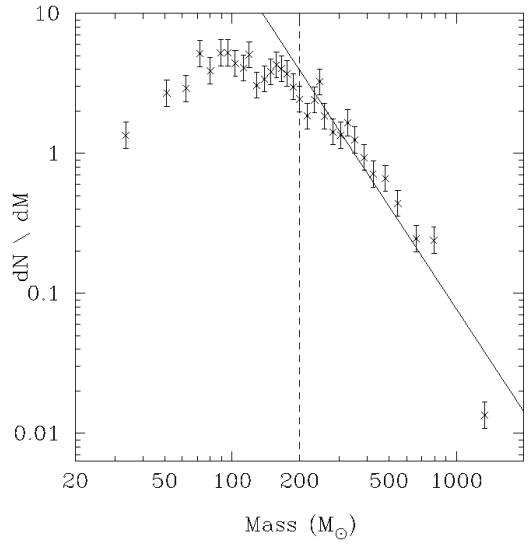

Figure 4.5: Differential CMF of the W51 GMC, with the sample average completeness limit, M_{limit}, of the clumps indicated by a vertical dashed line. The data are fitted with a single power law for masses $M_{LTE} > M_{limit}$. We find that the CMD is best described by $\alpha = -2.4^{+0.2}_{-0.1}$.

only fit to the upper mass end of our CMD, with masses of the order of $10^2 - 10^3\,M_\odot$. At these high masses it is worth noting that with a tentative upper mass limit to the IMF of $\sim$300 $M_\odot$ (Crowther *et al.*, 2010) these are the clumps most likely to form hierarchical multiple systems, i.e. binaries or stellar clusters. We refrain from comparing this higher mass end of our CMD to any cluster mass function because, as with the IMF, there are many pitfalls in a direct comparison including changes over time caused by gas expulsion, the loss of stars and the destruction of the clusters itself (Parmentier *et al.*, 2009).

Previous studies of the W51 GMC have investigated the form of the mass distribution (or function): Okumura *et al.* (2000) looked at the IMF for central part of the W51 GMC and found $\alpha = 2.8$ and Kang *et al.* (2009) looked at the mass function for YSOs associated with the active region of the W51 GMC and observed $\alpha = 2.26$. Our single power law fit with $\alpha = 2.4^{+0.2}_{-0.1}$ is in agreement with those later MFs observed within the W51 GMC and the Salpeter IMF.

4.3 Outflows

The previous sections in this Chapter have focused on the physical properties of the dense clumps within the W51 GMC. This work indicates that star formation within the W51 GMC is likely to diminish in the future. What it has not yielded was the *current* status of ongoing star formation. The methods by which it is possible to search for signs of current star formation is to: *i)* search for associated YSO, *ii)* obtain SEDs of the clumps, *iii)* search for associated outflows. The first two methods are problematic as it would require the analysis of two-dimensional data in an environment that has a complex structure in three-dimensions. The

latter of these methods is ideal as we already have the data by which to search for molecular outflows, with ^{12}CO (3-2) data being ideal as it is more sensitive to warmer gas (Hatchell *et al.*, 2007). Hatchell and Dunham (2009) also conclude that outflow mapping is as as good as using Spitzer data to identify protostars.

4.3.1 Outflows: identifiers

Molecular outflows are powered by the release of gravitational potential energy of a collapsing protostar and an accreting disk, and are driven by conservation of angular momentum. They are believed to be driven by jets or winds with momentum transferred to the molecular material via entrainment (see Arce *et al.* 2007 and references therein). They are ideal for tracing current star forming activity that may otherwise be subject to heavy extinction (Lada, 1985; Fukui *et al.*, 1993; Shepherd and Churchwell, 1996), however (as will become evident in the following sections), identifying outflows in the W51 GMC is a non-trivial task. Classically the search for outflows has been tackled either through looking for their presence via: *i)* the use of single spectra (Shepherd and Churchwell, 1996; Hatchell *et al.*, 2007; Hatchell and Dunham, 2009; Curtis *et al.*, 2010b; Graves *et al.*, 2010). *ii)* in position-velocity diagrams (Zhang *et al.*, 2001; Graves *et al.*, 2010) *iii)* visualisation in three-dimensional space (Borkin *et al.* 2008; Arce *et al.* 2010). The molecule of choice for these studies is ^{12}CO as its high abundance and lower excitation temperature makes the faint wing emission easier to detect.

Method *i)* allows for an automated detection of outflows based on a broadened line profile, due to Doppler shifts, of an optically thick species, as shown in Fig. 4.6 (e.g. Shepherd and Churchwell (1996); Hatchell *et al.* (2007); Hatchell and Dunham (2009); Curtis *et al.* (2010b); Graves *et al.* (2010)). With identification typically based on the criterion that line emission must be above a certain threshold (i.e. 2 or 3σ) at a particular velocity (v) away from the systemic velocity (v_0) of the material (typically defined by the centroid of C^{18}O emission). Confirmation of outflow status may then be obtained by looking for spatially resolved outflows beyond the emission from the cloud core as depicted in Fig. 4.6 (Goldsmith *et al.* 1984; Lada 1985; Zhang *et al.* 2001, or renzograms i.e. Kregel *et al.* 2004; Hatchell *et al.* 2007). Using single spectra to identify outflows allows their identification to be automated, however, this approach has its drawbacks, particularly in complex regions with multiple components lying along the same line of sight. If multiple components overlap in both position and velocity, as in the W51 GMC, confusion may cause misidentification.

Position-velocity (pv) diagrams (method *ii)*) allows structures spanning out in velocity to be identified (e.g. Zhang *et al.* 2001; Buckle *et al.* 2010; Davis *et al.* 2010; Graves *et al.* 2010), as seen in Fig. 4.7. In Fig. 4.7 the strong outflow present stretching out over tens of km s^{-1} is clear in comparison to the systemic velocity located around $\sim$8 km s^{-1} as is evident from the ^{13}CO and C^{18}O emission. The W51 GMC extends over $\sim$20 km s^{-1} in velocity often, as in the case of the W51A region, within the same region. This makes identification of outflows in such regions non-trivial.

More recently with improvements to imaging techniques outflows have been identified using three dimensional techniques. Arce *et al.* (2010) used a programme called 3D Slicer[2] for the three-dimensional visualisation of the Perseus molecular cloud (see Fig. 4.8) in ^{12}CO.

[2] www.slicer.org

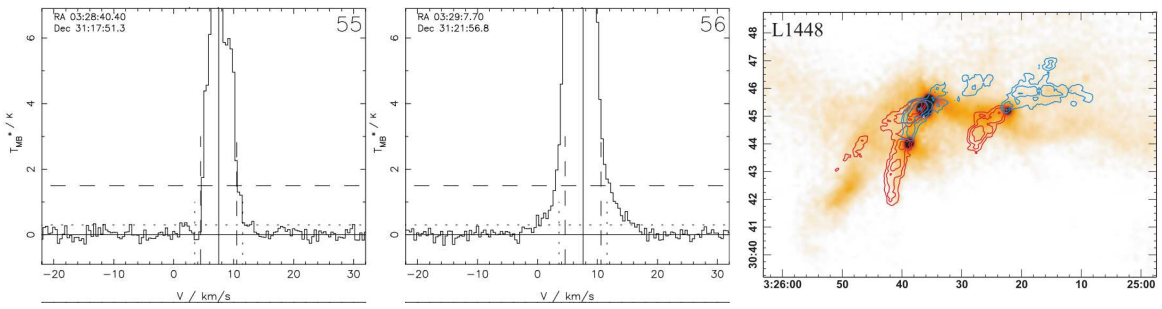

Figure 4.6: Identifying outflows in the Perseus molecular cloud. Left and middle: Using ^{12}CO spectra (reproduced from Hatchell and Dunham 2009). Right: SCUBA 850 μm emission with ^{12}CO integrated intensity contours overlaid from -25 to 0 km s^{-1} (blue) and 8 to 25 km s^{-1} (red, reproduced from Curtis *et al.* 2010b).

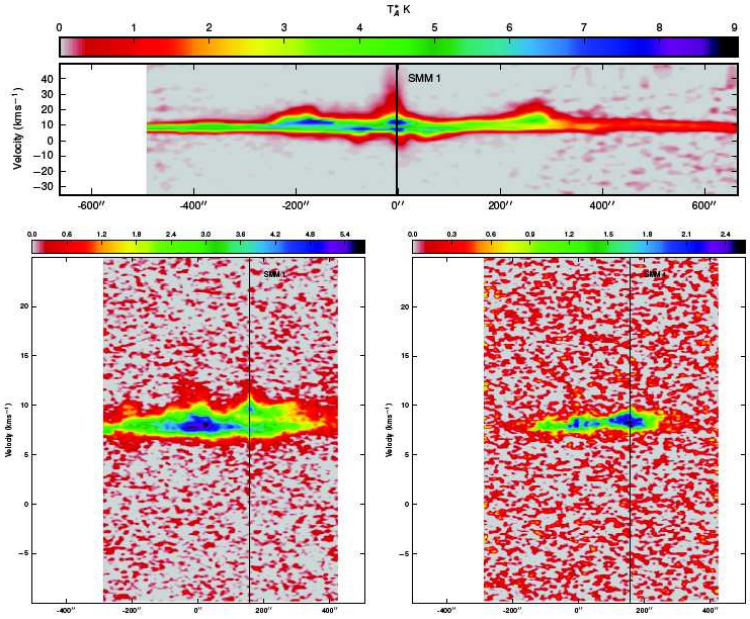

Figure 4.7: Outflows in the Serpens molecular cloud. Top: ^{12}CO. Bottom left: ^{13}CO. Bottom right: C^{18}O (reproduced from Graves *et al.* 2010).

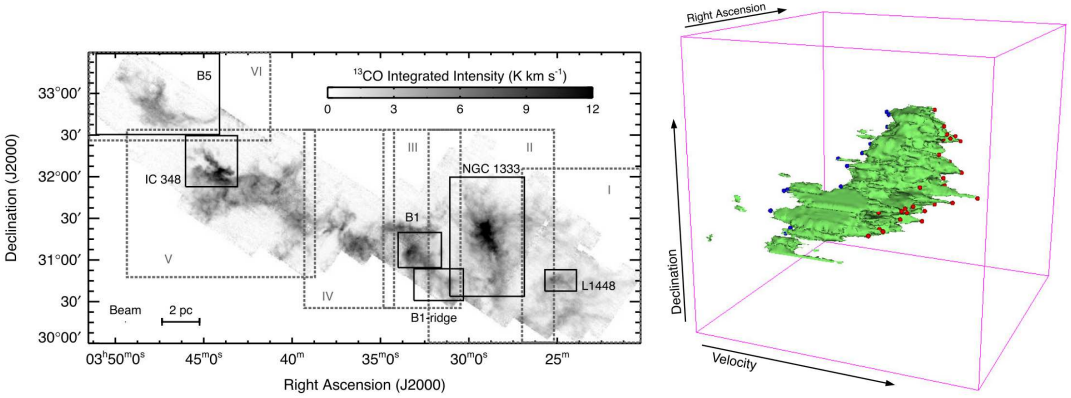

Figure 4.8: Left: Integrated intensity image of the Perseus molecular cloud mapped in ^{13}CO (1-0). Right: Zoom in of region B5 (as labelled in image on right) in ^{12}CO presented in position-position-velocity space (reproduced from Arce *et al.* 2010).

Arce *et al.* uses the three-dimensional images to identify 60 new (and 36 known) outflow candidates. This work clearly shows the potential for three-dimensional visualisation as a key tool in the search for outflows within molecular clouds.

4.3.2 Outflows: the complexity of W51

With the above in mind the question to ask is: how should we investigate outflows within the W51 GMC? Which method is most appropriate? The two problems we face in identifying outflows in the W51 GMC are due to *i)* distance *ii)* complexity (multiple cloud components along the line of sight). The distance problem is nicely illustrated by considering the Serpens molecular cloud as discussed by Graves *et al.* (2010). At a distance of 230 pc and taking a resolution of 14" we find that if we placed the Serpens molecular cloud (which has angular extent of ~ 1200") at the same distance as the W51 GMC, Serpens would be covered by three beams. The complexity problem is illustrated in Fig. 4.9. An additional problem is faced if we approach the outflow problem using the catalogue produced based on ^{13}CO emission. This is because ^{13}CO may not trace (or only weakly trace) outflow candidates and any strong outflow candidates ^{13}CO does trace may have been split into multiple clumps.

These problems are tackled by both restricting this search to a region which should not be affected by complexities and blending and by searching for outflow candidates by eye using the GAIA-3D graphical tool[3].

With regards to the first point, it is more conducive to search for outflow candidates away from the region where the W51 complex is interacting with the HVS (referred to as W51A), and focus on the part of the HVS which is also referred to as W51B. To this end I focus the field of view for the outflow search to 20'×20' (see purple region in Fig. 4.9).

With regards to the second point, searching for outflow candidates in the three-dimensional data by eye, this clearly has both advantages and disadvantages. The disadvantages are i) identifications are subjective ii) biased to less crowded regions iii) not complete iv) difficulty in specifying an explicit search criterion. The advantage is that the eye is able to easily pick out subtle features within data. Some of the problems outlined may be overcome by working on signal-to-noise ratio cubes which allowing for a base level criterion to be created.

The particular advantage of using the GAIA-3D graphical tool is that it allows the data to be viewed in three-dimensions and from any angle. It allows for multiple cubes to be displayed at one time (see Fig. 4.10) which means extended emission (traced by ^{12}CO) located away from the systemic velocities (as traced by ^{13}CO and C^{18}O) are easily identifiable. Using the 'display image plane' tool also allowed the velocity range of individual outflows to be traced.

4.3.3 Outflows: in the W51 GMC

To place a quantitative value on the number of outflows present within the search data cube we decided on the following outflow criterion: i) outflows must be detected at $10\,\sigma$ within the ^{12}CO data, ii) they must extend $> 10\,\mathrm{km\,s^{-1}}$ in velocity. ^{13}CO and C^{18}O data provided information on the systemic velocity of the cloud material. 10σ was chosen as so that most

[3]http://astro.dur.ac.uk/∼pdraper/gaia/gaia3dvis/index.html

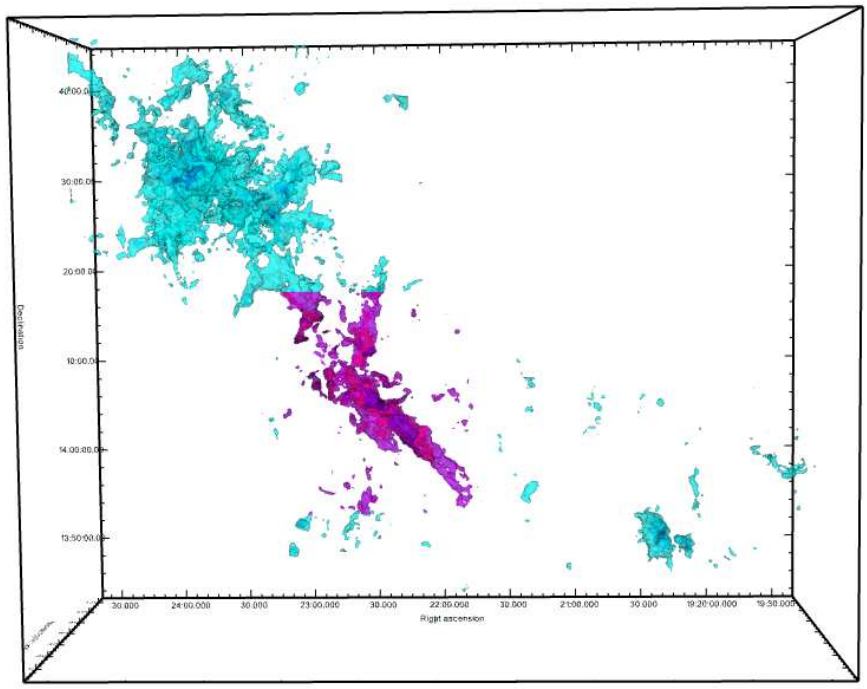

Figure 4.9: A three-dimensional (space-velocity) image of the W51 GMC region as mapped by HARP (presented using GAIA-3D) shown in blue and purple (levels are at 10, 20, 30 and 40 K). The complexity that hampers the identification of outflows are clearly seen. As a result we choose to zoom in on the particular region shown in purple.

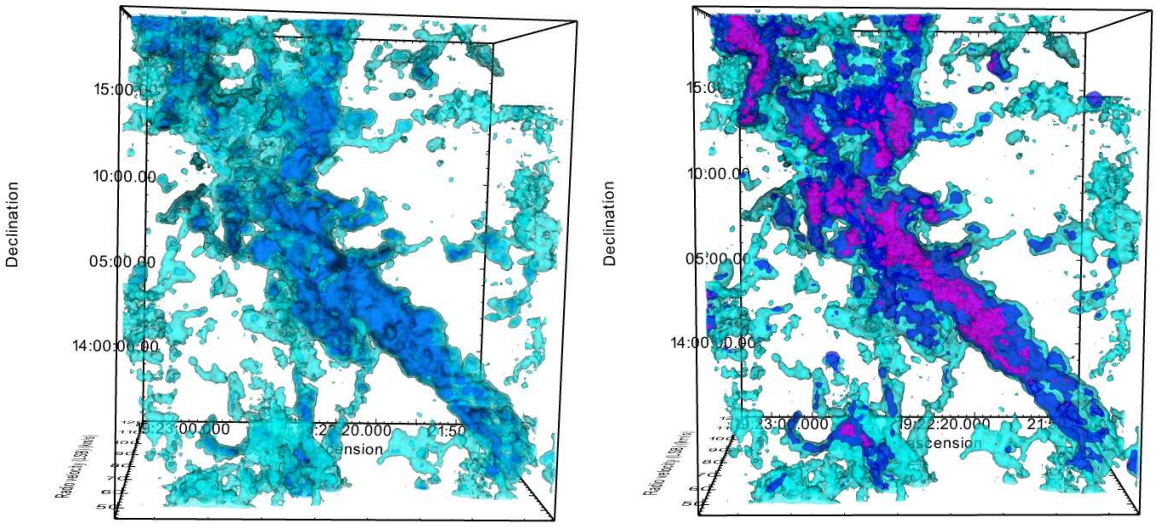

Figure 4.10: 3D (position-position-velocity) images of the zoomed in region from Fig. 4.9. In both images the velocity axis goes into the paper. Left: image in ^{12}CO (colour corresponding to $10\,\sigma$, $20\,\sigma$, and $30\,\sigma$). Right: image composed of ^{12}CO ($10\,\sigma$, light blue) ^{13}CO ($10\,\sigma$, dark blue) and C^{18}O ($5\,\sigma$, purple).

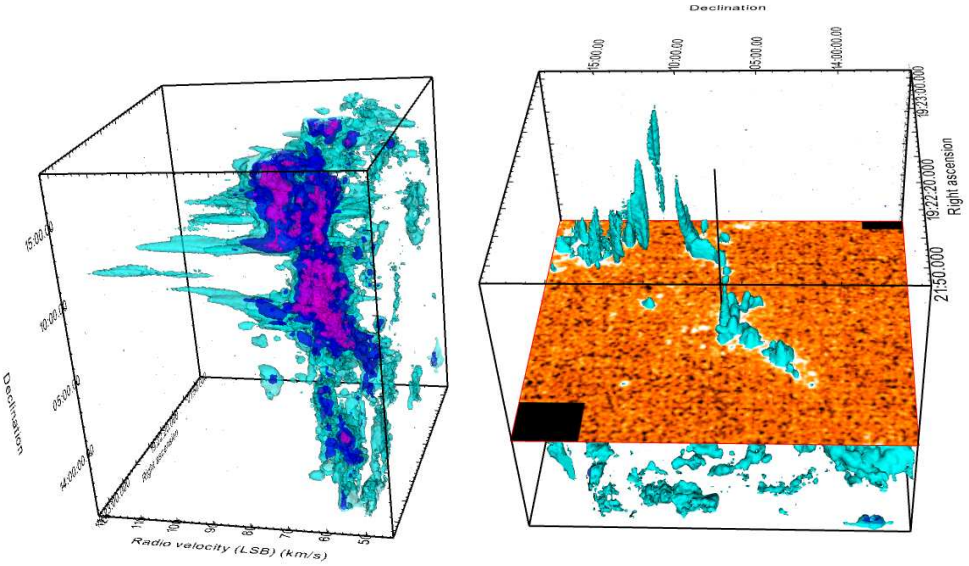

Figure 4.11: Image of the HVS region, as depicted in Fig. 4.9. Left: image in Vrad-Dec-RA space (same colours and levels used in Fig. 4.10). Right: image at a level of 10σ, with the image plane shown at $74\,\mathrm{km\,s^{-1}}$, Black line indicates the location of one of the molecular outflows (d) identified in Table 4.3

ID	RA	Dec	v_{lower} ($\mathrm{km\,s^{-1}}$)	v_{upper} ($\mathrm{km\,s^{-1}}$)	v_{range} ($\mathrm{km\,s^{-1}}$)	v_{red} ($\mathrm{km\,s^{-1}}$)	v_{blue} ($\mathrm{km\,s^{-1}}$)
a	19:22:54	14:09:45	67	99	33	32	*
b	19:22:54	14:10:57	87	119	32	52	-
c	19:22:47	14:12:03	82	110	28	43	-
d	19:22:26	14:06:50	52	77	25	10	15
e	19:22:57	14:09:37	66	88	22	21	**
f	19:22:55	14:11:12	94	113	20	46	-
g	19:22:49	14:13:60	73	93	20	26	-
h	19:22:58	14:13:08	61	81	20	14	*
i	19:23:03	14:13:08	65	85	20	18	*
j	19:22:45	14:12:25	82	101	19	34	-
k	19:22:51	14:15:19	74	89	16	22	*
l	19:22:47	14:14:50	82	95	13	28	-
m	19:22:54	14:15:34	74	85	12	18	-
n	19:22:45	14:13:52	83	94	11	27	-

Table 4.3: Outflows in the W51 GMC region identified at 10σ from ^{12}CO 3D data. RA and Dec indicate the coordinate positions of outflow material at the maximum extent in velocity. v_{lower} and v_{upper} denote the range (in radial velocities) over which the outflow emission was observed (producing v_{range}). The red and blue shifted velocities (v_{red}, v_{blue}) are calculated from the systemic velocity of the region ($67\,\mathrm{km\,s^{-1}}$). *Indicates confusion at low velocities. **Indicates outflow structure at an angle.

of the material would be traced without hampering identification by an excess of emission. At 5σ it was found that outflows previously observed to be two distinct components (based on their shape: i.e. indentations and differences in velocity range) became merged, with the excess emission making identification difficult in regions closer to the systemic velocity of the cloud. $10\,\mathrm{km\,s^{-1}}$ was chosen because below this threshold confusion arose (the systemic velocity of the region examined extended by $\sim$10 $\mathrm{km\,s^{-1}}$ in velocity).

Using GAIA-3D outflow positions were identified by using an image plane in spatial space which can be scrolled along in velocity space. Outflows that extended $\pm10\,\mathrm{km\,s^{-1}}$ beyond the systemic velocity of the region (taken to equal $67\,\mathrm{km\,s^{-1}}$) above $10\,\sigma$ were recorded in Table 4.3 as they appeared in the spatial plane at their maximum extent in velocity. This method although quite rudimentary should provide a good guide to the number of bright outflow candidates within the region studied.

Numerous outflows candidates are easily identified from the GAIA-3D images using this method. From the criterion outlined above we find 14 candidate outflows, with velocities ranging in extent to $43\,\mathrm{km\,s^{-1}}$ (with a median of $28\,\mathrm{km\,s^{-1}}$). These outflow velocities are calculated relative to the systemic velocity of the cloud which is calculated from the peak of the integrated intensity spectra for the whole region in ^{12}CO, ^{13}CO and C^{18}O, and was found to be $67\,\mathrm{km\,s^{-1}}$. These outflows are listed in Table 4.3 and have positions depicted in Fig 4.13. These molecular outflows are similar in velocity extent to those observed by Beuther *et al.* (2002) who determined velocity ranges in 21 star forming regions and found the maximum extent in velocity to be $56\,\mathrm{km\,s^{-1}}$ in one region with a median of $20\,\mathrm{km\,s^{-1}}$. We also see that eight of the 14 outflows are detached lobes from the systemic cloud velocity, as observed in Fig. 4.11 and Fig. 4.13.

Although these numbers are lower limit estimates to the total number of outflows within this region what we do find from this search is that there is a clear concentration of outflows towards the W51A region. This concentration indicates that the *current* star formation activity is not as evenly distributed within the region.

In the images it is clear that identification of outflows at high velocities (i.e. $> 74\,\mathrm{km\,s^{-1}}$) is more straightforward than the identification of outflows at lower velocities (i.e. $< 55\,\mathrm{km\,s^{-1}}$) due to confusion with bulk emission from the cloud. We see that most outflows extend $\sim$ 30" in RA and Dec space.

4.4 Current and future star formation within W51

Understanding what the future holds for star formation within the W51 complex is a non trivial task. In Section 4.2.1 we saw that the SCFE was well below the current observed rate of star formation within W51, by an order magnitude (as determined by Okumura *et al.* 2000), indicating that star formation within W51 is likely to diminish in the future. In contrast to this picture we saw that *current* star formation, identified by the numerous molecule outflows from the ^{12}CO data (see Section 4.3.3), is clearly active within regions of the W51 complex, albeit from the data examined within a confined region towards W51A.

To place both future and current star formation in a spatial context with respect to past star forming events, we utilise the locations of young clusters catalogued by Bica *et al.* (2003) and

RA	Dec	Type*
19:22:15	+14:03:32	IRC
19:22:26	+14:06:54	IRC
19:23:14	+14:27:33	IRGr
19:23:19	+14:29:23	IRCC
19:23:29	+14:31:43	IRCC
19:23:33	+14:29:47	IRCC
19:23:41	+14:29:15	IRCC
19:23:43	+14:29:55	IRCC
19:23:42	+14:30:47	IRCC
19:23:43	+14:30:34	IRCC
19:23:40	+14:31:13	IRCC
19:23:48	+14:33:15	IRCC
19:23:51	+14:32:57	IRCC
19:23:02	+14:16:41	IRC**

Table 4.4: Table of clusters within the W51 GMC as used in Fig 4.12. *type as denoted in Bica *et al.* (2003) where IRC, IRGr, and IRCC, are notation for infrared cluster, infrared cluster candidate and stellar group respectively. **as observed by Kumar *et al.* (2004).

Kumar *et al.* (2004). The catalogue by Bica *et al.* (2003) presented new observations and previous results by Goldader and Wynn-Williams (1994). The clusters identified by Bica *et al.* (2003) were observed in J, H and K bands by 2MASS (Two Micron All Sky Survey: Skrutskie *et al.* 1997) and the clusters identified by Goldader and Wynn-Williams (1994) were made with the NICMOS infrared camera on the University of Hawaii 2.2 m telescope. In addition to this catalogue we also include the cluster associated with the HII region G49.2–0.3 used from Kumar *et al.* (2004) based on J, H and K band observations using the 3.8 m United Kingdom Infrared Telescope (UKIRT). This particular cluster was not catalogued by Bica *et al.* (2003) as it was not detected by 2MASS. Due to the improvement/depth of UKIDSS data in comparison to 2MASS all the clusters within the Bica *et al.* (2003) catalogue were inspected by eye in the UKIDSS Galactic plane Survey data (Lucas *et al.*, 2008)[4] to improve confidence in using these clusters. The criterion for a detection based on K-band images with nebulosity observed *in addition to* an observed heating source. The clusters used, after inspection in UKIDSS data, are given in Table 4.4.

We first consider how the super-critical clumps compare to the locations of these clusters. As we have no velocity information we plot both the W51 complex and HVS clumps together with the clusters on Fig. 4.12. In this figure we find that by eye there is no apparent correlation between either the clusters or the super-critical clumps. We note that the sup-critical clumps, in a similar fashion to the clusters appear to be spread throughout the region, although the super-critical clumps are more spread out. This spread of star forming indicators was also observed by Kang *et al.* (2009) who looked at the spatial distribution of YSOs in the W51 GMC, and found them scattered across the region, albeit with concentrations towards some of the HII regions identified by Koo and Moon (1997b).

[4]see: http://surveys.roe.ac.uk/wsa/

Finally we compare the locations of our outflows, ^{13}CO clumps and the young clusters as plotted in Fig. 4.13. As stated in Section 4.3.3 we find the outflows to be concentrated towards the W51A region. We see no association of the outflows with any of the supercritical clumps but we do see one clear association of a cluster with an outflow (outflow candidate (d) with G49.0-0.3, out of a total of three clusters).

Previous studies suggested that the active star forming nature of the W51 GMC is due to a collision between the W51 complex and the HVS (Arnal and Goss 1985; Pankonin *et al.* 1979; Carpenter and Sanders 1998; Okumura *et al.* 2001; Kang *et al.* 2010) as discussed in Section 3.1.7 and depicted in Fig. 3.2. Kang *et al.* 2010 propose that the majority of the YSO clusters and HII regions within the W51 GMC were a result of a cloud-cloud collision, with G49.0-0.3 and G48.9-0.3 examples of star formation resulting from expanding HII shells, away from this collision front. With outflows dominated towards G49.2-0.3 it appears that the molecular outflows observed may well be a result of cloud-cloud collisions dominating current star formation.

4.5 Summary and Conclusions

In this Chapter I presented an analysis of the physical properties of the dense molecular clumps in the W51 GMC identified by CLUMPFIND in Chapter 3. I then looked at their global properties and finished by searching for evidence of outflows within a defined region within the W51 GMC. From this work presented in this Chapter I make the following conclusions:

1. The dense molecular clumps observed have excitation temperatures of 12 K (7 – 56 K), densities of 5.6×10^{21} cm^{-2} (7.4×10^{20} – 5.6×10^{22} cm^{-2}), surface densities of 0.02 g cm^{-2} (0.002 – 0.19 g cm^{-2}) and masses of 90 M$_\odot$ (10 – 1,700 M$_\odot$).

2. The GMC has a large mass reservoir (1.5×10^5 M$_\odot$) for future star formation with 10% of the clumps by number found to be super-critical.

3. A clump formation efficiency, CFE, of 14% for the W51 GMC, 11% for the W51 complex and 29% for the HVS. A look at this fraction in terms of super-critical clumps yields a super-critical clump forming efficiency, SCFE, of 0.5% for the W51 GMC, (0.6% and 0.1% for the W51 complex and HVS respectively). This indicates that the star formation efficiency will diminish from the current reported value of 2–8% by Okumura *et al.* (2000) in the future unless further external triggering occurs.

4. The CMD for the W51 GMC can be described by a single power law described by an exponent $\alpha = 2.4^{+0.2}_{-0.1}$. Both the W51 complex and the HVS are also best described by this single power law within the errors. This power law is consistent with the upper end of double power laws for other star forming regions, the difference with the W51 GMC being that at such a large distance we are tracing larger and more massive structures and can only realistically fit a power law to higher mass clumps (> 200 M$_\odot$) due to sample completeness.

5. We find evidence for current star formation in the form of outflows, showing that star formation within the W51 GMC does appear to be currently ongoing despite the lack of super-critical clumps identified from the data.

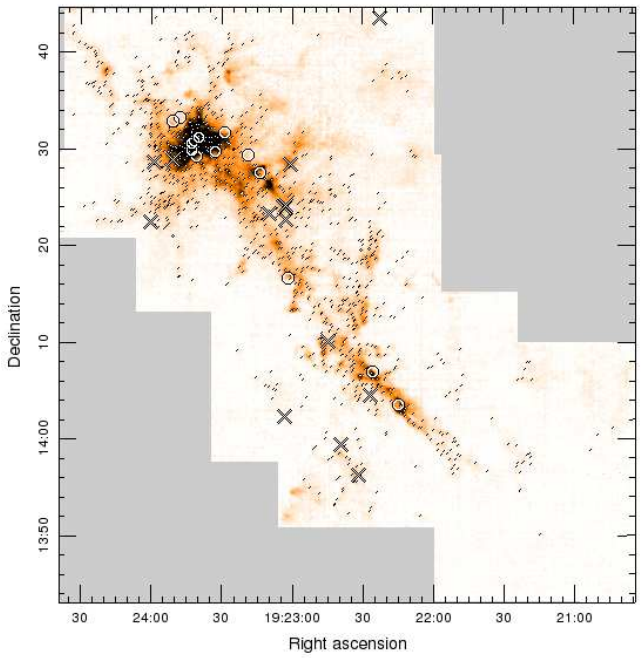

Figure 4.12: ^{13}CO (3 – 2) integrated intensity image of the W51 GMC complex scaled between 0 – 120 K km s^{-1}. Large crosses indicate the location of all super-critical clumps, small diamonds indicate the location of all sub-critical clumps and large circles indicate the location young clusters catalogued by Bica *et al.* (2003) and Kumar *et al.* (2004) as given in Table 4.4. With no velocity information available for the clusters the positions are on both images. The image exclude coverage on far right where emission is below 40 km s^{-1} as in Fig. 3.12.

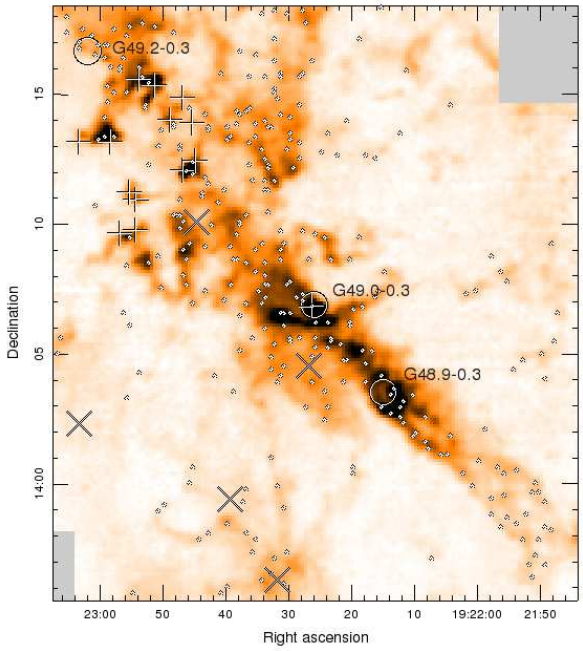

Figure 4.13: ^{12}CO (3 – 2) integrated intensity image of the HVS region, as depicted in Fig. 4.9. Image is scaled between (0–350 K km s^{-1}) with the outflows identified in Table 4.3 denoted by plus signs. The circles indicate the positions of young clusters from Table 4.4, crosses indicate the location of super-critical clumps, and small diamonds indicate the positions of sub-critical clumps.

6. It is found that the locations of the super-critical clumps reflects the distribution of young clusters in as much as they are spread throughout the GMC complex. By eye we see no correlation between the location of either of these classes of objects.

Previous studies have presented the W51 GMC as region of starburst-like activity that has occurred within the past 3 Myr (Okumura *et al.* 2000; Kumar *et al.* 2004; Clark *et al.* 2009) throughout the entire complex (HII regions well distributed), we find evidence of active star formation although we find that future star formation appears to diminish in efficiency-based on a low SCFE. The caveat here remains the fact that we are tracing the clumps only and activity within these clumps, on the scales of cores may present a different picture of the star formation within the W51 GMC.

Future investigations of the W51 GMC will benefit from observations covered by the Herschel key program Hi-GAL (Herschel Infrared GALactic plane survey) between 70 μm and 500 μm (Molinari *et al.*, 2010b), with the first results presented by Molinari *et al.* (2010a) of $2^\circ \times 2^\circ$ centred on $l = 30^\circ$ and 59° indicating the real and exciting potential of Hi-GAL. Data from SASSy, the SCUBA-2 "All Sky" Survey at 850 μm (Thompson *et al.* 2007; Mackenzie *et al.* 2010) will complement Herschel data.

Chapter 5

IRDCs in the SCUBA Legacy Catalogue

'In photography there are no shadows that cannot be illuminated.'
August Sander

Thus far this thesis has concerned itself with the dense molecular content of the Giant Molecular Cloud complex the W51 GMC and searching for the early signs of massive star formation within. For a long time astronomers believed that GMCs were the only sites of massive star formation. However observations over the past decade in the infrared and then sub-millimetre regime uncovered a new class of molecular cloud later found to contain evidence of massive star formation. This new class of molecular cloud is known as Infrared Dark Clouds (IRDCs) and is the focus for this Chapter.

5.1 Introduction and motivation

IRDCs (e.g. Fig. 5.1) were first observed in the mid-1990s by ISO (Perault *et al.*, 1996) and MSX, (Egan *et al.*, 1998) as silhouettes against the bright mid-infrared Galactic background. Initially, Egan *et al.* (1998) identified ∼2000 clouds by eye from the MSX Galactic Plane Survey images. It was not until 2006 that Simon *et al.* (2006a) created an automated identification process from which a comprehensive catalogue of IRDCs throughout the Galaxy was produced. This systematic study to identify IRDCs using MSX (see Section 5.2.1) identified 10,931 candidate IRDCs within which a total of 12,774 compact IRDC core candidates were detected.

Until recently, with the exception of distance estimates, only small samples of the IRDCs originally published by Simon *et al.* (2006a) had been investigated, with an observational bias towards the darkest high contrast clouds (Rathborne *et al.* 2006; Du and Yang 2008). The trends of global properties across a large sample of IRDCs have yet to be investigated, in particular the proportion of IRDCs that are associated with active star formation as opposed to IRDCs that are quiescent or starless.

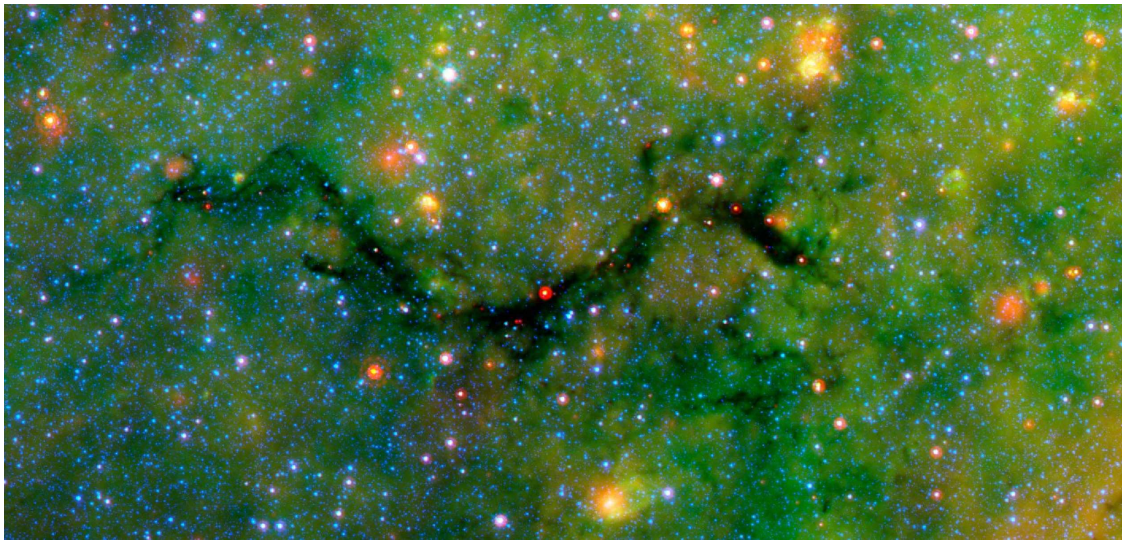

Figure 5.1: Spitzer image of the filamentary IRDC known as the Snake (G011.11-0.12). Image is composed of both IRAC and MIPS observations: 3.6 μm (blue), 8.0 μm (green), 24 μm (red) 1.0° × 0.77°. Image is approximately 0.5° by 0.25°. (Courtesy of: NASA/JPL-Caltech/S Carey (SSC/Caltech) http://sscws1.ipac.caltech.edu/Imagegallery/image.php?image_name=ssc2006-20a)

Recently Peretto and Fuller (2009) took advantage of the greater sensitivity and resolution of the Spitzer Space Telescope to produce "a catalogue of Spitzer dark clouds" using GLIMPSE archival data. Although smaller in coverage area this catalogue identified 11,303 clouds (compared to 6721 MSX IRDCs located within the GLIMPSE coverage area). This catalogue of IRDCs is not included in this investigation as it was not available when the study was undertaken.

In this chapter I address the issue of a lack of large studies of IRDCs by investigating candidate IRDC cores originally identified by Simon *et al.* (2006a) that are contained within the recently published SCUBA Legacy Catalogue by Di Francesco *et al.* (2008). In Section 5.2 I describe the cross matching method used on the two catalogues, obtain column density and mass estimates (or upper limits where applicable) and identify 24 μm embedded sources associated with the identified cores. The results of the cross matching procedure are presented in Section 5.3. I discuss the findings in Section 5.4 with a mention of the impact on two of the forthcoming JCMT Legacy surveys. Finally I make some concluding remarks in Section 5.5. This work was published in MNRAS in November 2009 (Parsons *et al.*, 2009).

5.2 Method

In this section I first outline the archival data from SCUBA and MSX used within this study. I then outline the process of cross identification process of the MSX IRDC cores identified by Simon *et al.* (2006a) to sources within the SCUBA Legacy Catalogue (Di Francesco *et al.*, 2008). I then present the column densities of these IRDC cores and for those cores with

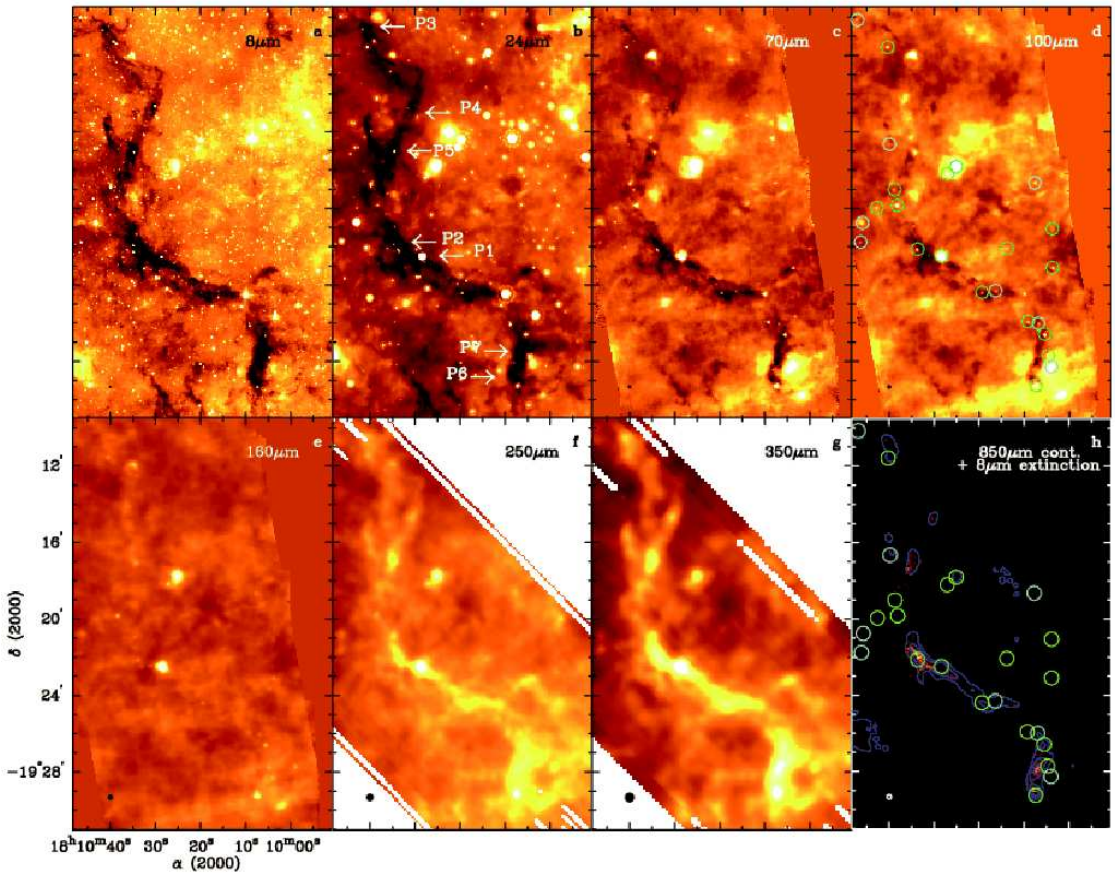

Figure 5.2: IRDC G011.11-0.12 from 8 μm to 850 μm in wavelength. a) Spitzer IRAC 8 μm image. b) Spitzer MIPS 24 μm image. The peak SCUBA positions (P1, P2,...) as assigned by Johnstone et al. (2003) are indicated. c) Herschel PACS 70 μm image. d) Herschel PACS 100 μm image. Sources with no 24 μm counterpart are circled in cyan, sources with 24 μm counterparts are circled in green. e) Herschel PACS 160 μm image. f) Herschel SPIRE 250 μm image. g) Herschel SPIRE 350 μm image. h) 8 μm extinction map (derived from Spitzer data) with (blue) SCUBA 850 μm continuum contours (levels are 0.4 0.8 1.2 Jy beam^{-1}). The approximate beam size is indicated in the lower-left corner of each panel (reproduced from Henning *et al.* 2010).

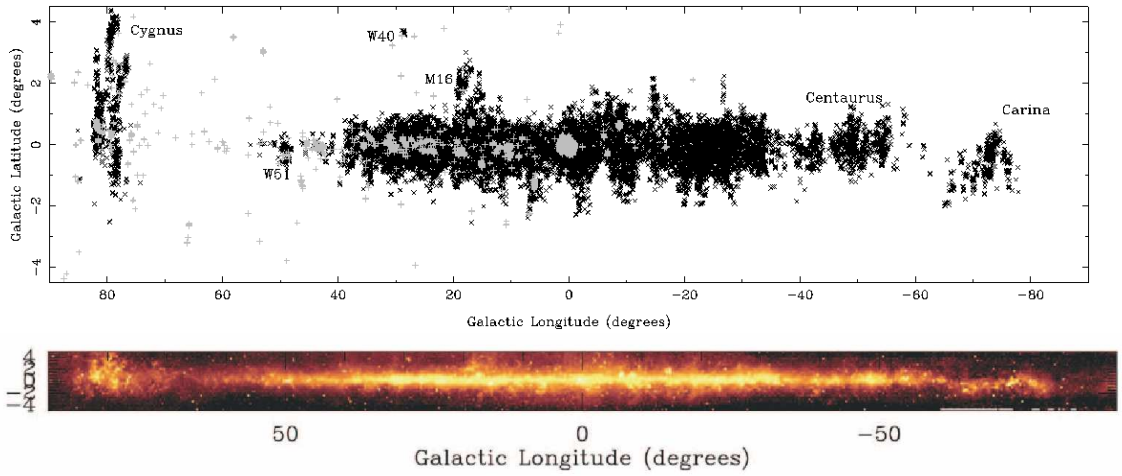

Figure 5.3: Distribution of IRDCs identified by MSX along the first and fourth quadrant of the Galactic plane are identified in black. Positions of cores within Extended Dataset from the SCUBA Legacy Catalogue are identified in gray. Prominent star-forming regions are labelled and the latitude axis of the plot is stretched in the top panel. For comparison, MSX emission at 8.3 μm from the same region is shown in the bottom panel. This image is reproduced from Simon *et al.* (2006a) with minor changes.

associated distance information I present mass estimates. Finally I investigate the number of IRDC cores containing embedded 24 μm emission: signs of potential star formation.

5.2.1 Archival data

In 2006a, Simon *et al.* produced a catalogue of 10,931 candidate IRDCs using data from the MSX satellite that covered the entire Galactic plane between $|b| \leq 5^\circ$ (shown in Fig. 5.3). Candidate IRDCs were identified by modelling the Galactic background diffuse emission at 8 μm, subtracting the 8 μm MSX images from this model and then dividing by the background model to produce what is known as a "contrast image", as shown in Fig. 5.4. This identification process at 8 μm utilises the combination of both good resolution and bright mid-infrared emission (bright emission from PAH, Polycyclic Aromatic Hydrocarbons, at 7.7 μm and 8.6 μm).

Regions of high extinction in the raw images appeared as positive objects with contrast values between 0 and 1 (1 for highly extinct objects). IRDCs were then identified by looking for extended contrast sources, those with 36 or more continuous pixels with a contrast greater than 2σ. Cores within the clouds were identified by decomposing the clouds using two-dimensional elliptical Gaussian fits (Simon *et al.*, 2006a). By definition each IRDC contains at least one core. Although discovered by their mid-infrared absorption, it is at sub-millimetre and far-infrared wavelengths that these objects have their peak emission.

Di Francesco *et al.* (2008) present a comprehensive re-reduction of the entire 8 year sub-millimetre continuum data set observed by SCUBA (Sub-millimetre Common User Bolometer Array, see Holland *et al.* 1999) on the JCMT in Hawaii. This data set is known as the SCUBA

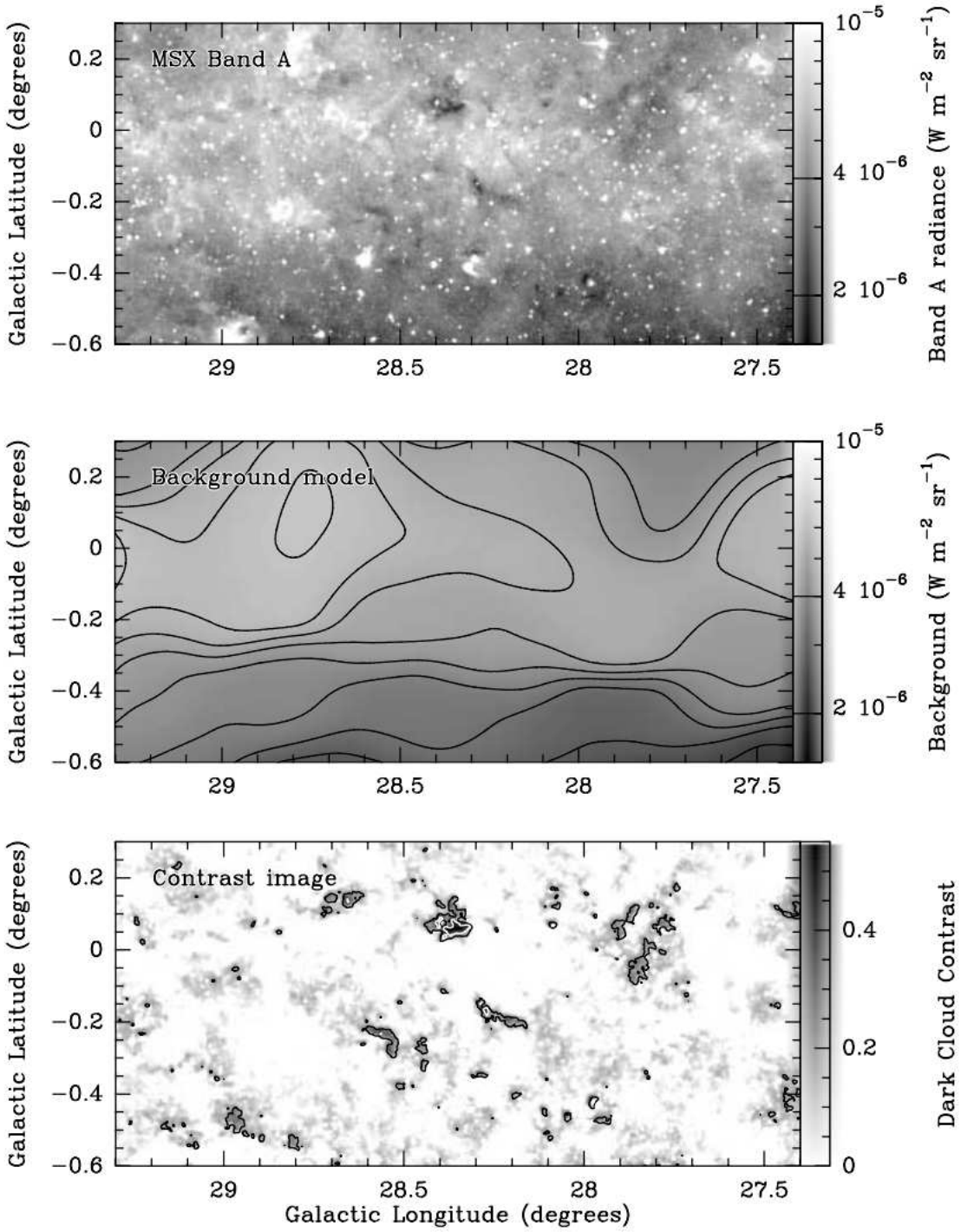

Figure 5.4: Image reproduced from Simon *et al.* (2006a). Top: MSX 8.3 μm image. Middle: Background model. Bottom: Contrast image determined from the original data and the background model.

Legacy Catalogue and covers a total area of just over 29 square degrees at 850 μm, a sample of which is shown in Fig 5.5. A consequence of the varying weather conditions and method of data acquisition, over the entire lifetime of SCUBA, is that the data is both non-uniform in noise and in the quality of opacity corrections.

In Fig 5.5 the differing observational techniques and implications this has on the catalogue can be seen. In the top image a coverage map for the area is shown, clearly seen are two regions that have been mapped using a rastering technique. The brightest points within these rasters (at a single position in the bottom raster and at three points in the top raster) are observations made using a different technique; jiggle maps. From this we see that one region may have been mapped by various techniques with the result being a variation in the quality of the data.

Di Francesco *et al.* (2008) divided the SCUBA Legacy Catalogue into a Fundamental and an Extended Dataset. The former uses data for which there is well known atmospheric opacity calibration data (from both skydips and the CSO radiometer, Di Francesco *et al.* 2008) and the latter contains all observations regardless of the data quality. Coverage by the Extended data set is greater in area than the Fundamental by 9.7 square degrees. Discrete objects were identified within the SCUBA Legacy Catalogue (from both the Fundamental and Extended Dataset independently) using Clumpfind[1] (Di Francesco *et al.*, 2008). This provides information on the properties of each object such as flux (at the peak and integrated over its area) and apparent size.

MIPSGAL[2] is a survey of the Galactic Plane from $10 < l < 65°$ and $-10 > l > -65°$ $|b| < 1°$ at 24 and 70 μm, using the MIPS instrument on Spitzer[3]. As a tracer of warm dust and with good resolution (6" angular resolution as opposed to 20" and 14" for MSX and SCUBA respectively), MIPSGAL 24 μm data are ideal for investigating warm embedded objects, such as Young Stellar Objects. Indeed van der Wiel and Shipman (2008) combined MIPSGAL data with IRAC (Infrared Camera on Spitzer), 2MASS (Two Micron All Sky Survey) and SCUBA data to identify Young Stellar Objects (YSOs) within IRDC MSXDC G048.65-00.29.

5.2.2 Cross identification

In total, 428 MSX IRDC cores from Simon *et al.* (2006a) were located in regions mapped by SCUBA (325 located in the Fundamental region and an additional 103 located in the Extended region). However the SCUBA Legacy Catalogue does not contain photometric measurements of objects located at the edges of maps (which may be subject to large scale background or noise fluctuations). In addition, regions of high noise persist within the catalogue due to the non-uniform way in which the data were taken. In order to make the catalogue more uniform we exclude data with an rms noise greater than 0.1 Jy pixel^{-1}. The pixel size for data in the SCUBA Legacy Catalogue is 6". This 0.1 Jy pixel^{-1} cut excludes the high noise Poisson tail present in the data (Di Francesco *et al.*, 2008) and gives the remaining

[1]The Clumpfind algorithm used to identify objects was adapted from Williams *et al.* (1994) (Di Francesco *et al.*, 2008).

[2]MIPS (Multiband Imaging Photometer for Spitzer) Galactic Plane Survey. Data available from http://irsa.ipac.caltech.edu/data/SPITZER/ MIPSGAL/images/

[3]The Spitzer Space Telescope is operated by the Jet Propulsion Laboratory, California Institute of Technology under NASA contract 1407.

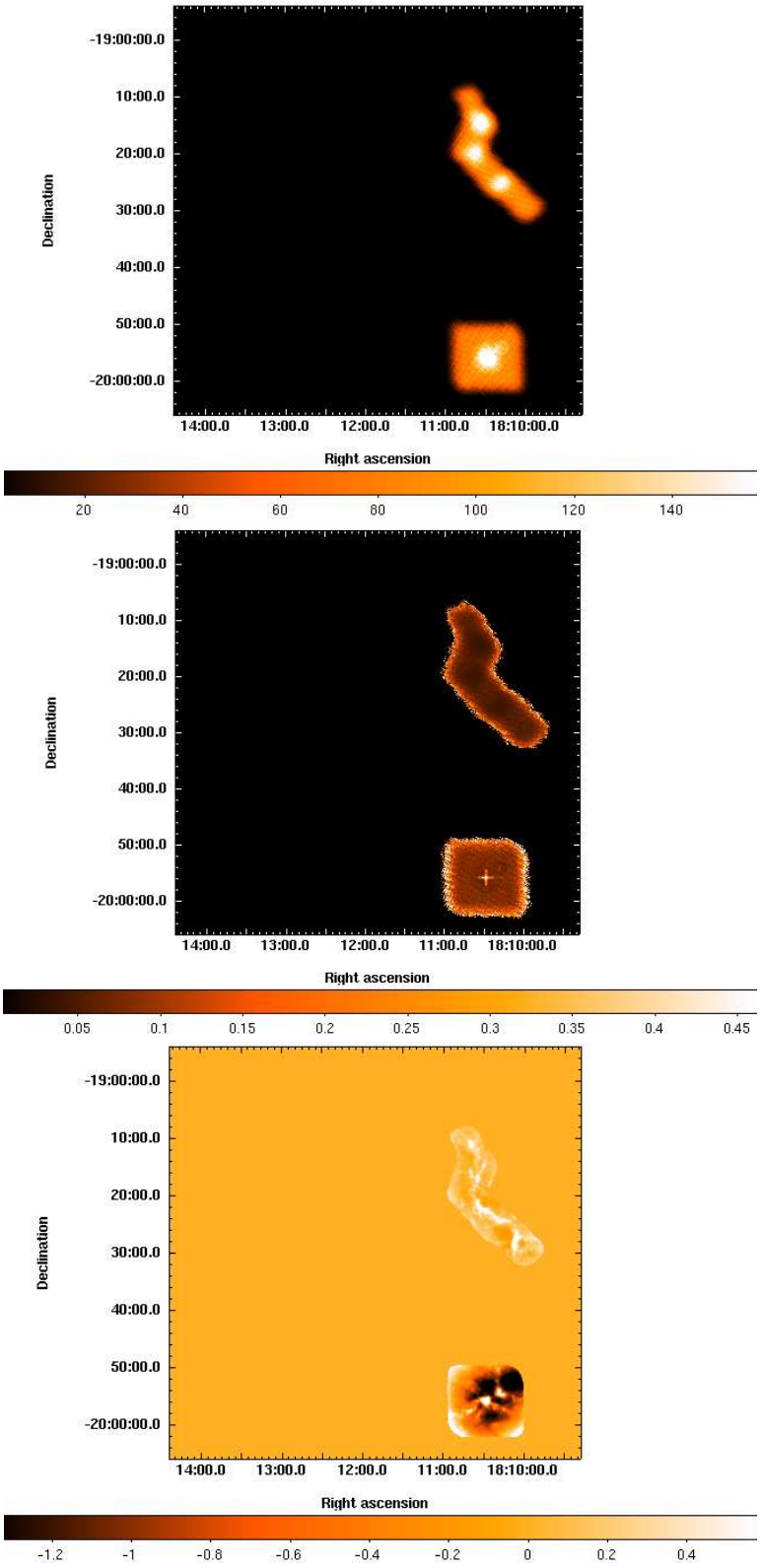

Figure 5.5: Examples of the IRDC data within the SCUBA Legacy Catalogue. Note the sky was divided into square-degree regions with 0.1° overlap with neighbouring fields (Di Francesco *et al.*, 2008). Top: Coverage map. Middle: Error map. Bottom: Emission map.

data approximately Gaussian noise statistics, with a mean and sigma of $0.05\,\mathrm{Jy\,pixel^{-1}}$ and $0.024\,\mathrm{Jy\,pixel^{-1}}$ respectively. Taking map edges into account and excluding regions with noise $> 0.1\,\mathrm{Jy\,pixel^{-1}}$ leaves us with 251 MSX IRDC cores within the SCUBA Legacy Catalogue mapped region. The 251 MSX candidate IRDC cores were then cross matched to sources identified within the SCUBA Legacy Catalogue (as defined by Clumpfind). IRDC cores were matched against both the Fundamental and the Extended data Catalogues.

For the cross identification process, the locations of the MSX IRDC cores were positionally matched using TOPCAT[4] to the locations of the Clumpfind SCUBA objects. The irregular morphology of the candidate objects in both the MSX $8\,\mu$m contrast images and the SCUBA $850\,\mu$m emission maps, meant that the task of cross matching cores between the two catalogues was non trivial. Simon *et al.* (2006a) identified IRDCs within the MSX $8\,\mu$m data as contiguous structures in the contrast images that were sufficiently extended to be real clouds and not artefacts. The cores within the clouds were identified using two dimensional elliptical Gaussian fits to these contiguous structures. In contrast, Di Francesco *et al.* (2008) created the SCUBA Legacy Catalogue using Clumpfind which identifies irregular objects by following intensity contours. Due to this different approach in identification between the two catalogues, the catalogued positions of IRDC cores and SCUBA clumps may differ by a considerable amount, even when the two are clearly morphologically associated with each other. A large positional matching radius was required to identify potential matches followed by further refinement by eye, checking that the individual IRDC cores were morphologically similar to the SCUBA $850\,\mu$m emission. A matching radius of 1' was chosen as Simon *et al.* (2006a) quotes that typical core diameters lie between 0.75' and 2'. For added confidence, those cores that were initially matched were checked for $850\,\mu$m emission at the location of the MSX core.

On several occasions multiple matches were made to the same SCUBA sources where Clumpfind had only identified one object. In these instances the closest positional Clumpfind match to the candidate MSX identified IRDC core was taken. The method by which the MSX candidate cores were matched to SCUBA cores meant that the closest SCUBA match was used even when multiple cores were nearby. A consequence of the differing techniques used to identify objects within the MSX and SCUBA catalogues was seen when classifying by eye those IRDC SCUBA detected candidates with and without embedded objects. Fig. 5.6, shows IRDC core 'MSXDCG028.37+00.07 (d)', Clumpfind identified two distinct objects in the $850\,\mu$m data but the MSX identification process identified the dark complex as one object.

Of the 251 IRDC cores located within the SCUBA Legacy Catalogue mapped region, a total of 46 core matches were manually excluded from the sample. In some cases, this was because the MSX-identified IRDC cores were located on positions of extended $850\,\mu$m emission which could not be morphologically matched to the compact candidate IRDC cores. Due to the large upper limit used for the matching radius a number of matches were also found to be inappropriate. In other cases, objects were found within 1' but not coincident with $850\,\mu$m emission. This may have occurred due to poor background modelling of the mid-infrared emission. The subtraction of a smoothed background model can potentially result in the creation of artefacts with high contrast values. Cores adjacent to bright extended $8\,\mu$m infrared emission, were also amongst those excluded. These objects were removed due to concerns highlighted by Simon *et al.* (2006a) over the process of creating a contrast image in

[4]TOPCAT: Tool for OPerations on Catalogues And Tables. See http://www.star.bris.ac.uk/~mbt/topcat/

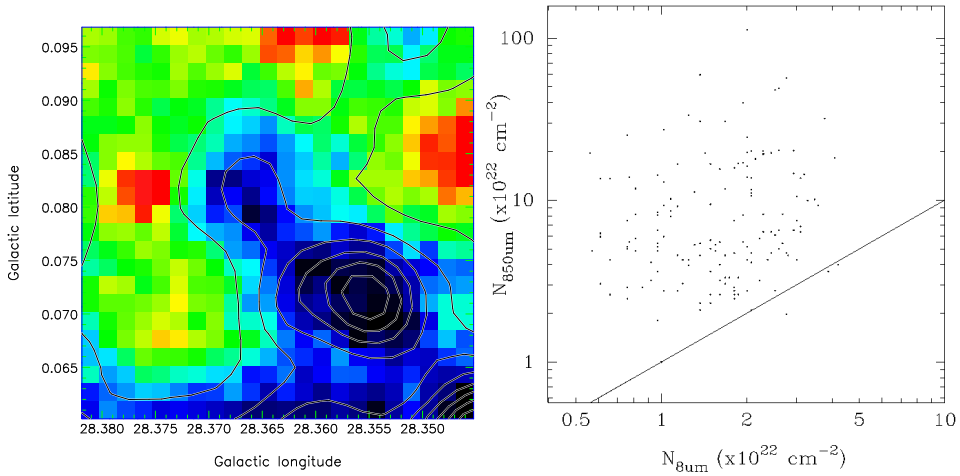

Figure 5.6: Left: image of IRDC core: MSXDCG028.37+00.07 (d). Image is MSX 8 μm stretched between zero and three sigma to emphasise decrements in the background emission. SCUBA contours overlaid at three sigma intervals. Right: plot of H_2 column densities obtained from 8 μm data compared to 850 μm data, the line of equality is plotted to show that the 8 μm column density underestimates the 850 μm column density.

a complex environment.

Finally of the 205 remaining IRDC cores, a total of 154 were matched to SCUBA objects from the SCUBA Legacy Catalogue of Di Francesco *et al.* (2008). The remaining 51 IRDC cores were identified as having no associated 850 μm emission. These MSX identified candidate cores could be due to column densities and dust temperatures below the detection limit of SCUBA. They could also be minima in the mid-infrared background. Alternatively they could be a result of uncertainties in the MSX IRDC candidate identification process, we explore these possibilities further in Section 5.4.2.

5.2.3 Column densities and masses of the cores

We derive peak column densities for all IRDC cores within our sample, whether detected at 850 μm or not, by applying the extinction law to the MSX 8 μm data:

$$I_i = I_b e^{-\tau_\lambda} \tag{5.1}$$

where I_i is the image intensity, I_b is the background model intensity and τ_λ is the dust opacity which equals the cross sectional area, σ_λ, multiplied by the column density, $N(H_2)$, i.e. $\tau_\lambda = \sigma_\lambda . N(H_2)$. The peak contrast value C is defined by Simon *et al.* (2006a) as:

$$C = \frac{I_b - I_i}{I_b} = 1 - e^{-\tau_\lambda} \tag{5.2}$$

It is then possible, by substituting $\tau_\lambda = N(H_2)\sigma_\lambda$ into equation 5.2, to derive:

$$N(H_2) = \frac{-ln(1-C)}{\sigma_\lambda} \tag{5.3}$$

We assume a value of $\sigma_\lambda = 2.3 \times 10^{-23}\,\mathrm{cm}^2$ for the cross sectional area of the obscuring dust particles at $8.8\,\mu$m (Ragan *et al.*, 2006). Column densities for the IRDCs derived by this method are contained in Tables B.1 and B.2. Fig. 5.7 shows the distribution of those cores detected and not detected at $850\,\mu$m with peak contrast. We see that the median column density for the SCUBA detected candidates and the SCUBA non-detected candidates is $1.7 \times 10^{22}\,\mathrm{cm}^{-2}$ and $1.0 \times 10^{22}\,\mathrm{cm}^{-2}$ respectively.

For comparison with the values determined from the $8\,\mu$m extinction we also calculated the peak column densities for cores detected at $850\,\mu$m, using the SCUBA $850\,\mu$m data to derive the mass (as defined by Hildebrand 1983) and assuming spherical geometry:

$$N(H_2) = \frac{F_\nu C_\nu}{B_\nu(T)\pi(tan(R_{850}))^2 2m_H} \tag{5.4}$$

F_ν is the observed peak flux; C_ν is the mass coefficient, $B_\nu(T)$ is the Planck function evaluated for dust temperature, T; R_{850} is the radius of the beam at $850\,\mu$m, which is larger than the beam FWHM of 19" due to convolution during the data reduction (with out which would be 14" Di Francesco *et al.* 2008) and m_H is the mass of a hydrogen atom. The value of $\mathrm{C}_\nu = 50\,\mathrm{g\,cm}^{-2}$ at $850\,\mu$m is taken from Kerton *et al.* (2001).

When evaluating the Planck function, a temperature of 15 K was assumed for all the cores as this is the midpoint of the observed range (8–25 K) in IRDC temperatures observed by Carey *et al.* (1998), Teyssier *et al.* (2002) and Pillai *et al.* (2006a). Decreasing or increasing the temperature to 8 or 25 K would increase or decrease these column density estimates by a factor of 3.5 and 2.2 respectively.

We compared the column densities derived by each method. In general the column density derived from the $8\,\mu$m extinction agrees with that derived from the $850\,\mu$m emission to within an order of magnitude. There is considerable scatter but the overall trend is that the $8\,\mu$m column density underestimates the $850\,\mu$m column density, as shown in Fig. 5.6. This suggests that the average temperature for the IRDC cores may be closer to 10 K than our assumption of 15 K. However due to the large uncertainties in mass coefficients, the $8\,\mu$m extinction law and contamination from foreground emission we do not expect close agreement between these two methods.

Masses were determined for the cores detected at $850\,\mu$m using the method of Hildebrand (1983), as detailed in Chapter 2 Section 2.6.4, i.e.

$$M = \frac{d^2 F_\nu C_\nu}{B_\nu(T)} \tag{5.5}$$

where d is the distance to the IRDC core. A dust temperature of 15 K was again assumed for all the cores. As before, decreasing or increasing the dust temperature to 8 or 25 K would increase or decrease the masses derived by a factor of 3.5 and 2.2 respectively. Kinematic distances exist for 33 of our cores detected at $850\,\mu$m from Simon *et al.* (2006a), who derived

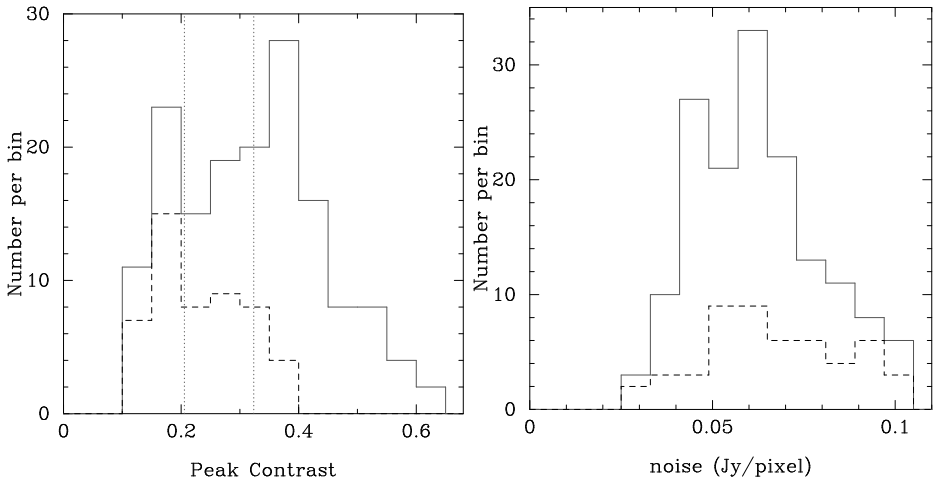

Figure 5.7: Left: Histogram of Peak Contrast values for cores detected at 850 μm (solid line) and cores not detected at 850 μm (dashed line). Vertical dotted lines mark the position of the peak contrast values that correspond to 1.7×10^{22} cm^{-2} and 1.0×10^{22} cm^{-2} (median column densities for cores detected and not detected at 850 μm respectively). Bin size used is 0.05. Right: Histogram of rms (Jy/pixel) for cores detected at 850 μm (solid line) and cores not detected at 850 μm (dashed line). Bin size used is 0.008.

distances by matching up the morphologies of candidate IRDC cores with CO morphologies from the GRS (Galactic Ring Survey). Our mass estimates for these 33 SCUBA detected cores, along with the distance estimates from Simon *et al.* (2006a) can be found in Table B.3.

5.2.4 Embedded 24 μm objects in the cores

Of the 205 IRDC cores, 103 were located within the coverage area of MIPSGAL, 34 of these were not detected at 850 μm. The cores were visually inspected at 24 μm and it was found that 48 of the cores detected at 850 μm are positionally associated with one or more 24 μm MIPSGAL sources (approximately half of the 69 cores detected at 850μm contain more than one 24 μm source). None of the 34 cores, not detected at 850 μm, are found to be associated with any MIPSGAL 24 μm sources. Fig. 5.9 shows two cores that are seen at both 8 μm and 24 μm, one with an embedded object and one without.

5.3 Results

In this section we look at the nature of those IRDC cores observed but not detected at 850 μm, at the overall detection rates as a function of peak contrast, and we investigate those cores with and without associated 24 μm emission.

5.3.1 MSX identified IRDCs in the SCUBA Legacy Catalogue

In total 205 candidate IRDC MSX cores were found to be within the SCUBA Legacy Catalogue coverage area. 154 candidate cores had detectable emission at 850 μm, and 51 candidate cores did not. Of the 154 cores detected at 850 μm, we find that they span a range of peak contrast values (0.11 – 0.62), column densities and masses, with the peak contrast distribution having a median of 0.32. 8 μm column densities range from 0.56×10^{22} to 4.21×10^{22} cm^{-2} with a median of 1.7×10^{22} cm^{-2}. Mass estimates of these candidates range from 50 to 4,190 M$_\odot$ with a median of 300 M$_\odot$. Peak contrast values for cores detected and not detected at 850 μm are given in Tables B.1 and B.2 respectively. The physical properties of those cores with distance information available (data taken from Simon *et al.* (2006a) and Jackson *et al.* (2008b)) are seen in Table B.3.

Those cores not detected at 850 μm are found predominantly at low contrast values (≤ 0.4), with a mean of 0.22 (seen in Fig. 5.7). This result is not surprising because SCUBA is naturally biased to detect high column density clouds (which would have high contrast values) and not detect low column density clouds (which would have low contrast values). A question that arises from this work is whether or not cores detected and not detected at 850 μm are from two separate populations, such as two physically different stages in the star forming process? To investigate this we do a Kolmogorov-Smirnoff (KS) test, as outlined in the following section.

5.3.2 KS testing for two separate populations

A KS two sample test is used to determine if there is a statistical difference between two populations by taking a null hypothesis that the two populations arise from the same distribution. The KS test works by calculating the maximum deviation between two cumulative distributions that contain a total of m and n data, that at a point x have cumulative values $S_m(x)$ and $S_n(x)$ respectively (Wall and Jenkins, 2003).

$$D = max|S_m(x) - S_n(x)| \tag{5.6}$$

It is then possible to reject the null hypothesis at a specified level of significance: as shown in Table 5.1 (see Wall and Jenkins 2003)

A KS two sample test, on the peak contrast values for cores with and without detected 850 μm emission, reveals that the cores are not likely to have been drawn from the same population to a certainty of 99 %. Inspection of the rms values for the 205 candidate IRDC cores, as with the 850 μm emission, reveals no significant difference in values between those cores detected at 850 μm and those not detected at 850 μm as seen in Fig. 5.7. Thus we are confident that the reason behind the cores not being detected at 850 μm is not due to them simply lying in high noise regions of the SCUBA Legacy Catalogue or that the IRDCs are badly selected due to their coincidence with local minima in the mid-infrared background. This possibility is suggested by Simon *et al.* (2006b) and Jackson *et al.* (2008b), who state that at low contrast values the number of mis-identified IRDCs is greater than at high contrasts.

Significance	Value of D
0.100	1.22K
0.050	1.36K
0.025	1.48K
0.010	1.63K
0.005	1.73K
0.001	1.95K

Table 5.1: KS test table for critical D (see equation 5.6), where $\mathrm{K} = \sqrt{\frac{m+n}{mn}}$. This table may be used if values m or n are greater than 25.

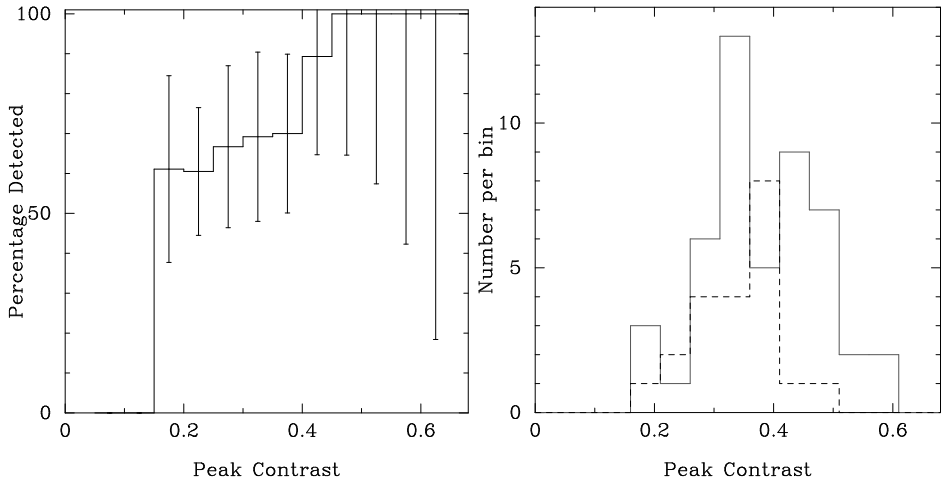

Figure 5.8: Left: Histogram of contrast value against detection rate (defined as IRDC cores with associated 850 μm sources). Bin size used is 0.05. Right: Histogram showing the distribution of the 69 cores detected at 850 μm within the MIPSGAL coverage area with (solid line) and without (dashed line) an embedded 24 μm object at each Peak Contrast value. Bin size used is 0.05.

5.3.3 Detection rates

We investigated the fraction of cores detected at 850 μm as a function of peak contrast to identify any trends in the detection fraction of IRDC cores. We calculated the detection fraction by dividing the number of cores with 850 μm detections by the total number of MSX IRDC cores within the SCUBA Legacy Catalogue at specific contrast values. Overall the fraction of IRDC cores detected by SCUBA is found to be 75%. At low contrast values ($\leq$0.4) we detect over 60% of the IRDC cores, whereas all IRDC cores are detected when the contrast is high (>0.6) as seen in Fig. 5.8. The error bars in Fig. 5.8 were calculated by assuming an uncertainty of $\sqrt{N}$ where N is the number of cores detected by SCUBA per bin and using propagation of errors.

5.3.4 MIPSGAL 24 μm sources associated with IRDCs detected at 850 μm

We present a histogram of the peak contrast of the 69 IRDC cores detected at 850 μm within the MIPSGAL coverage area in Fig. 5.8. Of the IRDC within the coverage area 48 cores were found to be associated with one or more 24 μm MIPSGAL sources directly identified from the MIPSGAL images (as shown in Fig. 5.9) and 21 were found not to be associated with any MIPSGAL sources.

To investigate if the cores with and without embedded 24 μm objects were drawn from the same population, a KS test was once again performed on their peak contrast distribution and it was found that they are highly likely to originate from the same population, with no distinct differences in their peak contrast distribution to a level of significance $> 99\%$.

5.4 Discussion

5.4.1 The reliability of the MSX IRDC catalogue

Originally, when the Simon *et al.* (2006a) catalogue was published, an initial reliability of 82% was reported for IRDCs with contrast values > 0.25. This initial reliability was estimated for the large high contrast clouds by comparison to other source lists from MSX and ISO data (Simon *et al.* 2006a and references there in). Later Jackson *et al.* (2008b) determined a reliability (against CS J=2–1 detections) for low contrast (0.2 - 0.4) objects of approximately 50% increasing to almost 100% at high contrasts (> 0.6), with an overall reliability of $\sim$59%. However the Jackson *et al.* (2008b) sample lacked very low contrast objects, the selection criteria used were peak contrasts > 0.32 and angular sizes > 42". Expanding this estimate to the whole MSX IRDC catalogue Jackson *et al.* (2008b) stated that it was $> 50\%$ reliable for all contrasts. These estimates of reliability were obtained via molecular line spectroscopy of ^{13}CO and CS data from Simon *et al.* (2006b) and Jackson *et al.* (2008b) respectively.

Our mean detection rate of IRDC cores with 850 μm emission is 75% (this value varies over a range of peak contrast values as seen in Fig. 5.8) which is greater than the reliability of the sample studied by Jackson *et al.* (2008b), reported to be 50%. However this detection rate does not take into account the number of inconclusive matches that make up 19% of the IRDC sample. The close correspondence of 850 μm emission, CS 2–1 and ^{13}CO detection rates for IRDCs places greater confidence in the high contrast Simon *et al.* (2006b) candidate IRDCs as true molecular clouds.

5.4.2 Cores not detected at 850 μm

Of the 205 cores within our sample 51 cores were not detected at 850 μm. Those cores detected at 850 μm were found to have higher peak contrast vales and column densities than those cores not detected at 850 μm. The difference in peak contrast values can be seen in Fig. 5.7. The median column density of the cores detected at 850 μm is a factor of $\sim$1.6 times greater than the cores not detected at 850 μm. A KS test of the peak contrast distribution between the cores detected at 850 μm and those that were not, found they are unlikely to be drawn from the same population.

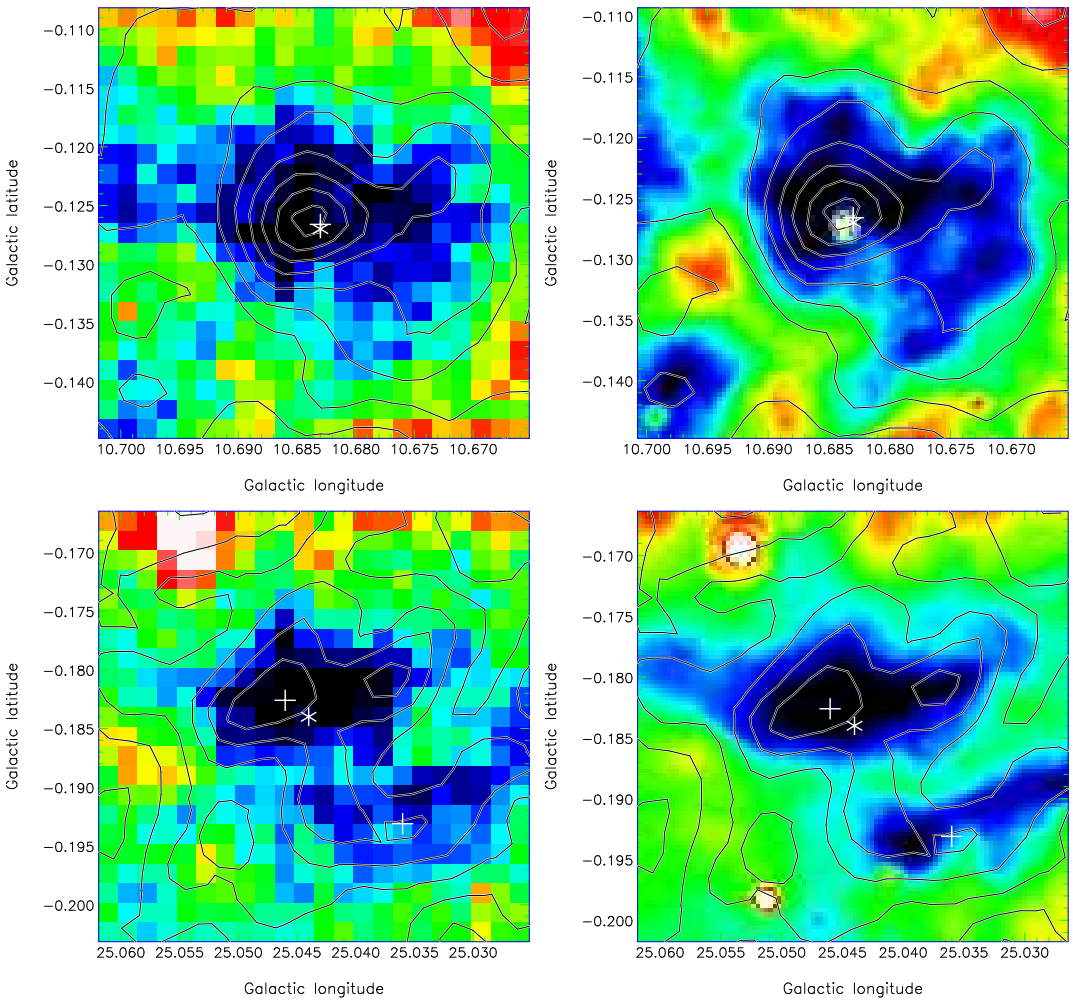

Figure 5.9: Images of two IRDC cores (top and above) identified in the SCUBA Legacy Catalogue. Images to the left are MSX 8 μm and images to the right are MIPSGAL 24 μm. In each image a star marks the location of the MSX identified candidate IRDC core and the cross marks location of the SCUBA Clumpfind object. Contours in all cases are SCUBA 850 μm. Top: Image of IRDC core: MSXDCG10.71−00.16 (b), with a clear association with a 24 μm object. Bottom: Image of IRDC core: MSXDCG025.04−00.20 (f).

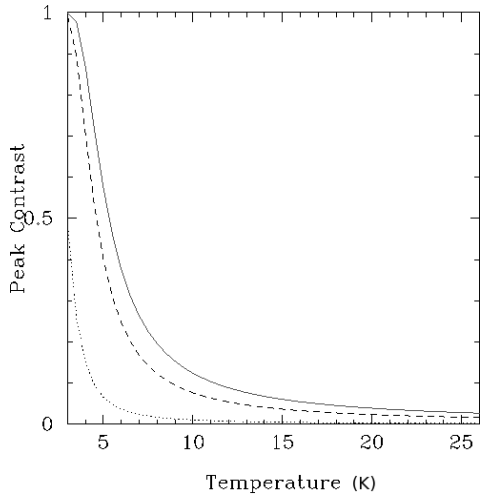

Figure 5.10: A graph to show the sensitivity of SCUBA at 850 μm (solid line) with respect to the detection of contrast values as a function of core temperature. The dashed line represents the predicted sensitivity of SASSy, which at 3 σ will equal 90 mJy. The dotted line represents the predicted sensitivity of JPS, which at 3 σ will equal 12 mJy.

Although the mid-infrared contrast value for a particular cloud should vary with the intensity of the background, it is possible to determine an estimate of the peak contrast sensitivity of SCUBA as a function of temperature by substituting equation 5.3 into equation 5.4, using an 850 μm flux limit of 3 σ (where σ is the median rms sensitivity of the SCUBA Legacy Catalogue) for F_ν and rearranging for C:

$$C = 1 - exp\left(-\frac{F_\nu C_\nu \sigma_\lambda}{B_\nu(T)\pi(tan(R_{850}))^2 2m_H}\right) \tag{5.7}$$

The median rms sensitivity value at 850 μm in the SCUBA Legacy Catalogue after applying our noise cut is 50 mJy beam^{-1}. We plot the limiting contrast of the SCUBA Legacy Catalogue as a function of temperature, derived using equation 5.7, in Fig. 5.10. We also plot the target sensitivity of the SCUBA-2 Legacy Survey SASSy (the SCUBA-2 "All Sky" Survey; Thompson *et al.* 2007) and JPS (the JCMT Plane Survey; Moore *et al.* 2005), which will be discussed further in Section 5.4.7.

Fig. 5.10 shows that the median sensitivity of the SCUBA Legacy Catalogue would be sufficient to detect the majority of the Simon *et al.* (2006a) IRDC cores if they have temperatures greater than 10 K. At this temperature we would detect IRDC cores with peak contrast greater than 0.15. This corresponds to the approximate completeness limit of the Simon *et al.* (2006a) catalogue, where the turnover in peak contrast occurs. This completeness limit is clearly seen in Fig. 5.8. In our sample of 205 IRDCs within the SCUBA Legacy Catalogue 94% have peak contrast values greater than or equal to 0.15.

The IRDC cores that are not detected at 850 μm are thus consistent with being low temperature, low column density cores but below the 0.1 Jy pixel^{-1} noise cut we applied to the SCUBA Legacy Catalogue. Fig. 5.10 shows that if they are true clouds they are likely to

have temperatures less than 10 K. Almost none were identified with 24 μm MIPSGAL sources, corroborating our low temperature hypothesis and implying that they are either transient or potentially prestellar cores.

If we consider the cores not detected at 850 μm to be low temperature, low column density cores, this requires that they have a temperature less than $\sim$10 K, whereas the lowest contrast objects in the sample could have temperatures less than 14 K. Typical temperatures for IRDCs range from 8–25 K (Carey *et al.*, 1998; Teyssier *et al.*, 2002; Pillai *et al.*, 2006a; Peretto *et al.*, 2010). However as we do not know how IRDC cores are distributed in temperature we cannot know if we ought to have detected the majority of these objects or not. We therefore cannot rule out the presence of a cold faint transient or prestellar population within the SCUBA non-detected sample, particularly at low contrast values where SCUBA is least sensitive. Recent theoretical models (Stamatellos *et al.*, 2007) suggest that the temperature of prestellar cores may be lower than suspected ($\sim$5 – 10 K), which would place the 850 μm fluxes of the IRDC cores below our detection limit.

An alternative hypothesis is that a number of the cores not detected at 850 μm are a result of the absence of background mid-infrared emission rather than its extinction by intervening cold dust in an IRDC. In this case some of the cores not detected at 850 μm would be localised "holes" or local minima in the mid-infrared background misidentified as IRDCs. This possibility is more likely for the higher contrast cores not detected at 850 μm, as our temperature constraints for these objects mean that they are less likely to be prestellar. Artefacts may also be present as a result of the background subtraction process, which would result in false IRDC detections particularly in regions of complex emission (Simon *et al.*, 2006b). Without deeper sub-millimetre continuum or molecular line data it is difficult to satisfactorily determine whether an IRDC core identified by Simon *et al.* (2006a) and not detected at 850 μm is a true cloud, void or artefact.

5.4.3 Cores detected at 850 μm

We identified 154 cores detected at 850 μm within the area covered by the SCUBA Legacy Catalogue. These cores have higher peak contrast values (as seen in Fig. 5.7) and column densities than those cores not detected at 850 μm. Clearly as these objects are seen in sub-millimetre emission they are not voids or artefacts in the MSX contrast images. We determine estimates of the mass of the 33 cores in our sample with kinematic distances (see Section 5.2.3). The median mass of cores within the sample is 300 $M_\odot$, with a minimum mass of 50 $M_\odot$ and a maximum mass of 4,190 $M_\odot$ (assuming a dust temperature of 15 K). Our results are consistent with those of Rathborne *et al.* (2006), who observed the 38 highest contrast clouds from Simon *et al.* (2006b) at 1.2 mm, taking into account differences in sample selection, assumed temperature and in the measurement of integrated fluxes (Rathborne *et al.* 2006, fit Gaussians to their sample whereas the SCUBA Legacy Catalogue uses Clumpfind).

Are these masses consistent with high mass star formation within IRDCs? There is considerable uncertainty regarding the minimum mass core needed to form a high mass star. By considering the observed range in star formation efficiencies Thompson *et al.* (2006) estimated that a core mass of at least 30–200 $M_\odot$ would be required to form a 10 $M_\odot$ star. Observed values for high mass star forming cores range from 720 $M_\odot$ to 10^4 $M_\odot$ (Hatchell *et al.*, 2000; Mueller *et al.*, 2002). More recently Kauffmann *et al.* (2010b 2010), suggested an empirically

derived equation for the mass threshold of massive star formation: $m(r) \leq 870\,\mathrm{M}_{\odot}(r/\mathrm{pc})^{1.33}$. Based on this equation, IRDC cores with diameters ranging between $1-10\,\mathrm{pc}$ (Rathborne *et al.*, 2006), would require masses greater than $360-7{,}400\,\mathrm{M}_{\odot}$ respectively, to obey this observed threshold. Our sample of SCUBA detected IRDC cores falls at the lower end of this range. We thus conclude that the masses of the IRDC cores in our sample are sufficient to undergo intermediate to high mass star formation.

5.4.4 IRDC cores detected at 850 μm without 24 μm sources: could they be "starless" IRDCs?

Approximately two thirds of the IRDC cores detected at $850\,\mu\mathrm{m}$ that are located within the MIPSGAL survey area are associated with embedded $24\,\mu\mathrm{m}$ sources (48 cores or 69% of the sample). As shown in Section 5.3.4, we carried out KS tests of the peak contrast and column density distributions for SCUBA detected IRDC cores with and without associated $24\,\mu\mathrm{m}$ sources and found no evidence for the existence of two populations (see right histogram in Fig. 5.8). This implies that the IRDC cores detected at $850\,\mu\mathrm{m}$ with and without associated $24\,\mu\mathrm{m}$ sources originate from the same column density population. For the limited sample of cores with known kinematic distances (see Table B.3) no correlation was found between the presence of an embedded object at $24\,\mu\mathrm{m}$ and the mass of the IRDC core.

Given the similar properties of the cores with and without associated $24\,\mu\mathrm{m}$ sources, the two types of core may be differentiated by evolutionary state. Those cores without associated $24\,\mu\mathrm{m}$ sources represent an earlier "starless" evolutionary stage compared to IRDC cores that have formed intermediate or high mass Young Stellar Objects and are associated with $24\,\mu\mathrm{m}$ sources. A range of evolutionary stages have been observed in a handful of IRDCs (Rathborne *et al.*, 2008), which supports this hypothesis. In this picture the "starless" IRDC cores (i.e. those without associated $24\,\mu\mathrm{m}$ sources) represent the cold quiescent initial conditions for high mass star formation as suggested by Carey *et al.* (1998) and Simon *et al.* (2006a). The SCUBA detected candidate IRDC cores with associated MIPSGAL $24\,\mu\mathrm{m}$ sources would then represent a star forming population of IRDCs with embedded (proto) stellar objects, and so we refer to these as star forming IRDCs.

Alternative explanations are that the starless IRDC cores detected at $850\,\mu\mathrm{m}$ are sterile, possibly unbound and transient, condensations that may never go on to form stars, or that they are forming stars, but with luminosities too low to be detected by MIPSGAL. In order to address the likelihood of the former explanation in detail, we would need to determine the virial masses and gravitational stability of a large sample of the starless IRDC cores (via additional spectroscopy). However we note that the Jeans Mass for a core of similar temperature and number density to the starless cores ($\sim$15 K and $10^4\,\mathrm{cm}^{-3}$) is $20\,\mathrm{M}_{\odot}$. Decreasing the temperature or increasing the number density will decrease the Jeans mass. The minimum mass of our sample of cores detected at $850\,\mu\mathrm{m}$ (with or without associated $24\,\mu\mathrm{m}$ sources) is $50\,\mathrm{M}_{\odot}$. Allowing for uncertainties in our derivation of the mass we thus conclude that it is unlikely that many of the IRDC cores fall below this Jeans Mass and so the majority of the IRDC cores detected at $850\,\mu\mathrm{m}$ ought to at least have the potential for star formation, in the absence of other processes such as magnetic and turbulent support.

This approach implicitly assumes that the IRDC cores are single gravitationally bound objects. If instead they are composed of numerous smaller cores fragmented below the scale of

the JCMT beam then this conclusion may not apply. Higher resolution interferometry would be needed to resolve potential substructure within the IRDCs in this case (e.g. Rathborne *et al.* 2008).

5.4.5 MIPSGAL sensitivity to YSOs

To assess the likelihood of the latter explanation that the starless IRDC cores are forming stars with luminosities below the detection limit of MIPSGAL we need to determine the sensitivity of MIPSGAL to YSOs as a function of YSO luminosity. Fortunately, a series of studies carried out by the Spitzer c2d[5] survey team on nearby star forming regions allows us to characterise the 24 μm flux density to total internal YSO luminosity fairly well for low mass YSOs.

Low mass YSOs

Dunham *et al.* (2008) find an approximately linear relationship between the MIPS 24 μm flux and total internal luminosity for low mass YSOs detected in the Spitzer c2d survey (see Fig. 5.11). This was found to be consistent with the predictions of radiative transfer models of low mass YSOs (Crapsi *et al.*, 2008). From linear least squares fitting of observed data Dunham *et al.* (2008) obtained the following parameters (at 24 μm):

$$log(\nu f_\nu) = [(0.87 \pm 0.20)\, log(L) \; - \; (10.05 \pm 0.17)] \text{ erg cm}^{-1}\text{ s}^{-1} \tag{5.8}$$

This particular relationship was for a flux normalised to a distance of 140 pc. When we combine the previous equation 5.8 with the relationship $f_\nu \propto d^{-2}$ we find:

$$f_{24_{\mu m}} = \frac{1}{\nu}\left(10^{(log(L^{0.87})-10.05)}\right)\left(\frac{140^2}{d(pc)^2}\right)\left(10^{23}\right) \text{ Jy} \tag{5.9}$$

From equation 5.9 we plot flux density as a function of distance for differing YSO luminosities (see Fig. 5.12). This flux density luminosity relation presented here was obtained from observations of low mass YSOs by Dunham *et al.* (2008), unfortunately no such similar study exists for high mass YSOs.

High mass YSOs

To obtain a flux density to luminosity relation for high mass YSOs we use the empirical mid to far-infrared flux relation of Lumsden *et al.* (2002). This method assumes that the bolometric luminosity of a MYSO is predominantly reprocessed by dust and is emitted in the far infrared[6]. Lumsden *et al.* (2002) converts the far infrared flux (f_{IR} in W m^{-2}) it into a flux density at 21 μm ($f_{21\mu m}$ in W m^{-2} Hz^{-1}, approximately the MIPS wavelength) utilising the following empirical relationship:

[5]The Spitzer Space Telescope Legacy program: "From Molecular Cores to Planet-Forming Disks" (Evans *et al.*, 2003)

[6]from the flux luminosity relationship: L = $4\pi d^2 f$

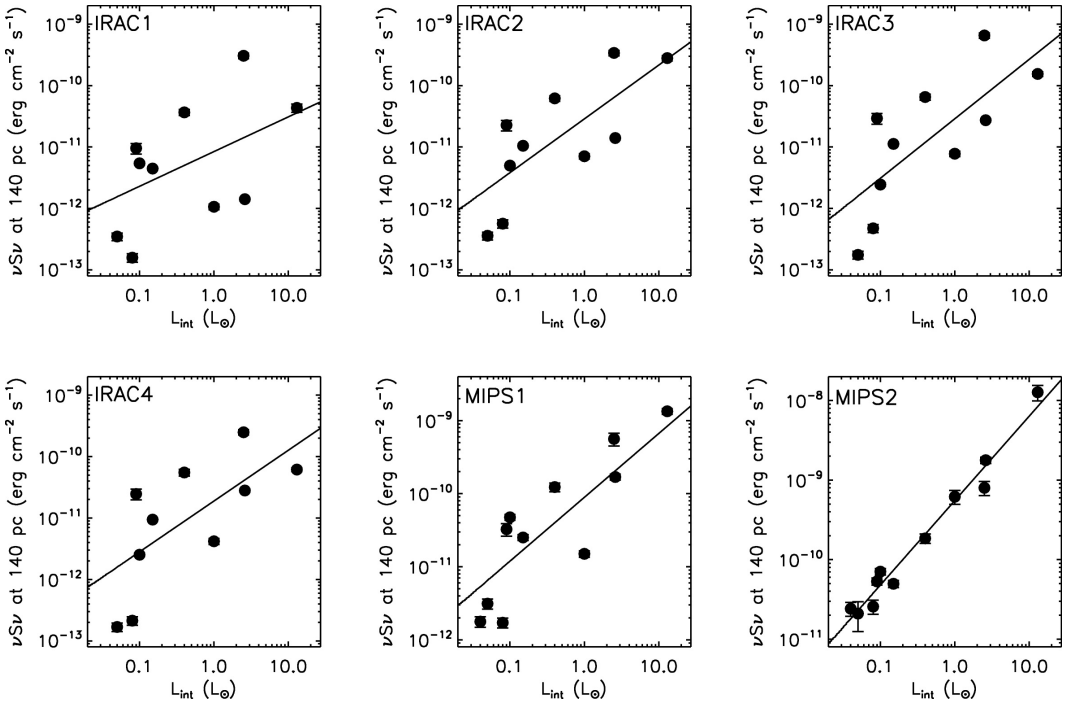

Figure 5.11: flux (flux density normalised for frequency and distance) versus luminosity (L_{int}) plots the for 11 embedded protostars observed by Dunham *et al.* (2008). From left to right, top to bottom: IRAC1 (3.6 μm), IRAC2 (4.5 μm), IRAC3 (5.8 μm), IRAC4 (8.0 μm), MIPS1 (24 μm), and MIPS2 (70 μm). The lines represent the results of linear least-squares fits at each wavelength (Dunham *et al.*, 2008).

$$f_{IR} \,/\, f_E = R \tag{5.10}$$

where R ranges between 5 and 40, and f_E is the MSX E band flux. To get the flux density we divide f_E by the MSX E band width $(4.03 \times 10^{12}\,\mathrm{Hz})$[7]:

$$f_{21\mu m} = 4.041 \times 10^{-14} \,/\, f_E \,\mathrm{Jy} \tag{5.11}$$

We plot this high mass relationship between flux density and distance (corrected for estimates of the 24 μm extinction of the IRDCs) for a range of YSO luminosities as a function of distance in Fig. 5.12.

Uncertainties

Uncertainties in Fig. 5.12 result from uncertainties in extinction and in the relationships between flux and luminosity as taken from Lumsden *et al.* (2002) and Dunham *et al.* (2008). The main source of error in Dunham *et al.* (2008) is the uncertainty in the relationship between flux and luminosity which were obtained from observations as well as theoretical models. This uncertainty is depicted in Fig. 5.12 by the shaded region in the plots to the left. The primary source of error in Lumsden *et al.* (2002) is due to the large range in observed flux ratio. This uncertainty is depicted in the middle and right plots with the lower estimate in the middle plots and the upper estimates in the plots on the right. From Fig. 5.12 we see that the relationships taken from Lumsden *et al.* (2002) and Dunham *et al.* (2008) are consistent with each other particularly the plots to the right and in the middle of Fig. 5.12.

The quoted 5σ point source sensitivity of MIPSGAL is 1.7 mJy at 24μm (Carey *et al.*, 2007). This limit will obviously vary from region to region depending upon the strength of the background emission and complexity of structures in the images. However the IRDCs presented here in general have low 24μm backgrounds and are relatively free from source crowding, hence we assume the given 5σ limit is valid, which is show in Fig. 5.12 by a dashed horizontal line.

Extinction

The effect of extinction from the environments surrounding the cores and from material contained within the cores themselves is to lower any observed radiation emitted from within. With these starless IRDC cores having high column densities ($\sim 2 \times 10^{22}\,\mathrm{cm}^{-2}$ from 8 μm and 850 μm data) and hence high opacities there are three possible situations we should consider for the flux that is observed: *i)* there may be no extinction *ii)* there may be a medium amount of extinction (taking this from the lower of the quoted column densities derived from the 8 μm data: $2.10 \times 10^{22}\,\mathrm{cm}^{-2}$) *iii)* there may be high extinction (taking this from the higher of the quoted column densities as derived from the 850 μm data: $1.76 \times 10^{23}\,\mathrm{cm}^{-2}$).

We consider the effects of extinction on the MIPSGAL sensitivity using the following relationship as outlined in Mitchell *et al.* (2001) and references therein:

[7] $1\,\mathrm{Jy} = 10^{-26}\,W\,m^{-2}\,Hz^{-1} = 10^{-23}\,erg\,s^{-1}\,cm^{-2}\,Hz^{-1}$

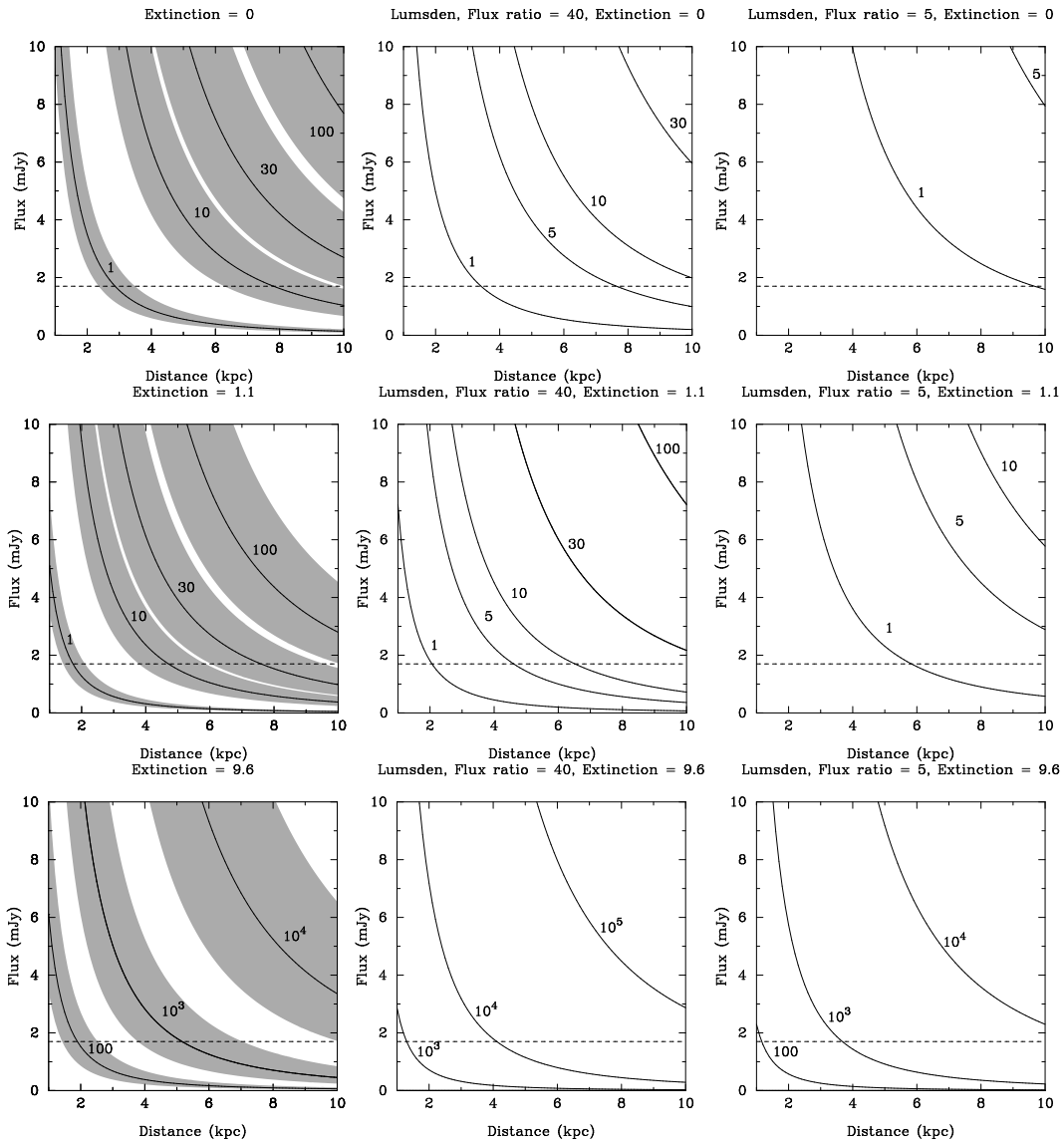

Figure 5.12: Left Plots: based on relationship between flux and luminosity, from observations and theoretical models as produced in Dunham *et al.* (2008). The shaded regions depict the uncertainty in this relationship. Middle and Right Plots: based on flux luminosity relationship published by Lumsden *et al.* (2002). Lower and upper estimates of flux for particular luminosities are plotted in the middle and right plot respectively. This range in flux originates from an observed range in F_{FIR}/F_E ratio which ranges from 5-40. The middle plot takes the value of 40 and the right plot takes the value of 5. Plots from top to bottom vary in A_{24}, from no extinction in the left to high extinction in the right plot. Labels in each plot denote the different luminosities, i.e. $1\,L_\odot$, $10\,L_\odot$, $30\,L_\odot$ and $100\,L_\odot$. The dashed horizontal line is the $5\,\sigma$ point source sensitivity of MIPSGAL at $24\,\mu$m.

$$R = A_v/E(B-V) \tag{5.12}$$

where R is the ratio between visual extinction (A_v) and colour excess ($E(B-V)$) and has been shown to be 3.1 by Rieke and Lebofsky (1985). The colour excess can be used to derive a column density from:

$$N_{H+H_2}/E(B-V) = 5.8 \times 10^{21}\,\mathrm{atoms\,cm^{-2}\,mag^{-1}} \tag{5.13}$$

found empirically by Bohlin *et al.* 1978. If we assume the extinction is such that all the hydrogen is in its molecular form and $N(H+H_2)\,\mathrm{atoms} = 2N(H_2)\,\mathrm{atoms}$, then we find:

$$A_v = N_{H_2}/9.4 \times 10^{20}\,\mathrm{mag} \tag{5.14}$$

The visual extinction in the previous equation, can be converted to K-band extinction (A_k) using the relationship:

$$A_v/A_k = 8.9 \tag{5.15}$$

published by Rieke and Lebofsky (1985) and then converted again to 24 μm extinction (A_{24}) using the relationship (Flaherty *et al.*, 2007):

$$A_{24}/A_k = 0.44 \pm 0.02 \tag{5.16}$$

combining the last five equations we derive a formula for A_{24}, in terms of column density:

$$A_{24} = N_{H_2}/1.9 \times 10^{22}\,\mathrm{mag} \tag{5.17}$$

If we apply this equation to the situations from before: *i)* no extinction, $A_{24} = 0$ *ii)* where there may be a medium amount of extinction ($2.10 \times 10^{22}\,\mathrm{cm^{-2}}$) we obtain $A_{24} = 1.1$. *iii)* where there may be high extinction ($1.76 \times 10^{23}\,\mathrm{cm^{-2}}$) we obtain $A_{24} = 9.6$. These last two values correspond to A_v of 23 and 194 respectively.

Taking typical values for $N(H_2)$, from Table B.1 ($10^{22}\,\mathrm{cm^{-2}}$), we see that the approximate extinction at 24 μm will be 1 mag. Using Pogson's equation[8] this equates to a reduction in flux by a factor of 2.5 at 24 μm. The luminosities found by Dunham *et al.* (2008) and Lumsden *et al.* (2002), taking interstellar extinction into account, imply that MIPSGAL is sensitive down to intermediate mass stars but is not sensitive to low mass stars ($< 2\,M_\odot$, Iben 1965). Although no emission is seen at 24 μm this is consistent with these stars having low masses and being simply not bright enough to be detected by MIPSGAL.

The effect of the differing extinction can be seen in Fig. 5.12 in which the top graphs are for no extinction, the middle graphs take the medium extinction case ($A_{24} = 1.1$), and the bottom graphs assume high extinction ($A_{24} = 9.6$). Errors on these estimates (obtained using the propagation of errors method) are of the order of ∼40%, predominantly resulting from

[8] $m - n = 2.5\log(f_n/f_m)$

the uncertainty in the empirically derived conversion from $N(H+H_2)/E(B–V)$ (Bohlin *et al.*, 1978).

Given the typical distance of IRDCs within our Galaxy (∼4.5 kpc; see Fig. 6 in Marshall *et al.* 2009), for the 'worst case scenario' MIPSGAL should be complete to embedded objects with luminosities above ∼1,000 $L_\odot$ (when high mid-infrared extinction is considered; $A_{24} = 9.6$, $A_v = 194$). This completeness limit indicates that it is not possible to rule out the presence of intermediate and low mass YSOs. From Iben (1965) we find that in the protostellar stages of evolution a star with a final main sequence mass $< 5\,M_\odot$ will never reach luminosities greater than 1,000 $L_\odot$. Greater constraints on the column densities of these objects are required to allow us to have a better handle on the potential luminosities of these cores and determine if indeed they are a low mass population of cores.

5.4.6 The lifetimes of starless and star forming IRDCs

From the previous section we have suggested that the starless cores may be evolutionarily related to those SCUBA detected cores associated with 24 μm objects but with luminosities below the detection limit of MIPSGAL. Going one step further we may assume that the starless and star forming SCUBA detected IRDCs are at different evolutionary stages in the formation of high mass stars and so we can estimate the statistical lifetime of the starless quiescent phase. If each starless IRDC core evolves into a corresponding star forming IRDC core with one or more embedded 24 μm source then the relative proportions of these objects in the sample should reflect the statistical life time of each phase. In the sample of SCUBA detected IRDCs lying within the MIPSGAL survey area we find twice as many star forming IRDC cores with 24 μm sources than starless IRDC cores. Thus if these two types of object do form an evolutionary sequence we would expect the starless phase to last half the lifetime of the star forming phase.

Estimates for the absolute lifetime of the embedded phase of high mass star formation range from 10^4–10^5 years for UCHII and embedded YSOs (Wood and Churchwell, 1989a,b), a few 10^4 years for methanol masers (van der Walt, 2005), and 1.2–7.9×10^4 years for embedded high mass protostars (Motte *et al.*, 2007; Pestalozzi *et al.*, 2007; Mottram *et al.*, 2011).

Taking the upper and lower bounds of these estimates we conclude that the starless phase of IRDCs, as an upper limit due to our assumption on evolution, last a few 10^3–10^4 years. A higher proportion (65%) of IRDC cores in the quiescent phase was reported by Chambers *et al.* (2009), although this was primarily due the additional constraints on what was classed as an active/star forming core (i.e. emission at 4.5 μm). By examining the results by Chambers *et al.* (2009) and using the same classification scheme used in this work (detection at 24 μm) we find a similar proportion of cores in the quiescent phase (38%). This proportions of starless and star forming IRDCs are consistent with the proportion of massive infrared quiet high mass protostars to the massive protostellar stage as found in the Cygnus X GMC by Motte *et al.* (2007). The lifetime of the starless IRDC phase is comparable to that found for the infrared quiet protostellar phase by Motte *et al.* (2007) who calculated the statistical lifetimes based on the proportion of massive infrared quiet high mass protostars to the massive protostellar stage as found in the Cygnus X GMC. Our statistical lifetime estimate for the starless IRDC phase is also approximately one to two orders of magnitude quicker than the extended lifetime of the low mass Class 0 evolutionary phase recently calculated by Evans *et al.* (2009).

Caution must be applied to comparing the estimated lifetime of starless IRDCs to the estimated lifetime of the high mass pre-stellar phase. As shown by Motte *et al.* (2007) for Cygnus X there are no high mass starless cores, which implies an age of less than 10^3 years for this phase. The "starless" IRDCs that we identify from their mid-infrared quietness may yet display other signs of star formation such as molecular outflows or methanol masers which would imply that they have a proto-stellar nature. This may be supported by the fact that their statistical lifetime is similar to the high mass proto-stellar phase identified by Motte *et al.* (2007). These "starless" cores may also be concealing intermediate mass stars by their high extinction. Future investigations of these clouds to search for tracers of high mass star formation are needed to estimate the lifetimes of the pre-stellar and proto-stellar phases found within these clouds. A number of forthcoming Galactic Plane surveys have these aims, such as the Methanol Multi Beam Survey (MMB; Green *et al.* 2009), the CORNISH[9] 5 GHz survey (Purcell *et al.*, 2008), the Herschel Hi-Gal Survey (Molinari *et al.*, 2005), and the JCMT Legacy Surveys SASSy and JPS (Thompson *et al.*, 2007; Moore *et al.*, 2005), see Section 5.4.7. Additionally if the cores go on to form clusters or groups of stars this would cause this lifetime estimate to lengthen as age estimates for the pre-stellar phase are increase with decreasing mass. Nonetheless we have shown that the lifetime of a quiescent (before it shows evidence of activity in the mid-infrared) IRDC is approximately half of that spent in the embedded phase.

It is possible to compare the lifetime we derive to those recently derived by Kim *et al.* (2010) who investigated YSOs within IRDCs (using the catalogue by Simon *et al.* (2006a) as well as other IRDCs reported within the literature: 13,650 IRDCs in total). Kim *et al.* (2010) found the fraction of IRDCs containing YSOs (using GLIMPSE, MSX and IRAS) was 34% (4,098/13,650), yielding a IRDC statistical lifetime of $10^4 \sim 10^5$. This is a much lower fraction and therefore larger than our result. Kim *et al.* (2010) attempted to explain this discrepancy by citing an investigation by M. Kim et al in prep who found that 30% of 24 μm sources in MIPSGAL are either Galaxies or AGB stars as opposed to early YSOs. Peretto and Fuller (2009) find 20-60% of IRDCs identified using Spitzer GLIMPSE and MIPSGAL data have associated 24 μm sources.

5.4.7 Predictions and implications for Galactic Plane surveys

The astronomical community are planning a number of uniform and sensitive surveys of the Galactic Plane in the far infrared and sub-millimetre that will detect a large number of the Simon *et al.* (2006a) IRDC catalogue in emission. We use the results drawn from the SCUBA Legacy Catalogue to make predictions for the number of IRDCs that will be detected by four surveys in particular: SASSy, the SCUBA-2 "All Sky" Survey (Thompson *et al.* 2007; Mackenzie *et al.* 2010), JPS, the JCMT Galactic Plane Survey (Moore *et al.*, 2005), Hi-GAL, the Herschel Infrared Galactic Plane Survey (Molinari *et al.*, 2005), and ATLASGAL the APEX Telescope Large Area Survey of the Galaxy (Schuller *et al.*, 2009). Each of these surveys will cover much larger regions of the plane than the SCUBA Legacy Cataogue and will be both deeper and more uniform, resulting in a much more unbiased survey of IRDCs that is free from the targeted and non-uniform nature of the SCUBA Legacy Catalogue. Fig 5.13 shows a region of the Galactic Plane with the coverage area of the SCUBA Legacy Catalogue

[9]The Co-Ordinated Radio 'N' Infrared Survey for High-mass star formation, Purcell *et al.* (2008)

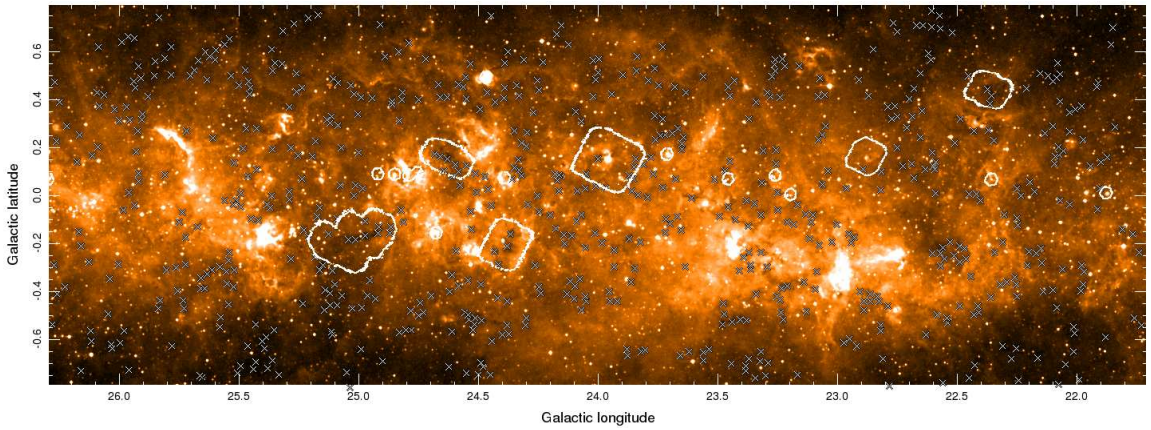

Figure 5.13: Image of a region of the Galactic plane. MSX 8 μm image with SCUBA coverage area contours overlaid. The crosses mark the locations of potential IRDC cores as catalogued by Simon *et al.* (2006a).

and the positions of Simon *et al.* (2006a) IRCDs, which clearly indicate the potential of these large area surveys to detect a large number of IRDCs.

As each of these surveys will detect IRDC cores by their emission rather than their extinction against the galactic mid-infrared background this means that they will also be sensitive to IRDCs located on the far side of the Galaxy that were not detected by Simon *et al.* (2006a). The forecast 1 σ sensitivities of Hi-GAL and JPS are 20 mJy beam^{-1} and 4 mJy beam^{-1} at 250 μm and 850 μm respectively, which are sufficient to detect cores of only a few tens of $M_{\odot}$ at 20 kpc (assuming 20 K dust with β=2 and a mass coefficient of 50 g cm^{-2}). SASSy and ATLASGAL will have 1 σ sensitivities of 30 mJy beam^{-1} and 50-70 mJy beam^{-1} at 850 μm which could detect cores of a few hundred $M_{\odot}$ out to 20 kpc. Taking the masses of known IRDC cores into consideration each of these surveys has the potential to detect these objects at the far side of the Galaxy. In addition, as we have shown in Section 5.4.2, the deeper surveys may find the low column density low temperature clouds that were not detected at 850 μm in the SCUBA Legacy Catalogue. Thus as well as the increased number of detections resulting from surveying a larger area of the plane, we expect that the surveys will also detect a greater number of 'IRDC cores' on the far side of the Galaxy and the colder population that we have not detected with SCUBA.

Estimating an upper limit to the number of IRDC cores that could be detected by the surveys is difficult. For the IRDC cores located on the far side of the Galaxy that have foreground emission preventing them being detected by Simon *et al.* (2006a), we may estimate their number by geometric means and considering the volume of the Galaxy probed by MSX. Following the argument presented by Rathborne *et al.* (2006) we estimate that the total number of IRDC cores in the Galaxy may be up to a factor of 3 greater than those detected by Simon *et al.* (2006a). To this number must be added an uncertain quantity of low column density cores whose intrinsic contrast falls below the Simon *et al.* (2006a) criteria for detection but whose column density is great enough to be detected by the surveys (particularly Hi-GAL and JPS). We see from Fig. 5.14 that the steep turnover of IRDC cores at low contrast values may indicate that the catalogue is incomplete at low contrasts. Without further information

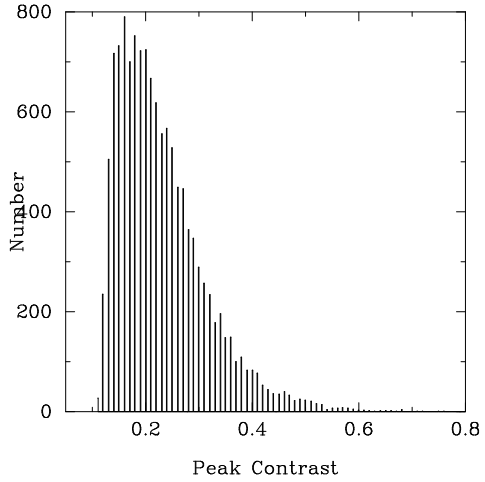

Figure 5.14: Number distribution of IRDC cores with peak contrasts, values taken from Simon *et al.* (2006a).

on the general temperature distribution of IRDCs it is not possible to place firm limits on the number of such cores and so whilst we note that the deeper surveys will detect this colder population (and Hi-GAL will determine the temperature distribution of IRDC cores) we do not include them in our estimate.

This lack of a temperature distribution also means that we cannot take the column densities estimated from the MSX 8 μm data (as contained in Table B.1) and convert these into flux estimates, as the lack of temperature information renders these into rather loosely determined upper flux limits. In addition the large uncertainties in grain properties, the 8 μm extinction law and contamination from foreground emission introduce a considerable scatter between column densities derived from 8 μm and 850 μm (see Section 5.2.3). We thus estimate lower limits for the detection rate of IRDC cores within the surveys by using the SCUBA detection fraction shown in Section 5.4.1. SASSy, JPS and Hi-GAL are deeper than the SCUBA Legacy Catalogue and so we expect these surveys to detect a greater fraction of IRDC cores, particularly at low contrast values where the surveys are more sensitive to low temperature low column density cores (see Fig. 5.10). Without knowing the temperature distribution of IRDC cores it is impossible to determine exactly what this fraction is, but given the greater sensitivities of these surveys they ought to detect at least the fraction of IRDC cores that SCUBA did. The depth of ATLASGAL is similar to the 0.1 Jy pixel^{-1} noise cut that we applied to the SCUBA Legacy Catalogue and thus ATLASGAL should detect a similar fraction of IRDC cores from Simon *et al.* (2006a).

Based upon detection fractions and the geometric argument of Rathborne *et al.* (2006) we estimate the number of IRDC cores, as catalogued by Simon *et al.* (2006a) that should be observed in current/future Galactic Plane surveys. ATLASGAL will survey the inner third of the Galactic Plane ($|l| < 60^\circ$ and $|b| < 1.5^\circ$), within which there are 11,529 IRDC cores from the Simon *et al.* (2006a) catalogue. Taking the SCUBA detection fraction of 75% we predict that ATLASGAL will detect at least 8,600 IRDC cores. We scale this number by

Survey	Coverage	IRDC cores	
		in area	predicted
ATLASGAL	$\|l\| < 60^\circ$ & $\|b\| \leq 1.5^\circ$	11,529	26,000
Hi-GAL	$\|l\| < 60^\circ$ & $\|b\| \leq 1^\circ$	10,644	24,000
SASSy*	$0^\circ < l < 245^\circ$ & $\|b\| \leq 5^\circ$	6,160	14,000
JPS	$10^\circ < l^{**} < 65^\circ$, $102.5^\circ < l^{***} < 141.5^\circ$ & $\|b\| \leq 1^\circ$	4,095	9,000

Table 5.2: Predictions for the number of IRDC coress, as catalogues by Simon *et al.* (2006a), likely to be detected in each survey based upon our detection fraction of 75% and the geometric argument of Rathborne *et al.* (2006). *The initial coverage area. **Covering the GLIMPSE-N region. ***Covering the FCRAO Outer Galaxy Survey region.

the geometric argument[10] of Rathborne *et al.* (2006) to estimate the number of cores that ATLASGAL will detect on the far side of the Galaxy and hence estimate that ATLASGAL may detect up to 26,000 IRDC cores. This is consistent with the preliminary results of the first 95 deg^2 of ATLASGAL which detects ∼6,000 sources, many of them infrared dark (Schuller *et al.*, 2009). These predicted values for ATLASGAL, and also Hi-GAL, SASSy, and JPS are presented in Table 5.2. By number we see that the predicted numbers of IRDC cores that ATLASGAL and Hi-GAL are expected to observe are higher than SASSy[11] and JPS, due to the larger area covered by these surveys. JPS and SASSy will however explore relatively unique parameter spaces. The high sensitivity JPS ($1\sigma \sim 4\,\mathrm{mJy\,beam^{-1}}$ at 850 μm) will be ideal for identifying the most low temperature low column density IRDC cores, as well as being able to go some way to investigating the issue of the origin of IRDC core candidates without detected 850 μm emission (as discussed at the end of Section 5.4.2). SASSy in contrast to the other surveys will have the benefit of observing greater latitudes of the Galactic Plane than any other survey and (as with JPS) will observe the outer Galaxy where low mid infrared backgrounds have restricted previous identifications of 'IRDCs' due to their selection bias.

5.5 Summary and Conclusions

From positional cross matching of the IRDC catalogue produced by Simon *et al.* (2006a) with the coverage area of the SCUBA Legacy Catalogue (as published by Di Francesco *et al.* 2008) we have identified candidate IRDC cores with and without associated 850 μm emission. Column densities were derived from the MSX 8 μm data by applying an extinction law to the peak contrast values (as defined by Simon *et al.* 2006a). For those cores that were associated with 850 μm emission, column densities were also derived assuming spherical geometry and the method of Hildebrand (1983). From our findings outlined within this paper we make the following conclusions:

1. We find 154 cores with 850 μm detected emission and 51 cores without 850 μm emission. Those cores associated with detectable 850 μm emission had a median peak contrast

[10]Sources within the solar circle at the near kinematic distance occupy one-third the area of sources at the far kinematic distance (Rathborne *et al.*, 2006)

[11]When considering the initial coverage area, see Table 5.2

value of 0.32, a median column density of $1.7\times10^{22}\,\mathrm{cm}^{-2}$ and a median mass of $300\,\mathrm{M}_{\odot}$. We found that the overall detection fraction of IRDC cores with $850\,\mu$m emission is 75%, a lower limit which is in good agreement with the CS detection rate of Jackson *et al.* (2008b).

2. Those cores without $850\,\mu$m emission are found to have no significant difference in peak contrast distribution than those cores detected at $850\,\mu$m. These cores are likely to be a population of low temperature low column density transient or prestellar cores. However, a small number of these cores could also be "holes" in the background mid-infrared continuum emission or artefacts as a result of the identification procedure. Further observations of the cores not detected at $850\,\mu$m, either through deeper sub-millimetre continuum data or molecular line data, are required to yield insight into the true nature of these objects.

3. Those cores detected at $850\,\mu$m have a range in mass of $50-4,190\,\mathrm{M}_{\odot}$, consistent with the lower mass end range observed in high mass star forming regions. Of these cores detected at $850\,\mu$m, 69% are found lying within the MIPSGAL survey area associated with an embedded object at $24\,\mu$m. A KS test gave no indication for the existence of two populations. This could suggest these cores are related evolutionarily. Those cores detected at $850\,\mu$m without $24\,\mu$m sources could be "starless" IRDCs or they may be forming stars but with luminosities too low to be detected. An alternative explanation for their origins are that they are unbound condensations that may never go on to form stars. To make more detailed conclusions about the nature of the SCUBA detected cores and their embedded mid-IR sources requires a deeper understanding of their physical properties from follow up molecular line mapping.

4. Based on the assumption that the "starless" and star forming cores are related evolutionarily we derive an upper limit of 10^3-10^4 years for the lifetimes of starless IRDC cores. This lifetime is found to be comparable to the infrared quiet protostellar phase by Motte *et al.* (2007) and is approximately one to two orders of magnitude less than the extended lifetime of the low mass Class 0 evolutionary phase recently calculated by Evans *et al.* (2009).

5. Based on SCUBA detection rates found, conservative predictions are made to lower limits of the number of IRDC cores that the Galactic Plane surveys ATLASGAL, Hi-GAL, SASSy and JPS will potentially detect: 8,600, 8,000, 4,600 and 3,000 cores respectively. If we apply geometric arguments to these values to scale to the number of such cores in the far Galaxy (Rathborne *et al.*, 2006) we see that ATLASGAL, Hi-GAL, SASSy and JPS have the potential to observe up to 26,000, 24,000, 14,000 and 9,000 infrared dark cores respectively throughout the Galaxy.

We are now entering into an exciting time for sub-millimetre and far infrared astronomy with the advent of Herschel and SCUBA-2. These two instruments will drive the observational investigations of IRDCs, and in turn will yield fresh insight into the role they may play in massive star formation.

Chapter 6

Conclusions

'I may have not gone where I intended to go, but I think I ended up where I needed to be'
Douglas Adams

The overarching aim of this thesis was to look at massive star formation from a dense clump/core perspective within the W51 GMC and in IRDCs. Past observations have shown that these two types of molecular clouds have the ability to produce massive stars, through observations of OB associations, HII regions, hot cores and maser emission. Further understanding of how the dense molecular content within these clouds go on to form stars is needed to fully understand how massive stars form. The approach used in this thesis, was to study large populations of these objects to enable conclusions to be made based on global properties. In particular I studied clumps and cores within GMCs and IRDCs, known sites of massive star formation. To this extent the dense molecular clumps located within the W51 GMC as mapped by HARP and the IRDC cores identified within the SCUBA Legacy Catalogue using MSX data were examined. The aims of this Thesis are outlined in Chapter 1 section 1.7.

6.1 Summary and main results

This investigation began with new high resolution and high S/N molecular observations of the entire W51 GMC using the HARP instrument on the JCMT. Observations of ^{12}CO, ^{13}CO and C^{18}O (3 – 2) were made to enable a study of the dense molecular content of this GMC. These observations were presented in Chapter 3. The W51 GMC was chosen as a result of its credentials as one of the most massive GMCs within the Galaxy, with a high star forming efficiency and a starburst-like history. Past studies have been hampered by its structural complexity, lying at the tangential point of the Sagittarius arm combined with its distance of ∼6.5 kpc. From the HARP observations I was able to produce a new catalogue of dense clumps within the W51 GMC that have been detected in ^{13}CO (3 – 2) and identified using the CLUMPFIND algorithm. From this I identified 1575 dense clumps of which 1130 are associated with the W51 GMC (defined as having emission $> 56\,\mathrm{km\,s^{-1}}$, a definition taken from Carpenter and Sanders (1998)). Catalogues of these clumps are given in Tables A.2 and ??.

In Chapter 4 the catalogues produced in Chapter 3 were utilised, along with the methods outlined in Chapter 2, to obtain physical properties. Excitation temperatures (12 K), column densities (5.6×10^{21} cm^{-2}), surface densities (0.02 g cm^{-2}) and masses (90 M$_\odot$) were derived for the dense molecular clumps observed. Summing the masses of the clumps observed we find the W51 GMC has a mass reservoir of 1.5×10^5 M$_\odot$. From this we find a CFE of 14% (slightly lower for the W51 complex and slightly higher for the HVS). Using the Virial mass estimate I found 4% of cores by mass to be super-critical which would then push a CFE for super-critical clumps down to 0.5% for the W51 GMC an order of magnitude less than the current SFE of the region, indicating star formation will diminish in the future. The CMD for the W51 GMC was found to be described by a single power law described by an exponent $\alpha = 2.4^{+0.2}_{-0.1}$. Both the W51 complex and the HVS were found to be best described by this single power law within the errors. This power law is consistent with the upper end of double power laws for other star forming regions, the difference with the W51 GMC being that at such a large distance we are tracing larger and more massive structures and can only realistically fit a power law to higher mass clumps. The detection of molecular outflows within this GMC indicates that region is host to current active forming stars. A total of 14 outflow sites were identified by eye with the aid of GAIA-3D with a concentration of outflows towards the W51A region. I ended this chapter by considering the distribution of super critical clumps, molecular outflows and young stellar clusters. The super critical clumps were found to be spread across the GMC region. The young clusters were also found to be distributed throughout the region but by eye no correlation was seen between the location of either of these classes of objects.

Finally in Chapter 5, IRDC core candidates identified by MSX (Simon *et al.*, 2006a) from 8 μm extinction were investigated using the SCUBA Legacy Catalogue. Of those IRDC candidate cores identified it was found that 153 had detectable emission at 80 μm, 75% of the population. Again I obtained physical properties of these objects, and upper limits to those cores without detectable 850 μm emission, using the methods outlined in Chapter 2. Of those cores located within the MIPSGAL area 69% are found associated with an embedded object at 24 μm. These associations are taken to be indicative of star forming activity, whilst those cores without associated 24 μm emission are deemed to be in a 'starless' phase of evolution. The catalogues of these cores are given in Tables B.1 and B.2 with mass estimates, to those cores with distance estimates, given in Table B.3. I then ended the chapter with predictions for the number of IRDC cores that current/future surveys undertaken may increase known IRDCs up to. These estimates were based on coverage areas with values between 9,000 (from JPS) up to 26,000 cores (based on ATLASGAL, with current detection fraction and geometric arguments).

6.2 Conclusion

Before this study the W51 GMC was known as a region of starburst-like activity that occurred within the past 3 Myr (Okumura *et al.* 2000; Kumar *et al.* 2004; Clark *et al.* 2009) throughout the entire complex (HII regions well distributed). Before this study it was unclear how the *future* star formation would progress within the region. Carpenter and Sanders (1998), discussed the possibility of further star formation induced by the passage of the spiral density wave. Kang *et al.* (2010) in contrast reported that star formation within the W51 GMC was currently undergoing a particularly active phase of star formation (by an order of magnitude

in the SFE) compared to an assumed average for the lifetime of the GMC, indicating that this level of star formation would be unlikely to be sustained. Our main conclusions with respect to star formation within the W51 GMC is that star formation within the W51 GMC is likely to *diminish* as we observe a decrease in SFE for super-critical clumps. W51 is showing signs of current star formation, with 14 outflows identified within one region, with velocities observed similar to those reported by Beuther *et al.* (2002). From observations of the locations of the clusters, outflows, and super-critical clumps, it is unclear whether star formation will continue in a distributed manner or will be confined to few locations within the GMC.

Alongside the evidence for current star formation within the W51 GMC, surface densities were found below the accepted surface density threshold ($1\,\mathrm{g\,cm^{-2}}$) for forming massive stars. This result is consistent with findings by Elia *et al.* (2010) and Roy *et al.* (2011), indicating that this result is independent of method, with low surface density values perhaps reflecting the time-dependant threshold.

From the study of IRDCs the main conclusions is that those candidate IRDC cores not detected at $850\,\mu$m are likely to be a population of diffuse cores or holes/artefacts. Based on detection fractions it was possible to make tentative estimates on the number of IRDC candidates likely to be observed by current and future facilities and it is already possible to see the potential of these facilities, i.e. 22 IRDCs observed within Hi-GAL survey during the science demonstration phase Peretto *et al.* (2010). Finally it was found that over two thirds of IRDC core candidates with associated $850\,\mu$m detections were associated with $24\,\mu$m MIPS objects, providing a statistical lifetime of $10^3 - 10^4$ for the IRDC starless cores.

This Thesis has sought to understand the early stages of massive star formation by utilising sub-millimetre observations of the clumps and cores from which they may ultimately form. Despite searching in two different classes of molecular clouds, the W51 GMC with a total mass of $10^6\,\mathrm{M_\odot}$ and $\sim$100 pc in length in contrast to IRDCs, known to have masses on the order of $10^4\,\mathrm{M_\odot}$ and sizes on the order of $\sim$5 pc. By comparing our results from the two classes of molecular cloud(s) we find column densities for the W51 GMC clumps were consistently lower than the IRDC cores ($10^{21}\,\mathrm{cm^{-2}}$ as opposed to $10^{22}\,\mathrm{cm^{-2}}$). This result however may be affected by the fact that the molecular line data was sensitive down to $\sim 7\times10^{20}\,\mathrm{cm^{-2}}$ in comparison to the $850\,\mu$m data which was sensitive down to $\sim 8\times10^{21}\,\mathrm{cm^{-2}}$ and differences in methods used, depletion, as well as biases to IRDCs observed (selection based on observations by SCUBA).

Despite the inherent difficulty in comparing both the W51 GMC clump data and the IRDC core data I note that with masses ranging between $50-4{,}190\,\mathrm{M_\odot}$, and a median of $300\,\mathrm{M_\odot}$ the IRDC cores are found to be more massive than the clumps observed within the W51 GMC (ranging between $10-1{,}700\,\mathrm{M_\odot}$, with a median $90\,\mathrm{M_\odot}$). Without having further information on the current star formation indicators e.g. molecular outflows, in the W51 GMC it is difficult to compare how the two classes of cloud compare with regards to star forming activity. We find 1% of W51 GMC clumps by number are super-critical and 30% of IRDC cores by number are associated with embedded $24\,\mu$m MIPS objects. Although not a like for like comparison we see more evidence for star formation occurring within the IRDC cores than the W51 GMC clumps.

6.3 The future

From the work presented in this Thesis there are clearly several recommendations for future studies, particularly in light of developments in astronomical facilities. I outline these ideas below:

- **Comprehensive study of outflows in the W51 GMC**
  Chapter 4 presented a brief look at outflows present within the a region of the W51 GMC. The distance and complexity of the region has prevented such an in-depth study to be presented in this Thesis but a full investigation into outflows within the W51 GMC is highly desirable, if not challenging. The potential of GAIA-3D as a tool for the identification of these outflows was demonstrated, particularly in Fig. 4.13. To aid in this investigation higher angular resolution observations would be desirable to spatially resolve individual outflows. Once the outflows and the material associated with them have been identified it will be possible to obtain momentum (p) and energy (KE) estimates for the GMC[1].

- **Constrain candidate IRDC cores not detected at 850 μm**
  The true nature of the candidate IRDC cores identified by Simon *et al.* (2006a) not detected at 850 μm is unknown, the may be true clouds, or may result from voids or artefacts. Follow up observations in ^{12}CO could either confirm their presence or at least improve on the current lower column density limit of these candidate cores.

- **Search for deeply embedded objects in the 'starless' IRDC cores**
  The question "are the starless cores truly starless?" arose in Chapter 5 and answering this question would impact on age estimates derived within that chapter. This question may be tackled by using Herschel 70 μm data. to look for cooler embedded objects than traced by Spitzer 24 μm. This question may also be tackled by fitting SEDs to the individual cores using Herschel data.

- **Obtain physical properties for the embedded and starless IRDC cores**
  KS test showed embedded and non-embedded cores came from the same population, an indicator that the non-embedded population are precursors to the embedded cores with this non-embedded phase being relatively long lived according to the statistics (69% more numerous). To investigate, further line observations to a sample of these cores have been taken of the embedded (ten observed) and starless (ten observed) IRDC cores primarily to search for trends within the data. The molecules observed include CO (3–2) to search for outflows, HCO+and H^{13}CO+ (3–2) to search for signs of infall motions (Mardones *et al.*, 1997), and HNC and HCN to study the chemical history of cores (it is understood that cores subject to heating show HNC/HCN ratios much smaller than unity whereas cores with a history of cold gas display large HNC/HCN ratios Tennekes *et al.* (2006).

[1] where $p = MV_{char}$ and $KE = \frac{1}{2}MV_{char}{}^2$ where V_{char} is the characteristic velocity estimated to be the difference between the systemic velocity and the maximum velocity extent of the outflow (e.g. Buckle *et al.* 2010)

Appendix A

The W51 dense molecular clump catalogue

A.1 Clumps with with velocities $< 56\,\mathrm{km\,s^{-1}}$

Table A.1: Properties for the 445/1575 clumps identified by CLUMPFIND within the region observed by HARP with velocities $<56\,\mathrm{km\,s^{-1}}$. Radal velocities (v_{rad}), line widths ($\triangle$v), average integrated intensities (I_{av}), opacities (τ_{13}), diameters (D), excitation temperatures (T_{ex}), column densities ($N(H_2)$), mass estimates (M_{LTE}) and virial parameter (α) are given. Clump names are created from the l, b and v_{rad} positions of the individual clump centroid position.

Clump name	v_{rad} (km/s)	$\triangle$v (km/s)	I_{av} (Kkm/s)	τ_{13}	D (pc)	T_{ex} (K)	$N(H_2)$ ($\times 10^{22}\,\mathrm{cm^{-2}}$)	M_{LTE} ($M_\odot$)	α
G49.49-0.39+56.65	55.8	1.1	40.4	6.93	1.1	39.2	4.36	869	1.7
G49.49-0.39+52.21	53.3	2.0	24.1	4.29	1.2	38.3	1.63	409	0.2
G49.38-0.25+50.17	50.3	1.6	17.0	2.40	1.1	31.4	0.72	136	0.1
G48.61+0.03+17.48	18.3	2.3	15.1	2.40	0.9	31.2	0.64	99	0.1
G49.38-0.26+50.84	50.3	1.3	13.0	2.61	0.7	28.0	0.61	57	0.1
G49.37-0.30+50.15	51.3	2.1	18.2	4.87	1.7	28.5	1.48	722	0.3
G49.40-0.25+49.86	50.3	1.1	14.6	1.62	1.0	26.6	0.51	87	0.2
G49.48-0.39+54.10	54.3	1.2	35.6	3.30	1.0	37.6	1.90	332	0.6
G49.39-0.31+52.27	52.8	1.2	17.7	1.90	1.3	33.6	0.62	175	0.2
G49.49-0.37+47.72	48.8	1.1	12.7	2.13	1.0	29.3	0.51	93	0.2
G49.37-0.27+50.53	50.3	1.2	16.0	1.89	0.9	28.1	0.60	79	0.2
G49.39-0.25+49.13	49.3	1.4	14.7	2.69	0.9	22.5	0.81	111	0.2
G49.39-0.26+49.91	50.3	1.0	15.0	1.63	0.9	28.9	0.50	69	0.2
G49.49-0.37+50.94	50.3	1.2	28.3	2.72	0.9	28.4	1.37	181	0.4
G49.35-0.30+52.59	52.3	2.6	12.0	4.59	1.1	26.8	0.95	210	0.1
G49.36-0.30+51.69	51.8	1.9	18.7	3.25	1.0	28.3	1.05	173	0.1

Clump name	v_{rad} (km/s)	$\triangle$v (km/s)	I_{av} (Kkm/s)	τ_{13}	D (pc)	T_{ex} (K)	N(H_2) ($\times 10^{22}$ cm^{-2})	M_{LTE} ($M_\odot$)	α
G49.34-0.28+49.53	49.8	0.8	5.1	1.14	0.9	18.1	0.20	26	0.1
G49.48-0.39+49.75	50.3	1.1	8.1	4.08	1.4	21.9	0.65	206	0.3
G48.61+0.01+18.74	19.3	1.0	15.8	1.96	0.8	21.5	0.71	76	0.3
G49.40-0.30+54.34	55.3	1.5	17.9	1.34	1.0	26.8	0.55	100	0.1
G49.35-0.29+52.47	52.8	1.2	15.5	1.90	0.7	23.0	0.65	56	0.1
G49.47-0.36+50.44	50.3	1.5	25.4	1.43	0.9	27.1	0.81	104	0.1
G49.33-0.28+51.14	51.3	1.8	4.6	2.68	1.1	17.1	0.33	74	0.1
G48.58+0.05+16.65	16.8	1.6	7.6	1.39	1.6	22.3	0.27	115	0.1
G49.52-0.37+51.45	51.3	1.2	15.8	2.38	0.9	21.4	0.82	124	0.2
G49.34-0.30+50.46	51.8	1.4	15.3	4.86	1.0	21.3	1.49	264	0.3
G49.48-0.36+48.83	50.3	1.7	16.0	3.18	0.9	22.3	1.01	137	0.1
G48.61+0.02+18.00	18.3	1.3	16.4	2.41	0.6	20.6	0.89	62	0.2
G48.63+0.23+14.83	14.8	1.8	4.2	1.53	0.9	21.6	0.16	24	0.0
G48.60+0.02+19.34	18.8	1.4	14.6	2.11	0.8	20.5	0.72	85	0.1
G49.56-0.35+55.80	55.3	1.6	8.3	2.93	1.4	20.5	0.53	170	0.1
G49.47-0.42+56.16	55.8	1.1	19.5	3.97	1.0	18.5	1.80	301	0.7
G49.33-0.27+50.64	50.8	1.0	14.5	1.62	0.7	17.2	0.73	61	0.2
G49.51-0.38+51.21	51.8	1.3	15.9	3.25	1.0	21.8	1.05	187	0.3
G49.46-0.37+52.75	52.8	1.1	10.1	1.57	0.8	18.5	0.46	45	0.1
G49.33-0.26+50.00	50.3	1.1	5.8	3.02	0.8	15.6	0.52	57	0.2
G49.39-0.23+48.80	50.3	1.7	9.9	1.19	1.1	23.1	0.32	66	0.1
G49.40-0.32+54.08	53.8	1.4	10.6	2.25	1.0	19.6	0.57	103	0.1
G48.62+0.02+17.99	17.8	0.9	12.9	1.55	0.5	21.5	0.50	23	0.1
G48.59+0.01+17.51	19.3	1.5	9.3	0.85	1.7	19.5	0.30	143	0.1
G48.57+0.06+15.06	15.8	1.4	11.8	3.63	0.9	19.6	0.94	139	0.2
G49.48-0.40+52.23	53.3	1.8	8.9	11.13	1.0	21.3	1.97	356	0.3
G49.36-0.27+49.31	49.8	1.2	4.6	0.53	0.9	16.5	0.16	20	0.0
G49.37-0.28+51.62	52.3	1.5	16.6	1.68	0.9	20.3	0.71	107	0.1
G49.50-0.37+52.17	51.8	1.2	12.0	3.09	0.8	18.9	0.87	102	0.2
G49.49-0.36+52.62	51.8	1.0	11.5	3.33	0.7	19.1	0.87	73	0.3
G49.35-0.28+51.11	51.8	0.9	10.7	3.28	0.9	17.1	0.91	115	0.4
G49.32-0.29+52.41	51.3	1.3	9.1	2.17	1.0	16.3	0.60	101	0.2
G49.50-0.36+49.50	50.8	1.0	16.4	2.51	0.8	18.7	1.01	105	0.4
G49.48-0.38+49.30	49.8	1.3	18.7	3.11	0.8	20.1	1.27	139	0.3
G48.59+0.03+16.39	16.3	1.3	11.3	0.91	1.0	19.6	0.37	63	0.1
G48.62+0.02+17.18	18.3	0.7	9.1	1.31	0.7	19.6	0.35	31	0.2
G49.41-0.31+51.89	53.3	1.6	17.7	2.56	1.0	21.9	0.95	156	0.2
G49.51-0.37+50.20	51.3	1.0	11.5	3.84	0.8	20.0	0.95	99	0.3
G49.34-0.30+50.73	50.8	1.2	7.4	2.32	1.0	17.7	0.46	78	0.1
G49.47-0.38+52.59	52.8	0.9	21.9	1.78	0.5	19.8	1.00	50	0.3
G49.40-0.29+48.29	49.3	1.8	8.5	1.88	0.9	19.8	0.40	51	0.1
G49.40-0.31+51.79	51.3	1.7	16.8	2.46	0.9	23.6	0.83	104	0.1
G49.47-0.42+54.15	55.8	1.1	7.2	1.05	1.1	15.5	0.33	70	0.1
G48.600.00+18.91	19.8	1.1	8.8	2.12	1.0	17.0	0.53	93	0.2

Clump name	v_{rad} (km/s)	$\triangle$v (km/s)	I_{av} (Kkm/s)	τ_{13}	D (pc)	T_{ex} (K)	N(H_2) ($\times 10^{22}$ cm^{-2})	M_{LTE} ($M_\odot$)	α
G48.64+0.02+14.46	14.3	1.0	5.5	0.96	1.0	16.3	0.23	36	0.1
G49.49-0.35+51.72	51.3	1.4	13.4	3.70	0.8	17.4	1.25	154	0.2
G48.62+0.09+16.93	17.8	1.2	3.7	2.97	1.6	16.7	0.30	134	0.2
G49.39-0.28+51.13	50.8	1.3	7.5	0.54	1.2	17.6	0.24	63	0.1
G49.47-0.38+49.35	50.8	1.2	12.1	1.35	0.9	16.8	0.57	82	0.2
G49.50-0.40+52.19	54.3	1.3	11.2	1.76	1.0	16.8	0.61	109	0.2
G49.32-0.28+51.09	52.3	1.0	7.0	1.30	0.7	14.4	0.41	36	0.1
G49.48-0.36+51.51	51.3	1.3	27.2	3.86	0.8	20.3	2.22	268	0.5
G48.58+0.06+16.23	15.8	1.9	4.2	3.63	1.1	18.2	0.36	79	0.1
G49.46-0.37+52.92	51.8	0.9	6.5	0.21	0.9	18.7	0.16	21	0.1
G48.56+0.05+17.78	17.8	1.4	5.9	0.79	1.0	16.1	0.23	43	0.1
G48.60+0.01+20.78	20.3	1.2	6.6	2.27	1.0	18.4	0.38	64	0.1
G49.49-0.41+53.84	53.8	1.0	14.5	5.09	0.8	18.2	1.73	184	0.6
G49.34-0.27+50.66	50.8	1.1	6.9	4.23	0.9	15.0	0.90	116	0.3
G49.53-0.36+51.92	52.3	1.4	9.2	2.30	0.9	16.2	0.64	86	0.1
G49.47-0.37+52.89	53.3	0.9	10.3	1.83	0.8	18.6	0.51	53	0.2
G49.48-0.36+52.23	51.3	1.2	12.0	3.69	0.8	18.8	1.02	123	0.3
G49.31-0.30+52.02	51.3	1.6	7.8	2.27	0.9	14.6	0.63	87	0.1
G49.61-0.36+54.14	54.3	0.9	6.9	1.80	1.2	19.6	0.32	76	0.2
G49.46-0.36+50.16	50.8	1.3	11.3	0.20	0.8	20.0	0.26	30	0.1
G49.42-0.33+52.61	52.8	1.8	12.6	1.83	1.5	16.7	0.71	269	0.2
G49.38-0.35+51.13	51.3	1.2	6.4	1.22	1.3	15.2	0.33	90	0.1
G49.57-0.26+53.23	52.8	1.1	10.8	1.41	1.4	24.7	0.36	130	0.2
G49.62-0.36+55.13	54.3	0.9	4.1	2.25	0.8	16.8	0.27	29	0.1
G49.46-0.38+54.68	55.3	1.6	11.2	2.13	1.1	13.6	0.98	184	0.2
G49.54-0.37+52.69	52.3	1.1	5.1	0.90	0.9	15.5	0.22	33	0.1
G49.45-0.37+50.96	51.3	1.6	7.3	0.94	1.2	14.4	0.36	88	0.1
G48.59+0.02+15.54	16.3	1.1	4.8	0.93	1.0	15.9	0.21	37	0.1
G49.51-0.35+49.31	49.3	0.9	3.8	1.51	1.0	15.4	0.21	36	0.1
G49.40-0.22+49.91	50.3	1.9	12.0	1.56	1.0	20.4	0.49	88	0.1
G49.57-0.27+49.83	50.8	1.3	7.7	0.99	1.0	23.1	0.23	37	0.1
G48.65+0.11+18.53	19.3	1.1	4.1	1.40	1.3	16.2	0.21	56	0.1
G49.45-0.35+50.32	50.8	1.1	8.1	0.89	1.4	15.4	0.36	112	0.2
G49.32-0.27+52.26	52.3	0.9	2.9	1.55	0.9	12.4	0.24	32	0.1
G49.33-0.30+51.19	51.3	1.2	7.0	2.49	0.8	15.7	0.54	59	0.1
G49.46-0.43+55.49	55.8	1.8	9.6	4.49	0.8	14.9	1.33	161	0.2
G49.50-0.39+54.20	55.8	1.1	10.7	1.68	0.8	18.9	0.49	61	0.2
G49.33-0.26+50.83	51.3	0.8	7.0	3.15	0.8	14.8	0.72	80	0.4
G49.39-0.31+48.70	50.3	1.1	3.9	0.43	1.0	16.3	0.13	21	0.0
G48.60+0.25+7.31	6.8	1.2	6.7	1.87	1.0	17.6	0.36	65	0.1
G48.60+0.24+9.32	9.3	1.0	4.0	1.99	1.2	16.4	0.25	61	0.1
G49.34-0.24+50.22	50.3	1.1	5.1	3.54	1.9	14.0	0.63	384	0.4
G48.64+0.10+18.07	18.3	1.3	3.7	3.24	1.1	13.1	0.48	106	0.2
G49.28-0.31+51.21	51.3	0.8	2.4	2.22	1.2	12.3	0.27	71	0.2

Clump name	v_{rad} (km/s)	$\triangle$v (km/s)	I_{av} (Kkm/s)	τ_{13}	D (pc)	T_{ex} (K)	$N(H_2)$ ($\times 10^{22}$ cm^{-2})	M_{LTE} ($M_\odot$)	α
G49.50-0.41+53.50	54.3	1.3	7.0	1.40	0.8	14.5	0.41	50	0.1
G49.43-0.31+51.76	52.3	0.7	5.3	1.92	1.0	14.5	0.38	70	0.3
G49.43-0.32+53.75	53.8	0.8	4.2	1.78	0.8	14.8	0.28	29	0.2
G49.31-0.31+51.40	51.8	1.0	3.6	2.52	1.5	14.4	0.33	127	0.2
G48.63+0.01+16.77	17.3	1.1	8.3	2.08	0.9	13.7	0.71	98	0.2
G49.40-0.28+50.87	50.8	1.1	9.3	1.64	1.0	14.2	0.62	111	0.2
G49.37-0.24+49.47	49.8	1.6	6.4	2.04	0.9	14.2	0.50	64	0.1
G49.51-0.42+53.93	53.8	0.9	6.2	0.61	0.8	13.7	0.29	30	0.1
G49.29-0.30+51.82	51.8	1.2	3.2	2.18	1.1	11.8	0.38	72	0.1
G49.50-0.35+48.88	49.3	0.8	5.4	0.65	0.8	17.0	0.19	19	0.1
G49.42-0.05+45.54	45.8	1.0	3.5	0.69	1.8	17.1	0.12	66	0.1
G49.42-0.21+50.02	50.8	1.2	9.4	1.54	1.4	17.9	0.44	140	0.2
G48.66+0.22+12.12	12.3	1.9	5.0	2.38	1.6	12.8	0.53	216	0.1
G49.47-0.34+50.81	50.8	1.1	8.2	1.52	0.9	14.9	0.49	76	0.2
G48.60+0.09+16.55	16.3	1.4	1.7	2.55	2.0	13.2	0.18	117	0.1
G49.48-0.34+51.20	51.8	1.1	7.7	2.53	0.8	13.9	0.74	87	0.2
G49.33-0.36+55.66	55.3	1.3	3.8	1.36	1.4	13.5	0.26	90	0.1
G48.57+0.02+17.69	18.8	1.7	6.6	1.93	1.3	12.9	0.59	168	0.1
G49.43-0.32+51.91	52.3	0.5	5.8	1.24	0.8	14.3	0.33	34	0.4
G48.65+0.22+15.45	15.3	1.7	2.3	3.15	1.2	14.2	0.25	65	0.1
G49.61-0.34+54.88	55.3	0.9	2.6	1.24	1.1	13.8	0.16	33	0.1
G49.40-0.23+49.76	50.3	1.1	11.2	1.59	1.0	21.6	0.44	71	0.2
G49.55-0.28+53.20	53.3	2.3	8.7	1.40	1.0	18.2	0.37	67	0.0
G49.32-0.24+49.40	49.8	1.2	4.3	2.01	0.9	12.5	0.43	65	0.1
G49.49-0.34+52.28	51.8	1.3	6.1	2.56	0.8	17.7	0.41	48	0.1
G49.47-0.34+48.65	50.3	1.9	4.0	3.50	1.3	13.6	0.52	141	0.1
G49.39-0.21+48.36	48.3	1.0	12.2	2.85	1.2	16.7	0.96	240	0.6
G48.620.00+18.17	18.8	1.0	7.8	2.36	0.8	12.3	0.90	93	0.3
G49.42-0.22+49.88	50.8	1.2	8.2	1.75	1.0	19.2	0.38	61	0.1
G48.55+0.07+17.56	18.3	1.0	2.3	2.43	0.9	12.7	0.25	36	0.1
G49.40-0.27+51.15	50.8	1.3	6.2	2.07	1.1	13.4	0.54	112	0.2
G49.39-0.33+53.25	53.8	1.4	7.6	0.79	1.1	13.3	0.42	78	0.1
G48.63+0.11+16.44	17.3	1.5	1.6	3.28	1.9	11.4	0.29	179	0.1
G49.46-0.33+50.52	50.8	0.9	6.9	2.46	0.9	12.9	0.74	111	0.4
G48.60+0.26+7.41	7.8	1.0	5.2	2.67	1.0	12.7	0.61	111	0.3
G49.48-0.33+49.86	50.8	1.7	4.2	1.96	1.6	13.6	0.34	147	0.1
G49.39-0.34+52.52	52.8	1.5	6.8	1.95	1.1	12.9	0.62	139	0.2
G48.55+0.01+15.94	16.3	1.2	2.1	1.39	1.6	11.6	0.19	86	0.1
G49.52-0.41+51.41	51.8	0.9	3.8	1.55	1.0	12.6	0.32	51	0.2
G49.42-0.04+45.28	45.8	1.2	2.6	1.61	1.3	12.2	0.23	68	0.1
G49.62-0.37+54.48	54.8	0.7	3.0	2.26	0.7	12.6	0.31	28	0.2
G48.67-0.30+33.42	34.3	0.9	3.4	4.32	0.9	11.3	0.79	119	0.4
G49.42-0.41+55.86	55.8	1.3	9.3	3.29	1.6	12.4	1.37	614	0.6
G49.46-0.34+49.83	50.3	1.0	6.7	1.71	0.8	12.8	0.57	61	0.2

Clump name	v_{rad} (km/s)	$\triangle$v (km/s)	I_{av} (Kkm/s)	τ_{13}	D (pc)	T_{ex} (K)	N(H_2) ($\times 10^{22}$ cm^{-2})	M_{LTE} ($M_\odot$)	α
G49.44-0.33+50.17	51.8	1.1	5.9	1.91	0.9	12.6	0.56	75	0.2
G48.64+0.23+5.79	6.8	1.1	3.7	2.60	1.0	12.6	0.44	69	0.2
G48.90-0.44+55.28	55.8	0.9	2.0	3.30	1.0	11.5	0.35	62	0.2
G49.56-0.28+52.54	52.8	1.4	4.6	2.48	0.7	16.1	0.34	31	0.1
G49.36-0.34+51.14	51.3	1.1	4.1	2.39	0.9	12.0	0.50	64	0.2
G48.65+0.01+15.68	16.3	0.7	3.2	2.28	0.7	11.5	0.41	39	0.2
G48.79+0.11+17.42	18.3	1.7	1.3	1.70	3.0	12.7	0.11	171	0.1
G49.53-0.39+49.43	50.8	1.3	2.4	1.52	0.9	11.7	0.23	33	0.1
G49.44-0.40+53.23	53.8	1.2	4.0	2.50	1.2	12.0	0.51	127	0.2
G49.57-0.38+52.28	52.3	0.9	3.4	1.19	1.2	13.2	0.22	55	0.1
G48.57+0.07+16.07	16.3	1.2	2.4	1.84	1.1	12.2	0.24	54	0.1
G49.35-0.33+50.36	50.8	1.1	3.1	1.04	1.1	11.8	0.24	51	0.1
G49.47-0.39+46.96	47.8	1.1	1.8	2.81	1.1	11.4	0.29	60	0.1
G49.31-0.26+51.49	51.8	0.9	2.2	0.64	0.9	11.8	0.15	22	0.1
G49.41-0.29+50.51	50.3	1.1	3.5	3.83	0.8	12.1	0.62	76	0.2
G49.43-0.32+49.97	50.8	0.8	3.1	2.02	0.8	11.7	0.35	38	0.2
G49.52-0.38+51.09	51.3	0.7	4.7	2.48	0.6	11.5	0.65	40	0.4
G48.650.00+17.27	17.3	0.9	3.2	1.64	0.8	11.5	0.34	36	0.1
G49.54-0.43+54.62	54.8	0.9	3.4	1.99	1.0	12.3	0.35	60	0.2
G48.64+0.02+17.38	17.3	1.3	3.4	4.19	1.1	10.8	0.86	187	0.3
G48.60+0.27+10.20	9.8	1.6	2.8	2.86	1.7	11.6	0.44	218	0.1
G49.46-0.35+47.84	48.8	1.1	5.8	2.61	1.0	12.3	0.72	121	0.3
G49.41-0.23+50.02	50.3	1.4	6.2	2.00	0.8	15.2	0.42	47	0.1
G49.33-0.25+49.50	49.8	0.9	4.3	2.34	0.8	11.9	0.53	53	0.2
G49.40-0.28+54.87	55.3	0.8	2.7	0.88	0.6	11.5	0.21	15	0.1
G49.44-0.33+53.64	53.8	0.9	3.7	1.89	1.2	11.8	0.40	99	0.3
G49.52-0.39+51.09	51.3	1.1	4.2	2.17	0.9	12.8	0.42	60	0.1
G49.36-0.25+50.16	50.3	1.1	3.0	2.90	0.8	9.6	0.78	81	0.2
G48.68+0.08+16.50	17.3	1.2	1.3	1.95	1.7	11.0	0.17	80	0.1
G49.53-0.43+54.44	54.8	0.8	4.5	1.97	0.6	11.7	0.51	36	0.2
G48.66-0.31+32.97	33.3	1.0	3.5	4.36	0.9	10.6	0.96	145	0.5
G49.39-0.28+54.07	54.8	1.0	4.4	1.72	0.8	11.9	0.44	49	0.2
G49.38-0.18+47.10	47.8	1.0	6.1	3.13	0.9	15.9	0.56	75	0.2
G49.42-0.40+55.49	55.8	1.3	4.4	1.85	0.8	11.0	0.55	55	0.1
G48.78-0.22+46.48	47.3	0.7	2.2	2.34	1.1	10.7	0.35	73	0.4
G48.79+0.09+48.92	48.8	0.8	1.7	2.53	1.2	11.0	0.27	68	0.2
G49.41-0.20+52.09	51.8	1.5	4.4	1.15	0.9	14.3	0.24	32	0.0
G48.77-0.22+46.95	47.3	0.9	1.5	2.69	1.5	10.8	0.26	105	0.2
G49.37-0.21+48.48	47.8	1.0	3.8	1.98	1.4	10.8	0.52	163	0.3
G48.64-0.31+33.33	33.8	0.9	2.0	5.38	1.7	10.7	0.67	320	0.6
G49.33-0.23+49.24	48.8	1.1	2.8	2.63	0.9	10.3	0.54	77	0.2
G48.65+0.28+10.19	10.3	1.2	2.2	2.99	1.1	10.7	0.43	96	0.2
G49.31-0.22+50.22	50.3	1.1	2.4	2.42	1.9	10.7	0.39	239	0.3
G48.79+0.02+49.84	50.3	0.7	2.2	4.72	1.7	10.6	0.66	316	0.9

Clump name	v_{rad} (km/s)	$\triangle$v (km/s)	I_{av} (Kkm/s)	τ_{13}	D (pc)	T_{ex} (K)	$N(H_2)$ ($\times 10^{22}$ cm^{-2})	M_{LTE} ($M_\odot$)	α
G48.63+0.23+6.64	6.8	0.8	4.0	3.58	0.6	12.7	0.61	39	0.2
G49.54-0.39+51.38	51.8	0.7	3.5	2.55	1.2	10.8	0.58	146	0.6
G49.37-0.36+51.51	51.8	1.0	2.8	2.20	0.8	11.2	0.38	38	0.1
G48.54+0.04+15.80	16.3	1.5	1.8	2.43	1.7	10.3	0.32	153	0.1
G48.52+0.07+13.47	13.8	0.8	1.9	2.31	0.8	11.0	0.28	33	0.2
G48.64+0.23+7.92	7.8	0.7	2.2	3.86	0.7	10.1	0.62	49	0.4
G49.29-0.28+50.81	51.3	1.3	2.0	2.74	0.9	11.3	0.31	47	0.1
G49.54-0.41+51.88	51.8	0.8	2.9	2.79	1.1	10.5	0.56	113	0.4
G48.91-0.45+55.55	55.8	1.4	1.3	6.74	1.6	10.1	0.63	279	0.2
G49.47-0.22+51.07	51.8	1.3	2.7	1.51	1.5	12.7	0.21	80	0.1
G49.55-0.34+53.00	53.3	1.0	2.8	2.55	1.3	11.7	0.38	105	0.2
G48.61+0.23+7.07	7.3	0.7	3.0	3.61	1.0	11.2	0.62	100	0.5
G49.40-0.19+47.64	47.8	1.3	5.3	1.86	0.7	14.1	0.39	32	0.1
G48.62-0.01+16.99	16.8	1.2	3.0	2.23	1.0	10.0	0.55	89	0.2
G48.64-0.02+17.10	16.8	1.1	3.1	1.38	0.8	10.2	0.40	43	0.1
G49.45-0.35+46.54	47.3	1.1	2.9	3.04	0.9	10.3	0.62	94	0.2
G49.57-0.41+54.12	55.3	1.1	2.4	2.02	0.8	11.2	0.31	37	0.1
G48.82+0.03+53.40	53.8	0.6	2.8	3.10	1.1	11.3	0.49	108	0.6
G48.62-0.01+16.57	16.8	0.9	2.9	3.20	0.8	10.1	0.68	66	0.3
G49.30-0.28+50.94	51.3	1.0	2.4	1.00	0.7	11.0	0.22	19	0.1
G48.63+0.22+8.05	8.3	1.2	2.1	3.29	1.1	11.0	0.42	79	0.1
G49.54-0.36+56.09	55.8	0.7	3.9	2.78	0.9	11.6	0.58	81	0.5
G48.64+0.22+9.66	9.8	0.9	2.9	3.30	1.1	10.3	0.68	149	0.4
G49.34-0.48+55.35	55.8	0.9	3.2	4.62	1.1	10.0	1.10	245	0.6
G49.55-0.36+53.59	53.8	0.9	3.8	2.95	0.8	11.0	0.67	65	0.3
G48.62-0.01+19.04	18.8	1.0	2.5	4.11	1.0	9.4	0.93	159	0.4
G49.38-0.16+47.17	47.3	1.0	4.6	5.07	1.2	13.3	0.89	204	0.5
G48.63-0.02+16.91	16.8	1.4	2.5	3.40	1.0	9.5	0.77	123	0.2
G49.55-0.25+52.97	51.8	1.7	5.9	3.19	2.0	13.6	0.71	505	0.2
G49.47-0.30+55.35	55.8	1.1	4.8	1.93	0.8	13.0	0.43	53	0.2
G48.63-0.15+15.64	15.8	0.8	1.8	2.08	2.2	10.9	0.25	200	0.4
G49.48-0.34+47.64	49.3	1.1	2.4	2.26	1.3	10.8	0.36	105	0.2
G48.53+0.11+16.46	16.8	1.0	1.6	1.75	1.3	10.5	0.21	61	0.1
G49.41-0.21+48.11	48.8	1.0	6.1	3.17	0.8	14.0	0.69	70	0.2
G49.43-0.38+53.07	53.3	0.9	2.7	1.92	1.1	10.4	0.40	86	0.2
G48.60+0.23+9.53	9.3	1.3	2.5	3.30	1.3	10.1	0.62	184	0.2
G49.36-0.38+50.58	50.3	1.5	2.5	1.92	1.1	10.4	0.37	72	0.1
G49.45-0.33+51.57	51.8	1.0	5.0	2.08	0.9	13.4	0.44	60	0.2
G49.40-0.20+48.30	48.3	0.8	7.4	1.93	0.7	13.9	0.58	53	0.3
G49.53-0.14+54.79	54.8	1.3	3.8	3.36	1.9	12.6	0.56	361	0.3
G49.36-0.37+50.83	51.3	0.8	3.1	1.73	0.8	11.2	0.36	44	0.2
G48.62+0.24+4.40	5.3	1.3	1.4	2.92	0.8	11.0	0.26	27	0.1
G49.31-0.27+51.26	51.8	0.8	3.2	2.03	0.6	10.3	0.51	36	0.2
G49.55-0.35+53.88	54.3	0.8	4.2	2.09	0.7	10.1	0.71	55	0.4

Clump name	v_{rad} (km/s)	$\triangle$v (km/s)	I_{av} (Kkm/s)	τ_{13}	D (pc)	T_{ex} (K)	N(H_2) ($\times 10^{22}$ cm^{-2})	M_{LTE} ($M_\odot$)	α
G48.58+0.05+19.04	18.8	1.1	1.9	2.00	0.9	10.7	0.26	37	0.1
G48.83+0.02+53.46	53.3	1.2	1.3	4.16	1.7	9.9	0.43	211	0.2
G48.62+0.22+7.41	7.8	1.3	2.9	4.56	1.3	10.2	0.92	254	0.3
G49.28-0.28+50.94	51.3	1.0	1.3	1.93	1.3	10.9	0.17	48	0.1
G49.37-0.18+48.97	48.3	0.9	3.7	1.22	1.0	13.9	0.22	37	0.1
G49.44-0.39+54.21	54.8	1.1	5.0	3.24	1.1	10.3	1.14	226	0.5
G48.65-0.31+32.97	33.8	0.8	3.2	2.33	0.8	10.1	0.59	69	0.3
G49.43-0.05+44.96	45.8	0.8	2.3	1.93	0.7	11.7	0.26	23	0.1
G49.52-0.35+50.25	50.3	0.6	2.0	2.00	0.8	10.5	0.30	33	0.3
G49.45-0.38+48.46	49.3	1.3	3.0	2.15	1.0	9.6	0.62	99	0.2
G48.80+0.11+49.17	49.3	0.5	2.4	2.92	1.2	11.5	0.39	91	0.6
G49.29-0.29+51.64	51.3	0.8	1.9	4.88	0.8	8.5	1.13	112	0.7
G49.31-0.36+55.56	55.8	0.9	2.7	1.69	0.9	10.4	0.37	50	0.2
G49.53-0.42+50.49	50.8	0.6	1.6	2.82	0.8	9.9	0.36	37	0.3
G48.79+0.01+50.28	50.3	1.1	2.0	2.92	1.1	10.7	0.37	71	0.1
G49.39-0.29+51.33	52.8	1.0	4.0	1.47	0.5	11.0	0.44	21	0.1
G49.47-0.32+55.65	55.8	0.9	5.6	1.74	1.1	14.7	0.37	75	0.2
G49.30-0.23+48.74	49.3	0.7	1.7	2.52	0.9	10.6	0.29	44	0.2
G49.39-0.17+47.41	47.8	1.0	4.5	3.21	0.9	12.6	0.63	96	0.3
G48.66+0.11+20.70	21.3	0.9	1.6	3.40	1.0	10.0	0.42	78	0.3
G49.46-0.39+49.24	49.8	1.0	2.3	2.26	0.7	8.5	0.71	63	0.2
G49.38-0.17+47.39	46.8	0.8	5.3	3.27	1.0	13.9	0.63	99	0.4
G48.61+0.24+5.03	6.8	0.9	2.8	2.81	0.9	10.5	0.53	71	0.3
G49.30-0.24+48.60	48.8	0.6	1.6	1.81	0.7	10.6	0.22	19	0.2
G49.33-0.24+48.63	49.3	0.9	2.8	2.86	0.6	10.1	0.60	41	0.2
G49.41-0.35+55.01	55.3	1.1	2.7	2.78	1.1	9.8	0.63	140	0.3
G49.36-0.06+50.07	51.3	2.2	2.3	4.79	1.6	9.7	0.89	380	0.1
G48.63-0.13+16.26	15.8	1.0	2.3	3.46	1.4	10.2	0.56	179	0.3
G49.32-0.26+50.46	51.3	0.9	2.3	1.14	0.7	10.8	0.23	17	0.1
G49.55-0.27+54.41	54.3	1.2	5.1	1.52	1.1	14.5	0.32	69	0.1
G49.36-0.23+48.46	48.8	1.4	2.5	1.56	0.9	10.9	0.29	38	0.1
G49.44-0.42+54.66	55.8	1.0	2.6	2.92	0.9	10.0	0.61	80	0.3
G49.45-0.35+46.37	46.8	1.0	1.7	3.79	0.7	9.1	0.64	53	0.2
G49.56-0.22+53.04	52.8	1.8	2.7	2.38	1.1	12.6	0.30	64	0.1
G49.52-0.02+54.66	54.8	0.9	2.7	3.71	0.7	9.9	0.77	70	0.3
G49.40-0.25+54.47	54.3	0.8	1.4	3.14	1.7	11.0	0.27	126	0.3
G48.86-0.49+53.80	53.8	1.1	3.4	5.63	1.5	11.2	1.04	399	0.6
G49.42-0.36+53.70	53.8	1.1	2.3	3.10	1.0	9.5	0.65	109	0.3
G49.54-0.27+50.87	51.3	1.1	2.6	2.64	1.0	12.5	0.31	56	0.1
G49.37-0.40+52.49	53.3	1.1	1.5	2.35	1.6	10.0	0.29	136	0.2
G48.59+0.27+7.49	7.3	0.9	2.9	3.01	0.8	10.2	0.65	78	0.3
G49.45-0.54+54.92	55.3	0.6	1.3	3.11	1.0	9.0	0.42	69	0.6
G49.35-0.33+53.51	53.8	1.0	1.9	3.48	1.2	9.6	0.57	150	0.3
G48.84-0.48+52.91	52.3	1.5	3.0	4.60	1.7	11.5	0.72	345	0.2

Clump name	v_{rad} (km/s)	$\triangle$v (km/s)	I_{av} (Kkm/s)	τ_{13}	D (pc)	T_{ex} (K)	$N(H_2)$ ($\times 10^{22}$ cm^{-2})	M_{LTE} ($M_\odot$)	α
G49.36-0.45+55.57	55.3	1.7	1.4	3.55	1.2	9.5	0.43	108	0.1
G49.44-0.26+49.39	49.8	0.7	3.6	3.45	0.5	14.1	0.43	19	0.2
G49.48-0.23+50.95	51.3	1.0	3.3	1.90	1.4	12.1	0.33	105	0.2
G48.95-0.39+51.91	52.3	0.9	1.8	6.01	1.8	9.4	0.94	492	1.0
G49.42-0.16+46.64	47.3	1.5	2.0	1.46	2.1	12.8	0.15	113	0.1
G49.30-0.36+54.44	54.8	1.4	1.6	2.21	1.6	10.1	0.27	122	0.1
G49.36-0.17+48.69	49.3	0.8	3.5	3.23	0.9	11.4	0.62	88	0.4
G49.55-0.44+54.63	54.8	1.6	1.5	3.96	1.7	9.8	0.49	240	0.1
G49.51-0.02+55.40	54.8	1.1	2.0	5.73	1.9	9.3	1.08	678	0.8
G49.32-0.20+50.33	51.3	0.9	1.6	4.83	1.2	9.9	0.58	148	0.4
G48.64+0.18+5.42	5.3	0.8	1.4	7.86	0.8	8.8	1.25	150	0.8
G49.27-0.30+52.87	52.3	1.2	1.5	6.58	1.0	7.9	1.54	264	0.5
G49.42-0.19+50.19	50.3	1.2	3.2	2.04	1.1	11.9	0.36	67	0.1
G49.44-0.27+50.91	50.8	0.9	3.6	2.22	1.0	11.8	0.43	71	0.3
G49.23-0.23+52.86	54.3	2.1	1.1	4.50	1.6	9.1	0.49	212	0.1
G49.25-0.31+52.29	52.3	1.8	0.8	4.49	2.2	8.2	0.51	414	0.2
G49.31-0.49+55.75	55.3	1.0	1.0	4.68	2.2	9.2	0.47	403	0.5
G48.53+0.07+14.02	13.8	1.0	1.8	2.54	0.9	9.0	0.51	65	0.2
G48.66+0.30+9.02	8.8	1.5	1.7	5.20	2.0	9.2	0.83	552	0.3
G48.63+0.16+50.91	51.3	0.9	1.1	2.09	1.8	10.2	0.17	99	0.2
G48.62+0.21+10.82	10.3	1.3	1.7	7.49	1.4	8.8	1.42	504	0.6
G48.68+0.25+14.47	12.3	3.8	0.9	3.36	2.4	10.3	0.20	201	0.0
G48.66-0.29+33.27	33.8	0.7	2.6	3.67	1.2	9.3	0.90	237	0.9
G49.35-0.42+57.23	55.8	3.0	1.2	5.54	2.2	8.9	0.70	559	0.1
G48.90-0.08+18.90	19.8	1.5	1.1	4.66	2.1	8.4	0.64	479	0.3
G49.32-0.48+54.93	54.8	1.0	2.5	5.32	1.3	8.9	1.41	425	0.8
G49.41-0.44+53.89	54.3	1.3	2.2	2.82	1.0	9.3	0.60	103	0.2
G49.47-0.29+55.62	55.8	1.0	2.7	3.57	1.2	11.1	0.54	138	0.3
G48.59+0.29+8.69	8.8	0.8	1.9	3.71	1.1	8.9	0.78	164	0.6
G49.39-0.19+49.67	49.8	1.3	2.9	3.50	0.9	11.3	0.56	79	0.1
G49.28-0.04+50.11	50.8	0.7	1.0	7.76	1.4	7.8	1.22	392	1.6
G49.41-0.24+45.31	45.8	0.9	2.8	2.59	1.1	12.5	0.34	72	0.2
G48.74-0.13+16.85	17.3	1.2	1.2	5.81	2.8	8.0	1.11	1512	1.1
G49.50-0.25+50.59	52.3	1.9	2.9	3.49	2.1	10.6	0.66	477	0.2
G49.44-0.25+49.01	49.8	0.6	2.1	2.51	0.6	11.8	0.28	17	0.2
G49.30-0.21+50.33	50.8	0.9	2.2	3.53	1.1	8.7	0.91	181	0.5
G49.39-0.22+46.19	46.8	0.7	3.2	1.50	0.6	11.5	0.32	20	0.2
G48.59+0.28+10.86	10.8	1.0	2.9	4.19	0.9	9.0	1.27	196	0.5
G49.53-0.32+50.62	50.3	1.6	1.0	2.83	3.0	10.0	0.21	322	0.1
G49.40-0.16+45.96	46.3	1.4	2.1	1.82	1.3	11.7	0.23	66	0.1
G49.51-0.14+54.44	54.3	0.9	2.2	1.97	2.0	11.7	0.25	163	0.3
G48.59+0.27+6.22	7.3	0.9	2.5	3.88	0.7	9.9	0.75	66	0.3
G49.40-0.18+48.73	49.3	0.8	4.1	3.40	0.9	11.3	0.76	101	0.5
G48.79+0.09+51.64	51.8	0.8	1.6	4.56	1.4	8.8	0.79	280	0.7

Clump name	v_{rad} (km/s)	$\triangle$v (km/s)	I_{av} (Kkm/s)	τ_{13}	D (pc)	T_{ex} (K)	N(H_2) ($\times 10^{22}$ cm^{-2})	M_{LTE} ($M_\odot$)	α
G49.43-0.24+51.06	50.8	1.3	3.9	2.29	1.6	12.3	0.44	180	0.2
G49.41-0.18+48.82	49.3	0.9	3.3	4.56	1.1	11.0	0.88	188	0.5
G49.41-0.35+51.82	52.8	1.1	3.5	3.25	1.1	9.4	1.05	225	0.4
G49.36-0.22+47.78	48.3	1.0	1.8	2.15	1.1	9.7	0.35	73	0.2
G49.33-0.25+53.07	53.3	0.6	1.3	2.84	0.7	8.8	0.41	33	0.3
G49.55-0.38+50.38	50.8	0.8	1.9	3.51	0.8	9.9	0.52	51	0.3
G49.46-0.28+50.53	50.8	0.9	2.4	2.60	1.4	11.6	0.34	107	0.3
G49.43-0.19+49.31	48.8	1.3	2.5	1.83	1.2	13.0	0.21	48	0.1
G48.61-0.01+16.20	16.3	0.8	2.1	4.35	0.9	8.6	1.09	137	0.6
G48.86-0.48+53.00	52.8	0.8	2.9	5.58	1.1	9.8	1.28	270	1.0
G48.67+0.13+17.57	18.8	1.8	2.3	4.05	1.4	9.9	0.72	246	0.1
G49.57-0.30+54.02	54.3	0.9	1.7	2.01	0.7	9.8	0.31	25	0.1
G49.34-0.46+55.29	55.3	1.2	1.6	3.30	1.6	9.0	0.56	249	0.3
G49.56-0.24+51.55	51.3	0.8	3.2	4.18	0.8	10.8	0.81	98	0.5
G49.12-0.19+51.78	51.3	1.8	0.9	4.90	2.0	8.5	0.53	345	0.2
G48.75+0.14+50.98	52.8	2.6	1.3	6.87	2.5	8.1	1.34	1479	0.2
G48.59+0.07+16.92	16.8	0.9	1.3	8.41	1.0	8.3	1.41	232	0.8
G49.46-0.32+50.03	50.8	1.0	2.7	3.76	1.3	10.9	0.61	174	0.4
G49.39-0.20+46.83	47.3	0.6	3.0	1.95	0.6	11.4	0.36	22	0.3
G48.71+0.14+5.78	6.3	1.4	1.9	4.94	1.5	9.0	0.97	358	0.3
G49.22-0.24+54.93	55.3	0.7	1.4	4.48	1.0	8.5	0.79	146	0.7
G49.40-0.36+49.69	50.8	1.0	2.6	3.76	1.1	8.8	1.10	235	0.6
G48.80-0.02+18.33	18.8	1.4	1.6	7.01	1.9	9.3	1.07	665	0.5
G49.37-0.35+47.57	48.8	1.5	1.3	2.56	1.0	8.9	0.39	63	0.1
G49.41-0.30+49.71	49.8	0.5	1.9	2.61	0.5	9.6	0.45	18	0.3
G48.65+0.04+14.65	14.8	1.2	1.7	3.62	1.0	8.2	0.91	143	0.3
G48.61+0.28+11.45	11.8	1.6	2.4	7.38	1.1	8.6	2.10	474	0.5
G49.54-0.26+52.02	52.3	0.6	4.2	2.56	0.6	11.8	0.56	37	0.4
G48.69-0.23+34.20	34.3	0.8	2.0	5.18	0.9	9.0	1.04	144	0.7
G49.57-0.25+55.98	55.8	2.2	3.5	2.45	1.0	11.4	0.50	78	0.0
G48.66-0.28+33.28	33.3	0.7	2.6	4.25	1.4	9.8	0.88	283	1.1
G49.37-0.17+49.01	49.3	0.7	3.8	2.51	0.6	11.2	0.56	30	0.3
G49.21-0.24+54.92	54.8	1.2	1.8	4.28	1.2	8.5	0.95	218	0.4
G48.65-0.34+32.66	32.8	0.6	1.6	5.79	0.9	8.7	1.04	153	1.0
G48.66+0.13+15.78	16.8	1.3	1.5	4.83	2.0	8.9	0.77	523	0.5
G48.99-0.51+46.69	46.8	0.8	1.1	4.14	1.8	8.9	0.50	265	0.6
G49.59-0.39+52.10	51.8	0.9	2.0	3.55	1.3	8.8	0.78	215	0.6
G48.81+0.03+53.09	53.3	0.7	2.1	3.39	0.8	8.8	0.80	90	0.6
G49.48-0.22+51.69	52.3	1.2	3.8	2.00	1.0	11.7	0.43	80	0.1
G49.43-0.34+50.40	50.3	0.9	3.0	3.64	0.7	9.4	1.00	88	0.4
G48.66+0.19+8.25	7.8	1.3	1.1	4.45	1.3	8.4	0.64	196	0.2
G49.36-0.44+54.85	54.8	0.9	1.3	2.88	0.7	8.9	0.42	33	0.2
G48.52+0.03+52.00	52.8	0.6	0.8	4.63	1.2	8.2	0.55	137	0.9
G48.68-0.22+34.20	34.8	1.0	1.6	6.18	2.1	8.5	1.17	917	1.3

Clump name	v_{rad} (km/s)	$\triangle$v (km/s)	I_{av} (Kkm/s)	τ_{13}	D (pc)	T_{ex} (K)	$N(H_2)$ ($\times 10^{22}$ cm^{-2})	M_{LTE} ($M_\odot$)	α
G49.55-0.37+55.55	55.3	1.1	2.5	3.30	0.7	10.1	0.63	57	0.2
G49.37-0.17+47.96	48.3	0.8	3.5	4.32	0.6	11.7	0.76	50	0.3
G48.61-0.01+19.14	19.3	0.9	2.1	2.81	1.0	8.6	0.72	116	0.4
G48.76-0.14+14.69	14.8	0.8	0.9	5.85	1.7	7.2	1.15	569	1.3
G49.47-0.32+53.67	53.8	0.6	2.5	2.74	0.8	11.3	0.40	42	0.3
G49.56-0.30+53.44	53.8	1.1	1.1	2.36	1.4	9.2	0.27	89	0.2
G48.66-0.00+16.21	16.3	1.3	2.4	4.96	0.9	8.7	1.35	204	0.3
G49.36-0.16+48.27	48.8	1.1	5.1	3.07	0.9	11.1	0.92	134	0.4
G49.36-0.05+51.00	51.3	0.7	2.8	4.34	0.6	9.4	1.09	65	0.6
G48.64+0.23+12.11	11.8	0.6	1.8	5.89	0.9	9.0	1.09	148	1.1
G49.15-0.31+55.24	55.8	1.5	1.5	4.61	0.9	7.6	1.32	203	0.3
G48.60-0.22+6.02	5.8	1.1	0.8	4.87	1.1	8.1	0.59	119	0.3
G48.74+0.05+49.38	49.3	0.6	1.3	3.79	1.1	9.0	0.50	109	0.7
G48.61-0.02+20.42	20.3	1.0	1.2	3.27	1.3	8.4	0.54	157	0.3
G49.55-0.38+49.41	50.3	1.0	1.8	5.21	1.1	8.9	1.02	227	0.5
G49.44-0.26+50.49	50.8	0.9	2.5	3.68	0.9	11.1	0.53	80	0.3
G49.49-0.22+52.05	51.8	1.2	3.3	4.75	1.6	11.3	0.85	394	0.4
G48.73+0.05+50.30	50.3	1.6	1.1	4.38	1.9	9.0	0.47	292	0.2
G48.78+0.09+51.94	51.8	0.7	2.3	4.18	1.0	9.0	0.96	154	0.8
G48.85-0.51+53.06	53.8	1.4	3.1	2.92	0.8	10.1	0.68	84	0.1
G49.37-0.04+50.98	50.8	1.6	1.1	4.75	1.2	8.4	0.68	172	0.2
G48.72+0.14+51.93	50.8	2.4	1.9	5.45	1.9	8.4	1.29	773	0.2
G48.73+0.22+10.71	11.3	1.1	2.1	7.53	1.4	8.8	1.74	600	1.0
G49.57-0.22+53.80	53.8	1.0	2.4	2.77	1.1	10.3	0.48	99	0.2
G49.44-0.29+54.61	55.3	1.3	3.1	2.88	1.1	11.4	0.50	105	0.2
G49.41-0.24+49.46	49.3	1.0	4.6	2.38	0.8	11.7	0.59	68	0.2
G49.45-0.32+50.93	50.8	0.9	2.3	3.46	0.7	10.1	0.59	45	0.2
G49.42-0.33+49.28	49.8	1.1	2.5	3.54	0.8	9.0	0.93	102	0.3
G48.69+0.13+5.42	5.8	0.9	2.3	3.26	1.5	9.3	0.73	266	0.6
G49.41-0.30+48.34	48.8	0.6	1.5	2.02	0.8	9.3	0.31	34	0.3
G48.73+0.14+8.69	8.8	0.9	1.2	4.78	1.3	8.7	0.65	192	0.5
G48.76-0.21+46.66	47.3	0.7	1.5	2.88	0.8	8.4	0.58	69	0.4
G49.54-0.42+54.92	54.8	1.0	2.9	4.05	0.9	8.3	1.60	202	0.7
G49.56-0.38+51.27	51.3	0.9	1.8	4.50	0.8	9.2	0.80	87	0.4
G48.61+0.22+7.31	7.8	1.5	1.5	7.20	1.1	9.6	0.92	193	0.2
G49.37-0.14+47.20	46.8	1.3	4.0	4.82	1.7	11.2	1.06	525	0.5
G48.86-0.51+53.87	54.3	0.6	2.9	6.22	1.1	9.6	1.50	294	1.7
G49.38-0.21+48.87	48.8	0.8	4.4	2.66	0.6	11.6	0.62	32	0.2
G48.60-0.01+16.09	16.8	1.1	1.6	4.54	1.1	8.9	0.80	175	0.3
G49.42-0.27+51.21	50.3	1.1	4.7	2.84	1.5	11.2	0.78	299	0.4
G48.59+0.28+5.58	5.8	0.7	1.5	5.49	0.8	8.2	1.21	129	0.9
G49.28-0.19+46.34	47.3	2.0	1.4	8.62	3.5	8.3	1.64	3487	0.7
G48.65+0.15+51.27	50.8	1.5	0.9	8.04	2.4	7.8	1.15	1172	0.6
G49.55-0.04+54.84	54.8	1.1	2.9	4.14	1.3	11.1	0.70	211	0.3

Clump name	v_{rad} (km/s)	$\triangle$v (km/s)	I_{av} (Kkm/s)	τ_{13}	D (pc)	T_{ex} (K)	N(H_2) ($\times 10^{22}$ cm^{-2})	M_{LTE} ($M_\odot$)	α
G49.34-0.37+51.56	52.3	0.7	1.7	3.92	0.9	8.5	0.85	110	0.6
G48.49+0.06+50.27	52.3	2.2	0.7	4.15	1.9	8.2	0.43	278	0.1
G49.26-0.08+48.28	48.8	1.4	2.7	6.04	1.4	8.5	1.97	698	0.7
G49.57-0.29+50.17	51.3	1.5	1.3	3.42	1.3	8.5	0.54	154	0.2
G49.46-0.26+49.74	49.8	1.1	3.4	4.84	1.5	9.9	1.27	470	0.7
G48.66+0.23+3.45	3.8	0.8	1.2	5.56	1.2	8.6	0.78	185	0.6
G49.29-0.24+52.19	52.3	1.3	1.8	5.12	1.2	8.2	1.26	315	0.4
G49.51-0.23+50.68	51.8	1.6	2.4	3.32	1.3	9.8	0.64	176	0.2
G49.49-0.26+49.14	50.3	1.4	1.8	3.01	1.2	9.9	0.43	111	0.1
G48.84-0.03+18.03	18.8	1.0	1.1	6.75	1.7	8.4	0.97	501	0.7
G49.29-0.05+46.34	45.8	1.3	1.4	10.02	1.5	7.1	3.46	1367	1.5
G49.35-0.43+52.45	52.8	1.2	1.0	4.19	0.9	7.8	0.70	104	0.2
G48.84-0.28+48.19	47.3	1.0	0.6	6.73	1.8	7.5	0.85	448	0.6
G48.80-0.17+13.18	12.8	1.5	0.9	7.73	2.4	7.3	1.52	1482	0.8
G48.68+0.21+13.59	13.3	1.0	1.3	8.78	1.3	7.6	2.11	600	1.2
G49.35-0.38+52.72	52.8	0.8	1.5	3.75	0.8	8.8	0.64	73	0.4
G48.71+0.12+51.65	52.3	1.1	1.1	8.28	2.0	7.6	1.73	1156	1.3
G48.97-0.14+50.60	51.8	0.9	2.3	4.24	0.8	8.4	1.26	141	0.5
G48.60+0.30+11.91	11.8	1.1	0.9	6.16	1.6	7.6	1.03	446	0.6
G49.57-0.39+54.10	54.3	0.9	1.3	5.17	1.0	9.0	0.68	107	0.4
G48.63+0.18+4.98	5.3	0.6	1.4	3.69	0.6	8.7	0.63	39	0.4
G49.47-0.21+44.33	44.3	1.6	1.4	1.93	1.5	10.6	0.20	76	0.1
G48.74+0.07+50.46	50.3	1.3	1.4	9.14	1.1	7.6	2.46	481	0.7
G48.79+0.10+52.06	52.8	0.7	1.1	5.15	1.6	8.9	0.58	260	0.9
G49.30-0.08+47.79	48.3	1.5	1.3	21.62	1.4	7.0	7.29	2338	2.2
G48.87-0.03+17.00	17.8	1.1	0.9	12.01	2.1	7.7	1.98	1535	1.6
G49.42-0.51+54.56	54.8	0.6	0.7	6.55	1.6	7.0	1.20	532	2.4
G49.47-0.54+54.86	54.8	0.7	0.8	4.69	1.2	7.9	0.64	166	0.8
G49.46+0.02+51.95	51.3	1.8	1.2	9.74	2.7	8.9	1.22	1553	0.5
G49.38-0.38+48.76	48.8	1.2	1.6	3.73	1.1	8.1	0.88	168	0.3
G48.66+0.05+17.17	16.8	1.2	0.7	16.74	1.8	7.0	3.16	1808	1.9
G49.50-0.11+54.90	55.3	1.1	1.5	5.20	1.8	9.5	0.65	348	0.4
G49.44-0.32+46.76	46.8	1.0	1.1	5.17	1.0	8.1	0.80	142	0.4

A.2 Clumps associated with the W51 GMC

Table A.2: Properties for the 1130/1575 clumps identified by CLUMPFIND associated with the W51 GMC. Radial velocities (v_{rad}), line widths ($\triangle$v), average integrated intensities (I_{av}), opacities (τ_{13}), diameters (D), excitation temperatures (T_{ex}), column densities ($N(H_2)$), mass estimates (M_{LTE}) and virial parameter (α) are given. Clump names are created from the l, b and v_{rad} positions of the individual clump centroid position.

Clump name	v_{rad} (km/s)	$\triangle$v (km/s)	I_{av} (Kkm/s)	τ_{13}	D (pc)	T_{ex} (K)	$N(H_2)$ ($\times 10^{22}$ cm^{-2})	M_{LTE} ($M_\odot$)	α
G49.49-0.37+59.93	60.8	1.9	103.3	3.15	0.6	56.1	5.58	366	0.4
G49.49-0.37+57.72	59.3	1.6	38.6	1.76	0.9	37.9	1.28	185	0.2
G49.48-0.40+56.33	56.8	1.4	32.7	3.98	0.8	30.7	2.15	259	0.4
G49.48-0.40+57.52	57.8	1.0	35.2	2.01	0.8	36.0	1.28	123	0.4
G49.48-0.39+57.69	57.8	1.0	26.6	1.71	0.7	35.7	0.87	67	0.3
G49.50-0.38+59.94	60.3	1.4	42.7	3.95	0.8	38.8	2.68	293	0.5
G49.49-0.38+59.60	59.8	1.4	35.4	5.39	0.7	40.7	2.98	264	0.5
G49.00-0.32+72.48	72.8	1.6	8.9	1.78	1.1	27.4	0.32	70	0.1
G49.50-0.36+60.11	60.8	1.4	35.7	2.90	0.8	41.8	1.71	201	0.3
G49.49-0.38+58.96	58.3	1.0	41.4	5.21	0.6	37.6	3.39	188	0.8
G49.47-0.39+56.32	57.3	1.9	25.2	2.26	1.0	29.7	1.04	170	0.1
G49.01-0.30+67.02	67.8	1.6	12.8	1.14	0.8	26.4	0.37	36	0.1
G49.48-0.39+59.44	59.8	0.9	33.6	4.65	0.8	36.3	2.47	250	0.8
G49.48-0.37+62.57	62.3	1.5	40.0	5.25	0.7	31.6	3.39	260	0.5
G49.22-0.34+67.78	68.3	1.6	15.7	3.54	1.2	23.4	1.06	243	0.2
G49.18-0.35+68.77	68.8	1.2	11.7	1.05	0.9	26.5	0.32	46	0.1
G49.50-0.37+59.90	60.8	1.2	35.3	5.24	0.6	38.5	2.90	190	0.5
G49.47-0.38+63.77	63.3	1.5	32.8	3.42	1.1	37.2	1.81	388	0.4
G49.47-0.40+54.69	56.3	1.6	24.2	2.72	1.3	28.2	1.17	355	0.3
G49.50-0.38+61.93	62.8	1.4	26.9	6.34	0.9	30.1	2.78	419	0.6
G49.48-0.36+58.06	59.8	1.7	29.4	2.89	1.1	37.7	1.40	274	0.2
G49.48-0.38+60.29	61.8	1.2	23.7	2.90	1.0	35.6	1.14	207	0.4
G48.99-0.30+67.44	68.3	2.2	21.4	2.27	1.1	27.5	0.91	178	0.1
G49.02-0.30+66.43	67.3	1.4	16.0	1.82	1.0	24.0	0.63	117	0.2
G49.02-0.27+69.43	69.3	1.1	8.3	1.63	0.9	30.5	0.27	38	0.1
G49.49-0.38+63.77	62.3	1.6	24.1	7.14	1.0	30.9	2.79	439	0.5
G48.93-0.28+70.05	70.8	1.5	17.4	1.11	1.1	31.6	0.46	97	0.1
G49.08-0.27+66.72	67.3	1.1	8.6	1.91	1.1	24.1	0.35	79	0.1
G49.48-0.36+60.75	60.8	2.5	33.5	2.86	0.8	30.5	1.65	163	0.1
G49.00-0.30+66.79	67.8	1.6	37.6	1.25	0.7	25.1	1.17	103	0.1
G49.50-0.37+62.72	62.3	1.4	27.8	7.53	0.7	31.3	3.38	307	0.5
G49.20-0.33+64.53	64.8	0.9	8.8	2.46	0.8	24.7	0.42	49	0.2
G49.01-0.31+67.92	68.3	1.0	14.1	1.38	0.7	23.0	0.49	42	0.1
G49.48-0.35+61.54	60.8	1.5	44.9	2.36	0.9	32.1	1.87	237	0.3

Clump name	v_{rad} (km/s)	$\triangle$v (km/s)	I_{av} (Kkm/s)	τ_{13}	D (pc)	T_{ex} (K)	N(H_2) ($\times 10^{22}$ cm^{-2})	M_{LTE} ($M_\odot$)	α
G48.93-0.27+69.20	69.8	1.3	25.6	2.20	1.1	31.5	1.02	226	0.3
G49.21-0.34+63.33	64.3	2.1	4.1	2.22	1.0	23.5	0.19	31	0.0
G49.48-0.37+61.53	61.8	0.9	31.0	2.77	0.7	31.9	1.46	126	0.5
G49.49-0.37+66.45	63.3	1.8	19.7	3.92	1.4	32.5	1.26	439	0.2
G49.51-0.36+61.39	62.3	1.3	25.3	1.58	0.8	27.8	0.84	94	0.2
G49.10-0.26+63.92	64.8	2.0	5.2	2.33	1.2	20.4	0.28	73	0.0
G49.51-0.35+63.07	62.3	1.5	24.5	1.58	1.0	28.5	0.81	128	0.2
G48.91-0.27+70.73	70.3	1.7	10.0	2.01	1.0	29.2	0.38	68	0.1
G49.00-0.31+66.15	67.3	1.4	16.0	1.27	0.9	23.8	0.52	73	0.1
G48.91-0.27+67.39	68.3	1.1	13.0	2.28	1.3	26.2	0.57	175	0.3
G49.10-0.25+66.45	64.8	1.5	9.0	3.41	1.1	18.8	0.71	144	0.2
G48.96-0.28+71.70	72.3	1.1	13.9	2.01	0.9	29.7	0.53	78	0.2
G49.50-0.42+60.53	60.8	1.4	26.8	1.29	0.8	27.0	0.81	93	0.2
G49.52-0.37+61.75	61.8	1.6	19.8	1.70	1.0	25.2	0.73	124	0.1
G49.04-0.29+66.80	66.3	1.1	8.6	2.03	1.2	22.6	0.38	91	0.2
G48.92-0.29+70.97	70.8	1.5	12.7	0.54	1.0	26.1	0.28	47	0.1
G49.12-0.26+64.59	65.3	1.2	9.4	0.60	1.2	19.2	0.27	71	0.1
G49.51-0.36+62.75	61.8	1.5	36.5	1.34	0.7	28.8	1.10	94	0.2
G49.49-0.41+61.26	61.3	1.7	27.2	1.30	0.7	28.0	0.81	72	0.1
G49.15-0.37+66.67	66.8	2.6	4.9	1.70	1.0	20.1	0.21	36	0.0
G49.08-0.28+71.50	72.3	1.2	6.7	1.88	0.8	22.4	0.28	35	0.1
G49.03-0.33+65.35	65.3	1.4	10.3	1.58	1.1	28.8	0.34	75	0.1
G49.03-0.30+64.10	64.3	1.1	4.6	3.79	1.0	21.2	0.36	56	0.1
G49.48-0.34+59.50	60.8	2.4	41.4	1.29	1.1	28.0	1.23	260	0.1
G48.91-0.28+66.34	67.8	1.3	11.4	1.43	0.9	26.5	0.37	49	0.1
G49.48-0.35+68.22	65.8	2.1	27.6	2.07	1.2	27.0	1.11	260	0.1
G49.09-0.25+64.56	64.8	1.2	7.6	1.80	0.8	19.6	0.35	40	0.1
G49.06-0.35+65.18	66.3	1.6	11.8	2.54	0.8	24.5	0.59	59	0.1
G49.09-0.28+69.90	70.3	1.1	7.8	0.62	0.9	24.4	0.19	24	0.1
G48.91-0.29+68.26	68.8	1.2	12.6	0.92	0.9	27.0	0.33	42	0.1
G49.16-0.36+66.95	67.3	1.6	6.0	0.46	1.2	17.5	0.18	44	0.0
G49.49-0.42+59.32	60.8	1.2	26.6	1.55	0.7	25.6	0.92	83	0.2
G49.49-0.40+59.06	60.8	1.6	34.2	1.23	0.6	26.1	1.03	59	0.1
G49.39-0.32+61.62	61.3	1.6	11.2	3.24	1.6	24.0	0.69	320	0.2
G49.06-0.32+66.62	66.8	1.0	12.4	1.08	0.8	23.2	0.38	37	0.1
G49.52-0.36+58.51	60.8	1.5	21.3	1.23	1.2	23.9	0.68	161	0.2
G48.94-0.28+69.45	70.3	1.2	15.9	1.19	0.9	25.3	0.48	72	0.1
G48.95-0.29+69.08	69.3	0.9	11.4	2.09	1.0	23.4	0.50	91	0.3
G48.95-0.27+70.01	71.3	1.1	8.8	1.30	1.2	24.1	0.28	69	0.1
G48.98-0.29+70.76	71.3	0.8	9.7	1.48	1.0	28.0	0.31	53	0.2
G49.12-0.29+69.23	69.8	0.9	3.9	1.59	1.0	19.5	0.17	26	0.1
G49.49-0.40+59.75	60.3	0.9	22.4	2.48	0.6	27.5	1.02	61	0.3
G49.10-0.28+69.56	69.8	0.9	7.9	0.74	0.8	20.7	0.23	22	0.1
G49.07-0.31+67.77	67.3	1.3	8.0	1.27	0.9	21.6	0.28	37	0.1

Clump name	v_{rad} (km/s)	$\triangle$v (km/s)	I_{av} (Kkm/s)	τ_{13}	D (pc)	T_{ex} (K)	N(H_2) ($\times 10^{22}$ cm^{-2})	M_{LTE} ($M_\odot$)	α
G49.27-0.34+67.29	67.3	2.3	12.9	3.71	1.7	23.1	0.91	440	0.1
G49.49-0.39+62.30	61.8	1.1	13.8	2.95	1.0	26.0	0.74	125	0.3
G48.96-0.30+68.43	69.3	0.9	8.0	2.28	0.9	23.9	0.37	57	0.2
G48.99-0.31+68.93	68.8	1.1	7.7	0.70	1.1	18.1	0.25	50	0.1
G49.41-0.37+70.17	70.8	1.2	9.5	2.14	1.2	23.7	0.42	104	0.2
G48.97-0.30+68.57	69.3	1.0	18.1	1.93	1.1	22.2	0.79	172	0.4
G49.02-0.30+64.31	64.3	0.9	7.4	4.03	1.4	19.5	0.65	215	0.5
G49.06-0.35+66.70	66.8	1.0	8.1	2.41	0.7	23.4	0.40	36	0.1
G49.09-0.26+64.19	64.8	1.3	6.5	1.48	1.1	19.4	0.27	51	0.1
G48.98-0.29+73.27	73.3	0.9	8.1	0.34	0.9	25.2	0.17	24	0.1
G49.51-0.38+56.24	57.3	1.7	24.2	1.71	1.0	22.2	0.97	162	0.2
G49.49-0.41+57.36	58.3	1.0	16.5	2.80	0.9	20.8	1.00	151	0.4
G49.21-0.34+67.28	67.8	1.3	8.0	4.49	0.9	20.3	0.75	100	0.2
G49.48-0.41+60.35	58.8	1.3	21.6	0.91	0.8	21.5	0.65	64	0.1
G49.51-0.37+60.20	61.3	1.0	25.8	1.56	0.7	26.6	0.87	63	0.2
G49.03-0.31+66.09	65.8	1.4	12.7	0.98	0.8	19.7	0.43	52	0.1
G49.07-0.29+64.95	64.8	1.1	6.4	2.32	1.2	19.5	0.36	88	0.2
G48.89-0.41+60.74	61.8	1.1	5.6	3.57	1.3	21.4	0.41	125	0.2
G48.89-0.28+68.30	68.3	1.1	8.3	1.35	0.8	24.9	0.27	27	0.1
G49.48-0.41+56.60	58.3	1.5	25.9	3.17	0.7	19.7	1.83	149	0.2
G49.49-0.35+61.72	62.3	0.7	16.6	2.33	0.7	30.8	0.69	58	0.3
G49.49-0.35+63.75	63.8	1.4	24.6	1.14	0.7	28.9	0.68	62	0.1
G49.07-0.35+65.02	65.3	1.7	15.7	2.30	1.0	20.9	0.81	142	0.1
G49.10-0.28+68.34	68.8	1.1	4.4	1.32	0.8	19.4	0.17	19	0.1
G49.18-0.33+68.15	67.8	1.1	12.3	4.43	1.1	21.3	1.09	206	0.4
G49.45-0.39+72.28	72.3	1.2	6.0	1.41	1.2	18.0	0.26	61	0.1
G49.51-0.35+63.90	64.3	1.0	17.2	2.31	1.0	22.0	0.85	137	0.4
G49.05-0.32+66.44	66.8	1.4	10.8	1.12	1.0	19.9	0.38	61	0.1
G48.90-0.28+67.82	68.3	1.0	12.5	1.82	0.7	23.0	0.51	38	0.1
G49.23-0.33+67.75	67.8	1.6	18.8	2.37	1.3	16.5	1.29	373	0.3
G49.45-0.38+72.71	72.8	1.2	4.9	1.83	0.9	18.3	0.25	36	0.1
G49.21-0.33+68.49	68.3	1.4	12.4	4.94	1.1	15.8	1.72	375	0.5
G49.53-0.35+61.16	60.8	1.9	19.9	2.00	1.1	20.2	0.96	195	0.1
G49.47-0.36+69.76	69.3	2.0	13.3	2.93	1.1	23.8	0.75	170	0.1
G49.47-0.33+60.83	60.8	2.1	26.2	1.78	1.4	20.9	1.13	390	0.2
G49.15-0.36+71.51	71.3	1.2	3.5	0.89	1.0	16.7	0.13	24	0.0
G49.50-0.35+64.31	64.3	1.5	35.1	1.88	0.7	25.0	1.38	106	0.2
G49.41-0.35+64.37	65.8	1.9	14.2	2.55	1.1	19.5	0.85	167	0.1
G49.29-0.06+59.82	60.3	1.2	4.3	2.21	1.1	17.0	0.27	56	0.1
G49.47-0.36+65.46	64.3	1.7	32.7	2.67	0.8	24.4	1.68	166	0.2
G49.03-0.27+64.68	64.8	0.8	3.1	2.65	1.1	21.6	0.17	37	0.1
G49.07-0.28+64.24	64.8	0.9	3.8	2.31	0.9	18.6	0.22	30	0.1
G49.11-0.29+62.71	63.3	1.0	5.2	1.25	1.4	17.1	0.23	82	0.1
G49.52-0.39+57.20	57.8	1.6	21.0	1.40	0.8	20.5	0.80	94	0.1

Clump name	v_{rad} (km/s)	$\triangle$v (km/s)	I_{av} (Kkm/s)	τ_{13}	D (pc)	T_{ex} (K)	N(H_2) ($\times 10^{22}$ cm^{-2})	M_{LTE} ($M_\odot$)	α
G49.17-0.34+66.10	67.3	0.8	6.1	2.93	0.8	17.5	0.46	48	0.2
G49.67-0.45+68.64	69.3	1.7	7.3	2.47	1.1	21.7	0.38	78	0.1
G49.54-0.40+58.62	59.3	1.6	9.0	1.43	1.4	19.7	0.36	112	0.1
G49.47-0.36+64.48	64.3	0.9	22.1	2.53	0.7	23.5	1.12	83	0.4
G49.44-0.36+65.46	65.8	2.1	23.0	2.50	1.3	19.5	1.35	385	0.2
G49.11-0.25+62.30	63.3	1.4	4.4	0.43	1.1	14.4	0.17	37	0.0
G49.11-0.27+68.29	68.3	0.7	6.3	1.28	0.7	16.0	0.31	24	0.2
G49.44-0.53+59.37	59.8	0.7	5.3	2.38	0.9	16.3	0.37	51	0.3
G49.48-0.43+62.77	62.8	1.4	10.6	0.72	1.4	16.5	0.39	121	0.1
G49.46-0.41+55.96	56.8	1.9	15.6	1.82	1.0	17.3	0.84	152	0.1
G49.08-0.28+64.88	65.3	0.6	8.4	1.31	0.6	18.4	0.35	20	0.2
G49.42-0.51+59.00	59.8	1.1	4.8	1.63	1.7	17.3	0.24	118	0.2
G49.09-0.27+64.79	64.8	0.8	6.6	0.77	0.8	17.0	0.24	28	0.1
G48.91-0.26+68.04	68.3	1.4	6.6	2.26	1.7	21.1	0.33	161	0.1
G49.47-0.42+59.75	59.3	0.9	12.4	2.32	1.2	16.1	0.87	233	0.6
G49.67-0.46+68.79	69.3	1.5	10.0	2.24	1.1	22.6	0.48	93	0.1
G49.41-0.35+69.50	70.3	1.0	6.8	0.78	1.1	18.7	0.22	47	0.1
G48.88-0.27+67.64	67.8	1.2	4.6	1.60	1.2	21.0	0.18	44	0.1
G49.51-0.39+59.07	59.3	1.5	19.5	2.08	0.8	19.1	1.02	117	0.2
G49.47-0.41+63.17	63.3	1.3	12.2	1.50	1.3	17.1	0.59	177	0.2
G49.20-0.34+72.08	72.3	1.4	2.5	0.69	1.0	16.9	0.09	14	0.0
G49.17-0.35+65.28	65.3	1.2	2.8	1.09	1.4	14.5	0.15	48	0.1
G49.19-0.33+65.32	65.8	0.9	5.9	3.85	0.8	18.4	0.53	64	0.3
G49.47-0.36+61.95	63.8	1.4	13.6	0.89	0.9	21.5	0.40	62	0.1
G49.16-0.21+64.86	64.8	1.0	7.8	0.75	1.0	20.1	0.23	37	0.1
G49.48-0.34+65.35	64.8	1.2	17.3	1.66	1.1	20.1	0.74	156	0.2
G49.48-0.42+61.33	60.8	1.4	13.8	2.63	1.0	16.6	1.02	171	0.3
G48.86-0.26+66.37	66.8	1.1	9.2	1.49	0.9	18.1	0.41	64	0.1
G49.47-0.37+55.22	56.3	1.2	13.6	0.62	1.0	20.6	0.37	59	0.1
G49.04-0.31+65.32	65.3	1.2	13.7	1.36	1.0	20.1	0.53	87	0.2
G49.03-0.27+68.64	69.3	0.9	4.5	0.80	0.9	16.5	0.17	23	0.1
G49.48-0.42+56.56	56.8	1.1	19.5	3.60	0.5	16.2	1.96	94	0.4
G49.49-0.43+56.55	56.8	1.1	15.6	3.62	1.0	16.2	1.56	262	0.6
G49.50-0.43+59.96	59.3	1.7	20.3	2.06	1.1	18.5	1.10	239	0.2
G49.50-0.34+64.57	64.3	1.5	29.3	2.01	0.8	23.3	1.26	121	0.2
G49.50-0.40+61.97	60.3	1.8	13.0	0.80	0.7	18.1	0.44	39	0.0
G49.37-0.35+64.62	65.3	1.9	10.8	4.58	1.5	18.6	1.14	444	0.2
G48.93-0.29+66.83	66.8	1.0	5.5	1.52	1.2	18.3	0.25	58	0.1
G48.96-0.29+73.25	73.3	1.3	5.5	1.21	0.8	20.3	0.20	21	0.0
G49.16-0.19+60.64	61.8	2.2	3.1	0.78	1.2	18.5	0.10	26	0.0
G49.47-0.43+57.76	57.3	1.0	11.9	4.14	0.7	15.3	1.47	138	0.5
G49.39-0.31+56.01	56.3	1.2	7.7	0.84	1.1	18.8	0.25	51	0.1
G49.46-0.35+60.18	60.8	1.9	17.7	0.63	1.2	19.8	0.51	123	0.1
G49.20-0.33+66.50	66.3	1.2	10.7	2.95	0.8	18.2	0.77	84	0.2

Clump name	v_{rad} (km/s)	$\triangle$v (km/s)	I_{av} (Kkm/s)	τ_{13}	D (pc)	T_{ex} (K)	$N(H_2)$ ($\times 10^{22}$ cm^{-2})	M_{LTE} ($M_\odot$)	α
G49.50-0.40+58.09	58.3	1.3	21.1	1.46	0.6	21.2	0.80	43	0.1
G49.09-0.28+64.73	64.8	0.7	4.6	1.01	0.8	17.2	0.18	22	0.1
G49.50-0.41+59.74	59.3	0.9	20.8	1.75	0.6	20.8	0.89	61	0.3
G49.44-0.52+59.16	59.8	0.8	4.9	2.18	0.9	17.6	0.29	38	0.2
G49.40-0.35+65.75	66.3	1.4	19.5	1.95	1.0	18.2	1.03	172	0.2
G49.51-0.35+67.41	65.8	1.7	8.8	3.25	1.3	19.5	0.65	183	0.1
G49.51-0.40+61.04	59.8	1.7	16.2	1.03	0.9	20.1	0.54	70	0.1
G49.50-0.40+57.60	58.8	0.8	15.6	1.21	0.7	20.8	0.54	51	0.2
G49.42-0.36+65.66	65.8	2.1	16.2	1.62	0.8	17.8	0.78	79	0.1
G49.03-0.35+65.29	65.8	1.0	4.0	1.16	1.1	18.9	0.15	28	0.1
G49.41-0.38+67.43	67.3	1.4	12.5	1.78	1.3	18.8	0.60	165	0.2
G49.46-0.35+68.45	67.3	2.0	21.3	2.86	0.8	20.1	1.35	134	0.1
G49.45-0.36+65.43	66.3	3.1	11.3	2.16	1.5	15.4	0.80	293	0.1
G49.38-0.34+64.50	65.8	1.5	21.9	3.93	1.4	18.1	2.06	679	0.6
G49.19-0.32+64.41	65.8	1.8	5.6	1.32	1.1	18.2	0.23	45	0.0
G48.87-0.27+67.09	67.3	1.1	5.1	1.65	0.9	18.3	0.24	36	0.1
G49.42-0.33+64.13	64.8	1.5	12.7	1.40	1.4	18.2	0.55	170	0.2
G48.98-0.30+72.37	72.8	1.2	7.6	1.79	0.7	16.9	0.42	34	0.1
G49.47-0.41+68.51	70.3	1.5	8.9	2.04	2.0	14.9	0.64	440	0.3
G49.04-0.28+68.94	69.3	0.9	3.0	0.05	0.8	15.2	0.09	9	0.0
G49.35-0.36+67.46	67.3	1.2	7.0	2.26	1.3	17.6	0.43	120	0.2
G49.13-0.28+67.55	67.8	1.2	3.8	1.62	1.1	15.1	0.23	47	0.1
G48.97-0.28+69.47	69.8	1.2	8.4	0.64	1.0	17.8	0.27	45	0.1
G48.88-0.25+67.23	67.8	1.2	4.0	1.55	2.3	16.8	0.20	186	0.1
G49.13-0.24+68.57	68.8	0.9	3.4	0.68	0.9	16.3	0.13	18	0.1
G49.46-0.42+63.60	64.3	1.6	11.8	0.76	1.1	16.3	0.45	101	0.1
G49.41-0.48+60.93	61.3	0.7	6.0	1.42	0.8	17.9	0.27	26	0.2
G48.97-0.30+66.33	66.8	1.0	5.7	1.50	0.9	18.6	0.25	35	0.1
G49.06-0.33+65.07	65.3	1.0	8.0	1.74	1.1	17.9	0.40	75	0.2
G49.01-0.32+67.50	67.8	1.2	6.4	1.31	1.1	16.2	0.31	70	0.1
G49.39-0.36+69.85	71.3	1.1	7.0	2.08	1.0	17.7	0.40	70	0.1
G48.97-0.30+72.28	72.8	1.0	7.2	0.23	0.7	18.1	0.19	14	0.1
G49.42-0.49+61.38	61.8	1.1	4.3	1.23	0.8	15.3	0.22	27	0.1
G49.06-0.29+69.38	69.8	0.8	2.7	0.42	1.1	15.7	0.09	19	0.1
G49.09-0.34+64.41	64.8	0.9	4.5	1.11	0.8	16.1	0.20	24	0.1
G49.11-0.27+62.82	63.3	1.1	5.8	1.70	1.1	12.8	0.49	106	0.2
G49.50-0.42+56.19	58.3	1.0	16.2	2.29	0.8	17.8	0.99	108	0.3
G49.51-0.42+63.79	62.8	0.9	6.0	0.82	1.0	17.2	0.22	34	0.1
G49.50-0.46+56.96	58.3	1.7	3.2	1.31	2.2	12.5	0.24	209	0.1
G48.90-0.26+67.64	68.3	1.6	8.0	1.50	1.1	17.7	0.37	83	0.1
G49.07-0.31+63.61	64.8	1.4	5.7	2.08	1.1	16.7	0.35	68	0.1
G49.50-0.42+62.13	61.3	1.0	8.5	1.19	0.8	19.5	0.31	38	0.1
G49.57-0.40+62.04	61.3	1.6	7.7	0.61	0.8	16.8	0.27	33	0.0
G49.21-0.35+63.13	63.8	1.5	4.3	1.19	1.1	14.1	0.25	50	0.1

Clump name	v_{rad} (km/s)	$\triangle$v (km/s)	I_{av} (Kkm/s)	τ_{13}	D (pc)	T_{ex} (K)	N(H_2) ($\times 10^{22}$ cm^{-2})	M_{LTE} ($M_\odot$)	α
G49.42-0.38+67.60	67.8	1.9	12.1	2.39	1.1	17.2	0.79	155	0.1
G49.40-0.36+65.06	65.8	1.4	15.1	1.34	1.0	16.4	0.73	135	0.2
G49.20-0.30+65.86	66.8	2.2	7.7	1.85	1.1	15.7	0.48	105	0.1
G49.04-0.36+65.94	66.8	1.2	3.1	1.30	1.2	15.1	0.17	41	0.1
G49.26-0.41+66.40	66.3	1.7	6.7	1.77	1.5	16.5	0.38	142	0.1
G49.47-0.34+68.51	68.8	1.5	15.5	2.60	0.9	18.9	0.97	146	0.2
G49.51-0.42+60.74	61.3	0.9	11.5	1.48	0.7	16.8	0.57	47	0.2
G49.41-0.36+64.00	65.3	1.7	11.6	1.22	0.7	16.9	0.51	48	0.1
G49.45-0.35+67.05	67.3	1.2	16.6	2.76	0.9	15.6	1.39	180	0.4
G49.05-0.36+66.59	67.3	1.9	3.8	0.27	0.9	16.7	0.11	17	0.0
G49.02-0.34+64.67	65.3	0.8	3.4	1.23	0.9	18.9	0.13	18	0.1
G49.07-0.32+60.65	60.3	1.4	12.2	4.59	1.2	16.8	1.45	369	0.4
G49.43-0.35+67.29	67.3	1.2	8.1	1.38	1.0	16.2	0.41	68	0.1
G49.37-0.35+67.26	66.8	1.1	10.0	4.72	1.1	16.8	1.22	248	0.5
G49.53-0.35+56.92	57.8	1.7	8.9	3.11	1.1	18.8	0.65	138	0.1
G49.42-0.37+66.23	66.8	1.1	11.5	2.78	0.7	17.0	0.86	78	0.2
G49.43-0.34+64.93	65.3	1.4	11.5	1.74	0.7	19.7	0.52	48	0.1
G49.17-0.34+68.56	67.8	1.3	8.8	0.88	0.9	15.9	0.36	46	0.1
G49.42-0.36+64.83	66.3	1.8	18.5	2.68	0.7	17.8	1.27	95	0.1
G48.97-0.31+66.92	66.8	1.1	5.4	1.73	0.8	15.7	0.32	34	0.1
G49.25-0.41+66.18	66.8	1.6	3.1	2.59	1.3	17.5	0.21	61	0.1
G49.08-0.34+65.58	65.8	1.2	4.7	2.09	0.9	17.0	0.28	42	0.1
G49.00-0.32+67.63	67.8	1.3	7.3	1.33	1.0	14.0	0.45	83	0.1
G49.47-0.44+56.84	56.8	1.6	8.3	2.18	1.3	16.1	0.56	166	0.1
G48.83-0.25+64.93	65.3	0.9	2.5	1.08	1.1	13.8	0.14	29	0.1
G48.82-0.25+61.60	62.3	1.5	2.5	1.80	1.2	14.3	0.18	46	0.0
G49.11-0.27+69.69	69.8	0.5	2.4	1.08	0.6	13.8	0.14	8	0.1
G49.42-0.44+71.33	71.8	0.9	7.2	2.26	1.0	16.2	0.49	85	0.3
G49.52-0.40+59.95	59.8	1.4	12.5	0.87	0.8	16.2	0.50	48	0.1
G49.19-0.18+64.50	64.3	1.1	7.0	2.61	1.1	16.4	0.53	99	0.2
G49.14-0.30+67.16	67.3	1.0	1.8	0.88	1.1	14.1	0.09	17	0.0
G49.17-0.21+60.33	61.3	1.1	9.8	4.27	1.1	15.8	1.20	252	0.5
G49.40-0.46+69.46	69.8	0.9	7.2	3.35	1.1	16.9	0.63	129	0.4
G49.25-0.33+67.04	68.3	1.4	9.5	2.91	1.1	14.6	0.93	176	0.2
G49.06-0.33+59.97	60.3	1.1	7.6	2.81	1.3	17.6	0.55	148	0.2
G49.18-0.21+63.06	63.8	0.9	9.4	4.74	0.9	16.6	1.17	154	0.6
G49.02-0.31+59.19	59.8	1.0	2.6	1.98	1.1	15.4	0.18	38	0.1
G49.18-0.19+65.96	65.8	0.9	6.9	2.67	0.9	15.6	0.56	83	0.3
G49.41-0.33+64.20	64.8	1.5	11.1	2.64	1.4	15.9	0.87	279	0.2
G49.48-0.58+69.40	69.8	0.8	1.5	2.49	1.7	15.7	0.12	57	0.1
G48.97-0.34+67.13	67.3	1.0	4.5	1.21	1.4	14.9	0.24	82	0.1
G49.48-0.40+68.35	68.3	1.4	9.3	2.42	1.5	14.1	0.84	323	0.3
G49.13-0.34+63.05	63.3	1.5	2.5	0.94	1.2	16.8	0.10	24	0.0
G48.89-0.28+65.10	65.3	0.8	5.3	0.73	0.9	16.0	0.20	26	0.1

Clump name	v_{rad} (km/s)	$\triangle$v (km/s)	I_{av} (Kkm/s)	τ_{13}	D (pc)	T_{ex} (K)	N(H_2) ($\times 10^{22}$ cm^{-2})	M_{LTE} ($M_\odot$)	α
G49.44-0.39+69.90	69.8	0.9	5.9	1.26	1.0	15.6	0.30	51	0.2
G49.46-0.42+69.64	69.8	1.3	5.9	0.74	1.4	15.2	0.25	78	0.1
G49.45-0.44+56.43	56.8	1.0	11.8	2.48	0.8	15.7	0.90	96	0.3
G49.34-0.35+64.91	66.3	1.0	8.0	2.35	1.1	15.6	0.59	122	0.3
G49.40-0.37+64.09	65.3	2.1	7.5	1.22	1.1	15.2	0.39	78	0.0
G49.40-0.36+65.82	65.8	1.3	10.1	1.73	0.8	16.9	0.54	57	0.1
G49.58-0.39+62.05	61.8	1.0	5.2	0.51	0.6	16.2	0.18	11	0.1
G49.36-0.35+65.04	65.3	1.5	14.4	4.26	1.0	17.1	1.57	290	0.3
G49.46-0.34+67.51	68.3	1.3	15.1	2.31	0.6	16.4	1.03	70	0.2
G49.15-0.22+61.08	61.3	1.9	4.1	1.72	1.5	16.2	0.23	88	0.0
G48.82-0.26+64.32	64.8	0.7	3.2	0.12	0.7	13.2	0.13	12	0.1
G49.50-0.45+56.91	57.3	1.2	5.4	3.21	0.9	12.0	0.84	114	0.2
G49.34-0.34+67.89	67.3	1.0	9.2	3.16	1.2	15.1	0.91	231	0.5
G49.23-0.35+68.21	68.3	1.3	6.0	0.90	1.0	15.5	0.26	42	0.1
G49.50-0.44+56.91	57.3	1.4	12.5	3.05	0.9	14.2	1.34	169	0.3
G49.52-0.41+60.75	60.3	1.2	8.9	0.87	0.8	15.3	0.39	42	0.1
G49.43-0.36+65.78	66.3	1.2	19.7	1.61	0.6	17.3	0.99	53	0.2
G49.18-0.20+61.85	62.3	1.1	9.6	3.32	0.7	14.3	1.09	102	0.3
G49.09-0.35+62.47	64.8	1.7	4.1	1.23	0.9	15.8	0.20	28	0.0
G49.14-0.33+62.85	63.3	1.1	4.5	2.19	0.7	12.9	0.44	41	0.1
G49.44-0.34+67.31	67.8	1.9	5.9	2.14	1.0	13.9	0.49	77	0.1
G49.37-0.36+68.13	68.3	1.0	4.8	3.07	1.0	16.0	0.42	77	0.2
G49.44-0.03+60.71	61.3	1.5	3.9	2.42	1.7	15.7	0.29	138	0.1
G49.46-0.40+69.19	71.3	1.9	11.2	2.18	0.9	15.3	0.81	120	0.1
G49.02-0.32+63.65	63.8	0.8	6.4	1.77	0.8	14.2	0.45	47	0.2
G49.42-0.35+65.88	66.3	1.7	15.6	2.01	0.6	18.2	0.84	52	0.1
G49.12-0.27+67.61	67.8	1.1	3.1	1.55	1.3	13.2	0.23	66	0.1
G49.02-0.32+60.19	59.8	0.8	3.7	3.13	1.1	14.4	0.39	75	0.3
G49.46-0.41+58.39	58.3	1.6	9.7	2.12	1.0	15.7	0.66	110	0.1
G49.28-0.05+58.07	58.3	1.2	3.1	4.91	1.4	12.5	0.64	217	0.3
G49.04-0.32+63.27	63.8	0.9	4.5	1.94	0.8	15.5	0.30	33	0.1
G49.29-0.34+66.94	67.8	1.7	13.6	3.70	1.9	16.6	1.34	836	0.4
G48.98-0.28+68.43	69.3	1.0	6.3	0.97	0.9	16.9	0.25	34	0.1
G49.15-0.36+75.01	74.8	1.4	2.9	1.13	0.8	12.9	0.19	20	0.0
G49.46-0.34+69.09	68.8	1.7	9.8	2.53	0.9	16.4	0.71	92	0.1
G48.96-0.31+66.38	66.8	0.8	4.1	0.91	1.1	13.5	0.23	44	0.2
G49.11-0.24+65.47	65.8	1.3	3.8	1.57	1.2	12.1	0.34	80	0.1
G49.50-0.42+54.57	56.3	1.2	5.9	1.57	0.9	15.7	0.33	43	0.1
G49.49-0.33+60.42	62.3	2.0	6.8	1.27	1.8	16.6	0.32	173	0.1
G49.13-0.32+61.85	60.8	1.1	6.0	5.21	0.8	13.1	1.21	136	0.4
G49.52-0.42+61.80	63.3	1.1	15.4	1.02	0.9	17.4	0.60	85	0.2
G48.98-0.27+71.75	72.8	1.2	5.6	1.52	0.9	14.9	0.33	45	0.1
G49.46-0.36+64.09	63.8	1.0	8.7	1.68	0.9	16.1	0.49	74	0.2
G49.45-0.36+70.60	70.3	2.1	3.4	2.37	1.2	14.0	0.30	81	0.0

Clump name	v_{rad} (km/s)	$\triangle$v (km/s)	I_{av} (Kkm/s)	τ_{13}	D (pc)	T_{ex} (K)	$N(H_2)$ ($\times 10^{22}$ cm^{-2})	M_{LTE} ($M_\odot$)	α
G49.48-0.38+69.62	68.3	1.5	8.7	3.82	1.2	17.1	0.86	207	0.2
G49.11-0.32+64.85	64.8	1.4	4.4	1.99	1.0	15.5	0.29	52	0.1
G49.42-0.42+71.00	71.3	0.9	4.8	2.06	1.0	15.8	0.32	57	0.2
G49.44-0.44+56.92	57.3	0.9	7.3	1.59	1.1	15.0	0.44	84	0.2
G49.07-0.38+73.07	73.8	2.1	6.8	1.34	1.1	15.5	0.36	78	0.0
G49.34-0.37+57.08	57.8	1.1	4.4	1.24	1.4	14.6	0.24	81	0.1
G49.46-0.45+67.23	67.3	1.2	4.8	1.46	1.0	14.8	0.28	46	0.1
G49.45-0.39+64.58	65.8	1.4	5.6	1.10	1.2	12.7	0.38	89	0.1
G49.42-0.49+70.97	70.8	1.0	4.3	1.90	1.0	12.4	0.42	74	0.2
G49.43-0.37+69.36	69.3	0.9	6.0	1.41	0.9	16.4	0.30	41	0.1
G49.13-0.32+60.20	60.3	1.1	4.3	4.14	0.9	12.0	0.85	109	0.3
G49.49-0.33+66.66	66.3	1.3	12.1	0.68	0.9	15.3	0.49	76	0.1
G49.20-0.19+61.89	62.3	0.8	5.0	1.79	1.0	13.6	0.39	63	0.3
G49.17-0.20+61.26	61.8	0.8	6.9	3.55	0.7	15.7	0.71	55	0.3
G49.43-0.50+70.22	71.8	1.0	2.5	3.13	1.1	12.2	0.36	74	0.2
G49.46-0.37+66.92	65.8	1.2	8.3	2.18	0.8	13.5	0.74	81	0.2
G49.55-0.42+66.55	67.3	1.7	5.2	1.49	1.1	14.3	0.33	67	0.1
G49.43-0.48+58.25	58.3	1.0	5.6	2.36	0.9	11.5	0.74	95	0.3
G49.10-0.17+60.47	60.8	1.7	3.5	1.52	1.4	15.1	0.20	63	0.0
G49.43-0.39+65.76	66.3	1.2	5.8	1.56	1.0	14.7	0.36	56	0.1
G49.48-0.44+58.61	58.3	1.3	7.6	2.29	0.9	12.0	0.90	122	0.2
G49.42-0.45+71.05	71.3	1.0	6.9	2.97	1.1	15.2	0.65	129	0.3
G49.50-0.43+57.90	58.3	1.1	8.8	2.20	0.6	15.6	0.63	40	0.2
G49.53-0.40+60.90	60.8	0.8	8.9	1.13	0.7	16.0	0.41	32	0.2
G49.53-0.42+63.40	63.8	1.4	6.0	0.53	0.9	16.5	0.20	26	0.0
G49.19-0.19+64.59	64.8	0.9	6.6	2.92	0.7	15.5	0.59	46	0.2
G49.59-0.41+62.95	64.3	1.1	8.7	1.04	0.7	15.3	0.41	35	0.1
G49.46-0.33+68.67	69.3	1.1	7.9	2.80	0.9	14.0	0.80	115	0.3
G49.54-0.36+57.43	57.8	1.4	8.1	1.55	1.0	13.9	0.55	88	0.1
G49.66-0.46+66.28	67.3	1.2	4.0	1.91	1.1	14.0	0.31	69	0.1
G49.43-0.43+57.23	57.3	1.2	9.4	2.07	1.6	15.1	0.67	300	0.4
G49.16-0.33+65.52	63.3	2.1	2.8	2.02	1.1	12.2	0.29	55	0.0
G48.98-0.33+63.51	64.3	1.6	4.6	2.09	1.3	12.2	0.50	146	0.1
G49.41-0.46+70.41	70.3	1.2	6.4	3.36	1.2	14.2	0.74	170	0.3
G49.59-0.41+65.62	65.3	0.8	4.9	1.13	0.8	15.4	0.24	25	0.1
G49.09-0.24+62.39	62.8	1.4	3.2	3.46	1.1	11.6	0.58	125	0.2
G49.17-0.22+64.07	64.8	1.3	7.4	2.11	0.8	14.6	0.57	65	0.1
G49.16-0.28+62.37	63.3	2.2	5.5	1.93	1.8	14.4	0.40	215	0.1
G49.04-0.33+64.29	64.8	0.9	5.1	1.50	0.8	13.9	0.34	33	0.1
G49.43-0.48+59.64	60.3	1.5	4.5	1.65	2.1	14.6	0.29	211	0.1
G49.36-0.32+61.11	61.3	1.2	6.5	2.57	0.9	13.8	0.64	96	0.2
G48.99-0.35+69.59	69.3	1.2	4.0	0.96	1.0	14.5	0.20	35	0.1
G49.55-0.39+61.25	61.3	2.2	8.6	1.36	1.0	14.2	0.52	85	0.1
G49.20-0.19+65.04	65.3	0.7	2.8	0.43	0.8	13.7	0.12	12	0.1

Clump name	v_{rad} (km/s)	$\triangle$v (km/s)	I_{av} (Kkm/s)	τ_{13}	D (pc)	T_{ex} (K)	$N(H_2)$ ($\times 10^{22}$ cm^{-2})	M_{LTE} ($M_\odot$)	α
G49.01-0.33+63.15	64.3	1.3	5.1	0.93	1.1	14.0	0.26	60	0.1
G49.19-0.19+62.12	61.8	0.9	9.0	3.05	0.6	13.4	1.07	75	0.3
G48.73-0.16+66.37	66.8	1.2	1.7	0.61	1.4	14.4	0.07	26	0.0
G49.24-0.32+68.81	68.8	1.1	4.7	1.89	0.9	12.0	0.48	65	0.2
G49.17-0.20+63.26	63.3	0.6	5.5	3.46	0.7	15.4	0.57	44	0.4
G49.06-0.46+57.75	57.8	0.7	3.1	1.47	0.8	13.2	0.22	27	0.1
G49.26-0.32+68.95	68.8	1.1	5.2	1.22	1.0	13.2	0.35	58	0.1
G49.46-0.42+57.16	56.8	1.3	10.3	5.12	0.7	14.4	1.72	157	0.3
G49.58-0.39+60.96	61.3	1.4	3.2	0.31	1.0	16.1	0.10	18	0.0
G49.16-0.33+61.19	62.3	1.4	3.0	1.53	1.0	12.1	0.27	47	0.1
G49.43-0.39+64.22	64.8	1.4	5.7	2.11	1.1	15.6	0.39	89	0.1
G49.47-0.34+66.24	65.8	1.2	6.4	1.31	0.9	14.7	0.36	48	0.1
G49.45-0.39+68.02	68.3	1.0	5.6	1.55	0.7	11.7	0.54	51	0.2
G49.39-0.34+68.59	68.3	0.9	5.6	1.61	1.2	14.0	0.39	89	0.2
G49.46-0.37+60.77	61.8	1.5	12.3	0.50	0.7	17.4	0.38	31	0.1
G49.49-0.45+59.52	59.8	1.0	5.2	1.84	0.8	11.5	0.57	58	0.2
G49.17-0.20+60.15	61.8	0.9	6.1	6.03	0.8	14.5	1.19	124	0.5
G49.53-0.41+58.88	59.8	1.1	10.2	1.49	0.7	15.2	0.59	46	0.1
G49.49-0.47+59.09	59.3	1.4	2.9	1.41	1.3	11.3	0.29	88	0.1
G49.38-0.36+68.24	68.8	0.9	4.7	2.62	0.9	13.8	0.46	58	0.2
G49.52-0.35+67.37	67.3	1.1	7.2	2.89	0.9	16.7	0.58	81	0.2
G49.14-0.32+60.45	60.3	1.2	3.8	0.81	0.8	12.3	0.25	29	0.1
G49.39-0.33+62.60	63.3	1.1	6.1	4.58	0.8	14.6	0.90	109	0.3
G49.32-0.34+67.24	67.3	1.2	5.4	2.00	1.1	13.2	0.48	96	0.2
G49.42-0.39+65.91	66.8	1.7	8.3	1.88	0.9	14.0	0.63	93	0.1
G49.40-0.49+63.39	63.8	0.8	2.6	0.29	0.9	15.4	0.09	14	0.1
G49.43-0.01+61.38	61.3	1.2	4.9	2.45	1.2	13.7	0.46	120	0.2
G49.68-0.45+66.80	67.8	1.6	5.0	2.71	1.2	15.4	0.42	99	0.1
G49.39-0.50+64.43	64.8	0.7	2.0	1.30	1.4	14.2	0.12	37	0.1
G49.27-0.31+64.90	66.8	3.2	5.9	2.00	1.8	11.4	0.72	389	0.1
G49.56-0.41+64.88	64.3	1.4	5.5	1.11	1.0	13.5	0.33	55	0.1
G49.50-0.32+63.94	63.8	2.2	11.1	2.08	1.3	14.2	0.88	242	0.1
G49.05-0.29+65.36	65.3	1.1	2.9	1.58	0.8	11.8	0.28	29	0.1
G49.48-0.60+69.49	69.8	0.8	1.2	1.63	1.5	11.9	0.11	42	0.1
G49.01-0.26+69.51	70.3	0.9	2.9	1.24	1.0	14.0	0.17	31	0.1
G49.43-0.41+72.01	72.8	0.8	3.8	1.27	1.2	14.3	0.22	53	0.2
G49.43-0.33+62.57	64.3	1.7	7.8	1.99	1.3	13.1	0.70	202	0.1
G48.98-0.27+64.14	64.3	1.3	3.1	2.24	1.0	14.2	0.26	41	0.1
G48.73-0.14+66.77	67.3	0.6	3.2	0.00	0.6	12.4	0.14	8	0.1
G48.92-0.31+67.36	67.3	1.5	3.6	1.78	1.8	13.4	0.28	158	0.1
G49.52-0.34+62.70	63.8	1.3	9.0	1.38	0.7	16.5	0.44	38	0.1
G49.47-0.33+68.01	68.3	1.0	7.6	2.46	1.0	13.4	0.76	120	0.3
G49.66-0.32+62.17	62.3	1.0	2.2	1.06	1.2	13.4	0.13	31	0.1
G49.48-0.39+66.85	66.3	1.5	7.3	3.06	1.0	14.0	0.80	134	0.2

Clump name	v_{rad} (km/s)	$\triangle$v (km/s)	I_{av} (Kkm/s)	τ_{13}	D (pc)	T_{ex} (K)	N(H_2) ($\times 10^{22}$ cm^{-2})	M_{LTE} ($M_\odot$)	α
G49.11-0.32+61.24	60.8	1.0	6.3	5.74	0.9	12.6	1.51	209	0.6
G49.54-0.34+55.82	56.8	1.4	5.0	1.98	1.2	14.4	0.37	93	0.1
G49.51-0.43+59.82	58.8	1.4	13.1	3.48	0.7	14.3	1.54	137	0.3
G49.51-0.41+56.69	56.8	0.8	9.6	2.96	0.9	13.2	1.13	157	0.6
G49.71-0.45+68.71	68.8	0.8	5.0	3.47	0.8	13.2	0.68	69	0.4
G49.24-0.31+65.95	65.8	1.2	6.4	2.30	1.0	11.5	0.84	147	0.3
G49.72-0.47+67.65	68.8	0.8	3.1	2.23	0.8	13.2	0.29	35	0.2
G49.33-0.34+57.77	58.3	1.0	3.1	1.76	0.8	13.8	0.23	27	0.1
G48.88-0.27+64.56	65.3	1.3	2.4	0.53	1.3	14.0	0.11	30	0.0
G49.73-0.46+68.52	68.8	0.7	3.1	2.64	1.3	14.5	0.28	83	0.3
G49.38-0.31+61.64	61.8	1.3	8.6	2.12	1.2	12.8	0.83	211	0.3
G49.51-0.43+54.63	57.3	1.5	8.1	3.16	1.1	13.8	0.94	176	0.2
G49.47-0.43+65.33	64.3	1.4	7.0	1.37	0.8	13.7	0.46	55	0.1
G49.35-0.36+57.45	57.8	0.9	2.8	0.88	1.1	12.8	0.17	34	0.1
G49.23-0.29+62.95	62.8	1.2	3.8	1.55	0.8	12.5	0.32	32	0.1
G49.08-0.29+64.41	64.8	1.1	4.5	1.09	0.8	13.7	0.26	27	0.1
G49.16-0.20+66.61	67.3	1.0	3.0	1.82	1.2	13.0	0.25	59	0.1
G48.78-0.26+66.20	66.3	0.7	2.1	1.19	1.2	14.1	0.12	30	0.1
G49.45-0.45+57.07	57.3	1.3	7.9	2.74	1.1	12.9	0.93	202	0.3
G49.42-0.54+59.33	59.3	0.9	2.3	1.76	1.4	11.5	0.25	85	0.2
G49.36-0.31+61.28	61.3	1.3	6.7	2.44	0.9	13.3	0.67	95	0.2
G48.85-0.24+65.05	65.8	1.2	4.8	1.93	1.1	14.2	0.36	78	0.1
G49.46-0.36+67.12	67.3	0.7	8.2	1.92	0.6	15.3	0.54	29	0.3
G49.54-0.43+65.49	66.8	1.3	8.2	0.97	1.1	14.7	0.40	85	0.1
G48.81-0.25+64.28	64.3	0.7	3.3	0.89	0.7	12.1	0.23	20	0.2
G48.77-0.15+66.76	66.8	1.3	1.9	3.49	2.3	10.6	0.43	374	0.3
G48.99-0.32+66.57	66.8	1.4	4.8	2.25	0.9	11.5	0.62	95	0.1
G49.50-0.44+63.80	62.3	1.0	6.5	1.57	0.9	12.2	0.58	89	0.2
G48.74-0.14+66.45	67.3	1.1	3.6	0.81	1.2	12.1	0.24	61	0.1
G48.98-0.26+64.77	64.3	1.5	3.6	3.13	1.0	14.1	0.39	63	0.1
G48.74-0.15+66.79	67.3	0.6	3.9	0.34	0.6	13.8	0.16	11	0.1
G49.53-0.33+66.61	66.3	1.3	4.1	1.99	0.9	15.2	0.28	40	0.1
G48.84-0.26+65.67	66.3	0.9	2.3	1.45	1.0	13.1	0.17	31	0.1
G49.53-0.36+66.48	65.8	2.0	4.7	1.57	0.9	13.5	0.34	43	0.0
G49.52-0.40+55.79	56.3	1.0	6.3	1.50	1.0	13.2	0.47	80	0.2
G49.39-0.37+65.54	66.3	1.3	4.7	1.02	0.9	13.1	0.29	36	0.1
G49.56-0.40+61.36	61.8	1.3	10.4	1.34	0.9	14.0	0.65	82	0.2
G49.70-0.46+68.27	69.3	1.5	3.4	1.76	1.4	13.4	0.27	89	0.1
G49.22-0.29+65.33	63.8	3.4	3.1	1.56	1.8	13.0	0.24	125	0.0
G49.40-0.39+67.88	67.8	1.6	3.8	0.82	1.1	13.1	0.22	45	0.0
G49.12-0.33+61.84	62.3	1.1	4.3	5.65	0.9	13.4	0.90	114	0.3
G48.92-0.37+67.16	66.8	1.3	1.3	1.17	1.5	11.8	0.10	41	0.0
G48.80-0.25+64.57	64.3	1.0	3.6	1.99	0.9	13.0	0.32	43	0.1
G49.36-0.26+61.99	61.3	1.8	3.8	3.28	1.5	10.5	0.84	309	0.2

Clump name	v_{rad} (km/s)	$\triangle$v (km/s)	I_{av} (Kkm/s)	τ_{13}	D (pc)	T_{ex} (K)	N(H_2) ($\times 10^{22}$ cm^{-2})	M_{LTE} ($M_\odot$)	α
G48.89-0.37+67.29	67.3	1.1	1.7	2.52	0.9	10.3	0.32	40	0.1
G49.58-0.41+60.88	61.8	1.2	3.2	1.12	0.8	14.8	0.17	19	0.0
G49.26-0.33+70.88	70.3	0.8	3.9	2.27	1.2	12.7	0.41	98	0.3
G49.07-0.35+59.37	59.8	1.4	3.3	1.39	1.0	12.2	0.28	47	0.1
G49.59-0.42+67.11	68.3	1.8	6.5	1.77	1.0	13.9	0.48	85	0.1
G49.10-0.32+59.41	59.8	2.7	2.6	2.39	1.4	14.3	0.23	71	0.0
G49.60-0.24+56.19	56.3	1.3	6.3	3.55	1.0	17.2	0.58	105	0.2
G49.52-0.37+65.88	65.8	0.9	5.3	1.72	0.7	12.5	0.48	38	0.2
G49.37-0.33+61.86	62.3	1.7	10.0	2.25	1.0	13.1	0.96	152	0.1
G49.48-0.45+58.83	58.8	1.1	5.8	2.10	0.8	12.5	0.59	56	0.2
G49.13-0.25+60.39	61.3	1.7	2.0	2.71	1.1	12.4	0.25	52	0.0
G49.52-0.43+59.65	59.3	0.7	7.3	1.61	0.8	12.9	0.59	58	0.4
G49.24-0.35+65.69	66.8	2.0	5.3	2.15	1.0	14.6	0.41	74	0.1
G49.44-0.34+64.16	65.3	1.4	8.8	1.90	0.9	13.2	0.75	97	0.1
G49.12-0.27+69.34	69.8	0.6	2.1	1.67	0.6	10.7	0.26	18	0.2
G49.41-0.47+71.35	71.8	1.0	4.5	2.62	1.1	12.5	0.54	120	0.3
G49.03-0.32+59.12	59.3	0.9	2.3	2.46	1.1	13.2	0.24	50	0.1
G49.52-0.33+62.38	63.3	1.4	7.7	2.19	0.9	13.8	0.67	92	0.1
G49.58-0.41+63.16	62.8	1.3	5.9	1.53	0.8	12.8	0.47	57	0.1
G49.12-0.32+60.59	60.8	1.0	5.7	4.16	0.8	13.9	0.83	87	0.3
G49.43-0.41+61.77	61.8	1.5	3.8	1.33	1.2	12.4	0.30	73	0.1
G49.14-0.30+60.64	61.3	1.1	3.2	1.43	1.3	11.1	0.34	98	0.2
G49.28-0.31+65.06	65.8	1.4	4.1	3.09	1.1	10.9	0.79	169	0.2
G49.53-0.42+67.01	65.8	1.3	3.4	1.43	1.0	12.9	0.25	45	0.1
G49.40-0.32+64.23	64.3	1.3	6.1	5.25	1.0	13.4	1.18	206	0.4
G49.41-0.47+55.40	56.3	0.8	3.4	1.22	1.2	13.7	0.21	50	0.2
G49.17-0.19+63.88	64.3	0.7	4.2	1.25	0.8	13.0	0.29	28	0.2
G49.18-0.22+65.01	64.3	0.9	3.8	0.54	0.7	12.0	0.23	22	0.1
G48.82-0.25+64.63	64.8	0.7	2.7	0.99	0.7	11.0	0.24	19	0.1
G49.54-0.33+62.64	62.8	1.5	5.0	1.28	0.9	13.7	0.32	45	0.1
G49.46-0.44+56.82	56.8	1.2	6.0	1.41	0.7	14.0	0.38	32	0.1
G49.52-0.43+55.85	56.8	1.3	5.7	2.44	0.8	13.3	0.58	60	0.1
G49.44-0.49+57.95	58.3	0.7	3.5	2.26	1.0	10.7	0.55	99	0.5
G49.47-0.31+60.39	59.8	2.0	14.5	1.01	1.3	18.3	0.53	147	0.1
G49.45-0.42+57.43	56.8	1.0	7.9	1.95	1.0	13.1	0.70	129	0.3
G49.53-0.36+57.21	57.8	1.3	8.4	1.32	0.7	15.1	0.45	38	0.1
G49.47-0.33+65.33	64.3	0.8	6.9	1.14	0.8	13.5	0.42	50	0.2
G49.12-0.25+60.39	61.3	1.3	2.3	2.82	1.2	12.1	0.32	81	0.1
G49.48-0.45+59.35	58.3	1.8	6.4	2.61	0.7	12.5	0.77	57	0.1
G49.14-0.22+66.65	66.8	1.3	2.6	2.05	1.4	11.8	0.30	96	0.1
G49.38-0.33+65.26	64.8	1.1	6.0	2.62	1.0	12.8	0.68	126	0.3
G48.86-0.25+65.47	64.8	1.0	5.4	1.63	1.0	12.5	0.46	82	0.2
G49.53-0.40+62.68	61.8	0.9	4.1	1.50	1.1	13.7	0.28	59	0.2
G49.38-0.29+56.27	56.8	1.2	4.7	1.30	1.0	13.0	0.33	61	0.1

Clump name	v_{rad} (km/s)	$\triangle$v (km/s)	I_{av} (Kkm/s)	τ_{13}	D (pc)	T_{ex} (K)	N(H_2) ($\times 10^{22}$ cm^{-2})	M_{LTE} ($M_\odot$)	α
G49.36-0.34+63.77	64.3	1.1	7.8	3.25	0.8	13.4	0.97	104	0.3
G49.58-0.40+60.92	61.8	1.0	3.6	1.23	0.7	13.9	0.22	20	0.1
G49.13-0.28+59.43	60.3	2.3	3.4	2.55	1.6	10.8	0.56	235	0.1
G49.54-0.42+68.93	67.8	1.4	3.7	1.22	0.7	14.4	0.20	19	0.0
G48.88-0.40+61.46	62.8	1.1	3.4	5.98	1.2	11.9	0.97	247	0.5
G49.47-0.44+57.39	58.3	1.1	4.2	2.32	1.0	12.5	0.46	78	0.2
G49.63-0.30+61.43	62.3	1.7	6.8	1.98	1.4	13.4	0.58	183	0.1
G49.51-0.33+63.73	63.3	1.2	10.5	1.61	0.7	15.0	0.64	55	0.2
G49.15-0.24+67.74	67.8	0.7	2.0	1.74	1.2	13.7	0.15	39	0.2
G48.95-0.32+64.94	65.3	1.0	4.4	2.31	1.1	11.8	0.55	107	0.3
G49.37-0.33+67.58	68.3	1.1	5.1	2.48	1.1	13.1	0.53	116	0.2
G49.32-0.34+56.25	56.3	2.1	5.1	2.04	1.3	12.5	0.51	151	0.1
G49.18-0.32+72.52	72.8	1.5	3.6	1.80	1.5	12.9	0.31	115	0.1
G49.54-0.34+60.43	61.3	1.0	5.1	1.52	1.1	13.4	0.37	74	0.2
G48.97-0.33+62.35	62.8	1.6	3.5	2.44	0.9	10.5	0.61	79	0.1
G49.29-0.22+64.23	64.8	1.7	3.2	2.56	1.4	11.3	0.47	164	0.1
G49.24-0.28+63.24	63.8	1.3	2.8	1.47	1.2	12.3	0.23	58	0.1
G48.85-0.26+65.76	66.3	0.8	3.5	2.13	0.7	13.7	0.30	27	0.1
G49.54-0.32+62.28	62.8	1.5	6.8	1.44	1.2	13.3	0.48	113	0.1
G49.43-0.43+72.70	72.8	1.2	5.0	2.01	0.8	12.3	0.51	58	0.1
G49.42-0.46+57.34	58.3	1.0	6.2	2.22	1.1	12.8	0.63	137	0.3
G49.08-0.31+58.53	58.8	1.4	2.4	2.45	1.3	12.3	0.28	87	0.1
G48.86-0.41+60.83	62.3	1.3	5.0	3.84	1.4	13.4	0.72	240	0.3
G49.60-0.41+62.95	62.3	1.2	5.7	2.17	0.9	13.0	0.55	76	0.2
G48.85-0.26+63.39	63.3	0.7	2.6	1.44	1.0	14.4	0.16	28	0.1
G49.27-0.40+64.94	64.8	1.2	3.1	1.12	1.2	12.2	0.23	56	0.1
G49.52-0.44+59.68	60.8	1.0	4.3	1.50	0.9	13.0	0.33	48	0.1
G49.51-0.45+58.27	58.3	0.7	3.8	2.37	0.7	10.7	0.61	44	0.4
G49.53-0.32+64.46	64.3	1.2	6.9	2.84	1.1	13.4	0.78	166	0.3
G49.35-0.33+63.37	63.8	1.3	5.9	1.98	0.9	12.6	0.56	83	0.1
G49.44-0.58+60.16	60.3	1.0	2.5	3.95	1.5	10.4	0.67	256	0.5
G49.55-0.34+56.82	56.3	1.2	7.4	2.88	0.9	13.6	0.80	109	0.2
G49.29-0.24+63.98	64.3	0.8	2.8	1.85	0.8	11.4	0.32	32	0.2
G49.45-0.50+59.08	58.8	1.1	1.5	2.43	1.3	9.7	0.32	97	0.2
G48.81-0.26+63.51	63.8	0.7	2.4	1.96	0.7	10.4	0.36	31	0.2
G49.17-0.20+65.15	65.3	0.8	3.4	1.81	0.8	12.1	0.34	42	0.2
G49.55-0.30+62.43	61.8	1.6	5.6	3.86	1.4	12.3	0.98	337	0.2
G49.38-0.34+68.48	68.3	1.1	3.2	2.21	0.9	12.6	0.33	48	0.1
G49.58-0.27+57.60	57.3	2.3	2.4	1.50	1.4	12.0	0.22	73	0.0
G49.45-0.32+58.41	59.8	1.7	14.1	2.26	1.1	15.1	1.07	233	0.2
G49.33-0.28+61.11	60.3	1.6	5.7	3.39	1.5	9.7	1.59	636	0.4
G49.43-0.47+70.79	70.8	1.1	5.1	2.30	1.1	11.7	0.64	121	0.3
G49.53-0.35+66.91	66.3	1.5	4.9	4.64	1.0	11.8	1.09	198	0.2
G49.58-0.26+55.97	56.8	1.9	5.6	2.07	1.4	13.7	0.47	165	0.1

Clump name	v_{rad} (km/s)	$\triangle$v (km/s)	I_{av} (Kkm/s)	τ_{13}	D (pc)	T_{ex} (K)	N(H_2) ($\times 10^{22}$ cm^{-2})	M_{LTE} ($M_\odot$)	α
G48.85-0.40+67.09	67.3	0.9	4.4	2.11	1.2	14.0	0.36	82	0.2
G49.56-0.39+62.26	62.8	1.0	3.6	1.68	0.8	13.1	0.28	30	0.1
G48.76-0.25+65.06	66.3	1.2	1.2	1.52	1.5	11.4	0.13	49	0.1
G49.37-0.34+68.94	68.8	1.0	4.8	1.93	0.9	12.4	0.47	61	0.2
G48.96-0.21+63.70	63.8	1.2	1.4	1.95	1.6	12.8	0.12	55	0.1
G48.92-0.28+64.46	65.8	1.4	3.4	2.87	0.8	12.9	0.41	47	0.1
G49.45-0.32+61.24	59.8	1.7	9.1	1.36	0.9	14.7	0.52	66	0.1
G49.57-0.42+58.60	59.3	1.0	2.7	2.15	1.1	12.2	0.30	59	0.1
G49.21-0.32+68.56	67.8	1.2	6.9	3.59	1.0	11.4	1.33	241	0.5
G48.79-0.24+63.50	63.8	0.6	2.9	2.33	0.8	11.3	0.39	49	0.4
G49.58-0.29+61.23	61.3	1.2	4.4	2.91	0.9	12.1	0.63	87	0.2
G48.97-0.31+71.34	71.8	0.9	2.2	3.41	0.8	10.2	0.54	53	0.2
G49.28-0.24+64.40	65.3	1.7	3.0	2.99	1.1	11.5	0.48	106	0.1
G49.55-0.42+61.12	59.8	1.5	6.3	1.51	0.8	11.3	0.65	71	0.1
G49.20-0.18+63.04	63.8	1.0	4.5	1.73	0.8	12.1	0.43	51	0.2
G49.48-0.44+66.69	64.8	1.7	4.5	3.52	1.4	10.3	1.10	362	0.3
G48.90-0.42+60.20	60.8	1.1	2.6	6.35	0.8	10.7	1.04	125	0.3
G49.42-0.45+59.24	59.3	1.3	4.9	2.39	1.2	11.8	0.63	159	0.2
G49.63-0.47+69.67	70.3	0.9	4.4	3.72	0.9	11.9	0.80	124	0.4
G49.71-0.45+68.82	69.3	1.0	2.5	2.52	1.1	12.3	0.30	58	0.1
G49.35-0.37+64.30	63.8	1.4	2.9	1.94	1.4	11.3	0.36	128	0.1
G49.12-0.27+64.26	64.8	1.1	2.6	1.64	0.8	10.1	0.39	37	0.1
G49.17-0.23+62.45	63.3	1.3	4.5	1.75	0.9	11.8	0.46	64	0.1
G48.79-0.23+62.64	63.3	1.0	1.6	3.23	1.2	10.7	0.32	77	0.2
G48.88-0.49+58.00	58.8	0.9	2.8	3.48	1.4	12.8	0.41	136	0.3
G48.90-0.37+67.23	67.3	1.2	2.0	2.62	1.1	10.0	0.42	94	0.1
G49.73-0.47+67.70	68.8	1.2	3.1	2.01	1.2	12.6	0.30	75	0.1
G49.63-0.46+69.28	69.8	0.7	2.5	2.13	0.7	12.3	0.27	24	0.2
G49.34-0.33+67.96	68.3	1.4	5.8	2.74	1.2	11.8	0.82	212	0.3
G49.41-0.47+70.63	70.8	1.3	5.7	3.08	0.7	12.1	0.85	69	0.2
G48.94-0.31+65.53	65.3	1.4	4.2	2.64	1.2	12.1	0.55	130	0.2
G49.41-0.48+57.11	57.3	1.0	6.1	3.67	1.2	11.6	1.15	303	0.6
G49.51-0.44+62.64	62.8	1.0	4.2	1.64	0.8	11.5	0.44	44	0.2
G49.46-0.44+59.67	58.3	1.2	4.5	1.74	0.8	11.7	0.48	57	0.1
G48.98-0.31+65.76	66.3	1.0	3.7	3.11	0.8	10.2	0.85	102	0.3
G49.52-0.42+58.65	58.8	0.8	4.9	0.84	0.8	11.9	0.35	33	0.2
G49.44-0.39+66.93	67.3	0.9	5.0	2.45	0.8	11.3	0.71	68	0.3
G49.50-0.45+56.15	56.8	0.7	2.7	1.54	0.6	10.3	0.36	21	0.2
G49.50-0.45+64.90	63.8	1.4	4.3	2.23	1.1	11.1	0.61	116	0.2
G49.54-0.34+63.03	64.3	1.3	3.5	1.83	0.9	13.1	0.30	44	0.1
G49.09-0.22+62.10	62.3	1.1	1.8	2.84	1.1	10.2	0.38	75	0.2
G49.53-0.39+58.76	59.3	1.4	5.3	1.83	0.7	13.0	0.45	34	0.1
G49.35-0.30+61.89	62.3	1.4	5.0	3.36	1.1	11.3	0.91	192	0.2
G48.86-0.08+60.93	61.3	0.9	2.3	2.89	1.0	11.0	0.40	66	0.2

Clump name	v_{rad} (km/s)	$\triangle$v (km/s)	I_{av} (Kkm/s)	τ_{13}	D (pc)	T_{ex} (K)	N(H_2) ($\times 10^{22}$ cm^{-2})	M_{LTE} ($M_\odot$)	α
G48.94-0.33+64.99	65.3	0.8	1.9	2.71	0.8	10.4	0.37	40	0.2
G49.43-0.46+70.77	71.3	1.0	3.4	3.62	0.9	12.2	0.56	79	0.2
G49.45-0.34+63.80	62.8	1.0	7.1	2.07	0.8	12.2	0.76	77	0.3
G49.52-0.38+55.82	56.3	1.1	5.1	1.33	0.9	13.1	0.36	45	0.1
G49.61-0.42+62.91	62.8	1.0	3.7	1.20	0.9	12.5	0.27	34	0.1
G49.42-0.47+57.45	57.8	1.1	5.8	3.20	0.8	11.1	1.10	117	0.3
G49.47-0.29+57.87	59.3	1.6	5.5	1.97	1.5	14.9	0.39	153	0.1
G48.95-0.20+63.47	63.3	1.0	2.0	1.53	1.0	11.8	0.19	32	0.1
G49.52-0.44+56.20	57.3	1.4	4.5	1.39	1.0	12.2	0.37	61	0.1
G49.30-0.23+63.65	64.3	1.1	4.5	2.58	1.3	11.4	0.65	185	0.4
G49.19-0.29+61.08	61.8	1.9	3.6	1.90	1.2	12.0	0.37	97	0.1
G49.12-0.29+60.19	60.8	0.8	2.9	3.05	0.8	9.6	0.76	79	0.4
G49.21-0.35+66.89	67.3	1.2	2.2	2.98	1.0	9.8	0.55	86	0.2
G49.02-0.32+64.35	64.8	0.9	3.7	2.01	0.7	11.5	0.44	36	0.2
G49.49-0.32+67.14	67.8	1.4	4.9	1.35	1.2	12.7	0.36	84	0.1
G49.45-0.40+55.78	56.3	1.3	5.7	2.17	0.9	11.4	0.73	98	0.2
G49.25-0.31+67.06	67.3	1.1	2.9	3.29	0.9	9.7	0.80	110	0.3
G49.55-0.43+59.13	59.8	1.3	3.2	2.42	1.0	11.5	0.44	77	0.1
G49.33-0.34+67.21	67.3	1.1	6.9	3.22	0.8	11.8	1.11	110	0.3
G48.86-0.39+66.81	66.8	1.2	2.7	3.98	1.2	12.6	0.45	117	0.2
G49.08-0.32+67.56	68.3	1.8	1.9	1.44	1.2	11.5	0.18	42	0.0
G49.55-0.31+62.00	62.3	1.4	3.6	1.66	1.5	12.0	0.34	134	0.1
G48.84-0.24+64.74	65.3	1.1	3.6	1.61	1.0	12.4	0.31	58	0.1
G49.12-0.29+60.02	60.3	0.9	2.6	4.18	0.7	9.4	0.97	81	0.4
G49.70-0.46+69.08	69.3	1.0	3.8	2.73	0.8	11.9	0.52	64	0.2
G49.10-0.28+61.61	62.3	1.1	3.4	4.70	1.1	10.0	1.20	244	0.5
G49.49-0.45+61.07	60.3	0.8	3.1	2.43	0.9	9.7	0.66	91	0.4
G48.81-0.22+64.03	64.3	0.6	1.4	3.72	1.2	9.6	0.44	102	0.6
G49.51-0.44+56.80	57.8	0.8	5.4	1.55	0.7	12.3	0.46	39	0.2
G49.21-0.32+71.40	70.8	1.3	3.5	2.41	1.1	11.5	0.48	101	0.1
G49.42-0.46+70.11	70.8	0.8	3.5	2.47	0.6	11.7	0.47	28	0.2
G49.45-0.54+60.10	60.8	0.8	2.6	2.73	1.1	12.0	0.36	76	0.3
G49.44-0.45+56.10	57.3	1.5	3.2	2.01	0.9	12.0	0.34	46	0.1
G49.21-0.32+64.50	65.8	1.8	7.6	1.84	1.0	11.1	0.93	150	0.1
G49.25-0.32+68.44	68.3	1.1	3.1	1.95	0.8	10.4	0.47	45	0.1
G49.53-0.39+59.93	59.8	1.2	4.6	1.63	0.7	11.7	0.46	40	0.1
G49.20-0.17+62.61	63.3	0.9	2.0	1.22	0.8	11.5	0.18	20	0.1
G49.41-0.47+57.59	57.8	0.8	4.6	1.50	1.0	11.9	0.42	72	0.3
G48.87-0.24+59.26	59.3	0.7	1.8	1.95	1.3	12.1	0.18	55	0.2
G49.44-0.38+74.32	74.3	1.0	2.0	1.36	0.8	12.3	0.16	15	0.1
G49.58-0.27+58.05	57.8	1.0	3.6	0.75	0.8	12.9	0.21	20	0.1
G49.47-0.29+61.42	60.3	1.3	5.7	2.15	1.0	14.1	0.47	86	0.1
G49.44-0.33+59.80	59.8	1.4	7.8	1.00	0.7	15.0	0.37	30	0.1
G49.57-0.41+63.62	62.3	1.0	5.7	2.19	0.7	12.6	0.59	55	0.2

Clump name	v_{rad} (km/s)	$\triangle$v (km/s)	I_{av} (Kkm/s)	τ_{13}	D (pc)	T_{ex} (K)	N(H_2) ($\times 10^{22}$ cm^{-2})	M_{LTE} ($M_\odot$)	α
G49.47-0.45+57.51	57.3	1.0	4.8	2.68	0.6	11.9	0.65	44	0.2
G49.12-0.30+61.61	61.8	1.0	2.9	4.40	1.0	9.4	1.15	189	0.6
G49.15-0.13+65.38	66.3	1.6	0.9	1.73	3.4	11.2	0.10	201	0.1
G49.31-0.29+67.53	68.3	0.9	2.0	3.39	1.1	9.5	0.62	119	0.4
G49.60-0.43+66.78	66.8	1.4	4.4	2.13	0.8	11.9	0.50	54	0.1
G49.56-0.30+65.63	66.8	1.1	3.8	3.89	1.2	11.9	0.71	177	0.4
G49.33-0.37+62.76	63.3	1.4	2.2	3.04	2.0	11.0	0.41	294	0.2
G49.32-0.31+60.21	59.8	1.4	4.8	2.23	0.9	10.6	0.75	113	0.2
G49.32-0.35+63.49	63.8	1.0	4.9	4.42	1.4	12.0	1.02	331	0.6
G49.61-0.33+61.36	59.8	2.0	2.8	2.08	1.4	10.8	0.40	135	0.1
G49.19-0.24+67.45	67.8	1.0	2.5	2.52	0.8	10.7	0.43	52	0.2
G49.45-0.36+56.26	57.3	1.1	3.3	3.51	1.2	10.2	0.83	198	0.4
G49.43-0.39+55.13	56.3	1.8	6.1	2.53	1.0	11.0	0.96	167	0.1
G49.23-0.30+65.61	65.3	1.3	4.8	2.29	1.0	10.7	0.74	119	0.2
G49.13-0.23+64.26	64.8	1.0	2.7	2.06	0.8	11.1	0.35	36	0.1
G49.47-0.48+59.93	59.3	1.5	2.6	3.45	1.4	9.1	0.93	293	0.3
G49.44-0.55+59.93	60.3	0.8	2.8	2.20	0.9	9.7	0.56	82	0.3
G49.13-0.23+66.78	66.3	1.0	3.7	1.80	0.7	11.1	0.45	38	0.1
G49.29-0.31+67.72	68.3	1.3	3.8	3.11	1.0	10.4	0.83	148	0.2
G48.93-0.44+60.27	60.3	1.0	1.4	5.85	0.7	10.0	0.63	46	0.2
G49.42-0.43+56.19	56.8	1.6	6.4	2.78	1.3	11.9	0.91	266	0.2
G48.92-0.45+58.48	58.3	1.3	0.9	3.86	2.2	9.7	0.28	240	0.2
G49.40-0.43+69.56	70.3	1.1	2.5	2.34	1.0	10.4	0.43	68	0.2
G49.35-0.34+57.25	57.3	1.0	1.7	1.91	0.7	10.7	0.23	20	0.1
G49.75-0.47+67.56	67.8	0.8	2.5	2.26	0.9	11.8	0.31	46	0.2
G49.24-0.30+64.34	64.8	1.1	3.6	2.45	1.0	11.2	0.53	83	0.2
G49.29-0.39+64.34	64.8	1.1	3.3	1.23	1.1	12.4	0.25	51	0.1
G49.32-0.32+59.28	59.8	1.0	3.0	2.67	1.1	11.2	0.48	104	0.2
G49.27-0.36+69.77	69.3	1.3	5.4	2.87	1.0	11.1	0.91	152	0.3
G49.32-0.33+68.25	67.8	1.0	4.5	2.73	1.3	11.2	0.71	200	0.4
G49.30-0.27+66.49	66.3	0.9	3.2	3.66	0.9	10.2	0.82	124	0.4
G48.88-0.40+61.10	61.8	0.6	1.8	7.81	0.8	9.8	1.09	113	1.0
G49.02-0.33+78.26	78.3	1.0	1.0	1.36	1.0	11.0	0.11	17	0.0
G49.39-0.42+67.57	67.8	1.1	1.8	1.60	1.3	11.3	0.19	56	0.1
G49.27-0.36+65.38	65.8	1.5	4.0	2.25	1.2	10.8	0.59	141	0.2
G49.30-0.36+64.59	65.8	1.7	5.2	2.62	1.8	10.6	0.92	480	0.3
G49.64-0.46+63.97	64.8	2.2	2.6	3.72	1.9	10.7	0.60	357	0.1
G49.19-0.24+64.14	63.8	1.2	2.8	1.27	0.8	11.3	0.26	32	0.1
G49.26-0.35+70.65	70.3	1.8	4.9	2.91	1.1	11.8	0.73	159	0.1
G49.43-0.57+60.78	60.8	1.2	2.2	2.56	1.1	11.2	0.33	69	0.1
G48.77-0.24+64.02	65.3	1.5	1.7	2.57	1.5	10.5	0.30	112	0.1
G48.91-0.16+62.11	62.3	1.1	1.1	2.58	2.3	11.1	0.17	153	0.1
G49.63-0.48+66.56	66.3	1.2	3.7	2.22	0.9	11.1	0.52	71	0.2
G49.31-0.39+65.16	65.8	2.4	1.1	2.00	2.4	10.5	0.17	175	0.0

Clump name	v_{rad} (km/s)	$\triangle$v (km/s)	I_{av} (Kkm/s)	τ_{13}	D (pc)	T_{ex} (K)	N(H_2) ($\times 10^{22}$ cm^{-2})	M_{LTE} ($M_\odot$)	α
G49.27-0.37+70.50	70.8	1.1	4.3	2.41	0.9	10.8	0.69	95	0.3
G49.45-0.44+68.23	68.8	1.5	3.9	3.35	1.0	10.8	0.82	131	0.2
G49.42-0.48+58.16	58.8	0.8	5.4	3.64	0.7	11.1	1.13	86	0.6
G49.07-0.20+62.90	62.3	1.6	0.8	4.07	1.7	9.0	0.34	168	0.1
G48.96-0.34+64.68	64.3	0.9	2.4	3.23	1.1	9.3	0.74	142	0.4
G49.09-0.33+59.13	59.3	1.6	4.6	2.52	0.9	11.0	0.72	99	0.1
G49.42-0.56+60.44	60.8	0.7	1.9	4.31	1.1	10.3	0.57	112	0.5
G49.29-0.37+65.56	65.8	1.5	7.2	1.99	1.2	11.7	0.82	196	0.2
G49.46-0.53+60.32	60.8	1.0	1.5	2.64	1.5	9.9	0.32	118	0.2
G49.56-0.42+60.08	59.8	1.2	5.3	1.66	0.7	12.9	0.43	35	0.1
G49.42-0.55+59.93	60.3	0.5	2.4	1.73	0.6	10.4	0.33	19	0.3
G48.90-0.18+63.00	63.3	0.8	2.7	2.49	0.8	10.8	0.44	42	0.2
G48.84-0.43+66.18	66.3	0.9	3.1	3.33	1.1	12.1	0.49	92	0.3
G49.29-0.26+65.89	65.8	1.5	4.4	1.63	1.0	10.7	0.55	102	0.1
G49.41-0.49+57.34	57.8	0.9	3.0	3.10	0.9	9.2	0.93	125	0.5
G49.61-0.41+63.35	63.3	1.3	3.0	1.95	1.1	10.9	0.40	86	0.1
G49.48-0.28+61.92	61.8	1.7	6.9	2.26	2.0	13.3	0.66	445	0.2
G49.23-0.30+67.07	66.8	1.3	4.5	3.06	0.8	10.7	0.89	107	0.2
G49.55-0.44+66.76	68.3	1.5	4.0	1.59	0.9	12.0	0.37	49	0.1
G49.62-0.34+60.12	60.3	0.9	4.4	1.54	0.8	12.0	0.39	40	0.2
G49.39-0.46+62.58	62.8	0.7	2.0	1.41	0.9	11.0	0.22	31	0.2
G49.54-0.44+63.48	63.8	1.3	4.0	2.19	0.8	10.3	0.66	72	0.2
G49.43-0.50+59.28	59.8	0.9	2.1	3.00	0.8	9.1	0.63	67	0.3
G48.92-0.32+64.88	65.3	1.3	2.7	2.49	1.1	11.3	0.40	86	0.1
G49.20-0.24+64.21	64.3	1.2	3.4	1.89	0.9	9.7	0.61	92	0.2
G49.61-0.47+69.24	69.8	1.4	3.0	2.96	1.3	10.3	0.63	176	0.2
G49.03-0.47+58.20	58.3	1.4	2.0	4.60	2.2	10.6	0.58	506	0.3
G48.86-0.07+60.89	61.3	1.3	3.1	2.99	1.2	10.5	0.62	161	0.2
G49.46-0.55+59.57	59.8	0.9	1.5	3.75	1.2	9.9	0.43	101	0.3
G49.66-0.48+65.17	65.3	0.8	1.6	2.49	1.6	10.9	0.25	112	0.3
G49.19-0.21+60.61	61.3	0.9	2.9	2.55	0.9	9.8	0.62	85	0.3
G49.30-0.29+66.12	65.8	1.4	3.1	3.98	1.5	9.3	1.15	455	0.4
G48.87-0.40+59.81	60.3	0.9	2.3	4.98	1.2	10.6	0.72	177	0.5
G48.98-0.32+78.58	78.8	0.6	1.2	4.33	0.5	8.7	0.57	28	0.3
G49.52-0.31+65.67	64.8	1.8	2.1	2.26	2.4	11.3	0.29	279	0.1
G49.20-0.17+65.64	65.8	1.2	2.3	2.99	1.4	10.1	0.53	174	0.3
G49.42-0.50+61.94	61.3	1.3	1.9	2.84	0.9	9.1	0.56	74	0.1
G49.40-0.38+62.25	62.3	1.2	2.3	2.17	1.0	10.9	0.33	58	0.1
G49.43-0.42+66.66	67.3	1.4	2.5	1.79	1.0	11.4	0.28	45	0.1
G49.60-0.25+57.31	56.8	1.2	4.7	4.61	0.9	14.0	0.74	110	0.2
G49.47-0.47+69.09	69.3	1.3	1.6	3.39	1.5	9.6	0.47	175	0.2
G49.51-0.44+61.80	61.3	0.8	4.3	2.99	0.7	11.7	0.66	55	0.3
G49.44-0.41+60.89	60.8	0.9	3.1	1.77	0.8	10.3	0.44	51	0.2
G49.30-0.25+64.59	65.3	1.0	4.0	2.99	0.7	10.0	0.94	81	0.3

Clump name	v_{rad} (km/s)	$\triangle$v (km/s)	I_{av} (Kkm/s)	τ_{13}	D (pc)	T_{ex} (K)	N(H_2) ($\times 10^{22}$ cm^{-2})	M_{LTE} ($M_\odot$)	α
G49.28-0.38+65.70	65.8	0.9	2.6	2.22	0.8	10.5	0.41	49	0.2
G49.13-0.24+64.15	64.3	0.7	2.7	2.03	0.8	10.4	0.42	48	0.3
G49.31-0.38+67.25	67.3	0.7	1.8	2.66	0.9	10.2	0.37	49	0.3
G49.60-0.41+65.71	65.8	0.8	2.1	1.93	0.9	10.8	0.29	38	0.2
G49.65-0.31+60.83	61.8	1.3	3.3	2.24	0.9	10.6	0.51	79	0.1
G49.09-0.32+60.89	60.8	0.8	3.6	2.32	0.8	10.0	0.67	77	0.4
G49.53-0.42+56.16	56.8	1.4	5.2	3.07	0.9	10.4	1.11	163	0.3
G49.68-0.47+68.35	68.3	0.9	3.0	2.47	1.1	10.4	0.54	117	0.3
G49.31-0.36+61.92	61.3	1.5	6.3	3.36	1.0	10.9	1.29	221	0.3
G49.25-0.33+63.52	64.8	1.0	2.5	3.79	1.3	9.4	0.84	250	0.5
G49.48-0.29+62.60	62.3	1.0	4.7	2.17	0.9	13.0	0.45	66	0.2
G49.36-0.31+56.77	56.8	0.9	2.3	2.52	1.0	11.6	0.31	50	0.2
G49.07-0.15+62.90	62.8	1.3	0.6	2.31	1.2	8.6	0.18	48	0.1
G49.48-0.47+63.04	63.3	1.0	1.9	4.05	1.5	8.5	0.96	368	0.7
G48.81-0.23+62.45	62.8	0.7	1.4	3.24	1.2	9.1	0.44	103	0.5
G49.41-0.40+67.83	68.3	1.5	4.3	2.20	1.1	10.8	0.64	136	0.2
G49.26-0.37+70.74	71.3	1.3	4.0	3.01	0.8	10.8	0.75	82	0.2
G48.83-0.44+65.76	65.8	1.0	3.3	2.88	0.7	12.5	0.43	34	0.1
G49.17-0.24+62.83	63.3	0.9	2.1	1.80	0.9	11.7	0.22	35	0.1
G49.31-0.25+65.55	65.8	0.9	3.5	2.80	0.8	10.2	0.73	75	0.3
G49.32-0.34+60.79	61.3	0.9	4.0	4.98	0.9	10.9	1.17	176	0.6
G49.35-0.26+61.24	60.8	1.3	3.7	4.02	1.0	8.7	1.74	322	0.5
G49.41-0.50+58.29	58.8	0.9	2.9	4.12	1.0	8.5	1.47	232	0.8
G49.44-0.29+61.51	60.8	1.8	6.9	3.22	1.1	12.9	0.93	207	0.2
G49.26-0.36+70.30	71.3	0.9	3.8	2.50	0.9	10.4	0.70	101	0.4
G48.95-0.17+62.89	62.8	1.2	1.8	3.33	1.3	10.0	0.45	123	0.2
G49.52-0.33+63.23	63.8	0.9	3.5	1.90	0.6	11.3	0.42	26	0.2
G49.47-0.44+66.22	65.8	1.3	4.1	3.28	0.9	9.6	1.17	151	0.3
G49.59-0.42+63.14	62.8	0.9	3.0	3.48	0.8	10.7	0.65	79	0.3
G49.14-0.26+60.99	61.3	1.2	2.4	3.28	1.2	10.1	0.59	151	0.2
G49.40-0.00+60.76	60.3	1.8	3.2	3.25	1.7	10.4	0.71	334	0.2
G49.54-0.43+59.43	59.3	1.3	6.0	3.02	0.9	11.5	0.98	151	0.2
G49.33-0.26+60.22	62.3	1.6	3.1	4.31	1.2	9.0	1.40	368	0.3
G49.09-0.35+58.73	59.3	1.1	3.3	3.58	1.1	10.1	0.85	189	0.4
G48.72-0.15+66.05	66.3	0.9	1.2	3.23	1.1	9.7	0.33	75	0.2
G49.05-0.45+70.20	70.3	1.6	1.9	3.40	1.2	9.4	0.59	139	0.1
G49.19-0.34+70.32	70.3	0.8	2.6	2.42	0.7	10.0	0.50	36	0.2
G49.05-0.33+59.94	60.3	0.6	2.1	2.46	0.7	10.6	0.36	33	0.3
G49.32-0.34+64.48	64.8	0.9	4.4	2.59	0.7	10.4	0.81	68	0.4
G48.74-0.12+65.82	66.8	0.9	1.4	2.95	1.1	9.3	0.41	89	0.3
G49.43-0.47+56.92	57.8	1.0	3.1	3.24	0.7	10.9	0.61	51	0.2
G49.33-0.36+64.56	64.8	1.6	4.9	2.99	0.9	10.3	1.05	163	0.2
G49.51-0.44+59.81	60.8	0.6	4.5	1.51	0.5	12.6	0.37	15	0.2
G49.66-0.30+62.15	62.3	0.7	3.3	2.25	0.6	10.7	0.50	35	0.3

Clump name	v_{rad} (km/s)	$\triangle$v (km/s)	I_{av} (Kkm/s)	τ_{13}	D (pc)	T_{ex} (K)	N(H_2) ($\times 10^{22}$ cm^{-2})	M_{LTE} ($M_\odot$)	α
G49.45-0.30+59.89	59.8	1.8	9.8	2.60	1.1	12.6	1.14	220	0.2
G49.56-0.37+58.34	58.8	1.4	2.1	1.78	1.5	11.1	0.25	92	0.1
G48.84-0.40+59.16	59.8	1.2	2.4	4.66	1.2	11.8	0.53	134	0.2
G49.35-0.27+62.84	62.8	1.1	4.0	4.39	1.2	9.0	1.80	443	0.9
G49.43-0.49+57.90	58.3	0.7	2.6	2.40	0.6	9.4	0.60	38	0.3
G49.24-0.36+65.20	66.8	1.8	1.8	2.28	1.4	11.4	0.24	75	0.1
G49.23-0.32+62.49	62.8	1.0	1.5	3.75	1.2	8.8	0.61	144	0.3
G49.59-0.29+63.49	63.8	1.1	2.3	2.40	1.2	12.0	0.28	69	0.1
G49.17-0.23+64.04	64.3	1.1	3.0	1.64	0.7	10.8	0.37	27	0.1
G49.60-0.24+57.48	57.8	1.0	5.4	3.04	1.1	12.0	0.81	152	0.4
G49.35-0.31+63.28	62.8	1.4	2.6	2.31	1.1	10.2	0.46	87	0.1
G49.30-0.37+67.16	67.3	1.3	3.0	1.98	1.1	10.3	0.47	95	0.1
G49.25-0.36+72.98	72.8	0.9	2.8	3.02	0.9	9.9	0.66	97	0.4
G49.65-0.29+60.78	61.3	1.1	4.7	3.01	1.0	11.2	0.82	129	0.3
G49.40-0.48+72.04	73.3	0.9	2.4	2.08	0.9	10.8	0.34	45	0.2
G49.21-0.18+62.48	62.3	0.7	1.9	2.88	0.8	9.9	0.45	47	0.3
G49.46-0.31+63.80	63.3	1.1	3.9	2.31	1.1	12.5	0.43	93	0.2
G49.46-0.32+64.57	64.3	0.7	4.6	2.66	0.8	14.7	0.41	47	0.3
G49.29-0.21+62.36	63.3	1.2	2.8	3.96	1.0	9.7	0.90	163	0.3
G49.13-0.30+69.24	68.8	0.8	0.9	2.72	1.0	8.7	0.29	49	0.2
G49.49-0.48+68.46	68.3	0.9	1.3	4.00	1.2	8.3	0.71	174	0.5
G49.22-0.30+67.80	67.3	1.2	2.9	2.70	0.9	10.3	0.57	84	0.2
G49.36-0.32+65.14	65.3	1.0	4.1	4.14	1.0	9.9	1.32	221	0.6
G49.44-0.46+59.46	58.8	1.2	3.9	2.93	0.9	10.4	0.81	125	0.2
G49.39-0.48+57.64	56.8	1.6	4.1	2.64	1.8	10.8	0.69	376	0.2
G49.53-0.44+63.56	63.8	1.2	4.9	1.96	0.8	11.9	0.54	65	0.1
G49.07-0.37+69.15	69.3	1.3	2.1	2.67	0.9	10.4	0.41	56	0.1
G49.33-0.33+67.08	67.8	1.0	3.3	2.60	0.9	10.8	0.55	80	0.2
G49.50-0.40+66.33	66.3	1.2	3.2	3.17	0.9	10.8	0.64	90	0.2
G49.41-0.42+55.90	56.3	1.2	3.6	1.96	0.8	10.7	0.51	61	0.1
G49.52-0.43+62.44	63.3	1.1	4.2	1.82	0.7	11.5	0.47	35	0.1
G49.52-0.32+66.79	66.3	1.1	3.0	3.16	1.3	10.2	0.70	201	0.3
G49.30-0.22+63.51	63.3	1.2	2.8	2.30	0.9	9.6	0.59	82	0.2
G49.34-0.33+61.71	61.3	1.4	4.8	2.48	0.9	10.8	0.78	120	0.2
G49.13-0.30+58.99	59.8	1.5	1.7	5.56	1.3	8.2	1.32	376	0.3
G49.64-0.49+66.70	66.3	1.4	2.2	3.53	1.4	11.2	0.43	153	0.1
G48.81-0.24+61.79	62.3	0.8	2.1	2.46	0.7	8.8	0.60	46	0.3
G49.10-0.31+61.04	60.3	1.2	3.9	2.78	0.7	10.2	0.81	58	0.2
G49.53-0.45+60.02	60.3	0.8	1.8	2.33	1.4	9.9	0.35	124	0.4
G49.75-0.47+68.14	68.3	1.0	2.7	4.31	0.8	10.7	0.73	80	0.3
G49.22-0.31+66.17	66.3	1.0	4.6	2.45	0.8	9.9	0.96	102	0.3
G48.74-0.13+66.49	66.8	0.7	2.2	3.40	0.9	9.2	0.71	103	0.6
G49.51-0.31+62.73	62.8	1.0	4.0	2.19	0.8	10.5	0.63	76	0.3
G49.12-0.25+68.63	69.3	0.6	1.6	3.18	0.6	8.4	0.68	45	0.5

Clump name	v_{rad} (km/s)	$\triangle$v (km/s)	I_{av} (Kkm/s)	τ_{13}	D (pc)	T_{ex} (K)	N(H_2) ($\times 10^{22}$ cm^{-2})	M_{LTE} ($M_\odot$)	α
G49.52-0.45+63.08	61.8	1.4	2.5	3.44	1.3	10.0	0.66	183	0.2
G48.89-0.43+57.58	58.3	1.1	1.8	5.61	0.9	9.7	0.81	122	0.3
G49.33-0.27+64.61	64.3	1.1	2.9	3.60	1.0	8.5	1.32	208	0.5
G49.66-0.29+60.46	61.8	1.4	1.4	1.98	1.8	10.9	0.19	101	0.1
G49.44-0.32+60.08	59.8	0.8	7.5	1.36	0.7	14.4	0.44	35	0.2
G48.96-0.34+62.68	62.8	0.8	2.4	1.88	0.7	8.8	0.59	55	0.3
G49.32-0.36+58.92	57.8	1.1	3.1	2.55	0.8	10.2	0.61	72	0.2
G49.51-0.40+55.51	56.3	0.9	4.9	1.63	0.6	11.5	0.51	27	0.1
G48.84-0.41+61.47	61.8	0.8	1.9	2.96	0.8	12.8	0.24	26	0.1
G49.22-0.31+64.99	65.8	0.9	2.8	2.99	0.7	9.7	0.72	62	0.3
G49.41-0.02+60.28	60.3	1.5	4.1	4.07	1.2	10.2	1.18	300	0.3
G49.45-0.58+60.54	60.8	0.9	1.8	2.90	0.8	9.7	0.44	52	0.2
G49.48-0.42+65.30	65.3	0.6	2.3	5.08	0.7	9.0	1.21	107	1.1
G49.17-0.32+69.37	70.3	1.3	2.3	2.93	1.2	10.2	0.50	133	0.2
G49.51-0.45+61.00	61.3	1.2	3.6	2.08	0.8	10.6	0.54	56	0.1
G49.50-0.34+69.40	68.8	0.9	3.2	3.67	0.8	11.8	0.58	65	0.3
G49.44-0.46+56.85	57.3	0.6	3.3	3.14	0.8	10.0	0.80	96	0.8
G49.55-0.35+58.03	58.3	0.9	3.2	1.77	0.8	10.8	0.40	39	0.2
G49.06-0.47+57.81	57.8	0.7	2.1	3.07	1.0	9.7	0.55	93	0.4
G49.29-0.35+67.35	67.3	1.2	4.7	3.02	0.8	10.3	1.01	100	0.3
G49.45-0.33+65.98	65.8	1.0	7.0	1.90	0.8	13.5	0.57	65	0.2
G49.69-0.46+67.44	68.3	0.8	3.9	2.89	0.7	10.8	0.73	61	0.3
G49.62-0.32+60.36	60.8	1.1	3.4	2.26	0.8	9.8	0.67	81	0.2
G49.37-0.30+61.34	61.3	0.9	4.0	3.09	1.0	9.8	1.03	190	0.6
G49.47-0.30+60.54	61.8	1.2	9.7	1.40	0.9	14.7	0.57	75	0.2
G49.37-0.25+60.17	60.8	0.9	1.7	3.43	0.9	9.1	0.57	79	0.3
G49.04-0.45+57.91	58.8	1.0	2.0	6.39	2.1	10.7	0.76	573	0.7
G49.02-0.28+69.13	69.3	0.9	2.0	2.69	0.8	9.3	0.53	53	0.2
G49.50-0.35+69.37	69.3	0.9	4.9	2.69	0.7	12.2	0.63	52	0.2
G49.33-0.20+63.68	63.8	1.1	1.6	2.37	1.1	9.5	0.35	73	0.2
G49.26-0.33+73.16	72.8	0.9	1.8	3.38	1.0	11.0	0.35	56	0.2
G49.32-0.27+63.96	64.3	1.1	3.5	4.15	1.1	8.8	1.60	300	0.6
G49.61-0.39+64.56	64.3	1.7	2.4	3.42	1.2	10.8	0.51	126	0.1
G49.09-0.32+62.61	62.3	1.1	2.8	2.69	0.7	9.9	0.63	48	0.2
G49.38-0.30+66.16	65.8	1.5	3.0	6.08	1.4	10.0	1.33	413	0.4
G48.69-0.17+65.28	65.8	1.1	1.7	4.14	1.0	9.3	0.64	101	0.3
G49.31-0.51+56.84	56.3	1.2	2.3	3.13	1.7	10.1	0.55	271	0.3
G48.81-0.30+65.03	65.3	1.1	1.0	4.47	1.4	11.5	0.23	80	0.1
G49.32-0.33+61.55	61.3	0.8	4.4	2.37	0.6	10.1	0.83	58	0.3
G49.59-0.20+58.72	58.8	2.6	2.0	3.62	2.5	12.3	0.33	363	0.1
G49.09-0.38+76.29	74.8	3.7	3.0	3.73	0.9	9.6	0.95	141	0.0
G48.98-0.34+74.78	74.8	1.6	1.0	3.41	1.6	8.9	0.38	170	0.1
G49.48-0.25+60.89	60.8	1.3	5.5	1.81	1.1	11.7	0.58	116	0.2
G49.36-0.18+63.63	63.8	2.1	1.9	3.76	2.6	9.6	0.60	697	0.2

Clump name	v_{rad} (km/s)	$\triangle$v (km/s)	I_{av} (Kkm/s)	τ_{13}	D (pc)	T_{ex} (K)	N(H_2) ($\times 10^{22}$ cm^{-2})	M_{LTE} ($M_\odot$)	α
G49.02-0.24+69.08	69.3	1.8	2.2	2.47	1.2	10.6	0.37	95	0.1
G48.72-0.13+66.34	66.3	0.9	1.4	3.17	1.2	9.1	0.46	122	0.4
G49.37-0.29+64.40	64.8	1.0	2.3	4.35	1.1	10.2	0.71	149	0.4
G49.56-0.29+62.03	61.8	1.8	3.3	2.74	1.3	9.9	0.72	218	0.1
G49.20-0.23+64.49	65.3	1.4	3.3	2.70	1.2	9.6	0.79	194	0.2
G49.05-0.41+62.17	62.3	1.4	1.1	2.88	2.0	9.5	0.28	188	0.1
G49.01-0.41+61.66	61.8	1.0	1.0	3.85	1.4	9.5	0.34	118	0.2
G48.99-0.24+67.33	67.8	1.6	1.7	2.62	1.4	10.5	0.31	102	0.1
G49.33-0.30+61.03	61.8	1.4	3.6	3.27	1.1	9.3	1.12	236	0.3
G49.57-0.48+60.53	60.8	0.9	1.5	3.78	1.2	10.4	0.40	101	0.3
G49.12-0.34+57.10	57.3	0.8	1.5	2.06	1.2	9.9	0.27	67	0.2
G49.57-0.50+60.96	61.8	1.6	1.7	3.21	1.4	9.5	0.48	151	0.1
G49.28-0.28+64.57	64.8	1.0	2.4	3.08	1.0	9.3	0.71	124	0.3
G49.66-0.49+68.33	69.3	0.7	1.6	2.82	1.1	9.6	0.39	81	0.4
G48.83-0.45+66.74	67.3	1.1	3.8	3.82	0.9	11.0	0.86	122	0.3
G48.87-0.48+57.27	57.3	1.0	2.3	5.03	1.5	10.6	0.73	269	0.5
G48.98-0.32+75.41	76.3	1.1	1.4	4.75	0.6	8.1	0.96	57	0.2
G49.07-0.23+62.93	62.8	1.4	1.8	4.57	1.1	9.5	0.73	145	0.2
G49.16-0.26+60.78	60.8	0.9	2.2	3.33	0.9	9.7	0.62	87	0.3
G49.60-0.26+59.84	59.3	1.4	2.3	2.95	1.2	11.0	0.42	108	0.1
G49.39-0.51+58.73	58.8	0.7	1.7	3.18	0.8	8.5	0.70	86	0.5
G49.31-0.27+67.61	67.8	0.8	2.3	4.12	0.8	9.2	0.94	108	0.5
G49.11-0.39+66.44	66.8	1.0	1.1	2.64	1.2	10.0	0.24	59	0.1
G49.05-0.38+72.33	72.3	1.9	2.6	5.17	1.0	8.9	1.44	255	0.2
G49.47-0.26+61.17	61.8	1.1	4.8	3.53	1.5	12.2	0.78	308	0.4
G49.36-0.45+66.42	67.3	1.6	1.9	2.68	1.3	9.1	0.55	156	0.1
G49.58-0.43+68.05	68.8	1.1	2.9	3.02	0.8	10.5	0.59	61	0.2
G49.59-0.28+60.90	61.3	1.1	2.6	1.94	1.0	9.4	0.53	85	0.2
G49.23-0.16+64.04	64.8	1.3	1.6	6.11	1.8	8.9	1.01	571	0.6
G48.83-0.22+64.39	64.3	1.7	2.6	4.78	0.9	9.6	1.05	158	0.2
G48.93-0.42+59.67	59.8	1.5	1.9	3.82	1.1	9.4	0.64	128	0.1
G49.58-0.45+65.26	65.8	1.7	1.7	5.35	1.1	9.2	0.89	184	0.2
G49.35-0.29+62.53	62.8	1.1	4.5	4.56	1.4	9.4	1.83	629	1.0
G48.89-0.05+59.67	59.3	1.0	3.4	3.08	0.8	10.4	0.74	78	0.3
G49.46-0.28+61.10	60.8	1.4	6.8	2.75	1.0	11.1	1.12	200	0.3
G49.76-0.46+67.82	68.3	0.8	2.2	2.84	1.0	10.3	0.45	78	0.3
G49.08-0.48+58.11	57.8	1.1	1.8	3.41	1.1	9.4	0.54	104	0.2
G49.37-0.21+61.37	61.8	1.3	1.8	4.38	1.5	9.3	0.73	285	0.3
G49.38-0.23+62.18	61.8	1.2	1.8	2.77	1.2	9.1	0.52	130	0.2
G49.62-0.41+64.92	64.3	1.9	3.1	3.17	0.9	9.8	0.80	116	0.1
G48.88-0.19+63.12	63.8	0.9	1.0	2.95	1.2	9.6	0.25	66	0.2
G49.30-0.05+58.70	57.8	1.3	2.6	5.49	1.6	10.0	1.03	478	0.5
G49.40-0.44+59.60	60.8	1.1	2.2	2.78	0.8	9.8	0.52	62	0.2
G49.62-0.39+63.34	63.3	1.4	2.3	3.78	1.0	8.9	0.94	161	0.2

Clump name	v_{rad} (km/s)	$\triangle$v (km/s)	I_{av} (Kkm/s)	τ_{13}	D (pc)	T_{ex} (K)	N(H_2) ($\times 10^{22}$ cm^{-2})	M_{LTE} ($M_\odot$)	α
G49.53-0.38+66.18	66.3	1.4	1.8	4.04	1.3	9.2	0.69	205	0.2
G49.60-0.22+57.34	58.3	1.4	3.5	3.50	1.2	10.9	0.74	174	0.2
G49.25-0.44+69.42	70.3	1.1	1.0	2.58	1.4	9.9	0.22	78	0.1
G49.29-0.29+63.14	64.3	1.2	3.4	2.95	0.9	8.3	1.41	213	0.4
G49.31-0.30+60.94	61.3	0.9	2.9	2.71	0.9	8.8	0.92	119	0.4
G49.03-0.37+72.13	73.3	1.7	1.3	4.10	1.6	9.3	0.50	206	0.1
G49.25-0.24+65.31	66.3	1.1	1.9	2.79	1.1	9.7	0.47	98	0.2
G49.49-0.27+61.54	61.3	1.4	3.3	2.50	1.0	12.7	0.37	59	0.1
G48.90-0.17+63.40	63.3	1.5	0.8	4.19	1.5	9.4	0.31	126	0.1
G49.22-0.25+64.02	64.8	1.1	2.1	2.34	1.3	9.6	0.46	137	0.2
G49.31-0.17+61.76	62.3	1.1	1.4	4.21	0.9	8.5	0.75	113	0.3
G48.85-0.06+59.50	61.8	1.9	3.0	4.42	1.2	8.9	1.41	325	0.2
G49.61-0.32+56.41	56.8	1.3	2.0	4.13	1.0	10.5	0.54	92	0.1
G49.35-0.44+66.72	67.3	1.2	1.4	2.70	1.3	9.6	0.33	103	0.1
G48.86-0.39+68.02	67.8	1.1	1.6	4.93	1.3	8.9	0.82	226	0.4
G49.24-0.20+59.16	59.3	0.6	1.1	4.04	1.1	8.8	0.50	100	0.7
G49.57-0.43+66.01	67.3	1.3	2.5	2.72	1.0	10.5	0.47	81	0.1
G49.43-0.31+59.80	60.3	1.5	4.8	4.46	0.9	10.2	1.51	232	0.3
G49.39-0.01+59.84	59.8	1.9	1.9	3.83	1.4	9.0	0.75	269	0.1
G48.78-0.25+64.23	64.8	0.7	2.2	3.10	0.6	8.7	0.79	44	0.4
G49.21-0.35+74.09	73.8	1.2	1.1	4.90	1.2	8.1	0.78	179	0.3
G49.38-0.48+68.73	68.3	1.5	1.7	3.11	1.2	9.5	0.46	116	0.1
G49.28-0.27+66.14	66.8	1.6	2.4	4.85	1.2	8.9	1.25	293	0.3
G49.39-0.23+63.31	62.3	2.6	2.3	2.37	1.6	11.9	0.28	118	0.0
G49.69-0.48+67.06	67.8	1.4	2.3	3.03	1.4	10.0	0.55	171	0.2
G49.32-0.24+64.84	65.8	1.0	3.2	3.60	1.1	9.0	1.18	261	0.6
G48.94-0.41+60.00	60.3	0.9	1.5	2.87	0.9	8.7	0.53	72	0.3
G49.42-0.23+62.10	61.8	2.2	1.9	2.36	1.6	11.1	0.28	114	0.0
G49.61-0.39+57.77	57.3	1.1	1.7	3.37	1.0	9.9	0.46	85	0.2
G49.30-0.21+61.19	62.8	1.7	2.6	3.45	1.1	8.8	0.99	201	0.2
G49.39-0.45+56.25	56.3	1.3	2.3	4.17	1.2	8.9	1.02	238	0.3
G49.40-0.30+61.83	61.8	0.9	2.6	4.38	1.0	9.7	0.95	163	0.6
G49.15-0.16+65.94	66.3	0.9	1.3	3.06	1.0	9.1	0.40	73	0.2
G48.72-0.13+59.97	59.8	0.9	0.7	3.89	2.6	8.6	0.31	361	0.4
G49.44-0.42+64.23	64.3	1.5	3.0	4.17	1.0	9.1	1.24	203	0.3
G48.84-0.23+62.30	62.8	0.9	1.9	3.39	0.7	9.7	0.55	43	0.2
G49.66-0.45+62.03	62.8	1.9	1.6	6.71	1.8	9.0	1.08	579	0.2
G49.08-0.24+63.06	63.3	1.3	2.1	3.17	1.0	9.4	0.62	113	0.2
G49.45-0.29+59.88	60.3	1.9	4.9	3.70	0.9	10.8	1.12	145	0.1
G48.94-0.30+60.60	60.8	0.7	1.0	3.21	1.0	9.0	0.33	61	0.3
G49.26-0.27+68.41	67.8	1.7	1.8	4.44	1.6	8.8	0.89	392	0.2
G49.61-0.44+63.75	64.8	1.2	1.5	3.10	0.8	9.0	0.51	52	0.1
G49.19-0.20+65.79	65.8	0.9	2.6	4.22	0.9	8.8	1.24	184	0.6
G49.57-0.47+70.26	69.3	1.3	2.3	3.27	0.9	8.8	0.84	130	0.2

Clump name	v_{rad} (km/s)	$\triangle$v (km/s)	I_{av} (Kkm/s)	τ_{13}	D (pc)	T_{ex} (K)	$N(H_2)$ ($\times 10^{22}$ cm^{-2})	M_{LTE} ($M_\odot$)	α
G49.30-0.24+60.52	60.8	0.7	1.6	3.61	0.9	8.6	0.68	89	0.6
G49.38-0.49+58.62	59.3	1.5	1.5	3.55	1.3	8.7	0.62	176	0.2
G49.19-0.21+61.41	61.3	1.0	3.4	4.41	0.6	9.5	1.29	74	0.4
G49.22-0.18+59.65	60.8	1.3	1.6	4.80	0.8	8.5	0.96	116	0.2
G49.25-0.21+63.47	64.3	1.7	2.6	3.79	1.5	9.2	0.96	350	0.2
G49.66-0.24+57.71	57.8	0.6	1.7	1.66	0.6	9.6	0.29	16	0.2
G49.23-0.36+63.50	64.8	1.1	1.9	3.81	1.1	9.3	0.67	140	0.3
G49.30-0.31+62.01	61.8	1.2	3.8	3.52	1.0	8.9	1.49	244	0.5
G49.67-0.34+61.87	62.8	1.1	1.0	3.16	1.1	9.0	0.35	69	0.1
G49.61-0.44+65.88	65.8	1.0	1.8	6.50	0.8	9.4	1.02	126	0.4
G49.59-0.48+69.51	69.8	0.9	2.3	2.98	0.6	9.2	0.69	44	0.2
G49.39-0.42+57.94	58.3	1.0	2.2	3.54	1.6	9.6	0.66	274	0.5
G49.28-0.18+62.68	63.3	0.8	1.7	3.81	1.2	8.4	0.84	197	0.7
G49.55-0.44+69.31	69.8	1.0	1.5	3.24	0.6	9.2	0.47	33	0.1
G49.37-0.28+63.43	64.3	1.2	2.8	3.38	1.0	8.8	1.06	192	0.4
G49.34-0.19+64.09	63.8	1.5	2.6	3.31	1.5	9.3	0.82	313	0.3
G49.24-0.22+63.42	63.3	1.3	2.0	4.06	1.5	8.6	0.97	372	0.4
G49.30-0.25+59.33	60.3	1.1	1.9	4.63	0.9	8.8	0.96	127	0.3
G49.42-0.32+66.40	64.8	3.0	1.8	3.37	1.3	9.6	0.52	149	0.0
G49.36-0.48+57.14	57.3	1.5	1.8	4.86	1.7	8.5	1.05	539	0.4
G49.08-0.26+62.64	63.8	1.5	1.2	5.63	1.2	8.1	0.99	244	0.3
G49.55-0.10+55.18	56.3	1.3	2.7	3.60	1.5	10.2	0.68	249	0.3
G48.86-0.43+59.13	59.3	1.2	1.0	5.41	1.4	10.1	0.40	144	0.2
G48.86-0.43+59.73	60.3	0.6	1.7	3.82	1.0	9.8	0.52	83	0.5
G48.84-0.40+58.20	59.3	3.3	1.3	11.88	2.0	9.6	1.32	929	0.1
G49.31-0.37+67.37	68.3	1.0	2.6	4.52	1.0	9.0	1.19	191	0.5
G49.35-0.28+66.50	65.8	2.7	1.6	5.82	1.2	7.9	1.46	378	0.1
G49.56-0.37+56.89	56.8	0.9	1.9	5.88	0.9	8.4	1.42	196	0.8
G49.53-0.43+57.59	57.8	0.9	3.3	3.09	0.6	8.8	1.14	63	0.3
G49.31-0.23+59.78	60.3	1.7	3.0	4.29	1.4	9.0	1.33	438	0.3
G48.90-0.40+56.26	56.8	0.7	0.7	4.85	1.4	8.5	0.42	132	0.6
G49.22-0.18+60.66	60.8	0.9	1.3	5.19	0.8	8.2	0.95	118	0.5
G48.89-0.32+69.61	70.3	1.0	1.7	2.42	0.8	9.1	0.44	45	0.2
G49.61-0.48+64.12	64.8	2.0	1.3	4.64	1.6	8.8	0.68	299	0.1
G49.29-0.20+62.36	63.3	1.7	2.8	4.06	1.2	9.5	0.99	244	0.2
G49.31-0.26+61.34	62.3	1.3	3.8	4.53	1.0	8.4	2.23	413	0.7
G49.64-0.32+61.43	62.3	0.9	3.1	3.44	0.9	9.2	1.02	145	0.6
G49.04-0.36+61.15	62.8	1.7	1.1	3.73	1.4	8.6	0.48	163	0.1
G49.44-0.44+72.06	72.8	0.9	1.7	4.74	1.2	8.8	0.88	227	0.6
G49.66-0.48+68.58	68.8	0.7	2.1	4.65	0.9	9.1	0.95	123	0.7
G49.44-0.49+62.40	63.3	1.0	1.7	5.48	1.0	7.7	1.59	288	0.7
G49.01-0.34+70.09	69.8	1.2	1.3	7.05	1.0	8.0	1.39	246	0.5
G49.38-0.49+70.20	69.3	1.4	1.6	3.23	1.0	9.3	0.48	80	0.1
G49.29-0.32+72.05	72.3	0.8	1.5	2.29	0.9	8.8	0.42	59	0.2

Clump name	v_{rad} (km/s)	$\triangle$v (km/s)	I_{av} (Kkm/s)	τ_{13}	D (pc)	T_{ex} (K)	$N(H_2)$ ($\times 10^{22}$ cm^{-2})	M_{LTE} ($M_\odot$)	α
G49.53-0.31+65.88	65.8	1.0	1.8	2.10	1.0	9.2	0.41	66	0.2
G49.47-0.46+66.77	67.3	0.6	1.7	3.72	0.8	9.2	0.60	74	0.6
G49.66-0.49+68.56	68.8	0.7	1.5	3.30	0.7	8.7	0.59	52	0.4
G49.19-0.25+60.60	61.8	1.3	1.2	2.57	1.1	8.9	0.36	69	0.1
G49.38-0.43+64.91	64.8	1.4	1.2	4.40	1.5	8.7	0.58	226	0.2
G49.44-0.31+55.89	56.8	1.0	4.8	1.85	0.8	11.7	0.52	64	0.2
G49.47-0.25+59.15	59.8	0.8	2.5	2.94	1.1	10.3	0.54	109	0.4
G49.44-0.41+58.85	59.3	0.6	2.0	3.77	0.9	8.6	0.89	124	1.0
G49.27-0.29+62.44	62.8	1.0	2.2	2.59	0.8	8.9	0.64	68	0.2
G49.24-0.36+68.09	68.3	1.2	2.0	3.69	0.9	9.4	0.67	89	0.2
G49.33-0.23+62.91	63.3	1.0	2.3	6.08	1.1	8.1	2.05	394	0.9
G48.99-0.34+70.15	70.8	0.6	1.3	2.92	0.7	8.6	0.47	38	0.4
G49.46-0.33+66.47	66.8	0.6	4.9	1.63	0.6	12.1	0.45	24	0.3
G49.44-0.28+60.01	60.8	1.6	4.5	2.63	1.2	11.8	0.62	152	0.1
G49.41-0.31+60.31	60.8	1.0	2.5	5.99	1.1	9.3	1.39	281	0.7
G49.58-0.30+61.36	61.3	1.0	2.5	1.96	0.8	9.7	0.45	52	0.2
G49.31-0.15+61.79	62.3	1.5	1.6	5.00	1.6	8.9	0.88	408	0.3
G49.30-0.20+62.28	62.8	1.0	3.0	4.11	0.7	8.3	1.70	127	0.6
G49.65-0.49+66.16	66.8	0.8	2.3	3.83	0.8	8.5	1.13	123	0.7
G49.34-0.31+66.50	65.8	1.5	2.3	3.39	1.2	8.8	0.90	229	0.2
G49.30-0.30+62.52	62.3	1.2	2.7	7.80	1.1	7.2	4.94	1003	1.8
G48.88-0.33+68.94	69.8	1.7	0.8	4.03	2.5	9.7	0.27	277	0.1
G49.27-0.38+68.06	68.3	1.4	2.1	3.49	0.8	9.1	0.74	83	0.2
G49.31-0.33+61.29	61.3	1.1	2.8	4.67	1.1	8.7	1.48	311	0.7
G49.29-0.27+61.68	61.8	1.4	3.3	6.58	1.0	8.8	2.41	428	0.6
G49.46-0.29+59.29	59.3	1.2	5.2	3.02	0.8	11.3	0.88	94	0.2
G49.50-0.39+65.43	65.8	0.7	3.8	5.04	0.6	10.0	1.39	75	0.8
G49.30-0.28+60.18	61.3	1.5	2.4	4.77	1.0	8.2	1.61	287	0.4
G49.32-0.12+59.15	58.8	1.4	1.2	5.66	1.9	8.0	1.01	607	0.4
G49.36-0.48+58.67	58.8	0.7	1.9	4.31	1.0	8.5	1.01	160	0.9
G48.72+0.03+59.20	59.3	0.9	1.5	4.40	2.0	9.4	0.59	423	0.7
G49.00-0.33+63.81	63.8	0.8	2.4	3.84	0.6	8.2	1.33	93	0.6
G49.19-0.16+64.63	64.3	0.9	1.7	5.32	1.2	8.8	0.99	255	0.7
G49.43-0.03+61.46	60.8	2.6	1.5	3.76	1.2	9.2	0.54	145	0.1
G49.65-0.47+66.35	66.3	1.1	3.2	4.88	0.6	9.0	1.62	106	0.4
G49.46-0.32+68.08	68.3	1.0	2.7	2.78	1.5	11.3	0.43	159	0.3
G49.55-0.44+68.77	69.3	0.8	1.4	1.45	0.7	10.1	0.19	17	0.1
G49.32-0.32+61.25	61.3	0.8	2.7	2.49	0.5	8.7	0.85	39	0.3
G49.48-0.23+59.24	59.8	1.7	6.0	4.44	1.2	10.7	1.66	428	0.3
G48.99-0.46+58.19	58.8	0.8	1.5	5.77	2.0	8.5	1.09	715	1.6
G48.97-0.18+62.08	62.3	0.9	1.1	3.38	0.8	8.5	0.49	52	0.2
G49.40-0.23+60.60	59.8	1.3	2.8	3.33	1.3	11.8	0.46	140	0.2
G48.80-0.23+58.90	61.3	2.4	0.9	5.34	1.7	7.8	0.78	368	0.1
G48.96-0.32+63.41	63.8	0.9	1.5	6.16	1.1	7.7	1.65	322	1.1

Clump name	v_{rad} (km/s)	$\triangle$v (km/s)	I_{av} (Kkm/s)	τ_{13}	D (pc)	T_{ex} (K)	N(H_2) ($\times 10^{22}$ cm^{-2})	M_{LTE} ($M_\odot$)	α
G49.51-0.37+66.69	66.3	0.9	3.6	3.93	0.6	9.5	1.25	77	0.5
G49.05-0.31+71.38	70.8	2.3	1.0	4.38	0.9	8.5	0.57	87	0.1
G49.50-0.26+60.21	60.8	1.2	2.7	2.76	1.1	10.5	0.52	113	0.2
G48.91-0.40+61.30	60.8	0.9	2.1	5.97	1.0	8.5	1.60	273	1.0
G49.06-0.21+62.94	62.8	1.7	1.4	4.86	0.9	8.4	0.88	125	0.1
G49.04-0.41+62.46	62.3	1.3	1.3	2.25	1.0	9.2	0.31	50	0.1
G48.96-0.18+62.93	62.8	1.3	2.0	3.97	0.6	9.4	0.70	43	0.1
G49.52-0.39+67.75	67.8	1.2	2.3	4.71	1.2	9.6	0.92	241	0.4
G49.63-0.33+62.40	62.3	1.0	2.1	2.82	0.8	9.6	0.53	65	0.2
G49.51-0.31+61.08	61.8	1.2	2.2	3.40	1.0	8.5	0.94	174	0.3
G49.09-0.34+56.74	56.8	0.7	1.6	2.35	0.8	9.3	0.38	41	0.2
G49.40-0.44+62.00	61.8	0.9	1.4	2.17	0.8	8.9	0.36	39	0.2
G48.79-0.40+65.21	65.3	0.6	2.1	3.93	0.9	9.7	0.69	87	0.6
G48.85-0.40+59.09	59.3	0.7	2.7	7.06	0.7	9.3	1.74	134	1.1
G49.40-0.40+55.27	56.3	2.8	1.5	3.39	1.4	8.9	0.57	203	0.1
G48.82-0.16+58.56	60.8	2.8	0.9	2.90	2.1	8.9	0.30	224	0.0
G48.88-0.04+60.04	59.3	1.3	2.5	3.77	1.1	9.1	0.96	217	0.3
G49.30-0.51+57.09	56.3	1.8	1.6	3.53	1.1	9.0	0.59	123	0.1
G49.60-0.43+64.04	64.3	0.8	2.3	5.04	0.6	9.0	1.17	67	0.4
G49.46-0.30+58.33	58.8	1.0	4.9	3.76	0.8	10.5	1.22	133	0.4
G48.83-0.46+66.79	66.8	0.8	1.5	5.67	1.1	10.0	0.63	124	0.4
G48.70-0.16+65.74	65.8	0.9	1.6	6.68	0.7	8.2	1.51	127	0.7
G48.78-0.41+66.78	66.8	1.0	2.2	5.49	0.9	9.0	1.24	164	0.5
G49.09-0.29+62.00	63.8	1.0	2.5	6.87	1.0	8.5	2.07	326	0.9
G49.20-0.20+61.04	60.8	1.3	1.7	3.91	1.1	8.7	0.79	172	0.2
G49.54-0.45+68.02	69.3	1.6	1.7	5.12	1.0	8.6	1.06	195	0.2
G49.28-0.33+72.39	72.3	1.0	2.5	4.53	0.8	8.6	1.33	132	0.5
G49.30-0.36+63.99	65.3	0.8	2.8	2.59	0.7	9.2	0.75	64	0.4
G49.64-0.40+62.06	63.3	1.5	1.6	4.24	1.3	9.5	0.58	160	0.2
G49.49-0.45+62.94	63.3	0.7	1.4	8.64	0.8	6.8	3.83	378	2.8
G49.31-0.32+61.85	61.8	0.7	2.4	2.16	0.7	8.7	0.68	60	0.4
G49.33-0.28+66.12	65.8	1.4	2.1	6.97	0.9	7.5	2.89	373	0.6
G49.32-0.26+65.24	65.8	1.0	3.3	3.46	0.9	8.6	1.39	184	0.6
G49.51-0.49+68.47	69.8	2.1	0.9	4.72	1.6	7.4	0.92	418	0.2
G49.24-0.13+64.41	65.3	3.0	1.1	3.79	2.0	8.5	0.53	347	0.1
G49.32-0.32+61.51	61.3	0.6	2.1	6.05	0.6	8.5	1.55	109	1.1
G49.21-0.31+63.23	64.3	0.7	2.1	2.72	0.5	9.1	0.62	31	0.3
G49.06-0.22+63.67	62.8	2.1	0.9	4.93	2.2	8.4	0.60	486	0.1
G49.62-0.24+56.83	57.3	1.1	2.8	2.59	1.0	11.8	0.37	58	0.1
G49.27-0.37+66.87	67.3	1.0	2.4	4.25	0.8	8.8	1.17	131	0.5
G49.54-0.30+64.66	65.8	1.4	2.1	4.44	1.2	9.3	0.87	199	0.2
G49.19-0.21+65.15	64.8	1.2	2.1	4.19	0.9	8.7	1.01	140	0.3
G49.30-0.19+61.72	62.3	1.1	2.6	4.75	1.1	8.2	1.81	387	0.8
G49.54-0.37+60.48	61.8	0.9	1.8	5.51	1.0	8.5	1.25	206	0.7

Clump name	v_{rad} (km/s)	$\triangle$v (km/s)	I_{av} (Kkm/s)	τ_{13}	D (pc)	T_{ex} (K)	$N(H_2)$ ($\times 10^{22}$ cm^{-2})	M_{LTE} ($M_\odot$)	α
G49.25-0.44+71.39	71.3	0.8	1.6	3.56	0.5	8.7	0.67	31	0.2
G49.63-0.34+60.52	60.8	0.8	1.6	2.66	0.6	9.3	0.41	29	0.2
G49.23-0.19+58.98	59.3	1.5	1.2	4.08	1.3	8.5	0.60	181	0.2
G49.54-0.28+56.31	56.8	1.8	3.3	3.32	1.1	10.6	0.72	163	0.1
G49.65-0.47+59.30	60.3	1.2	1.2	3.83	1.5	8.6	0.53	214	0.3
G49.40-0.45+61.06	61.3	0.7	1.9	2.63	0.7	8.8	0.59	54	0.4
G49.58-0.30+59.30	60.3	0.9	2.1	3.83	0.7	9.5	0.70	62	0.3
G49.62-0.23+58.36	56.8	1.0	3.2	2.02	1.4	11.4	0.39	124	0.2
G49.27-0.39+66.63	66.8	1.3	2.0	3.34	0.9	8.5	0.84	119	0.2
G49.31-0.29+62.31	61.8	0.9	2.3	5.88	0.9	7.7	2.34	353	1.3
G49.40-0.46+59.33	60.3	1.3	2.3	3.37	1.1	8.6	0.97	183	0.3
G49.38-0.31+65.38	65.8	0.8	1.9	3.75	0.8	8.9	0.75	74	0.4
G49.63-0.41+63.91	63.8	1.0	2.5	4.01	0.9	9.4	0.89	125	0.4
G49.32-0.29+64.71	64.3	1.0	2.4	8.65	1.1	7.3	4.53	902	2.2
G49.38-0.30+64.08	64.8	0.8	2.8	3.88	0.7	9.4	0.97	89	0.6
G49.20-0.25+63.12	64.3	1.2	2.3	5.18	0.7	8.7	1.34	106	0.3
G49.54-0.31+64.07	64.8	0.9	1.8	1.78	0.9	8.9	0.40	55	0.2
G49.46-0.03+62.87	62.3	1.8	1.6	5.86	3.1	8.9	1.00	1699	0.5
G49.21-0.25+61.70	62.3	1.1	2.2	4.13	1.0	8.5	1.09	180	0.4
G49.08-0.34+61.09	61.3	0.8	2.4	6.31	0.7	8.3	2.05	157	1.0
G49.57-0.46+67.23	68.3	1.5	1.4	5.07	1.1	8.5	0.86	161	0.2
G49.62-0.32+64.21	64.3	1.4	1.9	3.25	0.8	8.7	0.74	90	0.2
G48.82-0.46+67.79	67.8	1.0	1.6	6.32	0.7	10.0	0.74	67	0.2
G48.92-0.39+56.42	56.8	0.8	1.0	4.69	1.7	8.2	0.69	327	0.8
G48.90-0.20+59.65	60.3	0.8	0.9	3.89	1.1	9.2	0.34	73	0.3
G49.61-0.43+64.34	64.3	0.9	1.9	4.50	0.7	8.1	1.25	93	0.5
G49.29-0.18+62.62	62.8	1.1	1.9	4.38	1.0	8.9	0.92	144	0.3
G49.20-0.34+76.85	76.3	1.7	0.9	8.34	1.4	7.4	1.60	552	0.4
G48.87-0.06+59.69	60.3	1.4	2.8	5.27	1.2	8.6	1.73	398	0.5
G49.29-0.51+55.79	56.3	0.9	1.8	3.24	1.1	9.3	0.55	111	0.3
G49.40-0.31+59.96	60.3	0.9	2.7	2.60	0.7	9.9	0.57	47	0.2
G48.76-0.13+65.94	66.8	1.1	1.3	7.63	1.1	7.1	2.48	521	1.0
G48.80-0.45+65.98	66.3	0.8	1.6	6.31	1.2	9.5	0.85	199	0.7
G48.74-0.34+62.98	63.3	0.6	1.7	4.13	0.5	10.4	0.46	23	0.3
G49.40-0.51+59.29	59.3	0.6	1.5	6.73	0.7	7.6	1.95	141	1.5
G48.69-0.02+57.78	58.3	1.1	0.8	6.24	2.2	7.8	0.86	687	0.7
G48.85-0.47+68.21	68.3	1.2	1.3	5.81	1.4	9.5	0.66	205	0.3
G49.45-0.48+64.71	64.8	0.8	0.7	8.19	1.0	7.3	1.19	187	0.8
G48.99-0.37+60.22	59.8	1.6	1.2	4.54	1.4	8.5	0.67	235	0.2
G49.00-0.43+61.38	61.8	1.3	1.2	3.64	1.5	8.7	0.51	198	0.2
G48.82-0.23+59.51	59.8	0.7	1.3	4.31	0.7	8.6	0.69	64	0.4
G48.77-0.21+60.53	59.8	1.7	1.2	9.18	1.1	7.8	1.92	419	0.3
G48.97-0.37+59.34	60.3	1.3	1.1	5.34	1.8	7.9	0.94	507	0.4
G49.64-0.39+64.54	64.8	1.6	1.7	4.76	1.2	8.6	0.94	247	0.2

Clump name	v_{rad} (km/s)	$\triangle$v (km/s)	I_{av} (Kkm/s)	τ_{13}	D (pc)	T_{ex} (K)	$N(H_2)$ ($\times 10^{22}$ cm^{-2})	M_{LTE} ($M_\odot$)	α
G49.44-0.06+59.93	61.8	2.4	1.7	6.58	2.0	8.4	1.45	1044	0.3
G49.13-0.19+64.05	63.8	1.2	0.8	3.52	1.6	8.6	0.35	147	0.2
G49.62-0.40+57.45	57.8	0.9	0.9	5.57	1.4	8.5	0.60	208	0.5
G48.90-0.19+63.26	63.8	1.2	1.1	3.22	1.0	8.7	0.43	74	0.1
G49.16-0.25+65.27	65.3	1.4	1.2	2.99	1.0	8.2	0.51	89	0.1
G49.28-0.49+55.80	56.3	0.9	1.3	3.96	1.1	8.3	0.72	163	0.5
G49.15-0.24+63.36	63.8	0.9	1.7	3.53	0.8	8.8	0.67	71	0.3
G49.20-0.27+55.78	56.3	0.7	1.3	3.86	1.0	7.8	0.88	141	0.7
G49.13-0.48+58.10	57.8	2.2	1.4	4.68	1.5	8.7	0.74	278	0.1
G49.35-0.39+57.30	57.8	1.6	1.3	3.05	1.1	8.3	0.57	126	0.1
G49.71-0.34+57.73	60.8	3.2	1.0	3.59	2.4	9.3	0.33	328	0.0
G49.14-0.17+65.90	66.8	1.1	1.0	4.12	1.1	8.3	0.56	108	0.2
G48.98-0.25+70.75	70.8	1.0	0.9	4.09	1.3	8.4	0.47	141	0.3
G49.17-0.32+58.64	60.3	2.2	1.9	4.33	1.2	8.2	1.17	268	0.1
G49.66-0.40+57.07	56.8	1.3	0.9	6.26	1.8	8.6	0.68	358	0.3
G49.08-0.39+62.34	62.3	0.9	0.8	4.61	1.6	7.8	0.64	282	0.6
G49.19-0.17+57.25	60.3	3.3	0.8	4.37	2.5	8.1	0.53	569	0.1
G49.41-0.20+59.86	60.3	1.3	3.3	2.52	1.2	11.3	0.49	118	0.2
G48.75-0.20+66.22	66.8	1.1	0.9	4.66	1.1	8.1	0.64	123	0.2
G48.96-0.14+62.52	62.8	1.1	0.8	5.19	1.9	8.4	0.56	342	0.4
G49.04-0.46+70.05	69.8	1.1	0.8	4.41	0.8	8.0	0.57	58	0.2
G48.81-0.38+64.05	63.3	2.0	1.2	9.23	1.1	8.8	1.25	245	0.2
G48.71-0.00+58.44	59.8	1.5	0.8	7.34	2.4	8.0	0.91	858	0.5
G49.20-0.21+55.29	56.8	1.3	0.7	4.47	1.4	8.0	0.46	154	0.2
G49.27-0.22+65.17	65.3	1.5	1.5	3.64	0.8	7.9	0.95	111	0.2
G49.26-0.14+62.83	63.3	1.7	1.3	5.25	1.4	8.0	1.08	383	0.3
G49.14-0.25+63.86	63.8	0.9	1.6	5.03	0.7	8.2	1.17	90	0.5
G49.38-0.25+63.02	63.3	0.6	0.9	4.96	0.9	7.1	1.10	163	1.2
G49.56-0.51+62.78	62.8	1.2	1.2	3.83	0.8	8.5	0.58	62	0.1
G49.63-0.54+68.97	70.3	1.6	0.8	4.29	1.3	8.0	0.55	161	0.1
G49.33-0.21+63.51	63.3	1.0	2.0	5.17	1.0	7.9	1.64	302	0.8
G49.58-0.45+69.20	69.3	1.5	1.6	7.37	1.0	8.4	1.48	253	0.3
G49.21-0.20+65.37	65.8	1.0	1.1	3.60	1.1	8.1	0.57	121	0.3
G49.08-0.45+57.99	57.8	1.1	1.1	4.00	1.4	7.9	0.70	242	0.4
G48.61-0.17+55.44	56.3	1.1	0.8	4.66	1.4	7.6	0.71	257	0.4
G49.50-0.30+60.66	61.3	1.3	2.5	4.46	1.1	9.3	1.06	199	0.3
G49.53+0.01+55.84	56.3	1.0	1.5	7.55	2.0	8.0	1.69	1201	1.6
G49.34-0.49+60.17	59.8	1.3	1.1	4.53	1.7	8.0	0.81	380	0.4
G49.26-0.20+67.58	66.8	1.4	0.9	4.57	1.3	7.8	0.69	208	0.2
G49.51-0.23+62.78	62.8	1.5	1.5	3.84	2.7	9.7	0.48	578	0.3

Appendix B

MSX IRDCs within the SCUBA Legacy Catalogue

B.1 850 μm detected cores

Table B.1: Data for all MSX identified IRDC candidate cores within the SCUBA Legacy Catalogue, with a SCUBA detection. MSX ID's are taken from Simon *et al.* (2006a), table 1. SCUBA ID's are taken from Di Francesco *et al.* (2008), tables 2 and 3, where F stands for Fundamental catalogue and E stands for Extended catalogue. C is the peak contrast value, F_{850} is the peak flux at 850 μm, $N_8(H_2)$ is the column density derived form the 8 μ MSX data, $N_{850}(H_2)$ is the column density derived from the 850 μ data. Cores with MIPS data avaliable are denoted by a yes (if an embedded 24 μm source is present) or no (if an embedded 24 μm is not present) in the MIPS source column.

MSX ID (MSXDC)	SCUBA ID (JCMTS)	RA (hh:mm:ss)	Dec (°: ': ")	C	F_{850} (Jy/beam)	$N_8(H_2)$ $\times 10^{22}$ (cm^{-2})	$N_{850}(H_2)$ $\times 10^{22}$ (cm^{-2})	MIPS source
G000.06+00.21	(a)F_J174457.0-284618	17:44:55.4	-28:46:38	0.22	1.09	1.08	7.91	-
G000.07+00.24	(a)F_J174450.2-284449	17:44:50.7	-28:44:45	0.16	0.40	0.76	2.89	-
G000.08+00.19	(a)F_J174503.4-284618	17:45:03.8	-28:46:09	0.15	0.76	0.77	5.51	-
G000.13−00.14	(a)F_J174626.0-285437	17:46:26.8	-28:54:38	0.22	1.41	1.08	10.22	-
G000.20−00.25	(a)F_J174706.6-285314	17:47:06.3	-28:53:26	0.19	0.57	0.92	4.13	-
G000.21+00.23	(a)F_J174510.6-283812	17:45:13.8	-28:37:59	0.14	0.59	0.66	4.28	-
G000.25+00.02	(a)F_J174607.0-284130	17:46:07.9	-28:41:35	0.44	6.62	2.52	47.95	-
G000.32−00.23	(a)F_J174719.9-284656	17:47:19.3	-28:47:01	0.26	0.73	1.31	5.29	-
G000.32−00.18	(a)F_J174707.2-284432	17:47:08.6	-28:45:19	0.33	0.46	1.74	3.33	-
G000.33+00.05	(a)F_J174613.0-283654	17:46:12.7	-28:37:10	0.21	3.74	1.02	27.21	-
G000.35−00.24	(a)F_J174725.4-284538	17:47:23.3	-28:45:47	0.16	0.34	0.76	2.46	-
G000.40−00.21	(a)F_J174725.4-284156	17:47:25.3	-28:42:16	0.23	1.26	1.14	9.14	-
G000.40+00.04	(a)F_J174624.4-283331	17:46:24.7	-28:33:47	0.45	6.76	2.60	49.03	-

MSX ID (MSXDC)	SCUBA ID (JCMTS)	RA (hh:mm:ss)	Dec (°: ': ")	C	F_{850} (Jy/beam)	$N_8(H_2)$ $\times 10^{22}$ (cm^{-2})	$N_{850}(H_2)$ $\times 10^{22}$ (cm^{-2})	MIPS source
G000.59+00.01	(e)F_J174646.8-283155	17:46:47.5	-28:32:07	0.37	14.95	2.01	112.31	-
G000.59+00.01	(a)F_J174643.2-283007	17:46:42.9	-28:30:27	0.47	7.83	2.76	56.80	-
G000.59+00.01	(c)F_J174648.6-282944	17:46:49.2	-28:29:53	0.37	2.71	2.01	19.65	-
G000.59+00.01	(f)F_J174653.2-282632	17:46:53.0	-28:26:40	0.34	2.18	1.81	15.81	-
G000.59+00.01	(d)F_J174657.8-282332	17:46:59.7	-28:23:06	0.37	2.10	2.01	16.20	-
G000.59+00.01	(b)F_J174709.6-282208	17:47:09.3	-28:21:54	0.37	3.38	2.01	24.41	-
G000.68−00.18	(a)F_J174800.1-282714	17:48:01.2	-28:27:24	0.20	0.67	0.97	4.86	-
G000.72−00.08	(a)F_J174740.1-282132	17:47:39.0	-28:21:39	0.16	3.49	0.76	25.27	-
G000.87−00.01	(a)E_J174744.6-281150	17:47:45.4	-28:11:47	0.15	1.91	0.77	13.84	-
G000.90−00.02	(a)E_J174751.4-281039	17:47:51.1	-28:10:46	0.13	1.87	0.61	13.56	-
G000.94+00.00	(a)E_J174750.1-280803	17:47:49.5	-28:07:37	0.17	1.13	0.81	8.19	-
G000.97+00.04	(a)E_J174744.6-280445	17:47:45.3	-28:04:45	0.22	1.18	1.08	8.55	-
G000.98+00.09	(a)E_J174733.3-280302	17:47:32.7	-28:02:30	0.13	0.86	0.61	6.24	-
G000.97−00.06	(c)E_J174831.4-280826	17:48:30.3	-28:08:25	0.22	1.39	1.08	10.09	-
G001.01+00.05	(b)E_J174752.3-280321	17:47:53.0	-28:03:27	0.20	0.92	0.97	8.42	-
G000.97−00.06	(a)E_J174814.6-280550	17:48:15.3	-28:06:05	0.26	1.55	1.31	11.23	-
G001.01+00.05	(a)E_J174747.8-280157	17:47:49.1	-28:01:58	0.20	0.90	0.97	6.52	-
G001.02+00.02	(a)E_J174755.5-280239	17:47:57.0	-28:02:48	0.11	0.67	0.57	4.86	-
G001.11−00.16	(a)F_J174846.7-280338	17:48:47.9	-28:03:28	0.29	1.30	1.49	9.42	-
G001.11−00.16	(b)F_J174851.3-280356	17:48:52.4	-28:04:01	0.24	0.59	1.19	4.28	-
G001.13−00.26	(a)F_J174915.8-280531	17:49:16.5	-28:05:39	0.20	0.71	0.97	5.14	-
G001.26−00.23	(a)F_J174930.3-275848	17:49:31.4	-27:59:01	0.14	0.36	0.66	2.61	-
G001.26+00.04	(a)F_J174826.6-274949	17:48:25.3	-27:49:53	0.21	1.78	1.02	12.89	-
G001.29+00.03	(a)F_J174833.4-274836	17:48:32.5	-27:48:45	0.17	1.62	0.81	11.75	-
G001.31−00.04	(a)F_J174856.9-275047	17:48:57.0	-27:50:28	0.17	0.67	0.81	4.86	-
G001.34−00.08	(a)F_J174906.9-274946	17:49:06.7	-27:49:48	0.13	0.42	0.61	3.05	-
G001.47−00.03	(a)F_J174914.3-274211	17:49:13.2	-27:41:55	0.18	0.40	0.86	2.89	-
G001.46+00.03	(a)E_J174855.8-273917	17:48:56.3	-27:39:24	0.29	2.31	1.49	16.74	-
G001.51−00.10	(a)F_J174934.7-274212	17:49:36.7	-27:41:53	0.17	1.64	0.81	11.88	-
G001.53+00.14	(a)E_J174842.2-273230	17:48:41.0	-27:33:04	0.13	0.82	0.61	5.94	-
G001.61−00.02	(b)E_J174936.6-273248	17:49:36.5	-27:33:11	0.37	0.71	2.01	5.14	-
G001.61−00.02	(a)E_J174944.3-273330	17:49:44.4	-27:33:11	0.41	2.67	2.29	19.35	-
G001.67−00.18	(b)E_J175015.0-273437	17:50:16.0	-27:34:22	0.23	0.63	1.14	4.56	-
G002.51+00.18	(b)F_J175045.8-263945	17:50:43.4	-26:40:21	0.38	2.77	2.08	20.09	-
G002.51+00.18	(a)F_J175045.8-263945	17:50:48.5	-26:39:30	0.41	2.77	2.29	20.09	-
G008.83−00.05	(e)F_J180525.3-211926	18:05:27.7	-21:20:17	0.27	4.22	1.37	30.67	-
G008.83−00.05	(a)F_J180525.3-211926	18:05:26.3	-21:19:04	0.32	4.22	1.68	30.67	-
G009.84−00.03	(a)E_J180733.9-202613	18:07:37.4	-20:26:20	0.43	0.65	2.44	4.71	yes
G010.71−00.16	(g)E_J180944.4-194712	18:09:44.4	-19:47:02	0.35	0.46	1.87	3.33	yes
G010.71−00.16	(h)E_J180953.3-194806	18:09:52.5	-19:47:40	0.34	0.65	1.81	4.71	yes
G010.71−00.16	(b)E_J180938.7-194512	18:09:38.7	-19:45:15	0.49	2.79	2.93	20.22	yes
G010.71−00.16	(d)E_J180949.1-194442	18:09:48.9	-19:44:52	0.40	0.44	2.22	3.20	no
G010.71−00.16	(f)E_J180940.8-194336	18:09:41.5	-19:43:42	0.36	2.35	1.94	17.04	no
G010.71−00.16	(a)E_J180945.7-194206	18:09:45.5	-19:42:22	0.56	1.28	3.57	9.29	yes
G010.71−00.16	(e)E_J181009.0-194507	18:10:10.0	-19:45:13	0.38	0.63	2.80	4.56	no
G010.71−00.16	(c)E_J181003.1-194342	18:10:02.4	-19:43:28	0.44	0.84	2.52	6.09	yes
G010.99−00.07	(a)F_J181007.1-192755	18:10:07.2	-19:27:60	0.55	1.39	3.47	10.09	yes

MSX ID (MSXDC)	SCUBA ID (JCMTS)	RA (hh:mm:ss)	Dec (°: ': ")	C	F_{850} (Jy/beam)	$N_8(H_2)$ $\times 10^{22}$ (cm^{-2})	$N_{850}(H_2)$ $\times 10^{22}$ (cm^{-2})	MIPS source
G011.11−00.11 (g)	F_J181013.5-192419	18:10:13.7	-19:24:36	0.30	0.67	1.55	4.86	no
G011.11−00.11 (b)	F_J181018.2-192431	18:10:18.7	-19:24:42	0.43	0.88	2.44	6.37	yes
G011.11−00.11 (a)	F_J181033.0-192201	18:10:32.0	-19:22:31	0.50	1.45	3.01	10.52	yes
G011.11−00.11 (f)	F_J181033.0-192201	18:10:35.4	-19:21:02	0.30	0.73	1.55	5.29	yes
G011.11−00.11 (d)	F_J181037.3-191820	18:10:37.7	-19:18:27	0.31	0.36	1.61	2.61	yes
G011.11−00.11 (c)	F_J181034.8-191702	18:10:35.3	-19:17:20	0.40	0.80	2.22	5.81	yes
G011.11−00.11 (e)	F_J181039.9-191132	18:10:40.6	-19:10:58	0.31	0.76	1.61	5.51	yes
G012.44−00.14 (b)	F_J181320.6-181220	18:13:21.6	-18:12:17	0.34	0.36	1.81	2.61	yes
G012.44−00.14 (a)	F_J181341.7-181239	18:13:41.5	-18:12:32	0.45	1.43	2.60	20.37	yes
G012.44−00.14 (d)	F_J181331.6-181115	18:13:32.5	-18:11:18	0.29	0.36	1.49	2.61	no
G012.88+00.53 (a)	F_J181145.3-173044	18:11:44.8	-17:31:17	0.36	1.11	1.94	8.06	yes
G013.02−00.83 (a)	F_J181700.1-180202	18:17:00.7	-18:02:18	0.47	0.27	2.76	1.97	yes
G013.68−00.60 (a)	F_J181725.7-172049	18:17:27.6	-17:20:59	0.24	0.42	1.19	3.05	no
G018.50−00.16 (c)	E_J182517.5-125526	18:25:17.5	-12:55:31	0.27	0.29	1.37	2.10	no
G018.50−00.16 (d)	F_J182523.2-125450	18:25:23.3	-12:54:55	0.25	0.59	1.25	4.28	no
G018.50−00.16 (b)	F_J182520.4-125014	18:25:21.2	-12:50:18	0.29	0.32	1.49	2.31	no
G018.58−00.08 (b)	F_J182507.3-124750	18:25:07.6	-12:48:00	0.32	0.46	1.68	3.33	yes
G018.58−00.08 (a)	F_J182508.5-124520	18:25:08.9	-12:45:20	0.37	1.91	2.01	13.84	yes
G019.27+00.07 (a)	F_J182552.1-120456	18:25:54.0	-12:04:56	0.50	1.03	3.01	7.47	yes
G022.35+00.41 (b)	F_J183029.6-091238	18:30:28.7	-09:12:31	0.37	0.38	2.01	2.76	no
G022.35+00.41 (a)	F_J183024.4-091038	18:30:24.7	-09:10:47	0.51	1.89	3.10	13.69	yes
G023.86−00.19 (a)	E_J183526.9-080814	18:35:26.6	-08:08:22	0.32	0.42	1.68	3.05	no
G024.00+00.15 (a)	E_J183428.8-075220	18:34:29.5	-07:52:23	0.20	1.11	0.97	8.06	yes
G024.36−00.16 (a)	F_J183618.3-074102	18:36:17.5	-07:41:27	0.41	0.88	2.29	6.37	yes
G024.37−00.21 (a)	F_J183630.0-074208	18:36:30.2	-07:42:16	0.34	0.34	1.81	2.46	yes
G024.60+00.08 (a)	F_J183540.1-071838	18:35:39.4	-07:18:51	0.49	2.02	2.93	14.64	yes
G024.68+00.17 (a)	F_J183540.1-071514	18:35:41.2	-07:15:22	0.20	0.25	0.97	1.81	yes
G025.04−00.20 (g)	F_J183712.0-071126	18:37:12.8	-07:11:23	0.36	0.76	1.94	5.51	yes
G025.04−00.20 (e)	F_J183719.2-071144	18:37:18.8	-07:11:49	0.41	1.13	2.29	8.19	yes
G025.04-00.20 (b)	F_J183734.6-070726	18:37:34.8	-07:07:39	0.44	0.38	2.52	2.76	yes
G025.04−00.20 (f)	F_J183738.2-070550	18:37:38.2	-07:06:00	0.38	0.29	2.08	2.10	no
G028.37+00.07 (a)	F_J184250.6-040314	18:42:50.6	-04:03:30	0.61	2.52	4.09	18.27	yes
G028.37+00.07 (d)	F_J184248.2-040133	18:42:48.6	-04:01:42	0.47	0.65	2.76	4.71	yes
G028.37+00.07 (b)	F_J184255.4-040150	18:42:55.5	-04:01:47	0.51	0.95	3.10	6.89	no
G028.37+00.07 (e)	F_J184300.2-040132	18:43:00.5	-04:01:36	0.45	0.69	2.60	5.01	no
G028.53−00.25 (g)	F_J184417.3-040208	18:44:17.0	-04:02:18	0.27	0.61	1.37	5.40	yes
G028.53−00.25 (b)	F_J184422.5-040150	18:44:23.7	-04:02:09	0.38	0.57	2.08	4.13	yes
G028.53−00.25 (c)	F_J184415.6-040056	18:44:16.6	-04:01:02	0.34	1.03	1.81	7.47	yes
G028.53−00.25 (a)	F_J184418.1-035938	18:44:17.1	-03:59:37	0.41	2.65	2.29	19.20	yes
G028.53−00.25 (e)	F_J184418.1-035938	18:44:17.7	-03:58:16	0.29	0.69	1.49	5.01	yes
G028.61−00.26 (a)	F_J184428.1-035750	18:44:29.0	-03:57:46	0.27	0.32	1.37	2.31	yes
G030.77+00.22 (a)	F_J184647.8-014856	18:46:47.1	-01:49:03	0.25	4.62	1.25	33.48	yes
G030.97−00.14 (a)	E_J184821.9-014832	18:48:24.2	-01:48:25	0.38	1.89	2.08	13.69	yes
G031.03+00.26 (b)	F_J184701.4-013438	18:47:01.5	-01:34:47	0.29	0.78	1.49	5.66	yes
G031.03+00.26 (c)	F_J184707.4-013432	18:47:07.7	-01:34:42	0.29	0.50	1.49	3.63	yes
G031.03+00.26 (a)	F_J184701.4-013314	18:47:01.2	-01:33:23	0.31	0.55	1.61	4.00	yes
G031.23+00.05 (a)	E_J184807.5-012844	18:48:08.3	-01:28:50	0.21	0.82	1.02	5.94	yes

MSX ID (MSXDC)	SCUBA ID (JCMTS)	RA (hh:mm:ss)	Dec (°: ': ")	C	F_{850} (Jy/beam)	$N_8(H_2)$ $\times10^{22}$ (cm^{-2})	$N_{850}(H_2)$ $\times10^{22}$ (cm^{-2})	MIPS source
G031.27+00.08 (a)	E_J184807.9-012626	18:48:08.0	-01:26:43	0.16	0.69	0.76	5.01	no
G031.38+00.29 (a)	F_J184732.6-011338	18:47:34.0	-01:13:59	0.38	1.53	2.08	11.10	no
G031.97+00.07 (b)	F_J184922.1-005038	18:49:22.2	-00:50:47	0.42	0.59	2.37	4.28	yes
G031.97+00.07 (c)	F_J184926.9-005002	18:49:27.0	-00:50:11	0.35	0.36	1.87	2.61	no
G033.69−00.01 (e)	E_J185248.6+003602	18:52:49.6	+00:35:55	0.32	0.63	1.68	4.56	no
G033.69−00.01 (b)	E_J185252.6+003832	18:52:53.1	+00:38:10	0.38	0.65	2.08	4.71	no
G033.69−00.01 (c)	E_J185253.8+004120	18:52:53.0	+00:40:44	0.37	0.59	2.01	4.28	no
G033.69−00.01 (a)	E_J185257.0+004302	18:52:57.6	+00:42:59	0.38	1.60	2.08	11.60	yes
G034.43+00.24 (a)	F_J185318.9+012650	18:53:18.9	+01:26:39	0.34	0.38	1.81	2.76	yes
G038.95−00.47 (a)	F_J190407.5+050844	19:04:08.3	+05:08:49	0.53	1.37	3.28	9.94	yes
G048.52−00.47 (a)	F_J192207.4+133713	19:22:07.9	+13:36:58	0.38	0.29	2.08	2.10	no
G048.65−00.29 (a)	F_J192144.7+134925	19:21:45.3	+13:49:22	0.34	0.40	1.81	2.89	yes
G079.24+00.41 (b)	E_J203137.7+401935	20:31:38.1	+40:19:38	0.51	0.88	3.10	6.37	-
G079.24+00.41 (a)	F_J203157.6+401828	20:31:56.8	+40:18:12	0.52	1.99	3.19	14.43	-
G081.67+00.44 (a)	F_J203924.9+421555	20:39:21.0	+42:15:47	0.23	2.31	1.14	16.74	-
G081.73+00.59 (a)	F_J203859.3+422330	20:38:58.2	+42:23:55	0.27	8.19	1.37	59.39	-
G081.76+00.63 (a)	F_J203851.6+422717	20:38:52.6	+42:27:12	0.17	0.80	0.81	5.81	-
G351.52+00.69 (a)	F_J172056.6-354044	17:20:58.2	-35:40:28	0.39	2.48	2.15	17.97	-
G353.26−00.16 (a)	F_J172935.1-344316	17:29:33.6	-34:43:31	0.31	0.44	1.61	3.20	-
G353.37−00.33 (b)	F_J173012.1-344328	17:30:12.4	-34:43:45	0.38	1.47	2.08	10.65	-
G353.37−00.33 (a)	F_J173017.0-344217	17:30:18.8	-34:41:58	0.43	2.29	2.44	19.61	-
G353.90+00.25 (e)	F_J172902.5-335950	17:29:02.2	-34:00:12	0.46	1.13	2.68	8.19	-
G353.90+00.25 (a)	F_J172917.1-340017	17:29:12.8	-34:00:01	0.62	0.55	4.21	4.00	-
G353.90+00.25 (f)	F_J172917.1-340017	17:29:16.8	-34:00:25	0.46	0.61	2.68	5.40	-
G353.90+00.25 (c)	F_J172919.4-335550	17:29:19.1	-33:55:59	0.50	0.59	3.01	4.28	-
G353.90+00.25 (b)	F_J172928.5-335444	17:29:27.9	-33:55:06	0.59	0.50	3.88	3.63	-
G353.90+00.25 (d)	F_J172927.1-335302	17:29:25.0	-33:53:03	0.49	0.90	2.93	6.52	-
G359.05+00.00 (a)	F_J174321.6-294437	17:43:21.8	-29:44:43	0.27	0.63	1.37	4.56	-
G359.06−00.03 (a)	F_J174326.7-294531	17:43:29.7	-29:45:22	0.16	0.71	0.76	5.14	-
G359.08+00.04 (a)	F_J174314.8-294143	17:43:14.8	-29:42:02	0.20	0.50	0.97	3.63	-
G359.29−00.03 (a)	F_J174404.5-293302	17:44:03.5	-29:33:12	0.21	1.28	1.02	9.29	-
G359.37−00.28 (a)	F_J174514.5-293644	17:45:14.1	-29:37:27	0.12	0.27	0.56	19.57	-
G359.41+00.08 (a)	F_J174354.0-292314	17:43:53.9	-29:23:27	0.16	1.03	0.76	7.47	-
G359.46−00.03 (a)	F_J174428.9-292426	17:44:29.3	-29:24:18	0.28	2.42	1.43	19.54	-
G359.48−00.22 (a)	F_J174514.4-292902	17:45:15.1	-29:29:30	0.14	1.87	0.66	13.56	-
G359.59+00.02 (a)	F_J174436.3-291621	17:45:33.5	-29:24:26	0.31	1.87	1.61	15.56	-
G359.60−00.22 (b)	F_J174535.0-292456	17:44:32.0	-29:16:05	0.20	1.97	0.97	14.28	-
G359.60−00.22 (a)	F_J174535.0-292314	17:45:35.2	-29:23:15	0.36	5.50	1.94	39.96	-
G359.68−00.13 (a)	F_J174526.3-291608	17:45:25.3	-29:16:06	0.20	0.61	0.97	5.40	-
G359.80−00.13 (a)	F_J174539.0-291132	17:45:37.1	-29:11:25	0.32	1.62	1.68	11.75	-
G359.82+00.12 (a)	F_J174443.6-290127	17:44:43.1	-29:01:02	0.19	0.44	0.92	3.20	-
G359.83+00.18 (a)	E_J174429.3-285901	17:44:29.5	-28:59:13	0.21	0.38	1.02	2.76	-
G359.85+00.21 (a)	E_J174425.2-285643	17:44:25.3	-28:56:49	0.23	0.38	1.14	2.76	-
G359.87−00.09 (a)	F_J174544.0-290502	17:45:43.4	-29:05:22	0.25	5.44	1.25	3.95	-
G359.90−00.30 (a)	F_J174636.3-291011	17:46:35.8	-29:10:26	0.35	2.33	1.87	16.89	-
G359.91+00.17 (b)	F_J174444.4-285519	17:44:43.6	-28:55:28	0.45	0.90	2.60	6.52	-
G359.91+00.17 (a)	F_J174448.5-285349	17:44:47.6	-28:53:54	0.58	4.41	3.77	31.96	-

B.2 Cores with no 850 μm detection

Table B.2: Data for all MSX identified IRDC candidate cores within the SCUBA Legacy Catalogue, with no detection at 850 μm.

MSX ID (MSXDC)	l (°)	b (°)	RA (hh:mm:ss)	Dec (°: ': ")	Peak Contrast	$N_8(H_2)$ $\times 10^{22}$ cm^{-2}
G000.13−00.14 (b)	0.163	-0.164	17:46:38.8	-28:52:56	0.19	0.92
G000.13−00.19 (a)	0.131	-0.196	17:46:41.8	-28:55:34	0.21	1.02
G000.36−00.21 (a)	0.364	-0.216	17:47:19.6	-28:44:14	0.20	0.97
G000.73−00.01 (a)	0.733	-0.014	17:47:24.6	-28:19:02	0.15	0.77
G001.62−00.08 (a)	1.631	-0.092	17:49:48.6	-27:35:17	0.16	0.76
G004.33−00.04 (a)	4.336	-0.052	17:55:48.0	-25:14:19	0.34	1.81
G004.33−00.04 (c)	4.358	-0.056	17:55:51.9	-25:13:18	0.29	1.49
G006.06-01.39 (a)	6.063	-1.397	18:04:43.5	-24:24:28	0.23	1.14
G006.09-01.39 (a)	6.094	-1.396	18:04:47.3	-24:22:49	0.24	1.19
G006.09-01.36 (a)	6.094	-1.367	18:04:40.6	-24:21:58	0.20	0.97
G010.57−00.30 (a)	10.588	-0.311	18:10:08.1	-19:55:35	0.33	1.74
G010.94−00.05 (a)	10.944	-0.059	18:09:55.7	-19:29:35	0.18	0.86
G012.37+00.50 (c)	12.431	0.496	18:10:54.4	-17:55:22	0.29	1.49
G012.44−00.20 (a)	12.449	-0.201	18:13:30.9	-18:14:31	0.15	0.77
G012.88+00.53 (c)	12.886	0.528	18:11:42.5	-17:30:31	0.29	1.49
G013.15+00.09 (a)	13.154	0.099	18:13:49.6	-17:28:46	0.25	1.25
G017.00+00.67 (a)	17.003	0.661	18:19:22.5	-13:49:34	0.33	1.74
G017.01+00.78 (a)	17.013	0.789	18:18:55.8	-13:45:24	0.13	0.61
G017.03+00.71 (a)	17.029	0.719	18:19:13.0	-13:46:33	0.14	0.66
G017.10+00.71 (a)	17.096	0.699	18:19:25.1	-13:43:34	0.31	1.61
G017.10+00.71 (b)	17.129	0.711	18:19:26.4	-13:41:29	0.31	1.61
G018.99−00.30 (b)	19.004	-0.306	18:26:44.4	-12:30:45	0.28	1.43
G024.60+00.08 (b)	24.659	0.163	18:35:40.9	-07:16:57	0.32	1.68
G024.60+00.08 (d)	24.596	0.131	18:35:40.7	-07:21:11	0.29	1.49
G025.12−00.16 (a)	25.126	-0.162	18:37:42.6	-07:01:01	0.12	0.56
G025.37−00.06 (a)	25.419	-0.104	18:38:02.7	-06:43:48	0.26	1.31
G025.42+00.10 (a)	25.426	0.109	18:37:17.7	-06:37:34	0.14	0.66
G027.93−00.34 (a)	27.924	-0.344	18:43:30.8	-04:36:47	0.19	0.92
G031.32+00.09 (a)	31.326	0.094	18:48:10.4	-01:23:11	0.17	0.81
G031.33+00.12 (a)	31.336	0.124	18:48:05.1	-01:21:49	0.16	0.76
G033.69−00.01 (d)	33.639	-0.056	18:52:55.6	+00:36:14	0.35	1.87
G034.94+00.37 (a)	34.941	0.384	18:53:44.2	+01:57:47	0.18	0.86
G042.75+00.01 (a)	42.751	0.019	19:09:25.2	+08:44:19	0.21	1.02
G042.75−00.19 (a)	42.753	-0.202	19:10:13.0	+08:38:18	0.22	1.08
G080.88−00.12 (a)	80.886	-0.131	20:39:16.7	+41:17:23	0.21	1.02
G081.49+00.13 (a)	81.504	0.129	20:40:11.5	+41:56:17	0.40	2.22
G081.49+00.13 (b)	81.498	0.161	20:40:02.2	+41:57:11	0.34	1.81

MSX ID (MSXDC)	l (°)	b (°)	RA (hh:mm:ss)	Dec (°: ': ")	Peak Contrast	$N_8(H_2)$ $\times 10^{22}\,cm^{-2}$
G081.56+00.57 (a)	81.564	0.581	20:38:27.4	+42:15:40	0.16	0.76
G081.57+00.50 (b)	81.576	0.523	20:38:44.7	+42:14:07	0.27	1.37
G081.60+00.58 (a)	81.603	0.586	20:38:33.7	+42:17:42	0.17	0.81
G081.69+00.71 (a)	81.699	0.708	20:38:21.2	+42:26:43	0.19	0.92
G351.50+00.66 (a)	351.509	0.661	17:21:05.1	-35:41:56	0.17	0.81
G353.26−00.16 (f)	353.281	-0.207	17:29:28.1	-34:43:09	0.24	1.19
G353.90+00.25 (g)	353.886	0.254	17:29:13.6	-33:57:36	0.40	2.22
G353.98+00.39 (a)	353.993	0.391	17:28:57.7	-33:47:43	0.20	0.97
G359.25+00.01 (a)	359.254	0.016	17:43:46.2	-29:33:50	0.15	0.77
G359.28+00.02 (a)	359.298	0.031	17:43:49.0	-29:31:06	0.38	2.08
G359.28+00.02 (b)	359.298	0.006	17:43:54.9	-29:31:54	0.34	1.81
G359.79−00.25 (b)	359.799	-0.267	17:46:11.1	-29:14:48	0.23	1.14
G359.81−00.29 (a)	359.814	-0.297	17:46:20.3	-29:14:58	0.17	0.81
G359.82−00.37 (b)	359.843	-0.367	17:46:40.9	-29:15:40	0.27	1.37

B.3 Mass estimates

Table B.3: Mass estimates for IRDC cores with distances obtained by the GRS survey (Jackson *et al.*, 2008b). Galacitc coordinates quoted come from the MSX catalogue positions (Simon *et al.*, 2006a).

MSX ID (MSXDC)	SCUBA ID (JCMTS)	l (°)	b (°)	Peak Contrast	Flux[a] Jy	Distance kpc	Mass $M_\odot$	MIPS detected?
G018.50−00.16 (b)	F_J182520.4-125014	18.558	-0.159	0.29	1.79	4.1	240	No
G018.58−00.08 (b)	F_J182507.3-124750	18.566	-0.092	0.32	0.97	3.8	110	Yes
G018.58−00.08 (a)	F_J182508.5-124520	18.608	-0.076	0.37	4.51	3.8	500	Yes
G019.27+00.07 (a)	F_J182552.1-120456	19.289	0.076	0.50	3.24	2.4	130	Yes
G022.35+00.41 (b)	F_J183029.6-091238	22.356	0.416	0.37	2.02	4.3	290	No
G022.35+00.41 (a)	F_J183024.4-091038	22.374	0.444	0.51	4.94	4.3	720	Yes
G023.86−00.19 (a)	E_J183526.9-080814	23.871	-0.179	0.32	1.92	4.0	240	No
G024.36−00.16 (a)	F_J183618.3-074102	24.366	-0.159	0.41	1.77	3.9	190	Yes
G024.37−00.21 (a)	F_J183630.0-074208	24.378	-0.212	0.34	0.46	3.9	50	Yes
G024.60+00.08 (a)	F_J183540.1-071838	24.628	0.154	0.49	5.22	3.7	560	Yes
G028.37+00.07 (a)	F_J184250.6-040314	28.341	0.058	0.61	10.8	5.0	1010	Yes
G028.37+00.07 (d)	F_J184248.2-040133	28.364	0.079	0.47	2.52	5.0	100	Yes
G028.37+00.07 (g)	F_J184239.7-040027	28.366	0.121	0.38	1.36	5.0	100	No
G028.37+00.07 (b)	F_J184255.4-040150	28.376	0.053	0.51	3.34	5.0	310	No
G028.37+00.07 (e)	F_J184300.2-040132	28.388	0.036	0.45	2.18	5.0	130	No
G028.37+00.07 (f)	F_J184252.3-035956	28.403	0.064	0.43	3.72	5.0	4160	No
G028.53−00.25 (a)	F_J184418.1-035938	28.563	-0.232	0.41	12.8	5.7	4190	Yes
G028.61−00.26 (a)	F_J184428.1-035750	28.613	-0.262	0.27	0.56	4.2	80	Yes
G030.97−00.14 (a)	E_J184821.9-014832	30.978	-0.149	0.38	6.30	5.1	1270	Yes
G031.03+00.26 (b)	F_J184701.4-013438	31.023	0.261	0.29	2.97	6.6	520	Yes
G031.03+00.26 (c)	F_J184707.4-013432	31.036	0.239	0.29	1.32	6.6	160	Yes
G031.03+00.26 (a)	F_J184701.4-013314	31.043	0.273	0.31	3.43	6.6	460	Yes
G031.38+00.29 (a)	F_J184732.6-011338	31.393	0.299	0.38	6.96	6.6	2460	No
G031.97+00.07 (b)	F_J184922.1-005038	31.943	0.074	0.42	0.88	6.9	420	Yes
G031.97+00.07 (c)	F_J184926.9-005002	31.961	0.061	0.35	0.82	6.9	490	No
G033.69−00.01 (e)	E_J185248.6+00360	233.623	-0.036	0.32	1.76	7.1	690	No
G033.69−00.01 (b)	E_J185252.6+00383	233.663	-0.032	0.38	1.60	7.1	620	No
G033.69−00.01 (c)	E_J185253.8+00412	033.701	-0.012	0.37	1.35	7.1	530	No
G033.69−00.01 (a)	E_J185257.0+00430	233.743	-0.012	0.38	7.05	7.1	2750	Yes
G034.43+00.24 (a)	F_J185318.9+01265	034.431	0.241	0.34	1.20	3.7	100	Yes
G038.95−00.47 (a)	F_J190407.5+05084	38.959	-0.469	0.53	4.58	2.7	290	Yes
G048.52−00.47 (a)	F_J192207.4+13371	348.519	-0.467	0.38	0.76	2.8	50	No
G048.65−00.29 (a)	F_J192144.7+13492	548.658	-0.289	0.34	1.97	2.5	100	Yes

[a]Flux integrated over the area of the object as defined by Clumpfind Di Francesco *et al.* (2008)

Bibliography

Anathpindika, S. (2009). Supersonic cloud collision. I. *A&A*, **504**, 437–450.

Andre, P., Ward-Thompson, D., and Barsony, M. (1993). Submillimeter continuum observations of Rho Ophiuchi A - The candidate protostar VLA 1623 and prestellar clumps. *ApJ*, **406**, 122–141.

Andre, P., Ward-Thompson, D., and Barsony, M. (2000). From Prestellar Cores to Protostars: the Initial Conditions of Star Formation. *Protostars and Planets IV*, pages 59–+.

Arce, H. G., Shepherd, D., Gueth, F., Lee, C., Bachiller, R., Rosen, A., and Beuther, H. (2007). Molecular Outflows in Low- and High-Mass Star-forming Regions. *Protostars and Planets V*, pages 245–260.

Arce, H. G., Borkin, M. A., Goodman, A. A., Pineda, J. E., and Halle, M. W. (2010). The COMPLETE Survey of Outflows in Perseus. *ApJ*, **715**, 1170–1190.

Arnal, E. M. and Goss, W. M. (1985). Westerbork observations of 6 CM H2CO in W 51A. *A&A*, **145**, 369–376.

Ascenso, J., Alves, J., and Lago, M. T. V. T. (2009a). Mass segregation in young clusters: observational biases. *ApSS*, **324**, 113–119.

Ascenso, J., Alves, J., and Lago, M. T. V. T. (2009b). No evidence of mass segregation in massive young clusters. *A&A*, **495**, 147–155.

Baldry, I. K. and Glazebrook, K. (2003). Constraints on a Universal Stellar Initial Mass Function from Ultraviolet to Near-Infrared Galaxy Luminosity Densities. *ApJ*, **593**, 258–271.

Barbosa, C. L., Blum, R. D., Conti, P. S., Damineli, A., and Figuerêdo, E. (2008). High Spatial Resolution Spectroscopy of W51 IRS 2E and IRS 2W: Two Very Massive Young Stars in Early Formation Stages. *ApJL*, **678**, L55–L58.

Barnard, E. E. (1919). On the dark markings of the sky, with a catalogue of 182 such objects. *ApJ*, **49**, 1–24.

Bash, F. N., Green, E., and Peters, III, W. L. (1977). The galactic density wave, molecular clouds, and star formation. *ApJ*, **217**, 464–472.

Bate, M. R. and Bonnell, I. A. (2005). The origin of the initial mass function and its dependence on the mean Jeans mass in molecular clouds. *MNRAS*, **356**, 1201–1221.

Bate, M. R., Bonnell, I. A., and Bromm, V. (2003). The formation of a star cluster: predicting the properties of stars and brown dwarfs. *MNRAS*, **339**, 577–599.

Battersby, C., Bally, J., Jackson, J. M., Ginsburg, A., Shirley, Y. L., Schlingman, W., and Glenn, J. (2010). An Infrared Through Radio Study of the Properties and Evolution of IRDC Clumps. *ApJ*, **721**, 222–250.

Bergin, E. A. and Langer, W. D. (1997). Chemical Evolution in Preprotostellar and Protostellar Cores. *ApJ*, **486**, 316–+.

Beuther, H., Schilke, P., Sridharan, T. K., Menten, K. M., Walmsley, C. M., and Wyrowski, F. (2002). Massive molecular outflows. *A&A*, **383**, 892–904.

Bica, E., Dutra, C. M., Soares, J., and Barbuy, B. (2003). New infrared star clusters in the Northern and Equatorial Milky Way with 2MASS. *A&A*, **404**, 223–232.

Bieging, J. (1975). The W 51 source complex. In T. L. Wilson and D. Downes, editors, *H II regions and related topics*, volume 42 of *Lecture Notes in Physics, Berlin Springer Verlag*, pages 443–+.

Birkmann, S. M., Krause, O., Hennemann, M., Henning, T., Steinacker, J., and Lemke, D. (2007). A massive protostellar core with an infalling envelope. *A&A*, **474**, 883–890.

Blitz, L. (1993). Giant molecular clouds. In E. H. Levy & J. I. Lunine, editor, *Protostars and Planets III*, pages 125–161.

Bohlin, R. C., Savage, B. D., and Drake, J. F. (1978). A survey of interstellar H I from L-alpha absorption measurements. II. *ApJ*, **224**, 132–142.

Bok, B. J. and Reilly, E. F. (1947). Small Dark Nebulae. *ApJ*, **105**, 255–+.

Bonnell, I. A., Bate, M. R., Clarke, C. J., and Pringle, J. E. (1997). Accretion and the stellar mass spectrum in small clusters. *MNRAS*, **285**, 201–208.

Bonnell, I. A., Bate, M. R., and Zinnecker, H. (1998). On the formation of massive stars. *MNRAS*, **298**, 93–102.

Bonnell, I. A., Clarke, C. J., Bate, M. R., and Pringle, J. E. (2001a). Accretion in stellar clusters and the initial mass function. *MNRAS*, **324**, 573–579.

Bonnell, I. A., Bate, M. R., Clarke, C. J., and Pringle, J. E. (2001b). Competitive accretion in embedded stellar clusters. *MNRAS*, **323**, 785–794.

Bonnell, I. A., Vine, S. G., and Bate, M. R. (2004). Massive star formation: nurture, not nature. *MNRAS*, **349**, 735–741.

Bonnell, I. A., Smith, R. J., Clark, P. C., and Bate, M. R. (2011). The efficiency of star formation in clustered and distributed regions. *MNRAS*, **410**, 2339–2346.

Borkin, M., Arce, H., Goodman, A., and Halle, M. (2008). 3D Visualization and Detection of Outflows From Young Stars. In R. W. Argyle, P. S. Bunclark, & J. R. Lewis, editor, *Astronomical Data Analysis Software and Systems XVII*, volume 394 of *Astronomical Society of the Pacific Conference Series*, pages 145–+.

Brand, J. and Blitz, L. (1993). The Velocity Field of the Outer Galaxy. *A&A*, **275**, 67–+.

Breen, S. L., Ellingsen, S. P., Caswell, J. L., and Lewis, B. E. (2010). 12.2-GHz methanol masers towards 1.2-mm dust clumps: quantifying high-mass star formation evolutionary schemes. *MNRAS*, **401**, 2219–2244.

Buckle, J. V., Hills, R. E., Smith, H., Dent, W. R. F., Bell, G., Curtis, E. I., Dace, R., Gibson, H., Graves, S. F., and et al. (2009). HARP/ACSIS: a submillimetre spectral imaging system on the James Clerk Maxwell Telescope. *MNRAS*, **399**, 1026–1043.

Buckle, J. V., Curtis, E. I., Roberts, J. F., White, G. J., Hatchell, J., Brunt, C., Butner, H. M., Cavanagh, B., and et al. (2010). The JCMT Legacy Survey of the Gould Belt: a first look at Orion B with HARP. *MNRAS*, **401**, 204–222.

Burrows, A., Hubbard, W. B., Lunine, J. I., and Liebert, J. (2001). The theory of brown dwarfs and extrasolar giant planets. *Reviews of Modern Physics*, **73**, 719–765.

Burton, W. B. and Shane, W. W. (1970). Neutral Hydrogen in the Sagittarius and Scutum Spiral Arms. In W. Becker and G. I. Kontopoulos, editors, *The Spiral Structure of our Galaxy*, volume 38 of *IAU Symposium*, pages 397–+.

Carey, S. J., Clark, F. O., Egan, M. P., Price, S. D., Shipman, R. F., and Kuchar, T. A. (1998). The Physical Properties of the Midcourse Space Experiment Galactic Infrared-dark Clouds. *ApJ*, **508**, 721–728.

Carey, S. J., Mizuno, D. R., Kraemer, K., Shenoy, S., Noriega-Crespo, A., Price, S. D., Paladini, R., and Kuchar, T. (2007). MIPSGAL v2.0 Data Delivery Description Document (16 October 2007). *MIPSGAL documentation*.

Carpenter, J. M. and Sanders, D. B. (1998). The W51 Giant Molecular Cloud. *AJ*, **116**, 1856–1867.

Carr, J. S. (1987). A study of clumping in the Cepheus OB 3 molecular cloud. *ApJ*, **323**, 170–178.

Cavanagh, B., Jenness, T., Economou, F., and Currie, M. J. (2008). The ORAC-DR data reduction pipeline. *Astronomische Nachrichten*, **329**, 295–297.

Cesaroni, R. (2005). Outflow, Infall, and Rotation in High-Mass Star Forming Regions. *ApSS*, **295**, 5–17.

Chabrier, G. (2003). Galactic Stellar and Substellar Initial Mass Function. *PASP*, **115**, 763–795.

Chambers, E. T., Jackson, J. M., Rathborne, J. M., and Simon, R. (2009). Star Formation Activity of Cores within Infrared Dark Clouds. *ApJS*, **181**, 360–390.

Charnley, S. B. (1997). Sulfuretted Molecules in Hot Cores. *ApJ*, **481**, 396–+.

Cheung, A. C., Rank, D. M., and Townes, C. H. (1969). Detection of Water in Interstellar Regions by its Microwave Radiation. *Nature*, **221**, 626–628.

Churchwell, E. (2002). Ultra-Compact HII Regions and Massive Star Formation. *ARA&A*, **40**, 27–62.

Clark, J. S. and Porter, J. M. (2004). Triggered massive star formation in the vicinity of WR 48a. *A&A*, **427**, 839–847.

Clark, J. S., Davies, B., Najarro, F., MacKenty, J., Crowther, P. A., Messineo, M., and Thompson, M. A. (2009). The P Cygni supergiant [OMN2000] LS1 - implications for the star formation history of W51. *A&A*, **504**, 429–435.

Crapsi, A., van Dishoeck, E. F., Hogerheijde, M. R., Pontoppidan, K. M., and Dullemond, C. P. (2008). Characterizing the nature of embedded young stellar objects through silicate, ice and millimeter observations. *A&A*, **486**, 245–254.

Crowther, P. A., Schnurr, O., Hirschi, R., Yusof, N., Parker, R. J., Goodwin, S. P., and Kassim, H. A. (2010). The R136 star cluster hosts several stars whose individual masses greatly exceed the accepted 150$M_{\odot}$ stellar mass limit. *MNRAS*, **408**, 731–751.

Curtis, E. I. and Richer, J. S. (2009). The properties of SCUBA cores in the Perseus molecular cloud: the bias of clump-finding algorithms. *ArXiv e-prints*.

Curtis, E. I., Richer, J. S., and Buckle, J. V. (2010a). A submillimetre survey of the kinematics of the Perseus molecular cloud - I. Data. *MNRAS*, **401**, 455–472.

Curtis, E. I., Richer, J. S., Swift, J. J., and Williams, J. P. (2010b). A submillimetre survey of the kinematics of the Perseus molecular cloud - II. Molecular outflows. *MNRAS*, **408**, 1516–1539.

Cyganowski, C. J., Whitney, B. A., Holden, E., Braden, E., Brogan, C. L., Churchwell, E., Indebetouw, R., Watson, D. F., Babler, B. L., Benjamin, R., Gomez, M., Meade, M. R., Povich, M. S., Robitaille, T. P., and Watson, C. (2008). A Catalog of Extended Green Objects in the GLIMPSE Survey: A New Sample of Massive Young Stellar Object Outflow Candidates. *AJ*, **136**, 2391–2412.

Dame, T. M., Elmegreen, B. G., Cohen, R. S., and Thaddeus, P. (1986). The largest molecular cloud complexes in the first galactic quadrant. *ApJ*, **305**, 892–908.

Davis, C. J., Chrysostomou, A., Hatchell, J., and et al. (2010). The JCMT Legacy Survey of the Gould Belt: a first look at Taurus with HARP. *MNRAS*, **405**, 759–776.

Di Francesco, J., Johnstone, D., Kirk, H., MacKenzie, T., and Ledwosinska, E. (2008). The SCUBA Legacy Catalogues: Submillimeter-Continuum Objects Detected by SCUBA. *ApJS*, **175**, 277–295.

Diehl, R., Halloin, H., Kretschmer, K., Lichti, G. G., Schönfelder, V., Strong, A. W., von Kienlin, A., Wang, W., Jean, P., Knödlseder, J., Roques, J., Weidenspointner, G., Schanne, S., Hartmann, D. H., Winkler, C., and Wunderer, C. (2006). Radioactive ^{26}Al from massive stars in the Galaxy. *Nature*, **439**, 45–47.

Dobbs, C. (2007). *The formation of molecular clouds in spiral galaxies*. Ph.D. thesis, University of St Andrews Physics and Astronomy theses.

Dobbs, C. (2009). The Formation of GMCs by Agglomeration and Self Gravity in Spiral Galaxies. In *The Evolving ISM in the Milky Way and Nearby Galaxies*.

Du, F. and Yang, J. (2008). A ^{12}CO, ^{13}CO, and C^{18}O Survey of Infrared Dark Clouds. *ApJ*, **686**, 384–398.

Duarte-Cabral, A., Dobbs, C. L., Peretto, N., and Fuller, G. A. (2011). Was a cloud-cloud collision the trigger of the recent star formation in Serpens? *A&A*, **528**, A50+.

Dunham, M. M., Crapsi, A., Evans, II, N. J., Bourke, T. L., Huard, T. L., Myers, P. C., and Kauffmann, J. (2008). Identifying the Low-Luminosity Population of Embedded Protostars in the c2d Observations of Clouds and Cores. *ApJS*, **179**, 249–282.

Dyson, J. E. and Williams, D. A. (1997). *The physics of the interstellar medium*.

Egan, M. P., Shipman, R. F., Price, S. D., Carey, S. J., Clark, F. O., and Cohen, M. (1998). A Population of Cold Cores in the Galactic Plane. *ApJL*, **494**, L199+.

Elia, D., Schisano, E., Molinari, S., Robitaille, T., Anglés-Alcázar, D., Bally, J., Battersby, C., Benedettini, M., and et al. (2010). A Herschel study of YSO evolutionary stages and formation timelines in two fields of the Hi-GAL survey. *A&A*, **518**, L97+.

Elias, J. H. (1978). A study of the Taurus dark cloud complex. *ApJ*, **224**, 857–872.

Ellingsen, S. P., Voronkov, M. A., Cragg, D. M., Sobolev, A. M., Breen, S. L., and Godfrey, P. D. (2007). Investigating high-mass star formation through maser surveys. In J. M. Chapman & W. A. Baan, editor, *IAU Symposium*, volume 242 of *IAU Symposium*, pages 213–217.

Evans, N. J., Dunham, M. M., Jørgensen, J. K., Enoch, M. L., Merín, B., van Dishoeck, E. F., Alcalá, J. M., Myers, P. C., and et al. (2009). The Spitzer c2d Legacy Results: Star-Formation Rates and Efficiencies; Evolution and Lifetimes. *ApJS*, **181**, 321–350.

Evans, II, N. J., Allen, L. E., Blake, G. A., Boogert, A. C. A., Bourke, T., Harvey, P. M., Kessler, J. E., Koerner, D. W., and et al. (2003). From Molecular Cores to Planet-forming Disks: An SIRTF Legacy Program. *PASP*, **115**, 965–980.

Fich, M. and Tremaine, S. (1991). The mass of the Galaxy. *ARA&A*, **29**, 409–445.

Figuerêdo, E., Blum, R. D., Damineli, A., Conti, P. S., and Barbosa, C. L. (2008). The Stellar Content of Obscured Galactic Giant H II Regions. Vi. W51A. *AJ*, **136**, 221–233.

Flaherty, K. M., Pipher, J. L., Megeath, S. T., Winston, E. M., Gutermuth, R. A., Muzerolle, J., Allen, L. E., and Fazio, G. G. (2007). Infrared Extinction toward Nearby Star-forming Regions. *ApJ*, **663**, 1069–1082.

Fontani, F., Pascucci, I., Caselli, P., Wyrowski, F., Cesaroni, R., and Walmsley, C. M. (2007). Comparative study of complex N- and O-bearing molecules in hot molecular cores. *A&A*, **470**, 639–652.

Frerking, M. A., Langer, W. D., and Wilson, R. W. (1982). The relationship between carbon monoxide abundance and visual extinction in interstellar clouds. *ApJ*, **262**, 590–605.

Frieswijk, W. F., Spaans, M., Shipman, R. F., Teyssier, D., Carey, S. J., and Tielens, A. G. G. M. (2008). Spitzer's Mid-Infrared View on an Outer-Galaxy Infrared Dark Cloud Candidate toward NGC 7538. *ApJL*, **685**, L51–L54.

Frieswijk, W. W. F. and Shipman, R. F. (2010). Searching for dark clouds in the outer galactic plane. I. A statistical approach for identifying extended red(dened) regions in 2MASS. *A&A*, **515**, A51+.

Frieswijk, W. W. F., Spaans, M., Shipman, R. F., Teyssier, D., and Hily-Blant, P. (2007). Physical characteristics of a dark cloud in an early stage of star formation toward NGC 7538. An outer Galaxy infrared dark cloud? *A&A*, **475**, 263–275.

Fukui, Y., Iwata, T., Mizuno, A., Bally, J., and Lane, A. P. (1993). Molecular outflows. In E. H. Levy & J. I. Lunine, editor, *Protostars and Planets III*, pages 603–639.

Garden, R. P., Hayashi, M., Hasegawa, T., Gatley, I., and Kaifu, N. (1991). A spectroscopic study of the DR 21 outflow source. III - The CO line emission. *ApJ*, **374**, 540–554.

Genzel, R. and Stutzki, J. (1989). The Orion Molecular Cloud and star-forming region. *ARA&A*, **27**, 41–85.

Genzel, R., Becklin, E. E., Moran, J. M., Reid, M. J., Jaffe, D. T., Downes, D., and Wynn-Williams, C. G. (1982). Infrared and radio observations of W51 - Another Orion-KL at a distance of 7 kiloparsecs. *ApJ*, **255**, 527–535.

Goldader, J. D. and Wynn-Williams, C. G. (1994). Near-infrared observations of W51. *ApJ*, **433**, 164–178.

Goldsmith, P. F., Snell, R. L., Hemeon-Heyer, M., and Langer, W. D. (1984). Bipolar outflows in dark clouds. *ApJ*, **286**, 599–608.

Graves, S. F., Richer, J. S., Buckle, J. V., and et al. (2010). The JCMT Legacy Survey of the Gould Belt: a first look at Serpens with HARP. *MNRAS*, **409**, 1412–1428.

Green, J. A., Caswell, J. L., Fuller, G. A., Avison, A., Breen, S. L., Brooks, K., Burton, M. G., Chrysostomou, A., and et al. (2009). The 6-GHz multibeam maser survey - I. Techniques. *MNRAS*, **392**, 783–794.

Guinan, E. F., Eaton, J. A., Wasatonic, R., Stewart, H., Engle, S. G., and McCook, G. P. (2010). Times-Series Photometry and Spectroscopy of the Bright Blue Supergiant Rigel: Probing the Atmosphere and Interior of a SN II Progenitor. *Highlights of Astronomy*, **15**, 359–359.

Hasan, P. and Hasan, S. (2011). Mass segregation in diverse environments. *ArXiv e-prints*.

Hatchell, J. and Dunham, M. M. (2009). Star formation in Perseus. V. Outflows detected by HARP. *A&A*, **502**, 139–153.

Hatchell, J., Thompson, M. A., Millar, T. J., and MacDonald, G. H. (1998). Sulphur chemistry and evolution in hot cores. *A&A*, **338**, 713–722.

Hatchell, J., Fuller, G. A., Millar, T. J., Thompson, M. A., and Macdonald, G. H. (2000). SCUBA imaging of high mass star formation regions. *A&A*, **357**, 637–650.

Hatchell, J., Fuller, G. A., and Richer, J. S. (2007). Star formation in Perseus. III. Outflows. *A&A*, **472**, 187–198.

Henning, T., Linz, H., Krause, O., Ragan, S., Beuther, H., Launhardt, R., Nielbock, M., and Vasyunina, T. (2010). The seeds of star formation in the filamentary infrared-dark cloud G011.11-0.12. *ArXiv e-prints*.

Heyer, M., Krawczyk, C., Duval, J., and Jackson, J. M. (2009). Re-Examining Larson's Scaling Relationships in Galactic Molecular Clouds. *ApJ*, **699**, 1092–1103.

Hildebrand, R. H. (1983). The Determination of Cloud Masses and Dust Characteristics from Submillimetre Thermal Emission. *QJRAS*, **24**, 267–+.

Hindson, L., Thompson, M. A., Urquhart, J. S., Clark, J. S., and Davies, B. (2010). The G305 star-forming complex: wide-area molecular mapping of NH_3 and H_2O masers. *MNRAS*, pages 1441–+.

Holland, W. S., Robson, E. I., Gear, W. K., Cunningham, C. R., Lightfoot, J. F., Jenness, T., Ivison, R. J., Stevens, J. A., Ade, P. A. R., Griffin, M. J., Duncan, W. D., Murphy, J. A., and Naylor, D. A. (1999). SCUBA: a common-user submillimetre camera operating on the James Clerk Maxwell Telescope. *MNRAS*, **303**, 659–672.

Iben, I. J. (1965). Stellar Evolution. I. The Approach to the Main Sequence. *ApJ*, **141**, 993–+.

Imai, H., Watanabe, T., Omodaka, T., Nishio, M., Kameya, O., Miyaji, T., and Nakajima, J. (2003). The 3-D Kinematics of Water Masers in the W 51A Region. In J. Arthur & W. J. Henney, editor, *Revista Mexicana de Astronomia y Astrofisica Conference Series*, volume 15 of *Revista Mexicana de Astronomia y Astrofisica, vol. 27*, pages 202–202.

Jackson, J. M., Chambers, E. T., Rathborne, J. M., Simon, R., and Zhang, Q. (2008a). Infrared Dark Clouds. In H. Beuther, H. Linz, and T. Henning, editors, *Massive Star Formation: Observations Confront Theory*, volume 387 of *Astronomical Society of the Pacific Conference Series*, pages 44–+.

Jackson, J. M., Finn, S. C., Rathborne, J. M., Chambers, E. T., and Simon, R. (2008b). The Galactic Distribution of Infrared Dark Clouds. *ApJ*, **680**, 349–361.

Jackson, J. M., Finn, S. C., Chambers, E. T., Rathborne, J. M., and Simon, R. (2010). The "Nessie" Nebula: Cluster Formation in a Filamentary Infrared Dark Cloud. *ApJL*, **719**, L185–L189.

Kang, M., Bieging, J. H., Povich, M. S., and Lee, Y. (2009). Embedded Young Stellar Object Candidates in the Active Star-Forming Complex W51: Mass Function and Spatial Distribution. *ApJ*, **706**, 83–93.

Kang, M., Bieging, J. H., Kulesa, C. A., Lee, Y., Choi, M., and Peters, W. L. (2010). A CO Line and Infrared Continuum Study of the Active Star-forming Complex W51. *ApJS*, **190**, 58–76.

Kauffmann, J. and Pillai, T. (2010). How Many Infrared Dark Clouds Can form Massive Stars and Clusters? *ApJL*, **723**, L7–L12.

Kauffmann, J., Pillai, T., Shetty, R., Myers, P. C., and Goodman, A. A. (2010a). The Mass-Size Relation from Clouds to Cores. I. A New Probe of Structure in Molecular Clouds. *ApJ*, **712**, 1137–1146.

Kauffmann, J., Pillai, T., Shetty, R., Myers, P. C., and Goodman, A. A. (2010b). The Mass-size Relation from Clouds to Cores. II. Solar Neighborhood Clouds. *ApJ*, **716**, 433–445.

Kennicutt, Jr., R. C. (1983). The rate of star formation in normal disk galaxies. *ApJ*, **272**, 54–67.

Kenyon, S. J., Gómez, M., and Whitney, B. A. (2008). *Low Mass Star Formation in the Taurus-Auriga Clouds*, pages 405–+.

Kerton, C. R., Martin, P. G., Johnstone, D., and Ballantyne, D. R. (2001). A Submillimeter View of Star Formation near the H II Region KR 140. *ApJ*, **552**, 601–613.

Kim, G., Lee, C. W., Kim, J., Lee, Y., Ballesteros-Paredes, J., Myers, P. C., and Kurtz, S. (2010). Association of Infrared Dark Cloud Cores with YSOs: Starless or Starred IRDC Cores. *Journal of Korean Astronomical Society*, **43**, 9–23.

Kim, H., Nakajima, Y., Sung, H., Moon, D., and Koo, B. (2007). A Near-Infrared Study of the Highly-Obscured Active Star-Forming Region W51B. *Journal of Korean Astronomical Society*, **40**, 17–28.

Koo, B. and Moon, D. (1997a). Interaction between the W51C Supernova Remnant and a Molecular Cloud. I. H i 21 Centimeter Line Observations. *ApJ*, **475**, 194–+.

Koo, B., Lee, J., Seward, F. D., and Moon, D. (2005). Chandra Observations of the W51C Supernova Remnant. *ApJ*, **633**, 946–952.

Koo, B.-C. (1999). CO Observations of the W51B H II Region Complex. *ApJ*, **518**, 760–768.

Koo, B.-C. and Moon, D.-S. (1997b). Interaction between the W51C Supernova Remnant and a Molecular Cloud. II. Discovery of Shocked CO and HCO +. *ApJ*, **485**, 263–+.

Kramer, C., Stutzki, J., and Winnewisser, G. (1996). Structure and excitation conditions of the southern part of the Orion B molecular cloud: a CO multiline study. *A&A*, **307**, 915–935.

Kramer, C., Stutzki, J., Rohrig, R., and Corneliussen, U. (1998). Clump mass spectra of molecular clouds. *A&A*, **329**, 249–264.

Kregel, M., van der Kruit, P. C., and de Blok, W. J. G. (2004). Structure and kinematics of edge-on galaxy discs - II. Observations of the neutral hydrogen. *MNRAS*, **352**, 768–786.

Krishna Swamy, K. S. (2005). *Dust in the universe : similarities and differences*.

Kroupa, P. (2001). On the variation of the initial mass function. *MNRAS*, **322**, 231–246.

Kroupa, P., Tout, C. A., and Gilmore, G. (1993). The distribution of low-mass stars in the Galactic disc. *MNRAS*, **262**, 545–587.

Krumholz, M. R. and McKee, C. F. (2008). A minimum column density of 1gcm-2 for massive star formation. *Nature*, **451**, 1082–1084.

Krumholz, M. R., Klein, R. I., and McKee, C. F. (2005). Radiation pressure in massive star formation. In R. Cesaroni, M. Felli, E. Churchwell, & M. Walmsley, editor, *Massive Star Birth: A Crossroads of Astrophysics*, volume 227 of *IAU Symposium*, pages 231–236.

Krumholz, M. R., Klein, R. I., McKee, C. F., Offner, S. S. R., and Cunningham, A. J. (2009). The Formation of Massive Star Systems by Accretion. *Science*, **323**, 754–.

Kuiper, R., Klahr, H., Beuther, H., and Henning, T. (2010). Circumventing the Radiation Pressure Barrier in the Formation of Massive Stars via Disk Accretion. *ApJ*, **722**, 1556–1576.

Kumar, M. S. N., Kamath, U. S., and Davis, C. J. (2004). Embedded star clusters in the W51 giant molecular cloud. *MNRAS*, **353**, 1025–1034.

Kundu, M. R. and Velusamy, T. (1967). A study of galactic sources W 51 and W 44. *Annales d'Astrophysique*, **30**, 59–+.

Kurtz, S. (2005). Hypercompact HII regions. In R. Cesaroni, M. Felli, E. Churchwell, & M. Walmsley, editor, *Massive Star Birth: A Crossroads of Astrophysics*, volume 227 of *IAU Symposium*, pages 111–119.

Kurtz, S. and Hofner, P. (2005). Water Masers Toward Ultracompact H II Regions. *AJ*, **130**, 711–720.

Kurtz, S., Cesaroni, R., Churchwell, E., Hofner, P., and Walmsley, C. M. (2000). Hot Molecular Cores and the Earliest Phases of High-Mass Star Formation. *Protostars and Planets IV*, pages 299–+.

Kutner, M. L. and Ulich, B. L. (1981). Recommendations for calibration of millimeter-wavelength spectral line data. *ApJ*, **250**, 341–348.

Lada, C. J. (1985). Cold outflows, energetic winds, and enigmatic jets around young stellar objects. *ARA&A*, **23**, 267–317.

Lada, C. J. (1987). Star formation - From OB associations to protostars. In M. Peimbert & J. Jugaku, editor, *Star Forming Regions*, volume 115 of *IAU Symposium*, pages 1–17.

Lada, C. J. and Wilking, B. A. (1984). The nature of the embedded population in the Rho Ophiuchi dark cloud - Mid-infrared observations. *ApJ*, **287**, 610–621.

Ladd, E. F., Fuller, G. A., and Deane, J. R. (1998). C 18O and C 17O Observations of Embedded Young Stars in the Taurus Molecular Cloud. I. Integrated Intensities and Column Densities. *ApJ*, **495**, 871–+.

Lang, K. R. (1980). *Astrophysical Formulae*.

Langer, W. D. and Penzias, A. A. (1990). C-12/C-13 isotope ratio across the Galaxy from observations of C-13/O-18 in molecular clouds. *ApJ*, **357**, 477–492.

Larson, R. B. (1981). Turbulence and star formation in molecular clouds. *MNRAS*, **194**, 809–826.

Larson, R. B. (1982). Mass spectra of young stars. *MNRAS*, **200**, 159–174.

Leisawitz, D. (1990). A CO survey of regions around 34 open clusters. II - Physical properties of cataloged molecular clouds. *ApJ*, **359**, 319–343.

Leisawitz, D., Bash, F. N., and Thaddeus, P. (1989). A CO survey of regions around 34 open clusters. *ApJS*, **70**, 731–812.

Lis, D. C. and Carlstrom, J. E. (1994). Submillimeter continuum survey of the Galactic center. *ApJ*, **424**, 189–199.

Lis, D. C. and Menten, K. M. (1998). Infrared Space Observatory Long Wavelength Spectrometer Observations of a Cold Giant Molecular Cloud Core near the Galactic Center. *ApJ*, **507**, 794–804.

Lombardi, M., Alves, J., and Lada, C. J. (2010). Larson's third law and the universality of molecular cloud structure. *A&A*, **519**, L7+.

Lucas, P. W., Hoare, M. G., Longmore, A., Schröder, A. C., Davis, C. J., Adamson, A., Bandyopadhyay, R. M., de Grijs, R., and et al. (2008). The UKIDSS Galactic Plane Survey. *MNRAS*, **391**, 136–163.

Lumsden, S. L., Hoare, M. G., Oudmaijer, R. D., and Richards, D. (2002). The population of the Galactic plane as seen by MSX. *MNRAS*, **336**, 621–636.

Mac Low, M. and Klessen, R. S. (2004). Control of star formation by supersonic turbulence. *Reviews of Modern Physics*, **76**, 125–194.

Mackenzie, T., Braglia, F. G., Gibb, A. G., and et al. (2010). A Pilot Study for the SCUBA-2 'All-Sky' Survey. *ArXiv e-prints*.

MacLaren, I., Richardson, K. M., and Wolfendale, A. W. (1988). Corrections to virial estimates of molecular cloud masses. *ApJ*, **333**, 821–825.

Maddalena, R. J. and Thaddeus, P. (1985). A large, cold, and unusual molecular cloud in Monoceros. *ApJ*, **294**, 231–237.

Maíz Apellániz, J. and Úbeda, L. (2005). Numerical Biases on Initial Mass Function Determinations Created by Binning. *ApJ*, **629**, 873–880.

Mardones, D., Myers, P. C., Tafalla, M., Wilner, D. J., Bachiller, R., and Garay, G. (1997). A Search for Infall Motions toward Nearby Young Stellar Objects. *ApJ*, **489**, 719–+.

Marshall, D. J., Joncas, G., and Jones, A. P. (2009). Distribution and Characteristics of Infrared Dark Clouds Using Genetic Forward Modelling. *ApJ*, **706**, 727–737.

Martin, A. H. M. (1972). High resolution observations of W51. *MNRAS*, **157**, 31–40.

Mason, B. D., Hartkopf, W. I., Gies, D. R., Henry, T. J., and Helsel, J. W. (2009). The High Angular Resolution Multiplicity of Massive Stars. *AJ*, **137**, 3358–3377.

McKee, C. F. and Ostriker, E. C. (2007). Theory of Star Formation. *ARA&A*, **45**, 565–687.

McKee, C. F. and Tan, J. C. (2003). The Formation of Massive Stars from Turbulent Cores. *ApJ*, **585**, 850–871.

Megeath, S. T., Allgaier, E., Young, E., Allen, T., Pipher, J. L., and Wilson, T. L. (2009). Detection of Star Formation in the Unusually Cold Giant Molecular Cloud G216-2.5. *AJ*, **137**, 4072–4082.

Mehringer, D. M. (1994). Radio continuum and radio recombination line observations of W51. *ApJS*, **91**, 713–748.

Mellinger, A. (2008). *Star Forming Regions along the Milky Way: A Panoramic View*, pages 1–+.

Menten, K. (1991). Methanol Masers and Submillimeter WavelengthWater Masers in Star-Forming Regions. In A. D. Haschick & P. T. P. Ho, editor, *Atoms, Ions and Molecules: New Results in Spectral Line Astrophysics*, volume 16 of *Astronomical Society of the Pacific Conference Series*, pages 119–+.

Miller, G. E. and Scalo, J. M. (1979). The initial mass function and stellar birthrate in the solar neighborhood. *ApJS*, **41**, 513–547.

Mitchell, G. F., Johnstone, D., Moriarty-Schieven, G., Fich, M., and Tothill, N. F. H. (2001). A Submillimeter Dust and Gas Study of the Orion B Molecular Cloud. *ApJ*, **556**, 215–229.

Molinari, S., Swinyard, B., Barlow, M., Bernard, J. P., Boulanger, F., Testi, L., White, G., and Hi-Gal Team (2005). A Herschel Far Infrared Survey of the Galactic Plane. In *Protostars and Planets V*, pages 8163–+.

Molinari, S., Swinyard, B., Bally, J., and et al. (2010a). Clouds, filaments, and protostars: The Herschel Hi-GAL Milky Way. *A&A*, **518**, L100+.

Molinari, S., Swinyard, B., Bally, J., and et al. (2010b). Hi-GAL: The Herschel Infrared Galactic Plane Survey. *PASP*, **122**, 314–325.

Moore, T. J. T., Shipman, R. F., Plume, R., Hoare, M. G., and Jps International Collaboration (2005). Legacy Surveys with the JCMT: The JCMT Plane Survey. In *Protostars and Planets V*, pages 8370–+.

Moore, T. J. T., Bretherton, D. E., Fujiyoshi, T., Ridge, N. A., Allsopp, J., Hoare, M. G., Lumsden, S. L., and Richer, J. S. (2007). The star-forming content of the W3 giant molecular cloud. *MNRAS*, **379**, 663–673.

Motte, F., Andre, P., and Neri, R. (1998). The initial conditions of star formation in the rho Ophiuchi main cloud: wide-field millimeter continuum mapping. *A&A*, **336**, 150–172.

Motte, F., Bontemps, S., Schilke, P., Schneider, N., Menten, K. M., and Broguière, D. (2007). The earliest phases of high-mass star formation: a 3 square degree millimeter continuum mapping of Cygnus X. *A&A*, **476**, 1243–1260.

Mottram, J. C., Hoare, M. G., Davies, B., Lumsden, S. L., Oudmaijer, R. D., Urquhart, J. S., Moore, T. J. T., Cooper, H. D. B., and Stead, J. J. (2011). The Luminosity Functions and Timescales of MYSOs and Compact HII regions. *ArXiv e-prints*.

Mueller, K. E., Shirley, Y. L., Evans, II, N. J., and Jacobson, H. R. (2002). The Physical Conditions for Massive Star Formation: Dust Continuum Maps and Modeling. *ApJS*, **143**, 469–497.

Muench, A., Getman, K., Hillenbrand, L., and Preibisch, T. (2008). *Star Formation in the Orion Nebula I: Stellar Content*, pages 483–+.

Mufson, S. L. and Liszt, H. S. (1979). The H II region-molecular cloud complex W51. *ApJ*, **232**, 451–466.

Mundy, L. G. (1994). Properties of Dark Cloud and Warm Cloud Cores. In D. P. Clemens & R. Barvainis, editor, *Clouds, Cores, and Low Mass Stars*, volume 65 of *Astronomical Society of the Pacific Conference Series*, pages 35–+.

Myers, P. C., Linke, R. A., and Benson, P. J. (1983). Dense cores in dark clouds. I - CO observations and column densities of high-extinction regions. *ApJ*, **264**, 517–537.

Myers, P. C., Dame, T. M., Thaddeus, P., Cohen, R. S., Silverberg, R. F., Dwek, E., and Hauser, M. G. (1986). Molecular clouds and star formation in the inner galaxy - A comparison of CO, H II, and far-infrared surveys. *ApJ*, **301**, 398–422.

Nutter, D. and Ward-Thompson, D. (2007). A SCUBA survey of Orion - the low-mass end of the core mass function. *MNRAS*, **374**, 1413–1420.

O'Dell, C. R. (2001). The Orion Nebula and its Associated Population. *ARA&A*, **39**, 99–136.

Okumura, S., Mori, A., Nishihara, E., Watanabe, E., and Yamashita, T. (2000). The Initial Mass Function of a Massive Star-forming Region W51. *ApJ*, **543**, 799–821.

Okumura, S., Miyawaki, R., Sorai, K., Yamashita, T., and Hasegawa, T. (2001). A Large-Scale CO Mapping of the Central Region of W 51. *PASJ*, **53**, 793–798.

Olmi, L., Cesaroni, R., and Walmsley, C. M. (1993). Ammonia and methyl cyanide in hot cores. *A&A*, **276**, 489–+.

Onishi, T., Mizuno, A., Kawamura, A., Tachihara, K., and Fukui, Y. (2002). A Complete Search for Dense Cloud Cores in Taurus. *ApJ*, **575**, 950–973.

Ormel, C. W., Shipman, R. F., Ossenkopf, V., and Helmich, F. P. (2005). The modelling of infrared dark cloud cores. *A&A*, **439**, 613–625.

Ossenkopf, V. and Henning, T. (1994). Dust opacities for protostellar cores. *A&A*, **291**, 943–959.

Pankonin, V., Payne, H. E., and Terzian, Y. (1979). The structure of W51. *A&A*, **75**, 365–370.

Parmentier, G., Goodwin, S. P., Kroupa, P., and Baumgardt, H. (2009). Gas removal and the initial mass function of star clusters. *ApSS*, **324**, 327–332.

Parsons, H., Thompson, M. A., and Chrysostomou, A. (2009). Infrared dark cloud cores in the SCUBA Legacy Catalogue. *MNRAS*, **399**, 1506–1522.

Pascale, E., Ade, P. A. R., Bock, J. J., and et al. (2008). The Balloon-borne Large Aperture Submillimeter Telescope: BLAST. *ApJ*, **681**, 400–414.

Perault, M., Omont, A., Simon, G., and et al. (1996). First ISOCAM images of the Milky Way. *A&A*, **315**, L165–L168.

Peretto, N. and Fuller, G. A. (2009). The initial conditions of stellar protocluster formation. I. A catalogue of Spitzer dark clouds. *ArXiv e-prints*.

Peretto, N., Fuller, G. A., Plume, R., and et al. (2010). Mapping the column density and dust temperature structure of IRDCs with Herschel. *A&A*, **518**, L98+.

Pestalozzi, M. R., Chrysostomou, A., Collett, J. L., Minier, V., Conway, J., and Booth, R. S. (2007). A general catalogue of 6.7 GHz methanol masers. II. statistical analysis. *A&A*, **463**, 1009–1016.

Phillips, C. (1998). *Class II Methanol Masers at High Resolution*. Ph.D. thesis, AA(Joint Institute for VLBI in Europe, Postbus 2, 7990 AA Dwingeloo, The Netherlands; ¡EMAIL¿phillips@jive.nfra.nl¡/EMAIL¿).

Phillips, C. J. and van Langevelde, H. J. (2005). The Methanol Maser Emission in W51. *ApSS*, **295**, 225–229.

Pillai, T., Wyrowski, F., Carey, S. J., and Menten, K. M. (2006a). Ammonia in infrared dark clouds. *A&A*, **450**, 569–583.

Pillai, T., Wyrowski, F., Menten, K. M., and Krügel, E. (2006b). High mass star formation in the infrared dark cloud G11.11-0.12. *A&A*, **447**, 929–936.

Pineda, J. E., Rosolowsky, E. W., and Goodman, A. A. (2009). The Perils of Clumpfind: The Mass Spectrum of Substructures in Molecular Clouds. *ApJL*, **699**, L134–L138.

Plume, R., Jaffe, D. T., Evans, II, N. J., Martin-Pintado, J., and Gomez-Gonzalez, J. (1997). Dense Gas and Star Formation: Characteristics of Cloud Cores Associated with Water Masers. *ApJ*, **476**, 730–+.

Preibisch, T., Zinnecker, H., Weigelt, G., Hofmann, K., Schertl, D., and Balega, Y. (2000). Multiplicity of the Massive Stars in the Orion Nebula cluster and Implications on their Formation Mechanism. In F. Favata, A. Kaas, & A. Wilson, editor, *Star Formation from the Small to the Large Scale*, volume 445 of *ESA Special Publication*, pages 495–+.

Press, W. H., Flannery, B. P., and Teukolsky, S. A. (1986). *Numerical recipes. The art of scientific computing*.

Prialnik, D. (2000). *An Introduction to the Theory of Stellar Structure and Evolution*.

Purcell, C. (2006). What?s in the brew? A study of the molecular environment of methanol masers and UCHII regions. *Ph.D Thesis submitted to The University of New South Wales*.

Purcell, C. R., Hoare, M. G., and Diamond, P. (2008). The CORNISH Survey of the Galactic Plane. In H. Beuther, H. Linz, and T. Henning, editors, *Massive Star Formation: Observations Confront Theory*, volume 387 of *Astronomical Society of the Pacific Conference Series*, pages 389–+.

Ragan, S. E., Bergin, E. A., Plume, R., Gibson, D. L., Wilner, D. J., O'Brien, S., and Hails, E. (2006). Molecular Line Observations of Infrared Dark Clouds: Seeking the Precursors to Intermediate and Massive Star Formation. *ApJS*, **166**, 567–584.

Ragan, S. E., Bergin, E. A., and Gutermuth, R. A. (2009). Detection of Structure in Infrared-Dark Clouds with Spitzer: Characterizing Star Formation in the Molecular Ring. *ApJ*, **698**, 324–349.

Rathborne, J. M., Jackson, J. M., Chambers, E. T., Simon, R., Shipman, R., and Frieswijk, W. (2005). Massive Protostars in the Infrared Dark Cloud MSXDC G034.43+00.24. *ApJL*, **630**, L181–L184.

Rathborne, J. M., Jackson, J. M., and Simon, R. (2006). Infrared Dark Clouds: Precursors to Star Clusters. *ApJ*, **641**, 389–405.

Rathborne, J. M., Simon, R., and Jackson, J. M. (2007). The Detection of Protostellar Condensations in Infrared Dark Cloud Cores. *ApJ*, **662**, 1082–1092.

Rathborne, J. M., Jackson, J. M., Zhang, Q., and Simon, R. (2008). Submillimeter Array Observations of Infrared Dark Clouds: A Tale of Two Cores. *ApJ*, **689**, 1141–1149.

Rathborne, J. M., Johnson, A. M., Jackson, J. M., Shah, R. Y., and Simon, R. (2009). Molecular Clouds and Clumps in the Boston University-Five College Radio Astronomy Observatory Galactic Ring Survey. *ApJS*, **182**, 131–142.

Redman, M. P., Keto, E., and Rawlings, J. M. C. (2006). Oscillations in the stable starless core Barnard 68. *MNRAS*, **370**, L1–L5.

Reid, M. A. and Wilson, C. D. (2006a). High-Mass Star Formation. II. The Mass Function of Submillimeter Clumps in M17. *ApJ*, **644**, 990–1005.

Reid, M. A. and Wilson, C. D. (2006b). High-Mass Star Formation. III. The Functional Form of the Submillimeter Clump Mass Function. *ApJ*, **650**, 970–984.

Reid, M. A., Wadsley, J., Petitclerc, N., and Sills, A. (2010). Measuring the Clump Mass Function in the Age of SCUBA2, Herschel, and ALMA. *ApJ*, **719**, 561–575.

Rieke, G. H. and Lebofsky, M. J. (1985). The interstellar extinction law from 1 to 13 microns. *ApJ*, **288**, 618–621.

Rohlfs, K. and Wilson, T. L. (2004). *Tools of radio astronomy*.

Roy, A., Ade, P. A. R., Bock, J. J., and et al. (2011). The Balloon-borne Large Aperture Submillimeter Telescope (BLAST) 2005: A 10 $\deg^2$ Survey of Star Formation in Cygnus X. *ApJ*, **727**, 114–+.

Russeil, D. (2003). Star-forming complexes and the spiral structure of our Galaxy. *A&A*, **397**, 133–146.

Salpeter, E. E. (1955). The Luminosity Function and Stellar Evolution. *ApJ*, **121**, 161–+.

Sandell, G., Wright, M., and Forster, J. R. (2003). NGC 7538S-a High-Mass Protostar with a Massive Rotating Disk. *ApJL*, **590**, L45–L48.

Sato, F. (1973). On the Distance of the Galactic Radio Source W 51. *PASJ*, **25**, 135–+.

Sato, M., Reid, M. J., Brunthaler, A., and Menten, K. M. (2010). Trigonometric Parallax of W51 Main/South. *ApJ*, **720**, 1055–1065.

Scalo, J. M. (1986). The stellar initial mass function. *Fundamentals of Cosmic Physics*, **11**, 1–278.

Schneider, N. and Brooks, K. (2004). The Bias of Molecular Clump Identification Programs: the Example of the Carina Molecular Clouds. *Publications of the Astronomical Society of Australia*, **21**, 290–301.

Schneps, M. H., Lane, A. P., Downes, D., Moran, J. M., Genzel, R., and Reid, M. J. (1981). Proper motions and distances of H2O maser sources. III - W51NORTH. *ApJ*, **249**, 124–133.

Schuller, F., Menten, K. M., Contreras, Y., Wyrowski, F., Schilke, P., Bronfman, L., Henning, T., Walmsley, C. M., and et al. (2009). ATLASGAL - The APEX Telescope Large Area Survey of the Galaxy at 870 microns. *ArXiv e-prints*.

Scoville, N. Z. and Solomon, P. M. (1973). Molecular Clouds in W49 and W51. *ApJ*, **180**, 31–54.

Scoville, N. Z., Sanders, D. B., and Clemens, D. P. (1986). High-mass star formation due to cloud-cloud collisions. *ApJL*, **310**, L77–L81.

Sewiło, M., Churchwell, E., Kurtz, S., Goss, W. M., and Hofner, P. (2008). Internal Dynamics of the Hypercompact H II Region G28.20-0.04N. *ApJ*, **681**, 350–354.

Shepherd, D. S. and Churchwell, E. (1996). Bipolar Molecular Outflows in Massive Star Formation Regions. *ApJ*, **472**, 225–+.

Shinnaga, H., Phillips, T. G., Furuya, R. S., and Cesaroni, R. (2008). Submillimeter Observations of the Isolated Massive Dense Clump IRAS 20126+4104. *ApJ*, **682**, 1103–1113.

Simon, R., Jackson, J. M., Rathborne, J. M., and Chambers, E. T. (2006a). A Catalog of Midcourse Space Experiment Infrared Dark Cloud Candidates. *ApJ*, **639**, 227–236.

Simon, R., Rathborne, J. M., Shah, R. Y., Jackson, J. M., and Chambers, E. T. (2006b). The Characterization and Galactic Distribution of Infrared Dark Clouds. *ApJ*, **653**, 1325–1335.

Simpson, R. J., Nutter, D., and Ward-Thompson, D. (2008). The initial conditions of star formation - VIII. An observational study of the Ophiuchus cloud L1688 and implications for the pre-stellar core mass function. *MNRAS*, **391**, 205–214.

Skrutskie, M. F., Schneider, S. E., Stiening, R., Strom, S. E., Weinberg, M. D., Beichman, C., Chester, T., Cutri, R., and et al. (1997). The Two Micron All Sky Survey (2MASS): Overview and Status. In F. Garzon, N. Epchtein, A. Omont, B. Burton, & P. Persi, editor, *The Impact of Large Scale Near-IR Sky Surveys*, volume 210 of *Astrophysics and Space Science Library*, pages 25–+.

Smith, H., Buckle, J., Hills, R., Bell, G., Richer, J., Curtis, E., Withington, S., Leech, J., Williamson, R., Dent, W., Hastings, P., Redman, R., Wooff, B., Yeung, K., Friberg, P., Walther, C., Kackley, R., Jenness, T., Tilanus, R., Dempsey, J., Kroug, M., Zijlstra, T., and Klapwijk, T. M. (2008a). HARP: a submillimetre heterodyne array receiver operating on the James Clerk Maxwell Telescope. In *Society of Photo-Optical Instrumentation Engineers (SPIE) Conference Series*, volume 7020 of *Society of Photo-Optical Instrumentation Engineers (SPIE) Conference Series*.

Smith, L. F., Biermann, P., and Mezger, P. G. (1978). Star formation rates in the Galaxy. *A&A*, **66**, 65–76.

Smith, R. J., Clark, P. C., and Bonnell, I. A. (2008b). The structure of molecular clouds and the universality of the clump mass function. *MNRAS*, **391**, 1091–1099.

Sobolev, A. M., Cragg, D. M., Ellingsen, S. P., Gaylard, M. J., Goedhart, S., Henkel, C., Kirsanova, M. S., Ostrovskii, A. B., Pankratova, N. V., Shelemei, O. V., van der Walt, D. J., Vasyunina, T. S., and Voronkov, M. A. (2007). How do methanol masers manage to appear in the youngest star vicinities and isolated molecular clumps? In J. M. Chapman & W. A. Baan, editor, *IAU Symposium*, volume 242 of *IAU Symposium*, pages 81–88.

Sollins, P. K., Zhang, Q., and Ho, P. T. P. (2004). The Case for Local Collapse in the W51 Star-forming Region. *ApJ*, **606**, 943–951.

Solomon, P. M., Rivolo, A. R., Barrett, J., and Yahil, A. (1987). Mass, luminosity, and line width relations of Galactic molecular clouds. *ApJ*, **319**, 730–741.

Stahler, S. W. and Palla, F. (2005). *The Formation of Stars*.

Stamatellos, D., Whitworth, A. P., and Ward-Thompson, D. (2007). The dust temperatures of the pre-stellar cores in the ρ Oph main cloud and in other star-forming regions: consequences for the core mass function. *MNRAS*, **379**, 1390–1400.

Stanke, T., Smith, M. D., Gredel, R., and Khanzadyan, T. (2006). An unbiased search for the signatures of protostars in the ρ Ophiuchi molecular cloud . II. Millimetre continuum observations. *A&A*, **447**, 609–622.

Störzer, H., Zielinsky, M., Stutzki, J., and Sternberg, A. (2000). Low-J CO line emission from PDRs: a natural explanation for the narrow range of observed line ratios. *A&A*, **358**, 682–688.

Stutzki, J. and Guesten, R. (1990). High spatial resolution isotopic CO and CS observations of M17 SW - The clumpy structure of the molecular cloud core. *ApJ*, **356**, 513–533.

Tan, J. C. (2003). Theories of Massive Star Formation: Collisions, Accretion and the View from the "I" of Orion (Invited Review). In J. M. De Buizer & N. S. van der Bliek, editor, *Galactic Star Formation Across the Stellar Mass Spectrum*, volume 287 of *Astronomical Society of the Pacific Conference Series*, pages 207–218.

Tennekes, P. P., Harju, J., Juvela, M., and Tóth, L. V. (2006). HCN and HNC mapping of the protostellar core Chamaeleon-MMS1. *A&A*, **456**, 1037–1043.

Testi, L., Felli, M., and Taylor, G. B. (1999). Young massive stars in the ISOGAL survey. I. VLA observations of the ISOGAL l= +45 field. *A&AS*, **138**, 71–85.

Teyssier, D., Hennebelle, P., and Pérault, M. (2002). Radio-millimetre investigation of galactic infrared dark clouds. *A&A*, **382**, 624–638.

Thompson, M. A. (1999). Hot cores and HII regions: Molecular line observations of massive star formation. *Ph.D Thesis submitted to The University of Kent*.

Thompson, M. A., Hatchell, J., Walsh, A. J., MacDonald, G. H., and Millar, T. J. (2006). A SCUBA imaging survey of ultracompact HII regions. The environments of massive star formation. *A&A*, **453**, 1003–1026.

Thompson, M. A., Serjeant, S., Jenness, T., Scott, D., Ashdown, M., Brunt, C., Butner, H., Chapin, E., and et al. (2007). The SCUBA-2 "All-Sky" Survey. *ArXiv e-prints*, **704**.

Townes, C. H. (1993). The early years of research on astronomical masers. In A. W. Clegg & G. E. Nedoluha, editor, *Astrophysical Masers*, volume 412 of *Lecture Notes in Physics, Berlin Springer Verlag*, pages 3–11.

Townes, C. H. and Schawlow, A. L. (1975). *Microwave spectroscopy.*

van der Walt, J. (2005). On the number and lifetime of 6.7-GHz methanol masers. *MNRAS*, **360**, 153–158.

van der Wiel, M. H. D. and Shipman, R. F. (2008). Characterizing Star Formation Activity in Infrared Dark Cloud MSXDC G048.65-00.29. *A&A*, **490**, 655–664.

van Dishoeck, E. F. and Blake, G. A. (1998). Chemical Evolution of Star-Forming Regions. *ARA&A*, **36**, 317–368.

Wall, J. V. and Jenkins, C. R. (2003). *Practical Statistics for Astronomers*.

Walsh, A. J., Hyland, A. R., Robinson, G., and Burton, M. G. (1997). Studies of ultracompact HII regions - I. Methanol maser survey of IRAS-selected sources. *MNRAS*, **291**, 261–278.

Weaver, H., Williams, D. R. W., Dieter, N. H., and Lum, W. T. (1965). Observations of a Strong Unidentified Microwave Line and of Emission from the OH Molecule. *Nature*, **208**, 29–31.

Westerhout, G. (1958). A survey of the continuous radiation from the Galactic System at a frequency of 1390 Mc/s. *Bull. Astron. Inst. Netherlands*, **14**, 215–+.

Whittet, D. C. B. (1992). *Dust in the galactic environment*.

Williams, J. P. and McKee, C. F. (1997). The Galactic Distribution of OB Associations in Molecular Clouds. *ApJ*, **476**, 166–+.

Williams, J. P., de Geus, E. J., and Blitz, L. (1994). Determining structure in molecular clouds. *ApJ*, **428**, 693–712.

Williams, J. P., Blitz, L., and McKee, C. F. (2000). The Structure and Evolution of Molecular Clouds: from Clumps to Cores to the IMF. *Protostars and Planets IV*, pages 97–+.

Wilson, R. W., Langer, W. D., and Goldsmith, P. F. (1981). A determination. *ApJL*, **243**, L47–L52.

Wilson, T. L. (1999). Isotopes in the interstellar medium and circumstellar envelopes. *Reports on Progress in Physics*, **62**, 143–185.

Wilson, T. L. and Rood, R. (1994). Abundances in the Interstellar Medium. *ARA&A*, **32**, 191–226.

Wood, D. O. S. and Churchwell, E. (1989a). Massive stars embedded in molecular clouds - Their population and distribution in the galaxy. *ApJ*, **340**, 265–272.

Wood, D. O. S. and Churchwell, E. (1989b). The morphologies and physical properties of ultracompact H II regions. *ApJS*, **69**, 831–895.

Xu, Y., Reid, M. J., Menten, K. M., Brunthaler, A., Zheng, X. W., and Moscadelli, L. (2009). Trigonometric Parallaxes of Massive Star-Forming Regions: III. G59.7+0.1 and W 51 IRS2. *ApJ*, **693**, 413–418.

Yorke, H. W. and Sonnhalter, C. (2002). On the Formation of Massive Stars. *ApJ*, **569**, 846–862.

Zapata, L. A., Ho, P. T. P., Schilke, P., Rodríguez, L. F., Menten, K., Palau, A., and Garrod, R. T. (2009). A Ring/Disk/Outflow System Associated with W51 North: A Very Massive Star in the Making. *ApJ*, **698**, 1422–1428.

Zhang, Q. and Ho, P. T. P. (1995). Ammonia Maser in a Molecular Outflow toward W51. *ApJL*, **450**, L63+.

Zhang, Q., Hunter, T. R., Brand, J., Sridharan, T. K., Molinari, S., Kramer, M. A., and Cesaroni, R. (2001). Search for CO Outflows toward a Sample of 69 High-Mass Protostellar Candidates: Frequency of Occurrence. *ApJL*, **552**, L167–L170.

Zinnecker, H. and Yorke, H. W. (2007). Toward Understanding Massive Star Formation. *ARA&A*, **45**, 481–563.